Functional iron oxide-based hybrid nanostructures

Dissertation

zur Erlangung des akademischen Grades

doctor rerum naturalium

(Dr. rer. nat.)

im Fach Chemie

eingereicht an der

Mathematisch-Naturwissenschaftlichen Fakultät

der Humboldt-Universität zu Berlin

von

M.Sc. Valentina Rebuttini

Präsident der Humboldt-Universität zu Berlin
Prof. Dr. Jan-Hendrik Olbertz

Dekan der Mathematisch-Naturwissenschaftlichen Fakultät
Prof. Dr. Elmar Kulke

Gutachter/innen:
1. Prof. Dr. Nicola Pinna
2. Prof. Dr. Erhard Kemnitz
3. Dr. Habil. Frédéric Favier

Tag der mündlichen Prüfung: 02 Oktober 2014

Abstract

In view of the high surface-to-volume ratio, surface chemistry of nanoparticles significantly contributes in determining material properties. Therefore, the control on chemical surface composition is regarded as a crucial issue in manipulating and assembling nanoparticles for fabricating nanostructured hybrid materials exhibiting desired properties and functionalities.

This thesis describes diverse approaches of chemical functionalization as a general strategy to tailor material properties depending on the target application. Particular attention was dedicated to the surface chemistry of iron oxide nanoparticles. Crystalline 10 nm-sized magnetite nanoparticles synthesized through the "benzyl alcohol route" exhibit superparamagnetic behaviour. For this reason they are regarded as suitable solid supports for the fabrication of recoverable devices, which is a fundamental requirement for several of the reported studies.

Here it is demonstrated, *via* the fabrication of novel hybrid materials, that the ease of functionalization of iron oxide nanoparticles renders this material a versatile platform for the development of diverse surface chemistries.

The simplicity and versatility of post-synthesis strategies was demonstrated by coating magnetite nanoparticles with undecanoic acid and citric acid, which led to stable organic and aqueous nanoparticles dispersions, respectively. The influence that the ligand shell can have on the electronic properties of a single magnetite nanoparticle was a central aspect of this study.

A covalent organic functionalization strategy was developed for the synthesis of two recoverable magnetic molecular receptors. The first targeted the recognition of drugs metabolites and biomarkers. It is based on the use of organosilanes coupling agents for the coating of the iron oxide nanoparticles surface with a multifunctional organic shell constituted by PEG chains and amino groups. While the former impart partial water dispersibility, the latter permits the conjugation of tetraphosphonate cavitands through carbodiimide chemistry. A second approach aimed to the heterogeneous resolution of a racemic mixture of an inherently chiral cavitand. The organosilane shell was coupled with enantiopure N-methyl-L-alanine which showed a selective recognition of chiral phosphonate cavitands.

Further studies focused on the fabrication of nanocomposites. Graphene oxide-iron oxide composites were successfully fabricated through an *ex-situ* approach based on non-covalent interactions between the component phases. The effects of surface functionalities on the loading and distribution of iron oxide nanoparticles were studied by introducing selected functionalities at the graphene oxide surface through diazonium chemistry. Detailed structural and chemical characterization and study of the electrochemical properties were carried out in order to elucidate structure-properties relationship.

Finally, the development of a non-aqueous one-pot synthesis route to gold-iron oxide hetero-nanostructures was described. Two metal precursors and several reaction parameters were investigated and a particular emphasis was dedicated to study the influence of small organic molecules in promoting the formation of the heterostructures.

Kurzfassung

Die Eigenschaften von Nanomaterialien werden aufgrund ihres großen Oberfläche-zu-Volumen-Verhältnisses entscheidend von der Chemie der Partikeloberfläche bestimmt. Die gezielte Einstellung der Oberflächenzusammensetzung spielt deshalb eine entscheidende Rolle bei der Herstellung von nanostrukturierten Hybridmaterialien mit anwendungsorientierten Eigenschaften.

In der vorliegenden Arbeit wird das Prinzip der chemischen Oberflächenmodifikation als allgemeine Synthesestrategie beschrieben. Davon ausgehend werden verschiedene Ansätze der chemischen Funktionalisierung dargestellt, mit denen die Eigenschaften der erhaltenen Materialien eingestellt werden können. Im Fokus der Arbeit stehen Eisenoxid-Nanopartikel, die über die „Benzylalkohol-Route“ dargestellt werden. Die so erhaltenen kristallinen Nanopartikel mit Größen von 10 nm besitzen superparamagnetische Eigenschaften. Dadurch eignen sich die Partikel hervorragend als Feststoffträger für wiederverwendbare Sensoren, da deren Superparamagnetismus von grundlegender Bedeutung für die Wiederverwendbarkeit ist. Es wird auf Basis dieser einfachen und vielseitig anwendbaren Funktionalisierung die Herstellung von neuartigen Hybridmaterialien gezeigt. Ausgehend von diesen Materialien können weitere Oberflächenmodifikationen erfolgen. Durch Funktionalisierung von Magnetit-Nanopartikeln mit Undekan- und Zitronensäure konnten stabile Dispersionen der Nanopartikel in Wasser und organischen Lösungsmitteln erhalten werden. Der Einfluss der Ligandenhülle auf die elektronischen Eigenschaften der einzelnen Magnetit-Partikel stand im Mittelpunkt der durchgeführten Untersuchungen.

Zur Funktionalisierung zweier magnetischer molekularer Rezeptoren wurde eine Synthesestrategie entwickelt, bei der organische Gruppen kovalent angebunden wurden. Der erste Rezeptor kann zur Erkennung von Biomarkern und den Metaboliten von Pharmazeutika eingesetzt werden. Die Beschichtung der Oberflächen der Eisenoxid-Nanopartikel gelang dabei durch die Verwendung von Organosilan-basierten Kopplungsreagenzien. Auf diesem Wege wurden multifunktionelle organische Hüllen, bestehend aus PEG und Aminogruppen, erhalten. Während die PEG-Ketten die Löslichkeit in Wasser erhöhen, erlauben die Aminogruppen eine Anbindung der Tetraphosphonat-*cavitands* über Carbodiimid-Chemie. Der zweite Rezeptor konnte zur Auftrennung eines racemischen Gemisches eines chiralen *cavitand* eingesetzt werden. Dafür wurde die Organosilan-Hülle mit enantiomerenreinem N-methyl-L-alanin umgesetzt und eine selektive Erkennung der chiralen Phosphonat-cavitand erreicht.

Ein weiteres Augenmerk dieser Arbeit lag auf der Herstellung von Nanokompositen. Die Darstellung von Graphenoxid-Eisenoxid-Kompositen gelang erfolgreich durch ein *ex-situ* Verfahren. Die Bildung des Komposits erfolgte dabei unter Ausnutzung nicht-kovalenter Wechselwirkungen zwischen den beiden Komponenten. Es wurde der Einfluss der Oberflächenfunktionalitäten auf die Beladung und Verteilung der Eisenoxid-Nanopartikel untersucht. Dazu wurden *via* Diazoniumchemie verschiedene Funktionalitäten auf der Graphenoxid-Oberfläche eingeführt. Um die Beziehungen zwischen Struktur und Eigenschaften aufzuklären wurden umfangreiche strukturelle, chemische und elektrochemische Untersuchungen durchgeführt.

Im letzten Teil dieser Arbeit wird die Entwicklung einer wasserfreien *one-pot* Synthese von Gold-Eisenoxid-hetero-Nanostrukturen beschrieben. Unter Verwendung zweier verschiedener Metallpräkursoren wurde der Einfluss verschiedener Reaktionsparameter untersucht. Insbesondere wurden die Auswirkungen kleiner organischer Moleküle auf die Bildung der Heterostrukturen untersucht.

Table of Contents

Chapter 1

Surface modification and functionalization of metal and metal oxide nanoparticles and inorganic materials

1.1. Introduction

Nanometer-scale metal and metal oxide particles are promising materials because of their unique size-dependent electronic, magnetic, mechanical, optical and chemical properties, which greatly differ from the ones of the bulk material[1,2].

Many synthetic routes for the production of colloidal nanoparticles of a widespread variety of materials, showing good homogeneity in size and shape distribution, have been developed[3,4].

However, due to their high surface-to-volume ratio and to the interactions existing between nanoparticles in colloidal systems, nanoparticles present the high tendency to agglomerate. A crucial task when dealing with the synthesis of nanoparticles is to control colloidal stability in order to avoid agglomeration and preserve particles properties. Indeed, agglomeration could lead to the alteration or loss of some of the size-dependent properties of the material, thus invalidating the related applications[5].

In many cases, the synthetic procedures involve the use of surfactants or capping agents in order to avoid aggregation, and control particle size and shape. In other cases, colloidal stability is achieved in a post-synthesis step. Both approaches are referred to as surface modification procedures, since they provide particles which surface chemical composition differs from one of the pristine material.

Surface modification is a multipurpose process. It is performed to impart dispersibility in the desired solvent, phase compatibility thus allowing the fabrication of composite materials, and to improve chemical stability against oxidation and erosion by acids and bases[5,6].

Although size and shape of nanoparticles largely influence their properties, particles surface chemical composition plays a crucial effect on the final properties because of the high surface-to-volume ratio. Therefore, the control of particles surface chemical composition is a fundamental step when aiming at developing a reliable synthesis of nanoparticles showing reproducible chemical and physical properties. Moreover, surface modification and functionalization procedures allow optimizing or tailoring nanoparticles properties in function of the desired applications.

The challenge of surface functionalization relies in developing methodologies which allow introducing the desired functionalities in a controlled way, without affecting the intrinsic properties of the core particles. In these terms, the concept of surface functionalization extends from the introduction of simple functional groups, to active molecules (e.g. biological molecules or fluorescent dyes), to inorganic shells[5]. Moreover, surface modification and functionalization strategies are regarded as

fundamental for controlling the organized assembly of nanoparticles into hierarchical ordered structures[7].

This chapter will briefly describe the principles at the base of nanoparticles aggregation and the basic approaches for surface modification of nanoparticles. Moreover, it will shortly introduce few surface functionalization strategies, from conjugation of active molecules to inorganic functionalization with the fabrication of hybrid materials. Surface functionalization of carbonaceous materials will be also described.

1.2. Principles of nanoparticles aggregation, stabilization and surface modification

1.2.1. Principles of aggregation and stabilization of nanoparticles

The term nanoparticles indicates those particles which have at least one of their dimensions ranging from 1 to 100 nm. For this reason, they show a large surface-to-volume ratio and consequently they display a high tendency to agglomerate in order to minimize the deriving high surface energy.
Moreover, in colloidal systems, particles are subjected to Brownian motion, which diffusion coefficient increases as particles size decreases. This means that, regardless the dispersion medium, particles are likely to collide with each other and the probability of the collision becomes larger by decreasing particle dimensions[8]. Additionally, particles in a colloid are subjected to attractive interactions deriving from the combination of the dispersion forces (van der Waals interactions) of all the atoms constituting the particles[9,10].
Therefore, due to the combination of chance to collide deriving from Brownian motion and attractive interactions, particles in a colloid present a relatively high tendency to aggregate. Aggregation can be prevented by generating a potential barrier between nanoparticles[8,11]. Stability against aggregation for aqueous colloidal systems was first explained through the DLVO (Derjaguin-Landau-Verwey-Overbeek) theory. DLVO theory states that particles in a colloid might bear a surface charge, which depends on the surface potential of the particles, their chemical composition and dispersing conditions (e.g. pH of the dispersing medium). When particles bear a surface charge, they tend to attract counter-ions from the dispersing medium generating an electrical double layer. The electrical double layer associated to every particle generates repulsive forces between nearby particles. The balance between such electrostatic repulsion forces and attractive interactions regulate the stability of nanoparticles in the dispersing medium. However, electrostatic repulsion forces depend on several factors, such as pH and ionic strength of the dispersing medium, and are therefore regarded as very labile. Moreover, the simple stabilization by electrostatic repulsion forces was demonstrated to be not sufficient for particles of size < 20 nm[8,11]. In this case, the repulsive forces are very small and the correlated potential barrier becomes also small and insufficient to stabilize particles. Finally, DLVO theory can not be extended to

hydrophobic systems. Therefore, other theories were formulated in order to control colloidal stability. The so-called steric stabilization was introduced slightly later than DLVO theory[9,10]. When adsorbing a polymer at particles surface, this constitutes a steric barrier that hinders aggregation in two ways:

- when particles get closer, the polymeric shells tend to overlap. Consequently, the degrees of freedom of the polymer chains decrease (*entropic* contribution);
- the overlap of polymeric shells causes the expulsion of solvent molecules from the solvation shell of the polymer. This causes the generation of a counteracting osmotic pressure that re-calls solvent molecules into the overlapped portion of the polymeric shells (*enthalpic* contribution).

As a result, the sum of the *enthalpic* and *entropic* contributions forces particles to stay apart and stabilize them against aggregation.

In order for steric stabilization to be effective, polymers needs to present functional groups showing high affinity for the nanoparticles material, thus allowing the adsorption of the molecule at particles surface. Moreover, the portion of polymer molecule that extends in the solvents needs to show a high affinity for the solvent itself in order to be efficiently solvated by the dispersing medium. Finally, the polymer should entirely coat particles surface in order to avoid a concurrent adsorption of the molecule on the surface of neighboring particles. In this contest, block copolymers are particularly effective because their chemical structure can be tailored in order to have a fragment that strongly binds at nanoparticles surface and a remaining portion showing high affinity for the solvent[10].

It must be highlighted that particles stabilization is often accomplished by both electrostatic and steric effects (*electrosteric* stabilization), depending on the chemical nature of the adsorbed organic molecules and the dispersing conditions[12]. For example, in aqueous media *electrosteric* stabilization can occur when the adsorbed polymer presents functional groups that can be protonated or deprotonated.

However, stabilization, either steric or electrostatic or a combination of both can be achieved also using small molecules. Indeed, small organic molecules can be as effective as polymers; citrate-capped gold nanoparticles synthesized through the Turkevich method being a good example[13].

The mechanism through which small organic molecules can stabilize particles is the same of polymers: the portion of the molecule exposed in the dispersing medium needs to present good affinity for the solvent, and at least one functional group that shows affinity for the particle material and strongly binds on it is required. Adsorption at particles surface can occur either by chemisorption, physisorption or electrostatic interactions. These adsorption modes differ for the strength of the interaction between the ligands and the particles surface atoms. While in chemisorption interactions occur by formation of ionic or covalent bonds, in physisorption interactions occur principally through van der Waals interactions and therefore are remarkably weaker than in the first case. Moreover the adsorbed organic layer can easily desorb. The third case, namely electrostatic interactions, is verified particularly in aqueous dispersions. Depending on pH and ionic strength of the medium, particles

surface atoms can adsorb water molecules or other ions thus generating a net surface charge that should stabilize particles in dispersion.

Moreover, intermolecular forces between the adsorbed species within the organic shell contribute to the formation of a densely packed stabilizer shell and consequently to a more effective stabilization. A dense organic shell will contrast interparticles interactions and usually it shows a higher resistance to displacement by the effect of collision with other particles or molecules present in the colloidal system[5]. Small organic molecules present the advantage of usually leading to more densely packed surface layers than polymers.

1.2.2. Approaches to the surface modification of nanoparticles

Two different approaches to surface modification of nanoparticles exist, namely *in-situ* modification and post-synthesis modification.

The *in-situ* modification strategy consists in the introduction of the more appropriate stabilizing agent (ligand) in the reaction medium where the synthesis of the nanoparticles takes place. The ligand molecules are thought to participate in binding growing nuclei or particles during the synthesis of the material through a dynamic process of adsorption and desorption, therefore stabilizing particles against aggregation and prevent them from uncontrolled growth[14]. The ligand can be represented by the solvent itself, by a reactant, or by a surfactant which contains a moiety affine to the material phase and another part which is affine to the solvent of reaction. While the advantage of the *in-situ* stabilization is clear, that is preventing agglomeration during particle formation, it must be taken into account that ligand molecules might participate in the synthesis of nanoparticles. Sometimes, this could represent a positive effect. Several examples were reported for the synthesis of metal nanoparticles where the introduced ligand behaved both as stabilizer and reactant[15,16]. Moreover, the ligand does not only prevent aggregation, but it can help in controlling the size, size distribution and shape of the final nanocrystals. It is believed that surfactants influence the shape of the final nanoparticles by preferentially adsorbing on specific crystallographic faces on which the crystal growth will be hindered[14,17]. A typical example is represented by the synthesis of Au nanorods, using cetyltrimethylammonium bromide (CTAB) as surfactant. Although the mechanism is not fully understood yet, it was suggested that the CTA^+ cations preferentially adsorb on lateral faces of gold seeds particles formed in the reaction medium. Au seeds have pentatetrahedral symmetry and thus expose different crystal faces, exhibiting different surface energies. The CTA^+ ions adsorbed on the lateral faces hinder further addition of reactants on these sites. Therefore, addition of reactants (Au(III) species and reducing agent) can occur only at the free faces of the seeds (ends of the rod), leading to the growth along a specific direction and consequent formation of the rod shape[18].

On the other hand, in many cases participation of ligand in particles formation is not desired because it could lead to the degradation of particles properties. For instance, it was studied that large excess of

catechol ligands present during the synthesis of titanium oxide (TiO_2) nanoparticles leads to a decrease of the crystallinity of the material and a consequent detrimental effect on its photocatalytic properties[19,20].

Another aspect to consider when adopting *in-situ* modification of nanoparticles is that the choice of the ligand is usually influenced by the reaction conditions and the stability, or incompatibility, of the ligand with the experimental procedure. As a consequence, nanoparticles may present a surface chemical composition that is not suitable for the further application of the material. For instance, magnetic nanoparticles are often synthesized in organic media, with the aid of lipophilic surfactants, because those processes lead to higher crystallinity and better control over the particles size distribution with respect to aqueous routes[21]. Therefore, the as-synthesized particles often present apolar surfaces (e.g. exposing long alkyl chains on their surface), hence being dispersible only in apolar media. However, magnetic nanoparticles find large application in the biomedical field, for which water solubility is required.

Moreover, synthesis in non-aqueous media often prevent the possibility to introduce specific functional groups (such as carboxyl or amino groups) at particles surface, due to the incompatibility of the related multifunctional ligand with the reaction conditions. This hinders further particles functionalization, thus limiting their properties and application fields[22].

For these reasons, *in-situ* modification procedures are often followed by a ligand exchange/phase transfer process.

Ligand exchange procedures enable the replacement of the originally adsorbed stabilizer molecules with a second ligand, which can confer the required properties to the particles. In the simpler cases ligand exchange is performed to impart dispersibility in a selected medium or compatibility with a second phase (e.g. in the case of composite materials). Ligand exchange can be either performed in a single phase, or in a biphasic system. Single phase approaches are used when the new ligand and the particles are soluble in the same solvent. In the opposite situation biphasic conditions are used[23-25]. In any case, the affinity of the incoming ligand for the investigated material is crucial for the result of the process. Complete replacement of the original ligand shell is achieved when the incoming ligand presents a higher affinity for the nanoparticle material. When the affinity is equal or lower, a mixed organic shell can be obtained. Moreover, the process is largely influenced by the concentration ratio between the new stabilizer agent and the starting one. As a general observation, an excess of "new" ligand should favor the complete replacement of the existing adsorbed layer[26].

However, ligand exchange is susceptible of some disadvantages. The creation of a mixed organic shell is often undesired since its composition can not be controlled. Moreover, partial aggregation of particles during the exchanging step might occur[5].

The post-synthesis approach is a generic term which identifies all those procedures aimed to modify the surface of preformed nanoparticles. Post-synthesis modification strategy is more versatile than the *in-situ* approach. The choice of the ligand is less limited and it is generally driven by the target

properties to impart to the nanoparticles. It should be pointed out that, particularly for nanoparticles synthesized through non-aqueous approaches, the post-synthesis modification procedure can be regarded as a ligand exchange step. Indeed, species deriving from the reaction mechanism, either as side-products or un-reacted precursors, might be adsorbed at particles surface. Therefore, post-synthesis modification should be effective in replacing these pre-adsorbed species[9]. However, adsorption of ligands on formerly bare surface was also observed[27].

As previously anticipated, either small organic molecules or polymers can be employed. The use of multifunctional molecules, thus bearing functionalities that will not be involved in the adsorption on nanoparticles, allows for further functionalization. Introduction of the proper functional group at the particle surface provides a binding site on which biomolecules, fluorescent dyes or other desired species can be grafted, influencing the material properties and widening its applications range[28-31].

1.2.3. Surface modification with small organic molecules

The choice of the more appropriate ligand is, in first place, dictated by the inherent chemical nature of the nanoparticle material. For instance, thiols, disulfide and phosphines are particularly suitable for modification of metal particles surface. Carboxylate, catechol and phosphate functionalities are instead largely used for metal oxides.

Thiols and disulfides are regarded as the most suitable species to stabilize metal nanoparticles, such as Au, Ag, Pt, and Cu. The most reported example refers to the powerful binding affinity toward Au surfaces. On gold, thiol functionalities spontaneously chemisorb through formation of a gold-thiolate bond which energy was estimated at about 50 Kcal/mol[32,33]. The great binding affinity offers a very stable organic layer at particles surface, which is exploited for preserving chemical stability of the metal nanoparticles in their working conditions. Many of the noble metals are used for biological applications and the great binding affinity of thiols enables the formation of a stable organic layer that is exploited to reduce the toxicity of some elements and to avoid specific and undesired binding from biological compounds[34].

Phosphines are another class of compounds showing affinity for metals. Although the strength of the interaction is lower than the one of organosulfur compounds, a good stability can be achieved by using polyphosphines. They usually interact through a chelating fashion and are largely used for palladium particles. Amines and ammonium ions are also used in modifying metal particle surfaces[35].

Concerning metal oxide nanoparticles, carboxylic acids are largely used due to the affinity toward diverse transition metal oxides, such as iron oxides (Fe_xO_y) and titanium oxide (TiO_2)[5,35]. Adsorption of carboxylic acid at metal oxide surface was found to occur through coordination of the carboxylate moiety to the metal atoms at particles surface. The carboxylate moiety acts as a ligand for vacant coordination sites of surface metal atoms[36]. The carboxylate-metal coordination modes were thoroughly investigated by Deacon and Philips[37], and can be resumed in two main coordination

modes: unidentate and bidentate. In case of a bidentate coordination, either chelating or bridging modes can be observed (figure 1.1). Evaluation of the coordination mode for a specific metal-carboxylate complex can be performed by means of infrared spectroscopy, calculating the difference between the wavenumber positions ($\Delta\nu$) of the asymmetric (ν_{as}) and symmetric (ν_s) stretching modes of the coordinated carboxylate functionality ($\Delta\nu = \nu_{as} - \nu_s$)[37-39].

Although alcohols do not show remarkable affinity for metal oxides hence leading to poor particles stabilization, catechol-derived ligands show a significantly higher affinity and are therefore largely used. Such affinity arises from the ability of the two adjacent hydroxyl groups of the enediol functionality to coordinate surface metal atoms in a chelating fashion[40-43]. Phosphonic acids and phosphonates show a binding affinity towards metal oxides such as TiO_2 and Fe_xO_y larger than carboxylic acids[44,45]. These groups chemisorb at oxides surface forming a M-O-P bond (M = metal atom) via a heterocondensation reaction between the surface hydroxyl groups and the P-O-X (X = H, alkyl residue) and phosphoryl oxygen[46]. Moreover, phosphonic acids and phosphonates can adsorb at the metal oxide surface in a mono-, bi- or tridentate mode; the last one providing the more stable organic shell (figure 1.1).

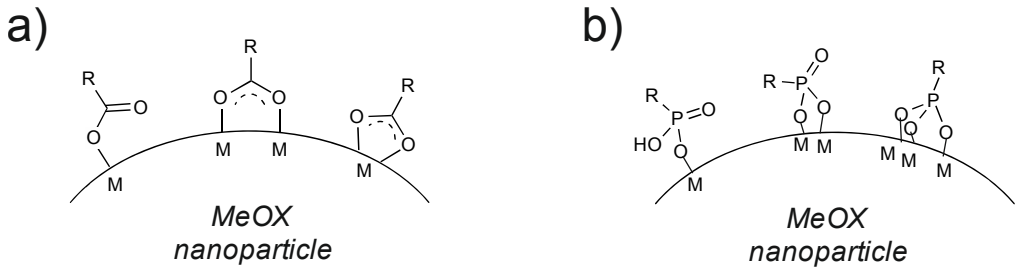

Figure 1.1: Binding modes of carboxylate (a) and phosphonic acids (b) on the surface of metal oxides nanoparticles.

1.3. Functionalization of inorganic materials

The term functionalization refers to the procedure of surface modification aimed at introducing selected functional groups at nanoparticles surface[35]. In most of the cases, functionalization of nanoparticles is required for developing further surface chemical modification, such as introducing active molecules or compounds. Chemical functionalization provides a material with enhanced or novel properties tailored on target applications (e.g. biological receptors).

Functionalization of nanoparticles can be achieved through two strategies, namely direct and multi-step functionalization[35,47]. Direct functionalization represents the simplest and more appealing strategy because it allows introducing the desired functionality in a single step. It is usually performed either by *in-situ* surface modification or post-synthesis modification approaches. Requirement for the added ligands or, more generally, compounds is to present at least two functionalities: one that will interact with the material at nanoparticles surface and another that will be exposed at the particles surface towards the surrounding medium. Direct functionalization allows introducing simple functionalities

such as amino, carboxyl, hydroxyl groups, or small and simple molecules (e.g. amino acids). Introduction of more complex functionalities or molecules is usually limited by steric hindrance, incompatibility with the synthesis/functionalization media and tendency to react with particles surface groups of the incoming species[35,47].

On the contrary, multi-step functionalization consists in a first step of surface modification aimed at preparing nanoparticles surface to be further reacted with the interested functional species. Also for this purpose, a bifiunctional ligand is required. The as-introduced surface functionalities will act as anchoring sites for grafting the desired molecules or developing a more complicate chemistry to fabricate more complex architectures. Surface chemistry performed in multi-step approaches commonly consists in typical organic chemistry reactions, such as grafting through the formation of amide and ester bonds. Consequently, several reactants or difficult purification procedures may be needed. For this reason, it is preferable for the ligand molecules introduced during the first step to strongly bind to nanoparticles surface, in order to limit desorption during the further reaction and purification steps. Phosphonic acids and thiols bearing terminal functionalities represent a valid platform for multi-step functionalization procedures. As previously mentioned, the high strength of the sulfur-metal and M-O-P bonds ensures a stable organic ligand shell that will hardly desorb from particles surface during the further steps of modifications.

Organo alkoxysilanes represent a valid alternative for functionalization of metal oxides nanoparticles because they can react with particles surface hydroxyl groups, thus providing a covalent molecular layer[35].

1.3.1. Functionalization of metal oxide nanoparticles mediated by organofunctional alkoxysilanes

Organosilanes are widely employed for surface functionalization of metal oxides, particularly silica[48,49] and iron oxide nanoparticles[50,51]. Organosilanes are bifunctional molecules of the general formula $(X)_3$-Si-R, where "X" represents the group that will chemisorb at particles surface, commonly chlorine (Cl) or an alkoxy-group (methoxy $–OCH_3$, or ethoxy $–OC_2H_5$). The organic fragment "R" represents the functionality that will be exposed at particles surface. An advantage of using organosilanes consists in the large variety of molecules commercially available that allows introducing diverse functionalities, from amino groups to thiols and short poly(ethylene glycol) (PEG) chains (figure 1.2).

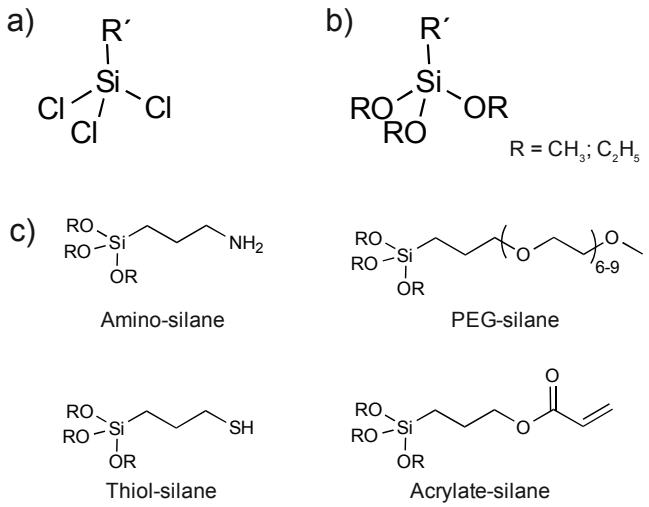

Figure 1.2: Structure of organo trichlorosilane (a), structure of organo trialkoxysilanes and structures of some of the commercially available organo alkoxysilanes used in surface functionalization procedures of metal oxide nanoparticles (c).

As already anticipated, chloro- and alkoxysilanes react with the surface hydroxyl groups of metal oxides; this reaction is usually referred to as silanization. In analogy with the sol-gel synthesis of silica, the reaction commonly proceeds through the initial step of hydrolysis of the anchoring group (in case of alkoxysilane, hydroxyl groups are formed) and consequent condensation with particles surface hydroxyl groups leading to formation of covalent M-O-Si bonds. However, regardless the used silane, homocondensation reactions (condensation between molecules of silanes leading to the formation of oligomers) can occur (figure 1.3). Obviously, reaction conditions should be carefully set in order to favor condensation at particles surface and limit homocondensation processes. The solvent, the choice of the catalysts (either acid or base) and the ratio between the organosilane and nanoparticles represent the most important parameters that influence the result of the reaction[52].

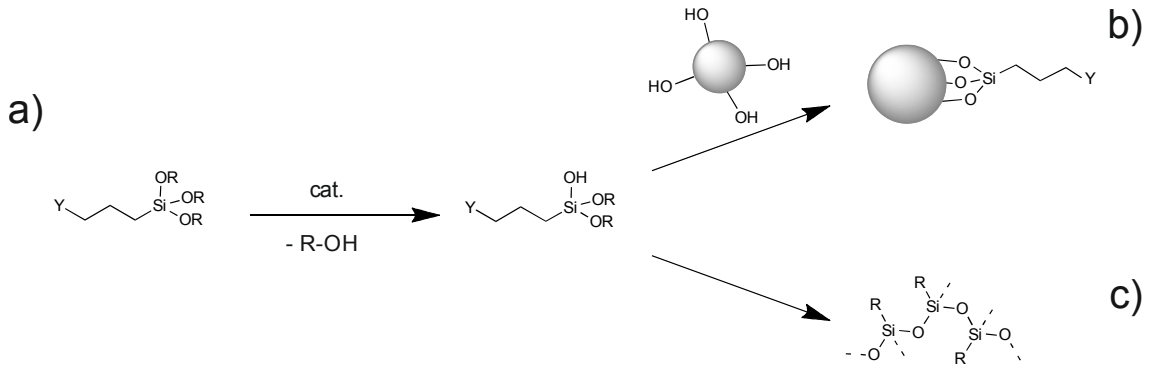

Figure 1.3: Schematic representation of the reaction steps for the grafting of organo alkoxysilanes at oxide particles surface. Upon the initial step of hydrolysis of the alkoxy groups (a), condensation with surface hydroxyl groups of nanoparticles (b) or homonucleation to form oligomers (c) can occur.

Chlorosilanes, and especially trichlorosilanes, show the higher reactivity; indeed usually no catalyst is needed. However, this leads to some drawbacks: (i) poorly controllable homocondensation reactions, (ii) ill-defined covalent molecular layers, and (iii) scarce reproducibility[32,35]. Some drawbacks could be

circumvented by modulating the reactivity of the precursor choosing di- or monochlorosilanes. Nevertheless, chlorosilanes present the disadvantage of leading to HCl liberation, which might compromise particles chemical stability. For these reasons, alkoxysilanes are often preferred to perform silanization reactions.

The versatility of functionalities that can be introduced using organosilanes makes these compounds largely used to modify iron oxide nanoparticles[50]. Most of the examples reported in literature describe the introduction of amino groups and short PEG chains through silanization reactions[53-55].

In view of the widespread potential applications of iron oxide nanoparticles in the biomedical field, introduction of PEG chains is a powerful tool to render them hydrophilic and biocompatible. Compared to non-covalent adsorption approaches, introduction of PEG through silanization reaction provides a covalent and likely more densely packed organic shell, thus preventing desorption and ensuring better stability for *in-vivo* applications[56,57].

On the other hand, grafting amino groups at iron oxide nanoparticles surface allows further conjugation with biomolecules, drugs and several other compounds[58,59].

Conjugation is often performed through reaction between the surface amino functionalities and carboxyl residues of the desired molecule to form amide bonds. Coupling of amino and carboxyl groups is commonly performed through the carbodiimide-based chemistry. The carbodiimide-based chemistry is a popular and routine strategy in organic chemistry, which well applies both to organic and aqueous media, thus being suitable also for conjugation of biomolecules. In a typical coupling reaction the first step consists in the activation of the carboxyl group using a carbodiimide reagent and the consequent formation of an *O*-acylisourea intermediate. Carbodiimide compounds are commercially available reactants, with N,N'-dicyclohexylcarbodiimide (DCC) and 1-ethyl-3-(3-dimethylaminopropyl)carbodiimide (EDC) being the more employed ones. While DCC is used for organic solvents, EDC is suitable for aqueous media and thus largely employed in coupling biological compounds. The formed *O*-acylisourea is a highly reactive intermediate species susceptible to nucleophilic attack by amines, and can be therefore converted into the desired amide. However, this intermediate species can easily undergo hydrolysis in presence of traces of water or side-reactions like the condensation with other carboxyl groups, hence limiting the yield of the conjugation process. Addition of N-hydroxysuccinimide (NHS) or sulfo-NHS can be used to enhance the coupling yield. NHS leads to the formation of a succinimide ester (NHS-ester) as intermediate species. Analogously to the *O*-acylisourea, it is susceptible to nucleophilic attack by amines. However, its higher stability helps limiting hydrolysis or side-reactions (figure 1.4).

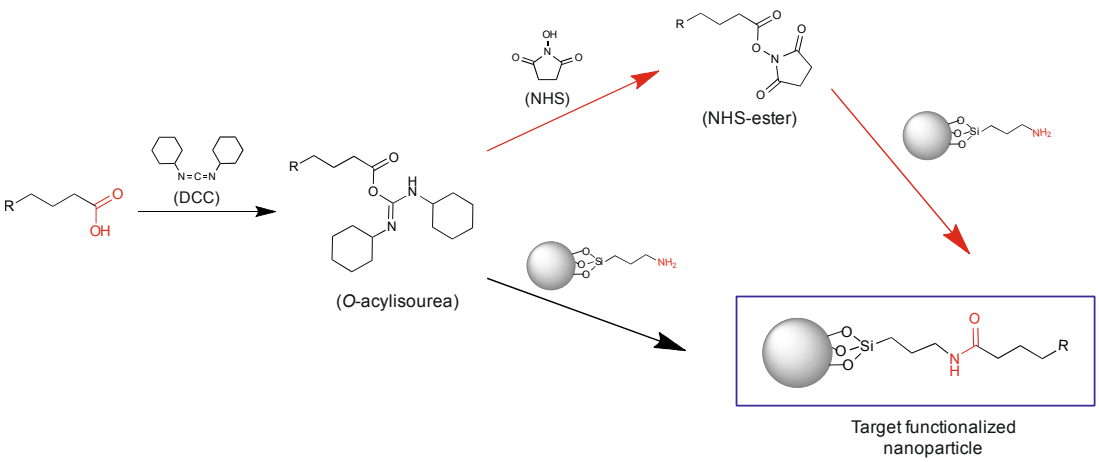

Figure 1.4: Schematic representation of the carbodiimide-based chemistry for coupling carboxyl and amino moieties to yield amide linkage. The two alternative pathways are described, namely employing DCC only (black arrows) and employing additional NHS (red arrows). Both of the pathways lead to the same final nanoparticles (blue rectangle).

Several examples were reported in the literature on coupling biological receptors on iron oxide nanoparticles through the aforementioned approach[55].

However, conjugation does not only occur through formation of amide bonds. By choosing the more appropriate functionalities exposed at particles surface, conjugation chemistry can be extended to a large variety of compounds.

Moreover, extending the coupling approach to diverse compounds is facilitated by the existence of diverse conjugation strategies, such as click chemistry[60] and glutaraldehyde-mediated strategy[61].

The main advantage of conjugation of active compounds to nanoparticles using silane as coupling agents consists in the stability of the organic layer, given by the covalent character of the functionalization. Moreover, this strategy allows protecting the inorganic core from the surrounding environment, preserving its chemical and physical properties. Finally, this technique might allow a controlled design of nanoparticles surface and it is regarded as a valid approach for the fabrication of multifunctional nano-sized materials.

1.3.2. Inorganic functionalization: fabrication of carbon-based composites and hybrid nanomaterials

Besides the traditional methods of surface modification of nanoparticles with organic molecules, a largely exploited way to achieve enhancement of colloidal and chemical stability and the introduction of novel functionalities is coating by inorganic compounds (inorganic functionalization). Inorganic functionalization is referred to as a strategy for the fabrication of hybrid nanomaterials.

Hybrid nanomaterials are composed of few distinct phases, of which each contributes a different function. In general, the contact between the phases confers to the hybrid material novel or enhanced properties and functionalities that differ from the one of the individual components[52,62,63].

Heterostructured materials consisting of different phases can be synthesized either through "seed mediated growth" approaches or one-pot strategies. The "seed mediated growth" approach represents the most popular approach and consists in adding the suited precursor into a dispersion of preformed nanoparticles, which act as the nucleation seeds for the second material. On the contrary, the less investigated one-pot strategies consist in placing all the reactants participating to the synthesis of the desired material in the same growing medium at the same time[14] (figure 1.5).

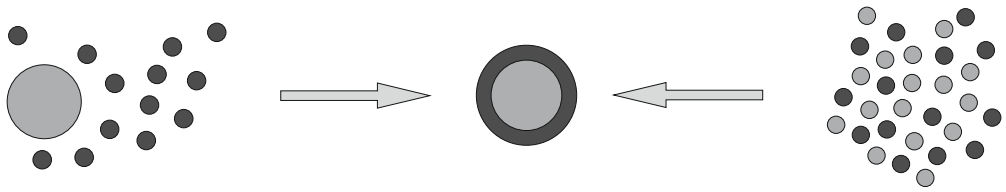

Figure 1.5: Schematic representation of "seed mediated growth" (left side) and one-pot (right side) approaches for the fabrication of hybrid materials.

In both of the cases, the heterostructure will form only upon heterogeneous nucleation of one of the phases onto preformed (either *in-situ* or added as seeds) nanoparticles of the other material (refer to chapter 6 for a more detailed discussion).

The simplest and more popular example of inorganic coating, which is generally achieved through "seed mediated growth" approach, is represented by growing silica shells at particles surface. Silica coating is performed on metal[64,65] as well as on semiconductor[66] and metal oxide[67,68] nanoparticles, and is usually carried out following the Stöber method[69]. The reasons of using silica to coat inorganic nanoparticles are numerous: it is a low-cost material and it prevents direct contact of the underlying core particle with the surrounding environment thus preserving its chemical stability and physical properties. Moreover, silica presents good stability in aqueous media and good biocompatibility, thus being particularly suitable for biological applications. Finally, further surface functionalization of silica-shells can be performed using organo alkoxysilanes[48,49], *via* the same approach described in the previous paragraph. Further functionalization often consists in binding molecules such as biological compounds or fluorescent dyes, and allows extending the applications range of the material[70].

Several other examples of hetero-structured materials composed of completely different phases were reported. Particularly, special attention is devoted to hybrid materials represented by the combination of a metal domain, usually a noble metal such as Au, Ag and Pt, with a metal oxide, which can be a magnetic[71,72], or a semiconductor material[73-75]. In particular, the system gold-coated iron oxide nanoparticles is largely investigated because it is regarded as a promising material for several different application fields, from biotechnology to catalysis[76].

Another class of composite materials which is extremely investigated nowadays consists of graphene-based substrates (graphene, graphene oxide, reduced graphene oxide) coupled with metal or metal oxide nanoparticles[77]. Decoration with metal and metal oxide nanoparticles is usually regarded as a strategy to functionalize carbonaceous materials. In analogy with the previously described inorganic

functionalization, adsorption of nanoparticles confers novel or enhanced properties to the carbonaceous materials. In particular, the chemical nature of the nanoparticles and the interaction between the phases determines the final applications of the composite. Large interest is dedicated to the investigation of composite materials for energy, catalysis and sensor applications[78-80].

Graphene-based materials represent a useful support for dispersing nanoparticles and limiting their aggregation due to their high surface area. At the same time, nanoparticles are believed to reduce re-stacking of the carbon sheets[81,82]. Such effects are important for further applications in energy storage and sensing devices, and in catalysis. *Ex-situ* and *in-situ* strategies are employed to fabricate the aforementioned composites[83].

The *ex-situ* approach consists in decorating carbon substrates with preformed nanoparticles. Nanoparticles can be loaded either through non-covalent interactions or covalent linkages. Non-covalent approaches are based on van der Waals, π-π interactions or hydrogen bonding between the two phases. The strength of the interactions is one of the factors determining particles loading[83-85]. However, a preliminary surface modification step on one or both of the component materials is regarded to favor adsorption of nanoparticles[83]. In this contest, it must be pointed out that several strategies for organic functionalization of carbonaceous supports were developed, either through non-covalent or covalent approaches. Depending on the chemical properties of the support, non-covalent functionalization is achieved by hydrogen bonding (graphene oxide), van der Waals and π-π interactions (graphene)[85]. Covalent functionalization can be performed by grafting functionalities either through formation of carbon-carbon bonds (Diels-Alder reaction, 1,3-dipolar cycloaddiction and diazonium chemistry)[86,87] or exploiting functionalities present at carbon surface (carboxyl groups, epoxydes)[88]. Organic functionalization will be discussed more in details in chapter 3.

Surface modification step is particularly necessary for both of the components when the composite is fabricated through a covalent approach. In this case, anchoring of the nanoparticles is achieved via coupling reactions between complementary functionalities at the surface of the two materials[83].

On the contrary, in *in-situ* approaches the proper metal or metal oxide precursor is reacted in presence of the desired carbon-material. For this purpose, either previously functionalized carbon materials or inherently functional substrates, such as graphene oxide, are preferred. It is generally believed that the oxygen-containing groups on graphene-oxide sheets might act as nucleation sites for the metal oxide, thus favoring the fabrication of the composite material[89]. Introduction of selected organofunctional groups acting as coordinating sites for the metal cations or growing nuclei might favor the fabrication of a composite with a better defined structure.

In the field of inorganic functionalization, significant effort is dedicated to design the interface between the component phases in order to fabricate composite materials with a defined and reproducible structure and to elucidate structure-properties relationships[90,91].

1.4. Aim and outline of the work

The central theme of this doctoral thesis lies in the investigation of the chemical functionalization of inorganic nanoparticles as a strategy to tailor the properties of a material depending on the target application. Particular attention will be dedicated to the surface chemistry of iron oxide nanoparticles.
Magnetite nanoparticles synthesized through the "benzyl alcohol route" present an average size of 10 nm, thus they exhibit superparamagnetic behaviour. For this reason, they are regarded as suitable solid supports for the fabrication of recoverable systems, which is a fundamental requirement for several of the reported studies. In view of their ease of functionalization, iron oxide nanoparticles represent a versatile and convenient platform for the development of diverse surface chemistries for the synthesis of hybrid materials. Therefore, the investigation will be focused on describing the choice and the role of selected chemical functionalities in controlling the formation of the target material. Finally, the suitability of the diverse functionalization approaches for a desired application will be showed.

Chapter 2 illustrates the simplicity and versatility of a post-synthesis stabilization procedure on magnetite nanoparticles using small organic molecules, and it recalls attention on the impact that the ligand shell may have on the investigation on particles physical properties. The as-modified nanoparticles constituted the material of analysis for investigations on the electronic properties of a single magnetite nanoparticle.
The discussion is focused in the description of the stabilization procedure, comparing the chemical and structural properties of the material before and after functionalization procedure.
The study of physical properties of the as-modified particles was performed by the group of Professor Hervé Aubin (Laboratory of physics and study of materials - ESPCI - Paris) and is resumed in a dedicated section.

Chapter 3 describes the fabrication of a graphene oxide-iron oxide composite material *via* an *ex-situ* approach. Particularly, the discussion is focused on the investigation about the non-covalent interactions between the component phases. The effects of surface functionalities on the loading and distribution of iron oxide nanoparticles are investigated by introducing selected functionalities at graphene oxide surface. Particularly, 4-carboxyphenyl groups will be covalently grafted *via* diazonium chemistry and a detailed characterization of the chemical and structural properties of the materials is reported. Finally, due to the potential applicability of these materials as hybrid supercapacitors, structure-properties relationships will be investigated by analysing their electrochemical performances.

Chapter 4 reports the fabrication of a magnetic molecular receptor. In particular, magnetite nanoparticles surface was decorated with cavitand molecules. Different approaches of surface functionalization were adopted and special emphasis is placed in describing the developed strategies.

Fluorescent spectroscopy was employed in order to investigate the efficiency of the device for molecular recognition of target guest molecules.
This work was performed in collaboration with the group of Professor Enrico Dalcanale from the University of Parma (Italy). The used cavitand molecules were kindly synthesized by Dr. Elisa Biavardi, who also performed the fluorescence spectroscopy analyses.

Chapter 5 illustrates the fabrication of a magnetic molecular receptor for the heterogeneous resolution of a racemic mixture of an inherently chiral cavitand. The organic functionalization of the magnetic core (magnetite nanoparticles) was designed on the basis of the peculiar properties of cavitand molecules as molecular receptors. A covalent strategy based on silane coupling agents and conjugation mediated by the carbodiimide chemistry was adopted in order to fabricate a recoverable device. The illustrated preliminary results demonstrate the efficiency of the fabricated material in enantioselective molecular recognition.
This work, which is still ongoing, is carried out in collaboration with the group of Professor Enrico Dalcanale from the University of Parma (Italy). The used cavitand molecules were kindly synthesized by Dr. Roberta Pinalli, who also performed the enenatioselective recognition tests.

Chapter 6 reports the fabrication of gold-iron oxide hetero-nanostructures. In particular, the work focuses on the development of a novel microwave-assisted non-aqueous one-pot synthesis route. With this purpose, the possibility of extending the well-known "benzyl alcohol route" to the synthesis of metal nanoparticles is investigated. Two different metal precursors, namely chloauric acid ($HAuCl_4$) and gold(III) acetate ($Au(OAc)_3$), were investigated, and the role that several parameters may have in determining the structural properties of the final materials is described in details. Particular attention is devoted to investigate the influence of small organic molecules in favoring the formation of the gold-iron oxide heterostructure and the influence in the structural and morphological properties of the materials.

1.5. Bibliography

(1) Goesmann, H.; Feldmann, C.: Nanoparticulate Functional Materials. *Angewandte Chemie International Edition* **2010**, *49*, 1362-1395.

(2) Patzke, G. R.; Zhou, Y.; Kontic, R.; Conrad, F.: Oxide Nanomaterials: Synthetic Developments, Mechanistic Studies, and Technological Innovations. *Angewandte Chemie International Edition* **2011**, *50*, 826-859.

(3) Niederberger, M.: Nonaqueous Sol–Gel Routes to Metal Oxide Nanoparticles. *Accounts of Chemical Research* **2007**, *40*, 793-800.

(4) Park, J.; Joo, J.; Kwon, S. G.; Jang, Y.; Hyeon, T.: Synthesis of Monodisperse Spherical Nanocrystals. *Angewandte Chemie International Edition* **2007**, *46*, 4630-4660.

(5) Sperling, R. A.; Parak, W. J.: Surface modification, functionalization and bioconjugation of colloidal inorganic nanoparticles. *Philosophical Transactions of the Royal Society a-Mathematical Physical and Engineering Sciences* **2010**, *368*, 1333-1383.

(6) Lu, A.-H.; Salabas, E. L.; Schueth, F.: Magnetic nanoparticles: Synthesis, protection, functionalization, and application. *Angewandte Chemie-International Edition* **2007**, *46*, 1222-1244.

(7) Curri, M. L.; Comparelli, R.; Striccoli, M.; Depalo, N.; Fanizza, E.: Inorganic Nanocrystals: Patterning and Assembling. In *Encyclopedia of Inorganic Chemistry*; John Wiley & Sons, Ltd, 2006.

(8) Iijima, M.; Kamiya, H.: Surface Modification for Improving the Stability of Nanoparticles in Liquid Media. *KONA Powder and Particle Journal* **2009**, *27*, 119-129.

(9) Garnweitner, G.: In-situ versus post-synthetic stabilization of metal oxide nanoparticles. In *The delivery of nanoparticles*; Hashim, D. A. A., Ed.; InTech, 2012; pp 71-92.

(10) Shukla, S.; Seal, S.: Sol-gel-derived oxide and sulfide nanoparticles. In *Synthesis, functionalization and surface treatment of nanoparticles*; Baraton, M.-I., Ed.; American Scientific Publishers, 2003.

(11) Hidehiro, K.; Motoyuki, I.: Surface modification and characterization for dispersion stability of inorganic nanometer-scaled particles in liquid media. *Science and Technology of Advanced Materials* **2010**, *11*, 044304.

(12) Segets, D.; Marczak, R.; Schäfer, S.; Paula, C.; Gnichwitz, J.-F.; Hirsch, A.; Peukert, W.: Experimental and Theoretical Studies of the Colloidal Stability of Nanoparticles−A General Interpretation Based on Stability Maps. *ACS Nano* **2011**, *5*, 4658-4669.

(13) Turkevich, J.; Stevenson, P. C.; Hillier, J.: A study of the nucleation and growth processes in the synthesis of colloidal gold. *Discussions of the Faraday Society* **1951**, *11*, 55-75.

(14) Casavola, M.; Buonsanti, R.; Caputo, G.; Cozzoli, P. D.: Colloidal strategies for preparing oxide-based hybrid nanocrystals. *European Journal of Inorganic Chemistry* **2008**, 837-854.

(15) Han, M. Y.; Quek, C. H.; Huang, W.; Chew, C. H.; Gan, L. M.: A simple and effective chemical route for the preparation of uniform nonaqueous gold colloids. *Chemistry of Materials* **1999**, *11*, 1144-1147.

(16) Hoppe, C. E.; Lazzari, M.; Pardinas-Blanco, I.; Lopez-Quintela, M. A.: One-step synthesis of gold and silver hydrosols using poly(N-vinyl-2-pyrrolidone) as a reducing agent. *Langmuir* **2006**, *22*, 7027-7034.

(17) Xiao, J.; Qi, L.: Surfactant-assisted, shape-controlled synthesis of gold nanocrystals. *Nanoscale* **2011**, *3*, 1383-1396.

(18) Murphy, C. J.; Sau, T. K.; Gole, A. M.; Orendorff, C. J.; Gao, J.; Gou, L.; Hunyadi, S. E.; Li, T.: Anisotropic Metal Nanoparticles: Synthesis, Assembly, and Optical Applications. *The Journal of Physical Chemistry B* **2005**, *109*, 13857-13870.

(19) Chen, X.; Mao, S. S.: Titanium Dioxide Nanomaterials: Synthesis, Properties, Modifications, and Applications. *Chemical Reviews* **2007**, *107*, 2891-2959.

(20) Garnweitner, G.; Ghareeb, H. O.; Grote, C.: Small-molecule in situ stabilization of TiO_2 nanoparticles for the facile preparation of stable colloidal dispersions. *Colloids and Surfaces A: Physicochemical and Engineering Aspects* **2010**, *372*, 41-47.

(21) Sun, S.; Zeng, H.; Robinson, D. B.; Raoux, S.; Rice, P. M.; Wang, S. X.; Li, G.: Monodisperse MFe_2O_4 (M = Fe, Co, Mn) Nanoparticles. *Journal of the American Chemical Society* **2003**, *126*, 273-279.

(22) Qu, H.; Caruntu, D.; Liu, H.; O'Connor, C. J.: Water-Dispersible Iron Oxide Magnetic Nanoparticles with Versatile Surface Functionalities. *Langmuir* **2011**, *27*, 2271-2278.

(23) Gentili, D.; Ori, G.; Franchini, M. C.: Double phase transfer of gold nanorods for surface functionalization and entrapment into PEG-based nanocarriers. *Chemical Communications* **2009**, 5874-5876.

(24) Gittins, D. I.; Caruso, F.: Biological and physical applications of water-based metal nanoparticles synthesised in organic solution. *ChemPhysChem* **2002**, *3*, 110-113.

(25) Lattuada, M.; Hatton, T. A.: Functionalization of Monodisperse Magnetic Nanoparticles. *Langmuir* **2006**, *23*, 2158-2168.

(26) Warner, M. G.; Hutchison, J. E.: Synthesis and assembly of functionalized gold nanoparticles. In *Synthesis, functionalization and surface treatment of nanoparticles*; Baraton, M.-I., Ed.; American Scientific Publishers, 2003.

(27) Arita, T.; Yoo, J.; Ueda, Y.; Adschiri, T.: Size and size distribution balance the dispersion of colloidal CeO_2 nanoparticles in organic solvents. *Nanoscale* **2010**, *2*, 689-693.

(28) Brinas, R. P.; Hu, M.; Qian, L.; Lymar, E. S.; Hainfeld, J. F.: Gold nanoparticle size controlled by polymeric Au(I) thiolate precursor size. *Journal of the American Chemical Society* **2008**, *130*, 975-982.

(29) Funston, A. M.; Jasieniak, J. J.; Mulvaney, P.: Complete Quenching of CdSe Nanocrystal Photoluminescence by Single Dye Molecules. *Advanced Materials* **2008**, *20*, 4274-4280.

(30) Gupta, M.; Caniard, A.; Touceda-Varela, A.; Campopiano, D. J.; Mareque-Rivas, J. C.: Nitrilotriacetic Acid-Derivatized Quantum Dots for Simple Purification and Site-Selective Fluorescent Labeling of Active Proteins in a Single Step. *Bioconjugate Chemistry* **2008**, *19*, 1964-1967.

(31) Ren, T.; Mandal, P. K.; Erker, W.; Liu, Z.; Avlasevich, Y.; Puhl, L.; Muellen, K.; Basche, T.: A Simple and Versatile Route to Stable Quantum Dot-Dye Hybrids in Nonaqueous and Aqueous Solutions. *Journal of the American Chemical Society* **2008**, *130*, 17242-17243.

(32) Gooding, J. J.; Ciampi, S.: The molecular level modification of surfaces: from self-assembled monolayers to complex molecular assemblies. *Chemical Society Reviews* **2011**, *40*, 2704-2718.

(33) Leff, D. V.; Ohara, P. C.; Heath, J. R.; Gelbart, W. M.: Thermodynamic Control of Gold Nanocrystal Size: Experiment and Theory. *The Journal of Physical Chemistry* **1995**, *99*, 7036-7041.

(34) Daniel, M. C.; Astruc, D.: Gold nanoparticles: Assembly, supramolecular chemistry, quantum-size-related properties, and applications toward biology, catalysis, and nanotechnology. *Chemical Reviews* **2004**, *104*, 293-346.

(35) Neouze, M.-A.; Schubert, U.: Surface modification and functionalization of metal and metal oxide nanoparticles by organic ligands. *Monatshefte Fur Chemie* **2008**, *139*, 183-195.

(36) Dobson, K. D.; McQuillan, A. J.: In situ infrared spectroscopic analysis of the adsorption of aliphatic carboxylic acids to TiO_2, ZrO_2, Al_2O_3, and Ta_2O_5 from aqueous solutions. *Spectrochimica Acta Part A: Molecular and Biomolecular Spectroscopy* **1999**, *55*, 1395-1405.

(37) Deacon, G. B.; Phillips, R. J.: Relationships between the carbon-oxygen stretching frequencies of carboxylato complexes and the type of carboxylate coordination. *Coordination Chemistry Reviews* **1980**, *33*, 227-250.

(38) Deacon, G. B.; Huber, F.; Phillips, R. J.: Diagnosis of the nature of carboxylate coordination from the direction of shifts of carbon-oxygen stretching frequencies. *Inorganica Chimica Acta* **1985**, *104*, 41-45.

(39) Wu, X.; Wang, D.; Yang, S.: Preparation and Characterization of Stearate-Capped Titanium Dioxide Nanoparticles. *Journal of Colloid and Interface Science* **2000**, *222*, 37-40.

(40) Amstad, E.; Gillich, T.; Bilecka, I.; Textor, M.; Reimhult, E.: Ultrastable Iron Oxide Nanoparticle Colloidal Suspensions Using Dispersants with Catechol-Derived Anchor Groups. *Nano Letters* **2009**, *9*, 4042-4048.

(41) Niederberger, M.; Garnweitner, G.; Krumeich, F.; Nesper, R.; Colfen, H.; Antonietti, M.: Tailoring the surface and solubility properties of nanocrystalline titania by a nonaqueous in situ functionalization process. *Chemistry of Materials* **2004**, *16*, 1202-1208.

(42) Xu, C. J.; Xu, K. M.; Gu, H. W.; Zheng, R. K.; Liu, H.; Zhang, X. X.; Guo, Z. H.; Xu, B.: Dopamine as a robust anchor to immobilize functional molecules on the iron oxide shell of magnetic nanoparticles. *Journal of the American Chemical Society* **2004**, *126*, 9938-9939.

(43) Zhou, S.; Garnweitner, G.; Niederberger, M.; Antonietti, M.: Dispersion behavior of zirconia nanocrystals and their surface functionalization with vinyl group-containing ligands. *Langmuir* **2007**, *23*, 9178-9187.

(44) Lalatonne, Y.; Paris, C.; Serfaty, J. M.; Weinmann, P.; Lecouvey, M.; Motte, L.: Bis-phosphonates - ultra small superparamagnetic iron oxide nanoparticles: a platform towards diagnosis and therapy. *Chemical Communications* **2008**, 2553-2555.

(45) Sahoo, Y.; Pizem, H.; Fried, T.; Golodnitsky, D.; Burstein, L.; Sukenik, C. N.; Markovich, G.: Alkyl phosphonate/phosphate coating on magnetite nanoparticles: A comparison with fatty acids. *Langmuir* **2001**, *17*, 7907-7911.

(46) Guerrero, G.; Mutin, P. H.; Vioux, A.: Anchoring of Phosphonate and Phosphinate Coupling Molecules on Titania Particles. *Chemistry of Materials* **2001**, *13*, 4367-4373.

(47) Milosevic, I.; Guenin, E.; Lalatonne, Y.; Benyettou, F.; De Montferrand, C.; Geinguenaud, F.; Motte, L.: Input of microwaves for nanocrystal synthesis and surface functionalization focus on iron oxide nanoparticles. In *Microwave in nanoparticles synthesis*; Serpone, S. H. a. N., Ed.; Wiley-VCH, 2013.

(48) Bagwe, R. P.; Hilliard, L. R.; Tan, W.: Surface Modification of Silica Nanoparticles to Reduce Aggregation and Nonspecific Binding. *Langmuir* **2006**, *22*, 4357-4362.

(49) Soto-Cantu, E.; Cueto, R.; Koch, J.; Russo, P. S.: Synthesis and Rapid Characterization of Amine-Functionalized Silica. *Langmuir* **2012**, *28*, 5562-5569.

(50) De Palma, R.; Peeters, S.; Van Bael, M. J.; Van den Rul, H.; Bonroy, K.; Laureyn, W.; Mullens, J.; Borghs, G.; Maes, G.: Silane Ligand Exchange to Make Hydrophobic Superparamagnetic Nanoparticles Water-Dispersible. *Chemistry of Materials* **2007**, *19*, 1821-1831.

(51) Ninjbadgar, T.; Brougham, D. F.: Epoxy Ring Opening Phase Transfer as a General Route to Water Dispersible Superparamagnetic Fe_3O_4 Nanoparticles and Their Application as Positive MRI Contrast Agents. *Advanced Functional Materials* **2011**, *21*, 4769-4775.

(52) Posthumus, W.; Magusin, P.; Brokken-Zijp, J. C. M.; Tinnemans, A. H. A.; van der Linde, R.: Surface modification of oxidic nanoparticles using 3-methacryloxypropyltrimethoxysilane. *Journal of Colloid and Interface Science* **2004**, *269*, 109-116.

(53) Butterworth, M. D.; Illum, L.; Davis, S. S.: Preparation of ultrafine silica- and PEG-coated magnetite particles. *Colloids and Surfaces A: Physicochemical and Engineering Aspects* **2001**, *179*, 93-102.

(54) Durdureanu-Angheluta, A.; Dascalu, A.; Fifere, A.; Coroaba, A.; Pricop, L.; Chiriac, H.; Tura, V.; Pinteala, M.; Simionescu, B. C.: Progress in the synthesis and characterization of magnetite nanoparticles with amino groups on the surface. *Journal of Magnetism and Magnetic Materials* **2012**, *324*, 1679-1689.

(55) Turcheniuk, K.; Tarasevych, A. V.; Kukhar, V. P.; Boukherroub, R.; Szunerits, S.: Recent advances in surface chemistry strategies for the fabrication of functional iron oxide based magnetic nanoparticles. *Nanoscale* **2013**, *5*, 10729-10752.

(56) Zhang, J.; Rana, S.; Srivastava, R. S.; Misra, R. D. K.: On the chemical synthesis and drug delivery response of folate receptor-activated, polyethylene glycol-functionalized magnetite nanoparticles. *Acta Biomaterialia* **2008**, *4*, 40-48.

(57) Zhang, M.; Hu, W.; Earhart, C. M.; Tang, M.; Wilson, R. J.; Wang, S. X.: Silane-based functionalization of synthetic antiferromagnetic nanoparticles for biomedical applications. *Journal of Applied Physics* **2010**, *107*, -.

(58) Stutz, C.; Bilecka, I.; Thunemann, A. F.; Niederberger, M.; Borner, H. G.: Superparamagnetic core-shell nanoparticles as solid supports for peptide synthesis. *Chemical Communications* **2012**, *48*, 7176-7178.

(59) Yoon, T.-J.; Yu, K. N.; Kim, E.; Kim, J. S.; Kim, B. G.; Yun, S.-H.; Sohn, B.-H.; Cho, M.-H.; Lee, J.-K.; Park, S. B.: Specific Targeting, Cell Sorting, and Bioimaging with Smart Magnetic Silica Core–Shell Nanomaterials. *Small* **2006**, *2*, 209-215.

(60) Borase, T.; Ninjbadgar, T.; Kapetanakis, A.; Roche, S.; O'Connor, R.; Kerskens, C.; Heise, A.; Brougham, D. F.: Stable Aqueous Dispersions of Glycopeptide-Grafted Selectably

Functionalized Magnetic Nanoparticles. *Angewandte Chemie International Edition* **2013**, *52*, 3164-3167.

(61) Masthoff, I.-C.; David, F.; Wittmann, C.; Garnweitner, G.: Functionalization of magnetic nanoparticles with high-binding capacity for affinity separation of therapeutic proteins. *Journal of Nanoparticle Research* **2013**, *16*, 1-10.

(62) Carbone, L.; Cozzoli, P. D.: Colloidal heterostructured nanocrystals: Synthesis and growth mechanisms. *Nano Today* **2010**, *5*, 449-493.

(63) Costi, R.; Saunders, A. E.; Banin, U.: Colloidal Hybrid Nanostructures: A New Type of Functional Materials. *Angewandte Chemie International Edition* **2010**, *49*, 4878-4897.

(64) Graf, C.; Vossen, D. L. J.; Imhof, A.; van Blaaderen, A.: A general method to coat colloidal particles with silica. *Langmuir* **2003**, *19*, 6693-6700.

(65) Liz-Marzán, L. M.; Giersig, M.; Mulvaney, P.: Synthesis of Nanosized Gold−Silica Core−Shell Particles. *Langmuir* **1996**, *12*, 4329-4335.

(66) Koole, R.; van Schooneveld, M. M.; Hilhorst, J.; Donega, C. d. M.; t Hart, D. C.; van Blaaderen, A.; Vanmaekelbergh, D.; Meijerink, A.: On the incorporation mechanism of hydrophobic quantum dots in silica spheres by a reverse microemulsion method. *Chemistry of Materials* **2008**, *20*, 2503-2512.

(67) Deng, Y.-H.; Wang, C.-C.; Hu, J.-H.; Yang, W.-L.; Fu, S.-K.: Investigation of formation of silica-coated magnetite nanoparticles via sol–gel approach. *Colloids and Surfaces A: Physicochemical and Engineering Aspects* **2005**, *262*, 87-93.

(68) Lu, Y.; Yin, Y. D.; Mayers, B. T.; Xia, Y. N.: Modifying the surface properties of superparamagnetic iron oxide nanoparticles through a sol-gel approach. *Nano Letters* **2002**, *2*, 183-186.

(69) Stöber, W.; Fink, A.; Bohn, E.: Controlled growth of monodisperse silica spheres in the micron size range. *Journal of Colloid and Interface Science* **1968**, *26*, 62-69.

(70) Guerrero-Martinez, A.; Perez-Juste, J.; Liz-Marzan, L. M.: Recent Progress on Silica Coating of Nanoparticles and Related Nanomaterials. *Advanced Materials* **2010**, *22*, 1182-1195.

(71) Gong, P.; Li, H.; He, X.; Wang, K.; Hu, J.; Tan, W.; Zhang, S.; Yang, X.: Preparation and antibacterial activity of Fe_3O_4@Ag nanoparticles. *Nanotechnology* **2007**, *18*, 1-7.

(72) Yu, H.; Chen, M.; Rice, P. M.; Wang, S. X.; White, R. L.; Sun, S.: Dumbbell-like Bifunctional Au−Fe_3O_4 Nanoparticles. *Nano Letters* **2005**, *5*, 379-382.

(73) Li, H.; Bian, Z.; Zhu, J.; Huo, Y.; Li, H.; Lu, Y.: Mesoporous Au/TiO2 nanocomposites with enhanced photocatalytic activity. *Journal of the American Chemical Society* **2007**, *129*, 4538-4539.

(74) Oldfield, G.; Ung, T.; Mulvaney, P.: Au@SnO_2 Core–Shell Nanocapacitors. *Advanced Materials* **2000**, *12*, 1519-1522.

(75) Wu, X.-F.; Song, H.-Y.; Yoon, J.-M.; Yu, Y.-T.; Chen, Y.-F.: Synthesis of Core-Shell Au@TiO(2) Nanoparticles with Truncated Wedge-Shaped Morphology and Their Photocatalytic Properties. *Langmuir* **2009**, *25*, 6438-6447.

(76) Leung, K. C.-F.; Xuan, S.; Zhu, X.; Wang, D.; Chak, C.-P.; Lee, S.-F.; Ho, W. K. W.; Chung, B. C. T.: Gold and iron oxide hybrid nanocomposite materials. *Chemical Society Reviews* **2012**, *41*, 1911-1928.

(77) Stankovich, S.; Dikin, D. A.; Dommett, G. H. B.; Kohlhaas, K. M.; Zimney, E. J.; Stach, E. A.; Piner, R. D.; Nguyen, S. T.; Ruoff, R. S.: Graphene-based composite materials. *Nature* **2006**, *442*, 282-286.

(78) Cui, P.; Seo, S.; Lee, J.; Wang, L.; Lee, E.; Min, M.; Lee, H.: Nonvolatile Memory Device Using Gold Nanoparticles Covalently Bound to Reduced Graphene Oxide. *ACS Nano* **2011**, *5*, 6826-6833.

(79) Cui, S.; Mao, S.; Lu, G.; Chen, J.: Graphene Coupled with Nanocrystals: Opportunities and Challenges for Energy and Sensing Applications. *The Journal of Physical Chemistry Letters* **2013**, *4*, 2441-2454.

(80) Russo, P. A.; Donato, N.; Leonardi, S. G.; Baek, S.; Conte, D. E.; Neri, G.; Pinna, N.: Room-Temperature Hydrogen Sensing with Heteronanostructures Based on Reduced Graphene Oxide and Tin Oxide. *Angewandte Chemie International Edition* **2012**, *51*, 11053-11057.

(81) Chen, D.; Feng, H.; Li, J.: Graphene Oxide: Preparation, Functionalization, and Electrochemical Applications. *Chemical Reviews* **2012**, *112*, 6027-6053.

(82) Zubir, N. A.; Yacou, C.; Motuzas, J.; Zhang, X.; Diniz da Costa, J. C.: Structural and functional investigation of graphene oxide–Fe_3O_4 nanocomposites for the heterogeneous Fenton-like reaction. *Scientific Reports* **2014**, *4*.

(83) Bai, S.; Shen, X.: Graphene-inorganic nanocomposites. *RSC Advances* **2012**, *2*, 64-98.

(84) Chen, W.; Yan, L.; Bangal, P. R.: Preparation of graphene by the rapid and mild thermal reduction of graphene oxide induced by microwaves. *Carbon* **2010**, *48*, 1146-1152.

(85) Georgakilas, V.; Otyepka, M.; Bourlinos, A. B.; Chandra, V.; Kim, N.; Kemp, K. C.; Hobza, P.; Zboril, R.; Kim, K. S.: Functionalization of Graphene: Covalent and Non-Covalent Approaches, Derivatives and Applications. *Chemical Reviews* **2012**, *112*, 6156-6214.

(86) Baranton, S.; Bélanger, D.: Electrochemical Derivatization of Carbon Surface by Reduction of in Situ Generated Diazonium Cations. *The Journal of Physical Chemistry B* **2005**, *109*, 24401-24410.

(87) Quintana, M.; Vazquez, E.; Prato, M.: Organic Functionalization of Graphene in Dispersions. *Accounts of Chemical Research* **2012**, *46*, 138-148.

(88) Dreyer, D. R.; Park, S.; Bielawski, C. W.; Ruoff, R. S.: The chemistry of graphene oxide. *Chemical Society Reviews* **2010**, *39*, 228-240.

(89) Wu, Z.-S.; Zhou, G.; Yin, L.-C.; Ren, W.; Li, F.; Cheng, H.-M.: Graphene/metal oxide composite electrode materials for energy storage. *Nano Energy* **2012**, *1*, 107-131.

(90) Lai, L.; Yang, H.; Wang, L.; Teh, B. K.; Zhong, J.; Chou, H.; Chen, L.; Chen, W.; Shen, Z.; Ruoff, R. S.; Lin, J.: Preparation of Supercapacitor Electrodes through Selection of Graphene Surface Functionalities. *ACS Nano* **2012**, *6*, 5941-5951.

(91) Yu, S.-H.; Conte, D. E.; Baek, S.; Lee, D.-C.; Park, S.-K.; Lee, K. J.; Piao, Y.; Sung, Y.-E.; Pinna, N.: Structure-Properties Relationship in Iron Oxide-Reduced Graphene Oxide Nanostructures for Li-Ion Batteries. *Advanced Functional Materials* **2013**, *23*, 4293-4305.

Chapter 2

Functionalization of iron oxide nanoparticles with small organic molecules for the investigation of the electronic properties of a single nanoparticle

2.1. Introduction

The concept of stabilization of nanoparticles in dispersion arose several decades ago[1,2] and it still represents a central subject both in academia and, more recently, in industry[3].

Stabilization is accomplished by adsorbing at nanoparticles surface, molecules (ligands) bearing at least one functional group showing affinity for the investigated material, thus being able to interact with it. The part of the ligand exposed on particle surface influences solvent dispersibility, allows further interactions with other phases, but most of all it determines the nature of the stabilization.

Stabilization of nanoparticles can be achieved in two ways: by electrostatic repulsion forces and by steric effects[4,5]. The first one, electrostatic stabilization, is accomplished by adsorbing charged species or by the dissociation of surface groups present on nanoparticles. This method suffers several drawbacks since it is dependent on the pH and ionic strength of the dispersing medium, hence being labile. Furthermore, electrostatic stabilization can not be exploited in hydrophobic media. Steric stabilization is instead achieved by coating particles surface with polymer molecules. This approach provides a more stabile ligand shell and it is more versatile due to the wide variety of commercially available polymers which can promote dispersibility in both hydrophobic and hydrophilic solvents.

However, early examples (e.g. gold synthesis by Turkevich, date back to 1951[6]) proved that stable dispersions can be achieved by using simple small organic molecules as ligands. Depending on the chemical nature of the ligands, stabilization is achieved either by electrostatic repulsion forces, steric effect or a combination of both. The advantage of using these species is that, unlike polymers, they likely create organic layers which are more densely packed[7], due to the shorter chain length. Clearly, choice of the more appropriate molecule is fundamental for an effective stabilization. The additional advantage of using small organic molecules is usually reflected in a lower overall amount of organic matter coating nanoparticles than when using polymer ligands.

Organic shells are mainly used to achieve dispersibility in a desired solvent or interactions with other materials for fabricating composites; more generally, they are used to tune the range of application of the investigated material[8]. The organic coating interacting with nanoparticles might influence their physical or chemical properties and, whether this might be an advantage in some cases, it could represent a drawback when the main object of a research consists in investigating the fundamental properties of a material[9].

Many research studies are focused on magnetic iron oxide nanoparticles, particularly magnetite. Magnetite is indeed suitable for a wide range of applications varying from magnetic data storage and energy storage devices[10], to biomedical applications such as magnetic resonance imaging (MRI) contrast agent, hyperthermia and drug delivery[11]. Additionally, magnetite represents an interesting system for theoretical investigations about its inherent physical properties such as the conducting behaviour and magnetism.

Furthermore, organic coating of iron oxide nanoparticles is extremely versatile because of the affinity that several functional groups present for iron oxide. The most employed functionalities comprise phosphates and phosphonic acids[12], catechols[13,14] and carboxylic acids[15-17].

Usually, carboxylic acids represent the first choice when dealing with magnetite nanoparticles. They present good affinity for iron oxide and a wide variety of molecules ranging from simple aliphatic mono-carboxylic acids to molecules bearing more functional groups is commercially available. Therefore, they allow for simple stabilization in the desired solvent as well as for further modification of the organic ligand shell. Among all, oleic acid might be regarded as the most employed carboxylic acid used for stabilization of magnetite in organic solvents (e.g. hexane), while citric acid was largely used to achieve aqueous dispersions for biological applications[18].

Both of them were used either as *in-situ* stabilizers[19-21], thus introduced in the reaction mixture during the synthesis of iron oxide nanoparticles, or for post-synthesis treatments[22,23]. While the choice of the ligand for *in-situ* stabilization might be limited because strongly related to the reaction conditions (e.g. reaction temperature, solvent), post-synthesis methods permit to select the capping molecules depending on the final properties or targeted applications. Moreover, unlike post-synthesis stabilization, the ligand might severely influence the chemical, structural and morphological properties of the final particles when added during the synthesis, thus rendering sometimes the choice of the more appropriate stabilizer even more complicate[7].

The aim of this chapter is to illustrate the simplicity and versatility of a post-synthesis stabilization procedure using small organic molecules as well as the impact that the ligand shell may have on the investigation on particles physical properties.

Magnetite nanoparticles were chosen, on the one hand, because they are referred to as a suitable platform for post-synthesis coating procedures. On the other hand, understanding the non-equilibrium transport properties of strongly correlated systems such as charged ordered insulators or Mott insulators[24] represents a fundamental issue of condensed matter physics. In 1939, E. J. W. Verwey observed that in magnetite electronic transport depends on the temperature[25]. Particularly, the transition from insulator-to-metal is observed at the so called Verwey temperature (T_V). The ordering of Fe^{2+} and Fe^{3+} cations into alternating layers at temperatures lower than T_V is regarded as responsible of such transition. Therefore, magnetite represents an archetype of strongly correlated materials where non-equilibrium transport phenomena can be investigated. Although several studies were performed

on bulk magnetite or on thin films[26,27], increasing interest is focused on investigating charge transport properties in magnetite nanoparticles and, in particular, on single nanoparticles. Indeed, it is believed that the Verwey transition is altered by size effects[28]. For that purpose, stable dispersions of isolated magnetite nanoparticles represent the appropriate source from which single nanoparticles can be extracted. As previously mentioned, coating particles surface with the more suitable ligand is required in order to obtain stable particles dispersion and avoid aggregation.

However, the stabilizing agent should be carefully chosen in order to not alter the chemical and physical properties of the material, since many properties are influenced by the surface chemistry[9].

Two carboxylic acid molecules, particularly undecanoic acid and citric acid, will be used to impart organic and aqueous dispersibility to magnetite nanoparticles.

In line with the central theme of this thesis, more emphasis will be placed in the description of the stabilization procedure. The chemical and structural properties of the functionalized nanoparticles will be compared with the ones of uncoated nanoparticles.

The study of physical properties of the as-modified nanoparticles was performed by the group of Professor Hervé Aubin (Laboratory of physics and study of materials - ESPCI - Paris) and will be resumed in a dedicated section (Cf. paragraph 2.3.2).

2.2. Experimental section

2.2.1. Materials

Iron(III) acetylacetonate (anhydrous, 99% - STREM) and benzyl alcohol (puriss. 99% - Sigma Aldrich) were stored in a glovebox and used as received.

NaOH (puriss. p.a., pellets, 97% - Fluka Analytical), citric acid (99.5% - ABCR) and undecanoic acid (97% - ABCR) were used as received.

2.2.2. Methods

Magnetite (**Fe_3O_4**) nanoparticles were synthesized via the "benzyl alcohol route" as previously reported[29].

Briefly, the reaction mixture preparation was carried out in a glovebox (H_2O< 0.1 ppm, and O_2< 0.1 ppm). In a typical synthesis, 1.0 g (2.83 mmol) of iron(III) acetylacetonate was placed in a 45-mL inner volume Teflon cup and solubilised in 20 mL of benzyl alcohol. The Teflon cup was then slid into a steel autoclave which was carefully sealed and taken out from the glovebox. The reaction was performed in an oven heated at 175°C for 48 hours. The resulting nanoparticles were collected by centrifugation and washed twice with absolute ethanol and once with dichloromethane. Finally, nanoparticles were redispersed either in 12 mL of hexane or 12 mL of deionized water.

Undecanoic acid-functionalization: post-synthesis functionalization with undecanoic acid was achieved by adding 145 mg (0.778 mmol) of undecanoic acid to the hexane Fe_3O_4 dispersion which was then sonicated for 10 minutes at room temperature and subsequently centrifuged. The as-obtained supernatant containing undecanoic acid-coated Fe_3O_4 nanoparticles (**Fe_3O_4-UA**) was saved, while the precipitate was discarded.

Citric acid-functionalization: post-synthesis functionalization was carried out by solubilising 35 mg (0.182 mmol) of citric acid in 3 mL of the as-obtained Fe_3O_4 nanoparticles aqueous suspension. Subsequently, 5.5 mL of an aqueous NaOH solution (0.05 M) were added to the nanoparticles dispersion. The dispersion was sonicated at room temperature for 10 minutes and then centrifuged. The supernatant containing water-dispersible citrate-capped Fe_3O_4 nanoparticles (**Fe_3O_4-Cit**) was saved, while the precipitate was discarded.

For sake of analysis, small aliquots of both Fe_3O_4-UA and Fe_3O_4-Cit were purified from the excess of surfactant by evaporating the solvent at 50°C under reduced pressure and subsequently washing through magnetic separation with absolute ethanol. Nanoparticles were finally dried and used for KBr-pellet preparation.

2.2.3. Characterization techniques

X-ray powder diffraction (XRD) technique was used in order to study the crystallinity and the structural properties of the as-synthesized nanoparticles.
XRD patterns were measured using an X'Pert MPD Philips diffractometer (Cu Kα radiation at 45 kV and 40 mA) in the 2θ range from 5.00° to 80.00° with a scanning step of 0.2°.
Transmission electron microscopy (TEM) analysis was carried out in order to investigate the size and shape distribution of the nanoparticles before and after functionalization procedure.
TEM analysis was carried out on a Philips CM200 (LaB_6) microscope operating at an acceleration voltage of 200 kV.
Samples were prepared by depositing few drops of hexane (undecanoic acid-capped magnetite nanoparticle) or aqueous (citrate-capped magnetite nanoparticles) dispersions on a 300 mesh carbon film-coated copper grid. The solvent was allowed to evaporate prior to the analysis.
Fourier transform infrared (FTIR) spectroscopy analysis was performed in order to investigate the presence of an organic layer at the nanoparticles surface; for a complete comparison bare nanoparticles and pure ligands were also analyzed.

FTIR analyses were performed on a Thermo Scientific Nicolet iS5 spectrometer. Spectra were acquired in transmission mode (using the KBr pellets method) in the wavenumber range from 4000 to 400 cm^{-1}. All the spectra were acquired using a 4 cm^{-1} resolution and collecting 128 scans.
Baseline correction was applied to all the reported spectra.
Dynamic light scattering (DLS) measurements were carried out in order to determine nanoparticles average size and size distribution. The analysis was performed on a Malvern Zetasizer Nano ZS (ZEN3600).

2.3. Results and discussion

2.3.1. Synthesis and functionalization of magnetite nanoparticles

Magnetite (Fe_3O_4) nanoparticles were synthesized through the so-called "benzyl alcohol route"[29]. The "benzyl alcohol route" is a valuable alternative process for the synthesis of metal oxides, and particularly magnetite nanoparticles, with respect to the traditional co-precipitation method or other nonaqueous procedures which involve the use of large quantities of one or more surfactants, or more reactants[10,30]. It consists indeed in a one-pot reaction involving only a metal complex in the role of the metal oxide precursor, particularly iron(III) acetylacetonate, and of the solvent. Benzyl alcohol acts, at the same time, as solvent and as a reactant. Previous studies demonstrated that such a nonaqueous approach leads to crystalline magnetite particles which size could be easily tuned by changing few reaction parameters (e.g. reaction temperature)[29].
X-ray powder diffraction (XRD) analysis was performed on the as-synthesized magnetite particles and the measured pattern is shown in figure 2.1.

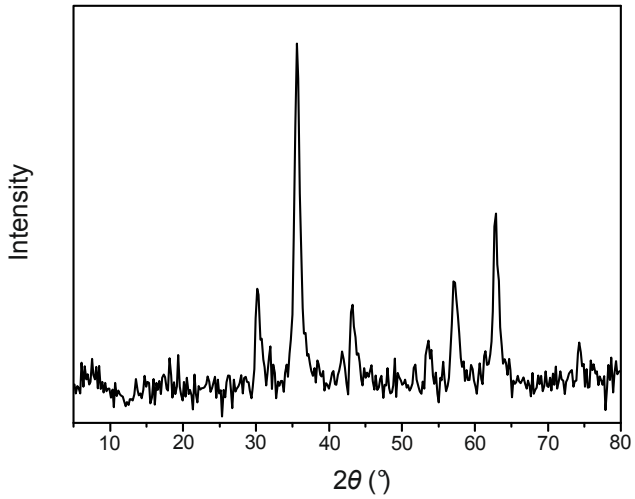

Figure 2.1: X-ray diffractogram of the as-synthesized Fe_3O_4 particles.

The X-ray diffractogram shows pattern in accordance with the structure of magnetite (JCPDS: 01-071-4918). Nevertheless, it should be taken into account that X-ray diffraction patterns for magnetite and maghemite (γ-Fe_2O_3) are very similar. Maghemite differs only for having two additional reflections of

quite low intensity at 23.8 and 26.1 2θ ° (JCPDS: 00-039-1346) that were not noticed in the measured diffractogram. Nevertheless, the presence of maghemite can not be unequivocally ruled out.

The average size of magnetite nanoparticles estimated by the Scherrer equation is about 10 nm.

The absence of any surfactants during the synthesis of magnetite generally leads to nanoparticles that tend to aggregate during the time, thus any nanoparticles dispersion will result in the formation of sediment. On the other hand, the absence of surfactants might be considered as an advantage because it allows nanoparticles to be treated with a simple post-synthesis functionalization process employing the most suitable ligand for the target applications. Synthesis in the presence of surfactants indeed will require a ligand exchange step for the replacement of the existing organic stabilizer with the desired one. Ligand exchange procedures are usually not simple to perform and they often lead to a partial aggregation of nanoparticles, which sometimes are irreversible.

In view of the further investigation about the electronic properties of a single magnetite nanoparticle, it was decided to coat nanoparticles with two different molecules. On the basis of the affinity between carboxyl functionalities and iron oxide, undecanoic acid and citric acid were employed as ligands. When coated by undecanoic acid (UA), nanoparticles present a surface alkyl chains layer (figure 2.2a); this renders possible to achieve stable particles dispersions in organic solvents (e.g. hexane). On the contrary, citric acid (Cit) presents three carboxyl moieties and a hydroxyl group. Citric acid is supposed to interact with the iron oxide particles through either one or two carboxyl moieties[31,32] (figure 2.2b). This would lead to the exposure of carboxyl and hydroxyl moieties at the particles surface rendering the latter dispersible in aqueous medium, particularly at basic pH[31]. The choice of the ligand, and therefore the resulting particle surface chemical composition, might influence the further studies of magnetite electronic properties.

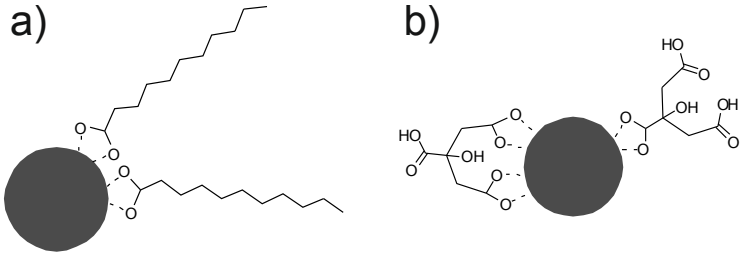

Figure 2.2: Representation of the possible adsorption configuration of undecanoic acid (a) and citric acid (b) at Fe_3O_4 nanoparticles surface.

In order to investigate the presence of an organic layer at particles surface and its chemical composition, all the materials were characterized by Fourier transform infrared (FTIR) spectroscopy. Figure 2.3 illustrates the spectra of pure undecanoic acid, pristine Fe_3O_4 and Fe_3O_4-UA.

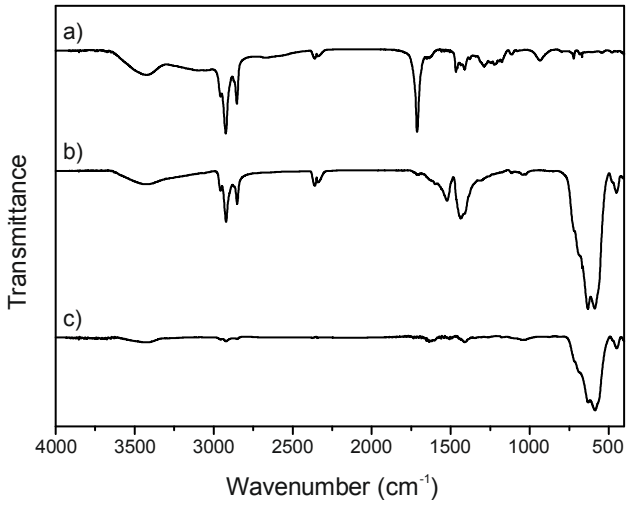

Figure 2.3: FTIR spectra of pure undecanoic acid (a), Fe_3O_4-UA (b), and pristine Fe_3O_4 (c). For sake of clarity, spectra are represented as stacked by an offset value.

Pristine Fe_3O_4 infrared spectrum (figure 2.3c) shows low-intensity absorptions at 2921 and 2852 cm^{-1} ascribable to aliphatic C-H bond stretching vibrations, which might be related to side-products deriving from the decomposition of iron(III) acetylacetonate. The other low intensity bands at 1624 and 1408 cm^{-1}, peaking in the typical spectral region where oxygenated functionalities as carboxyl groups absorb, might originate from the same compounds. However, the low intensity of those absorptions let suggest that the presence of the related organic compounds is limited to low amounts. The peaks at 629 and 586 cm^{-1} are characteristic of the Fe-O bond stretching in nanosized Fe_3O_4 nanoparticles.

FTIR spectrum of Fe_3O_4-UA nanoparticles (figure 2.3b) is featured by sharp peaks centred at 2959, 2921, and 2852 cm^{-1} which are assigned to the aliphatic C-H stretching vibrations of methyl groups and C-H asymmetric and symmetric stretching modes of methylene moieties, respectively. The positions of these peaks are comparable to the stretching modes of undecanoic acid aliphatic chains; therefore, they are indicative of the presence of UA molecules at particles surface. The absence in the Fe_3O_4-UA spectrum of the band at 1710 cm^{-1}, which is typical of C=O stretching mode in the pure undecanoic acid (figure 2.3a), let infer that no free carboxylic acid is present on particles surface upon coating procedure. A double band peaking at 1523 and 1437 cm^{-1} is instead present. These signals are typical of a carboxylate moiety[33,34], indicating that the ligand is adsorbed at the particle surface in its dissociated form. From the difference ($\Delta\nu$) between the position of the asymmetric (ν_{as}, 1523 cm^{-1}) and symmetric (ν_s, 1437 cm^{-1}) stretching modes of the carboxylate groups ($\Delta\nu$= 86 cm^{-1}), it might be suggested that the undecanoate species coordinate to the metal atoms in a bidentate chelating fashion[35,36].

A similar behaviour is observed for particles treated with citric acid (figure 2.4b).

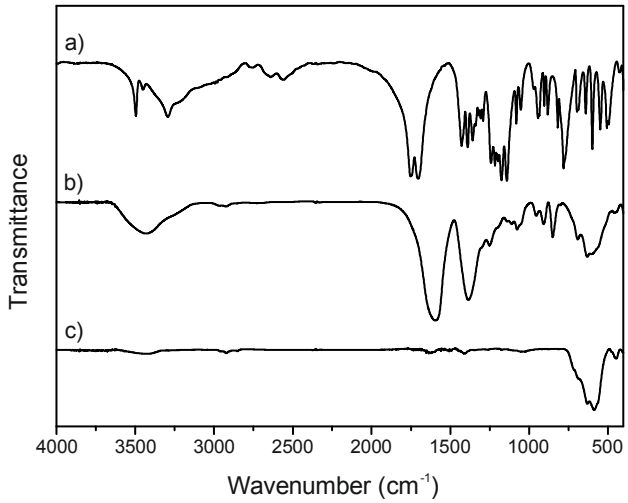

Figure 2.4: FTIR spectra of pure citric acid (a), Fe_3O_4-Cit (b), and pristine Fe_3O_4 (c). For sake of clarity, spectra are represented as stacked by an offset value.

The infrared spectrum of Fe_3O_4-Cit shows indeed two main peaks centred at 1594 and 1386 cm^{-1} that might be assigned, respectively, to the asymmetric and symmetric stretching of the carboxylate ions likely coordinated to the surface of the iron oxide nanoparticles. The absence of any absorption at 1703 cm^{-1}, which corresponds to the C=O stretching mode of the carboxylic groups of citric acid (figure 2.4a), reveals that no free acid is present in the investigated particles. On these bases it might be inferred, similarly to the previous example, that citric acid is adsorbed at particles surface in its dissociated form. Since citric acid possesses three carboxyl functionalities, to suggest the coordination fashion of citrate ions at particles surface is not as straightforward as in the case of Fe_3O_4-UA nanoparticles.

TEM analysis was performed on nanoparticles before and after functionalization procedure (figure 2.5).

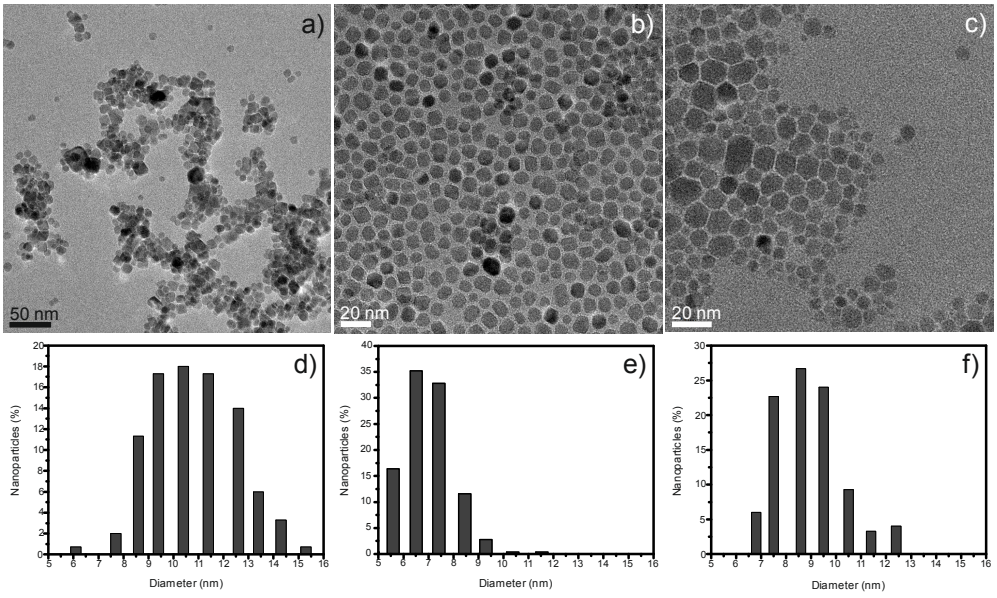

Figure 2.5: TEM images of pristine Fe_3O_4 (a), Fe_3O_4-UA (b) and Fe_3O_4-Cit (c) nanoparticles and the corresponding nanoparticles size distribution evaluated from TEM images (d, e, f).

TEM images of pristine Fe_3O_4 (figure 2.5a) reveal that nanoparticles are polydisperse in size as illustrated in the corresponding histogram (figure 2.5d). The latter shows a broad nanoparticles size distribution centred at about 11 nm, in agreement with the theoretical estimation of peak broadening of the X-ray diffractogram. Moreover, nanoparticles appear aggregated due to a lack of surface stabilization.

The successful coating by undecanoic acid and citric acid is indirectly also confirmed by the TEM images of the material after functionalization (figure 2.5b and 2.5c, respectively). The nanoparticles appear well separated from one other due to the stabilizing effect brought about from the ligand molecules. In the case of undecanoic acid, stabilization is achieved through the steric hindrance introduced by the long alkyl chains adsorbed at the particle surface, while the adsorbed citrate anions stabilize the particles *via* electrostatic repulsion forces. The functionalization process led to a narrower particle size distribution than pristine Fe_3O_4, being the average diameter at about 7 nm for Fe_3O_4-UA and 9 nm for Fe_3O_4-Cit, as depicted by the corresponding histograms (figure 2.5e and 2.5f, respectively).

These results suggest that a nanoparticles size selection was achieved upon surface modification procedure; similar results are usually obtained by means of analytical centrifugation[29]. It is suggested that surface modification likely induced the partial disruption of some agglomerates present in the as-synthesized material into smaller particles, which can be easily stabilized by the organic ligand. The larger particles or aggregates were subsequently removed through the last centrifugation step.

The possibility for citrate species to adsorb on particles surface through two or more carboxylate moieties might lead to a better efficiency in stabilizing larger nanoparticles with respect to undecanoic acid. This might be a possible explanation of the slightly larger nanoparticles average size and size distribution observed for Fe_3O_4-Cit.

Dynamic light scattering (DLS) measurements provided complementary information about particles size distribution and efficiency of the surface modification procedure. The analysis was performed on aqueous dispersions of pristine Fe_3O_4 and Fe_3O_4-Cit nanoparticles, and on hexane dispersion of Fe_3O_4-UA nanoparticles. It should be taken into account that the particles size evaluated by DLS technique is referred to as the hydrodynamic diameter. The hydrodynamic diameter corresponds to the diameter of the dispersed nanoparticles (or more generally of the scatterer objects) and the solvent molecules constituting their solvation shell. Therefore, it appears always larger than the average diameter evaluated by TEM analysis.

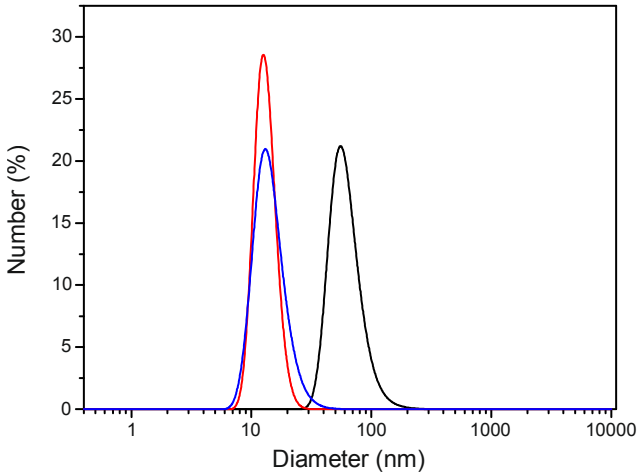

Figure 2.6: DLS plots of pristine Fe_3O_4 (black line), Fe_3O_4-UA (red line) and Fe_3O_4-Cit (blue line) nanoparticles.

Figure 2.6 shows the size distribution of magnetite nanoparticles before and after surface modification procedure. The average hydrodynamic diameter of as-synthesized nanoparticles was evaluated about 63 nm, revealing the presence of agglomerates. Moreover, the broadness of the measured DLS curve indicates that particles are polydisperse in size; in agreement with what observed by TEM analysis. However, upon surface modification procedure average particles size significantly decreased to 13 nm and 15 nm for undecanoate- and citrate-capped magnetite nanoparticles, respectively. At the same time, surface-modified magnetite nanoparticles presented a narrower size distribution than the corresponding uncoated nanoparticles. Particularly, undecanoated-capped particles presented the narrower size distribution.

These results are in agreement with the observations arose from TEM analysis, thus supporting the efficiency of surface modification procedure in disrupting particles agglomerates and leading to stable dispersions of individual particles.

This is the most important requisite for further investigations of the electronic properties of a single nanoparticle.

2.3.2. Investigation on the electronic properties of single magnetite nanoparticles[37,38]

The following part describes the results obtained from the studies on the electronic properties of a single magnetite nanoparticle. The work was performed by the group of Professor Hervé Aubin (Laboratory of physics and study of materials – ESPCI - Paris) and dealt with the investigation of diverse properties on Fe_3O_4-UA and Fe_3O_4-Cit nanoparticles. The aim of this paragraph is to resume the most representative results of those investigations, demonstrating the effectiveness application of the as-functionalized nanoparticles.

With numerous kinds of nanosized materials synthesized nowadays, such as metal, semiconductors, and magnetic materials, the study of their electronic properties became the central subject of many researches aimed to better characterize these materials.

Electron tunneling spectroscopy is well adapted for the study of the electronic spectrum of nanosized materials. In particular, this technique is featured by a high resolution which enables to study even single nanoparticles.

The tunneling electronic spectrum can be measured either with a scanning tunnel microscope (STM) or "on-chip", where the nanoparticle is trapped between two electrodes separated by a gap of a few nanometers. "On-chip" spectroscopy presents several advantages with respect to STM, but it requires the challenging step of trapping the nanoparticle within the nanogap.

Aubin et al. developed a new method for trapping nanoparticles within nanometer-spaced electrodes[37]. It allows a high success rate for nanoparticle trapping and, at the same time, the characterization of the nature of the current path that has been created. Indeed, the evolution of the current with time differs whether a single nanoparticle has been trapped between the electrodes or a percolating path involving many nanoparticles has been formed.

A typical chip circuit used for the study of nanoparticles and the typical current curve obtained when a single metal nanoparticle is trapped within the electrodes are shown in figure 2.7. The chip circuit usually contains 32 nanogaps and the distance between the electrodes is in the 10-20 nm range.

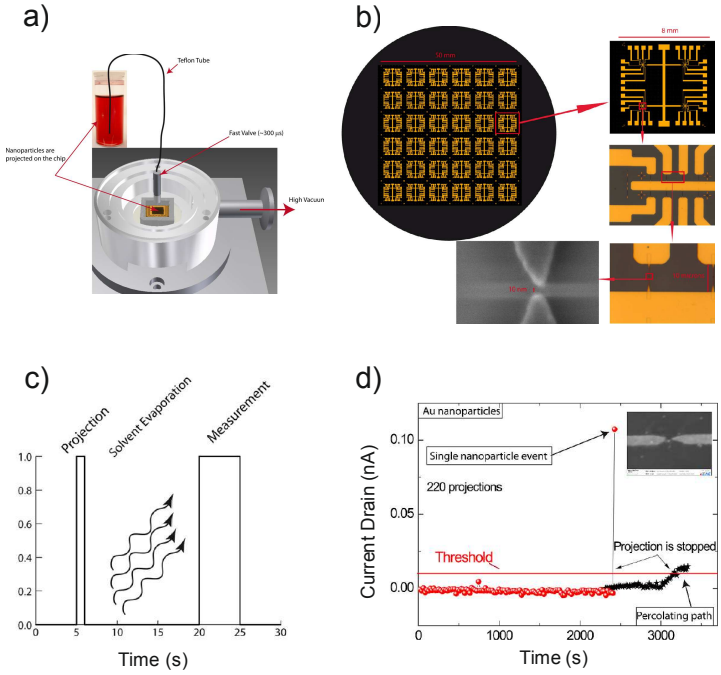

Figure 2.7: (a) High-vacuum chamber used for the projection of nanoparticles on the chip through a fast pulsed valve. (b) Chip circuit on which the nanoparticles are deposited. 36 chips are fabricated on a 3 inches wafer, and each chip contains 32 nanogaps. The distance between the electrodes is in the 10-20 nm range. (c) Sketch of a typical cycle. First, the nanoparticles in solution are projected onto the chip by opening the valve for a short time (<1 ms). Second, a delay between 10 and 20 s is applied to allow the full evaporation of the solvent. Third, the tunnel current is measured. (d) Projection curve for model citrate-capped gold nanoparticles. Each data point of the red dotted curve corresponds to a measurement of the tunnel current following the projection of nanoparticles. The projection stops when the measured tunnel current exceeds the threshold[37].

The current remains equal to zero after each projection until one nanoparticle gets trapped in the nanogap. At that moment the current suddenly jumps to a large value that stops the projection-delay-measure cycle (figure 2.7d).

Moreover, the method allows discriminating between conducting and poorly conductive or insulating materials. When poorly conducting nanoparticles are trapped, the tunnel current only increases progressively; this is the same phenomenon that would be observed whether a percolating path occurred.

The method was first developed using gold nanoparticles, but it was successfully extended to other systems such as magnetite nanoparticles[37].

Generally, one prerequisite of a successful trapping is the use of a stable and aggregate-free dispersion of nanoparticles, possibly quite diluted.

Fe_3O_4-UA nanoparticles were chosen because of the stable organic dispersions achievable, which were characterized by a narrow particle size distribution. Nevertheless, long aliphatic chain layers at particle surface generally create an insulating barrier that might alter further electronic properties analysis. For this reason, undecanoic acid was replaced by nitrosonium tetrafluoroborate ($NOBF_4$) through a ligand exchange procedure just before to carry out the projection of particles between the nanogaps[9,39].

Interestingly, the projection current response led to unexpected results. When the method is applied to Fe_3O_4, the tunnel current did not jump abruptly as a nanoparticle got trapped within the nanogap. The electronic current instead progressively increased until the projection system stopped when the current exceeded the preset threshold (data not showed).

Nevertheless, more studies of the projection process at low T (4.2K) suggested that a single nanoparticle was trapped within the nanogap, further on those studies were supported by scanning electron microscopy (SEM) images of the investigated circuit that showed the presence of an individual nanoparticle between the electrodes (figure 2.8a).

Numerous works reported that oxygen vacancies can be created in metal oxides by the application of a large electric field[40]. As oxygen vacancies are n-type dopants, this leads to electric-field-induced transition from insulator to metal, the so-called switching in current-voltage characteristics.

For that reason, a voltage pulse step was added in the typical projection cycle. Using this procedure, a projection curve corresponding to single-nanoparticle trapping event was observed, as showed in figure 2.8c.

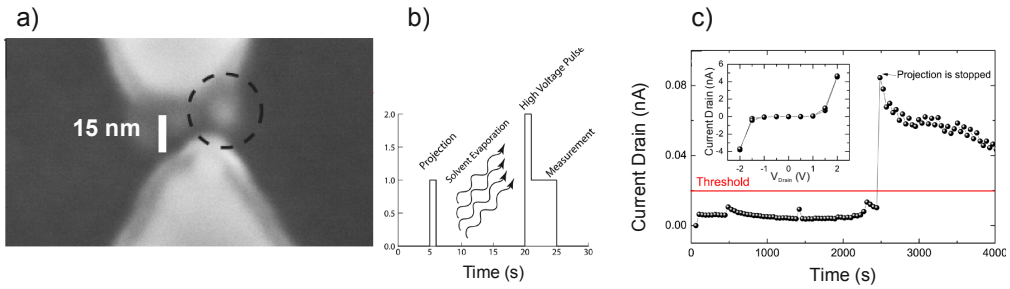

Figure 2.8: (a) SEM image of a single Fe_3O_4 nanoparticle trapped between two nanometer-spaced electrodes. (b) Sketch of a typical cycle (projection-evaporation-pulse-measure) for Fe_3O_4 nanoparticles. (c) Projection curve corresponding to the cycle represented in (b); the inset shows Current-Voltage (I-V) curve for the prepared sample[28,37].

This observation suggested that Fe_3O_4 nanoparticles were actually insulating, probably due to the presence of an oxidized layer constituted of maghemite. The application of a voltage pulse created oxygen vacancies which allowed the observation of electronic transport in those nanoparticles.

As previously mentioned, earlier studies by electron tunnelling spectroscopy were conducted on gold nanoparticles prepared by the Turkevich method, which actually leads to citrate-capped nanoparticles. Those studies revealed that the presence of the capping agent (citrate ions) at the particle surface did not interfere with the measurement of their electronic properties. Citric acid indeed contributes to the formation of the necessary tunnel barrier between the nanoparticle and the electrodes in between which the latter will be trapped[37]. On this basis, citrate-capped magnetite nanoparticles were chosen for the following study.

Magnetite has the AB_2O_4 inverse spinel structure in which the tetrahedral "A" sites are occupied by Fe^{3+} ions while the octahedral "B" sites are occupied by Fe^{2+} and the remaining Fe^{3+} cations. Electronic transport in magnetite was attributed to charge fluctuations between Fe^{2+} and Fe^{3+} sites and E.J.W. Verwey was the first to suggest that the nature of electronic transport changes depends on the temperature and that it exists a particular temperature value at which the transition from an insulating to a metallic behaviour is observed[41]. This phenomenon is called Verwey transition and it occurs at the temperature T_V equal to 120 K for bulk magnetite[25]. It was suggested by Verwey that at T lower than T_V Fe cations organize in alternating layers of Fe^{2+} and Fe^{3+} determining in this way the transition from metal to insulator behaviour. However, there are still controversies about the validity of the Verwey hypothesis and the nature of the electronic transport at T higher than T_V is poorly understood[42].

Moreover, in magnetite voltage induced resistance switching from insulating to a conducting regime has been also observed[43].

Therefore, detailed studies have to be performed in order to understand the phenomena inducing the Verwey transition in magnetite.

Through electronic tunnelling spectroscopy, it was possible to establish the phase diagram temperature/electric field for the Verwey transition and to demonstrate the phenomena of electric

field-induced breakdown of charge ordering in magnetite. Particularly, those results were accomplished by using the in-vacuum projection approach for "on-chip" tunnelling spectroscopy to trap a single Fe_3O_4 nanoparticle between two nanometer-spaced electrodes, as previously described.

Five chip circuits were measured applying different drain voltages varying from -2 to 2 V and at several temperatures in the range from 300 K to 4.2 K; the chips showed similar IV curves which are reported in figure 2.9a.

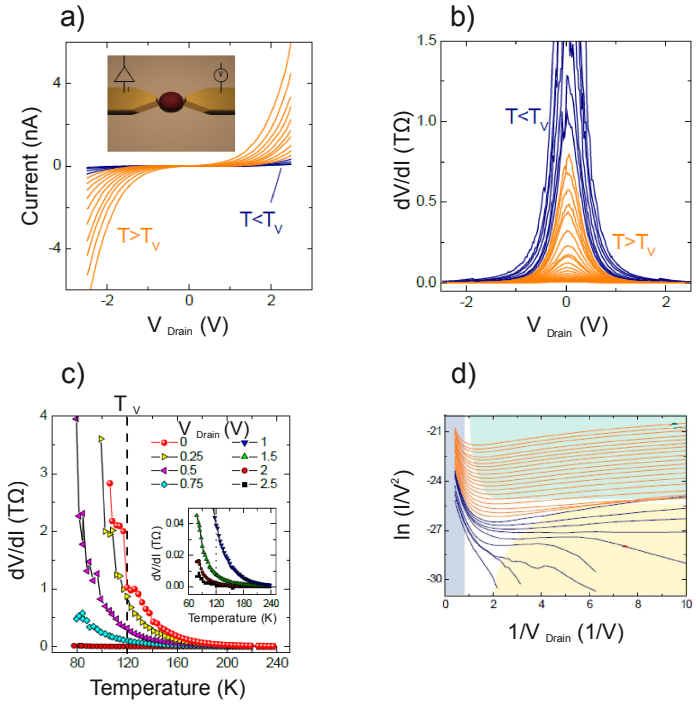

Figure 2.9: (a) IV curves of a single nanoparticle junction. (b) dV/dI as a function of voltage. (c) dV/dI as a function of temperature at selected drain voltages. The dashed line shows the Verwey transition temperature T_V ~ 120 K. (d) Fowler-Nordheim plot of the IV curves showed in (a). The colours indicate the three different identified regimes: polaron tunnelling (light blue area), low temperature insulating phase (yellow area), and high temperature conducting phase (green area)[38].

By extracting dV/dI as a function of temperature from these curves, it was observed that at a voltage V = 0 V the resistance increased abruptly at the Verwey temperature, T_V ~ 120 K, which is identical to the transition temperature observed in bulk magnetite.

The obtained results were depicted in a Fowler-Nordheim plot (figure 2.9d), which showed that three regimes could be identified on the basis of how the nature of electronic transport changes as a function of temperature and electric field.

At low voltage and high temperature (green zone), the curve has a positive slope indicating a linear tunnelling regime. At low voltage and low temperature (yellow zone), the slope becomes negative in the insulating phase. At high voltage (blue zone), the curve has a negative slope indicating the presence of localized states[38].

2.4. Conclusions

The functionalization of magnetite nanoparticles with undecanoic acid and citric acid was described.
The adsorption of those molecules at particles surface was proven by FTIR spectroscopy, which revealed that both ligands interact through carboxylate moieties. The evidence of the effectiveness of the coating procedure in leading to stable dispersion of individual nanoparticles was proven for both of the organic molecules by TEM and DLS analysis.
The simplicity and versatility of the coating procedure to obtain both organic and aqueous stable dispersions was demonstrated, only by choosing the ligand molecule more suitable for the required dispersing medium.
The practical applicability of a stable dispersion of individual nanoparticles for the investigation of the electronic properties of a single magnetite nanoparticle was demonstrated by the studies carried out by the group of Professor H. Aubin.
Besides the more specific results, those studies revealed the crucial aspect of choosing the proper stabilizer: when studying electronic properties of a single magnetite nanoparticle, the undecanoate surface layer had to be replaced by $NOBF_4$ prior the analysis due to its insulator effect. On the contrary, citric acid didn't represent an obstacle to the charge-transfer measurements. It indeed favoured the creation of the necessary tunnel barrier when performing "on-chip" electronic tunneling spectroscopy. That analysis permitted to clearly identify the Verwey transition in a single magnetite nanoparticle and to reveal that the transition temperature is electric field dependent.

2.5. Bibliography

(1) Derjaguin, B.; Landau, L.: Theory of the stability of strongly charged lyophobic sols and of the adhesion of strongly charged particles in solutions of electrolytes. *Progress in Surface Science* **1993**, *43*, 30-59.

(2) Mackor, E. L.: A theoretical approach of the colloid-chemical stability of dispersions in hydrocarbons. *Journal of Colloid Science* **1951**, *6*, 492-495.

(3) Studart, A. R.; Amstad, E.; Gauckler, L. J.: Colloidal Stabilization of Nanoparticles in Concentrated Suspensions. *Langmuir* **2006**, *23*, 1081-1090.

(4) Hidehiro, K.; Motoyuki, I.: Surface modification and characterization for dispersion stability of inorganic nanometer-scaled particles in liquid media. *Science and Technology of Advanced Materials* **2010**, *11*, 044304.

(5) Rozenberg, B. A.; Tenne, R.: Polymer-assisted fabrication of nanoparticles and nanocomposites. *Progress in Polymer Science* **2008**, *33*, 40-112.

(6) Turkevich, J.; Stevenson, P. C.; Hillier, J.: A study of the nucleation and growth processes in the synthesis of colloidal gold. *Discussions of the Faraday Society* **1951**, *11*, 55-75.

(7) Garnweitner, G.: In-situ versus post-synthetic stabilization of metal oxide nanoparticles. In *The delivery of nanoparticles*; Hashim, D. A. A., Ed.; InTech, 2012; pp 71-92.

(8) Ninjbadgar, T.; Brougham, D. F.: Epoxy Ring Opening Phase Transfer as a General Route to Water Dispersible Superparamagnetic Fe_3O_4 Nanoparticles and Their Application as Positive MRI Contrast Agents. *Advanced Functional Materials* **2011**, *21*, 4769-4775.

(9) Dong, A.; Ye, X.; Chen, J.; Kang, Y.; Gordon, T.; Kikkawa, J. M.; Murray, C. B.: A Generalized Ligand-Exchange Strategy Enabling Sequential Surface Functionalization of Colloidal Nanocrystals. *Journal of the American Chemical Society* **2010**, *133*, 998-1006.

(10) Frey, N. A.; Peng, S.; Cheng, K.; Sun, S.: Magnetic nanoparticles: synthesis, functionalization, and applications in bioimaging and magnetic energy storage. *Chemical Society Reviews* **2009**, *38*, 2532-2542.

(11) Laurent, S.; Forge, D.; Port, M.; Roch, A.; Robic, C.; Elst, L. V.; Muller, R. N.: Magnetic iron oxide nanoparticles: Synthesis, stabilization, vectorization, physicochemical characterizations, and biological applications. *Chemical Reviews* **2008**, *108*, 2064-2110.

(12) Lalatonne, Y.; Paris, C.; Serfaty, J. M.; Weinmann, P.; Lecouvey, M.; Motte, L.: Bis-phosphonates-ultra small superparamagnetic iron oxide nanoparticles: a platform towards diagnosis and therapy. *Chemical Communications* **2008**, 2553-2555.

(13) Amstad, E.; Gillich, T.; Bilecka, I.; Textor, M.; Reimhult, E.: Ultrastable Iron Oxide Nanoparticle Colloidal Suspensions Using Dispersants with Catechol-Derived Anchor Groups. *Nano Letters* **2009**, *9*, 4042-4048.

(14) Xu, C.; Xu, K.; Gu, H.; Zheng, R.; Liu, H.; Zhang, X.; Guo, Z.; Xu, B.: Dopamine as A Robust Anchor to Immobilize Functional Molecules on the Iron Oxide Shell of Magnetic Nanoparticles. *Journal of the American Chemical Society* **2004**, *126*, 9938-9939.

(15) Qu, H.; Caruntu, D.; Liu, H.; O'Connor, C. J.: Water-Dispersible Iron Oxide Magnetic Nanoparticles with Versatile Surface Functionalities. *Langmuir* **2011**, *27*, 2271-2278.

(16) Wu, W.; He, Q.; Jiang, C.: Magnetic Iron Oxide Nanoparticles: Synthesis and Surface Functionalization Strategies. *Nanoscale Research Letters* **2008**, *3*, 397-415.

(17) Sahoo, Y.; Pizem, H.; Fried, T.; Golodnitsky, D.; Burstein, L.; Sukenik, C. N.; Markovich, G.: Alkyl phosphonate/phosphate coating on magnetite nanoparticles: A comparison with fatty acids. *Langmuir* **2001**, *17*, 7907-7911.

(18) Sahoo, Y.; Goodarzi, A.; Swihart, M. T.; Ohulchanskyy, T. Y.; Kaur, N.; Furlani, E. P.; Prasad, P. N.: Aqueous Ferrofluid of Magnetite Nanoparticles: Fluorescence Labeling and Magnetophoretic Control. *The Journal of Physical Chemistry B* **2005**, *109*, 3879-3885.

(19) Hyeon, T.; Lee, S. S.; Park, J.; Chung, Y.; Na, H. B.: Synthesis of Highly Crystalline and Monodisperse Maghemite Nanocrystallites without a Size-Selection Process. *Journal of the American Chemical Society* **2001**, *123*, 12798-12801.

(20) Park, J.; An, K.; Hwang, Y.; Park, J.-G.; Noh, H.-J.; Kim, J.-Y.; Park, J.-H.; Hwang, N.-M.; Hyeon, T.: Ultra-large-scale syntheses of monodisperse nanocrystals. *Nat Mater* **2004**, *3*, 891-895.

(21) Sun, S.; Zeng, H.; Robinson, D. B.; Raoux, S.; Rice, P. M.; Wang, S. X.; Li, G.: Monodisperse MFe_2O_4 (M = Fe, Co, Mn) Nanoparticles. *Journal of the American Chemical Society* **2003**, *126*, 273-279.

(22) Park, Y.; Whitaker, R. D.; Nap, R. J.; Paulsen, J. L.; Mathiyazhagan, V.; Doerrer, L. H.; Song, Y.-Q.; Hürlimann, M. D.; Szleifer, I.; Wong, J. Y.: Stability of Superparamagnetic Iron Oxide Nanoparticles at Different pH Values: Experimental and Theoretical Analysis. *Langmuir* **2012**, *28*, 6246-6255.

(23) Roonasi, P.; Holmgren, A.: A Fourier transform infrared (FTIR) and thermogravimetric analysis (TGA) study of oleate adsorbed on magnetite nano-particle surface. *Applied Surface Science* **2009**, *255*, 5891-5895.

(24) Mott, N. F.: Metal-Insulator Transition. *Reviews of Modern Physics* **1968**, *40*, 677-683.

(25) Verwey, E. J. W.: Electronic conduction of magnetite (Fe_3O_4) and its transition point at low temperatures. *Nature* **1939**, *144*, 327-328.

(26) Li, X. W.; Gupta, A.; Xiao, G.; Gong, G. Q.: Transport and magnetic properties of epitaxial and polycrystalline magnetite thin films. *Journal of Applied Physics* **1998**, *83*, 7049-7051.

(27) Ramos, A. V.; Moussy, J.-B.; Guittet, M.-J.; Bataille, A. M.; Gautier-Soyer, M.; Viret, M.; Gatel, C.; Bayle-Guillemaud, P.; Snoeck, E.: Magnetotransport properties of Fe_3O_4 epitaxial thin films: Thickness effects driven by antiphase boundaries. *Journal of Applied Physics* **2006**, *100*, -.

(28) Mottaghizadeh, A.; Lang, P. L.; Cui, L. M.; Lesueur, J.; Li, J.; Zheng, D. N.; Rebuttini, V.; Pinna, N.; Zimmers, A.; Aubin, H.: Nanoparticles charge response from electrostatic force microscopy. *Applied Physics Letters* **2013**, *102*, -.

(29) Pinna, N.; Grancharov, S.; Beato, P.; Bonville, P.; Antonietti, M.; Niederberger, M.: Magnetite Nanocrystals: Nonaqueous Synthesis, Characterization, and Solubility†. *Chemistry of Materials* **2005**, *17*, 3044-3049.

(30) Laurent, S.; Forge, D.; Port, M.; Roch, A.; Robic, C.; Vander Elst, L.; Muller, R. N.: Magnetic Iron Oxide Nanoparticles: Synthesis, Stabilization, Vectorization, Physicochemical Characterizations, and Biological Applications. *Chemical Reviews* **2008**, *108*, 2064-2110.

(31) Goloverda, G.; Jackson, B.; Kidd, C.; Kolesnichenko, V.: Synthesis of ultrasmall magnetic iron oxide nanoparticles and study of their colloid and surface chemistry. *Journal of Magnetism and Magnetic Materials* **2009**, *321*, 1372-1376.

(32) Nigam, S.; Barick, K. C.; Bahadur, D.: Development of citrate-stabilized Fe_3O_4 nanoparticles: Conjugation and release of doxorubicin for therapeutic applications. *Journal of Magnetism and Magnetic Materials* **2011**, *323*, 237-243.

(33) Dobson, K. D.; McQuillan, A. J.: In situ infrared spectroscopic analysis of the adsorption of aliphatic carboxylic acids to TiO_2, ZrO_2, Al_2O_3, and Ta_2O_5 from aqueous solutions. *Spectrochimica Acta Part A: Molecular and Biomolecular Spectroscopy* **1999**, *55*, 1395-1405.

(34) Wu, X.; Wang, D.; Yang, S.: Preparation and Characterization of Stearate-Capped Titanium Dioxide Nanoparticles. *Journal of Colloid and Interface Science* **2000**, *222*, 37-40.

(35) Deacon, G. B.; Huber, F.; Phillips, R. J.: Diagnosis of the nature of carboxylate coordination from the direction of shifts of carbon-oxygen stretching frequencies. *Inorganica Chimica Acta* **1985**, *104*, 41-45.

(36) Deacon, G. B.; Phillips, R. J.: Relationships between the carbon-oxygen stretching frequencies of carboxylato complexes and the type of carboxylate coordination. *Coordination Chemistry Reviews* **1980**, *33*, 227-250.

(37) Yu, Q.; Cui, L.; Lequeux, N.; Zimmers, A.; Ulysse, C.; Rebuttini, V.; Pinna, N.; Aubin, H.: In-Vacuum Projection of Nanoparticles for On-Chip Tunneling Spectroscopy. *ACS Nano* **2013**, *7*, 1487-1494.

(38) Yu, Q.; Mottaghizadeh, A.; Wang, H.; Ulysse, C.; Zimmers, A.; Rebuttini, V.; Pinna, N.; Aubin, H.: Verwey transition in single magnetite nanoparticles. *Submitted* **2014**.

(39) Rosen, E. L.; Buonsanti, R.; Llordes, A.; Sawvel, A. M.; Milliron, D. J.; Helms, B. A.: Exceptionally Mild Reactive Stripping of Native Ligands from Nanocrystal Surfaces by Using Meerwein's Salt. *Angewandte Chemie International Edition* **2012**, *51*, 684-689.

(40) Odagawa, A.; Katoh, Y.; Kanzawa, Y.; Wei, Z.; Mikawa, T.; Muraoka, S.; Takagi, T.: Electroforming and resistance-switching mechanism in a magnetite thin film. *Applied Physics Letters* **2007**, *91*, -.

(41) Verwey, E. J. W.; Heilmann, E. L.: Physical Properties and Cation Arrangement of Oxides with Spinel Structures I. Cation Arrangement in Spinels. *The Journal of Chemical Physics* **1947**, *15*, 174-180.

(42) García, J.; Subías, G.: The Verwey transition—a new perspective. *Journal of Physics: Condensed Matter* **2004**, *16*, R145.

(43) Lee, S.; Fursina, A.; Mayo, J. T.; Yavuz, C. T.; Colvin, V. L.; Sumesh Sofin, R. G.; Shvets, I. V.; Natelson, D.: Electrically driven phase transition in magnetite nanostructures. *Nat Mater* **2008**, *7*, 130-133.

Chapter 3

Influence of surface chemical functionalities on the fabrication of graphene oxide-iron oxide composite materials

3.1. Introduction

3.1.1. Chemical modification of carbonaceous materials

The outstanding properties of graphene-like materials as high mechanical stability, good electrical conductivity, ease of handling[1-3], and the consequent wide range of application fields[4-6], motivated an increasing interest in such a material in the last decades[7].

Graphene oxide and its derivatives reduced graphene oxide and single-layer graphene are the most investigated materials[5]. A common characteristic to all those materials is the scarcity of specific surface functionalities. Indeed, graphene and reduced graphene oxide possess almost no functional groups beside some oxygen-containing moieties preferentially situated at the edges of the flakes[8-10]. On the other hand, graphene oxide is featured by a random composition and distribution of oxygen-containing groups that is strongly influenced by the starting material and experimental conditions[11,12], hence hardly predictable.

The interest in graphene-based composites drove the development of strategies aimed at chemically modifying carbon materials in order to introduce surface functionalities appropriate for the fabrication of the desired composite[13-16].

Chemical modification of graphene-like materials is usually achieved by covalent approaches, although non-covalent approaches exist too[17].

The simplest case of covalent chemical functionalization is represented by the oxidation of graphite to yield graphene oxide[1]. Nonetheless, the unpredictable composition of surface functionalities and the formation of undesired defect sites make this procedure ineffective when aiming to obtain specific functionalities. In that sense, oxidation of graphite might represent a starting point. Indeed, carboxyl moieties present at the periphery of the carbon sheets may be employed as anchoring groups to which covalently bind functional molecules through formation of ester or amide bonds[18-21]. Other works reported about epoxy groups as anchoring sites since they can be modified through ring-opening reactions[22-24]. However, those strategies might lack of control over reproducibility and grafting yields.

A peculiarity of carbon substrates is the capability to be modified through formation of covalent C-C bonds through some of the typical reactions of organic chemistry. Particularly, graphene reactivity toward Diels-Alder reactions[25] and 1,3-dipolar cycloaddition was investigated[26]. Another extensively investigated and likely more common way to covalently modify graphene-based materials is *via* diazonium chemistry[27-32].

The first example of chemical functionalization through diazonium chemistry was introduced in 1992 by Pinson et al.[33] who utilized an electrochemically-assisted procedure to graft several *para*-substituted phenyl moieties to diverse carbon substrates as glassy carbon and highly oriented pyrolytic graphite (HOPG)[34]. Electrochemical grafting is the most investigated procedure[35-38] but spontaneous functionalization, meant as traditional chemical synthesis in solution, is also used and was introduced first by Cabot Corporation[39].

In electrochemical grafting (or electrografting), the diazonium salt is reduced at the surface to be modified by applying to the latter a potential equal to or more negative than the one needed for the reduction of the specific diazonium salt[34,40]. On the contrary, spontaneous grafting is performed in solution by dispersing both the material to be modified and the diazonium precursor or salt in the same medium. In this case, the ability of the carbon surface to reduce the diazonium compound in order to initiate the reaction is the fundamental requirement[40,41]. Although electrografting is usually faster and leads to a larger coverage extent and to thicker phenyl layers than spontaneous procedure[42,43], the latter is simpler, more flexible and more convenient for mass production and for modification of powder materials [40,44]. In both of the cases, diazonium compounds are often generated *in-situ* from the corresponding aryl amine and in presence of a diazotization agent. This approach is indeed more convenient since it allows avoiding the difficult steps of purification and isolation typical of separate synthesis of diazonium compounds[35]. Moreover, *in-situ* generation of diazonium compounds is versatile since it can be performed either in aqueous or organic media, depending on the solubility of the employed diazonium precursor.

Despite the grafting mechanism on carbonaceous materials was not elucidated in detail yet[29], it is generally accepted that it proceeds through few fundamental steps, as described in figure 3.1.

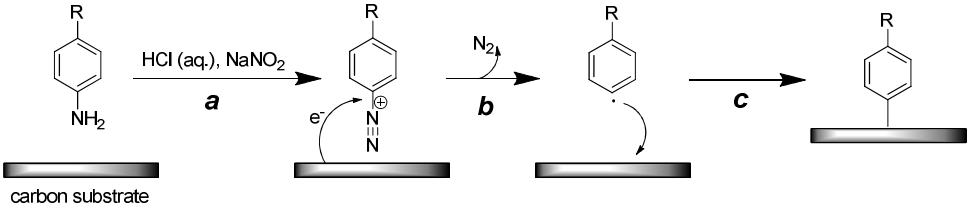

Figure 3.1: Illustration of the covalent functionalization of a carbonaceous material through diazonium chemistry. (a) The chosen aryl amine is dissolved in aqueous acid solution in presence of the carbon substrate. The diazonium compound is generated *in-situ* via the addition of $NaNO_2$ acting as the diazotization agent. (b) *Via* a concerted electron transfer process involving the carbon support, the diazonium compound is reduced to the corresponding aryl radical with concomitant release of N_2. (c) The aryl radical subsequently reacts with the carbon substrate to form a covalent C-C bond.

When the reaction is performed in aqueous medium, the carbon substrate is dispersed in aqueous acid (HCl) solution followed by the addition of the desired aryl amine. The diazonium compound is generated by the last addition of sodium nitrite ($NaNO_2$) which acts as the diazotization agent (figure 3.1a)[36]. Whereas organic medium is needed, the reaction is usually performed in acetonitrile, and *tert*-butylnitrite (*t*-Bu-NO_2) is mainly used as the diazotization agent[45].

The production of the aryl radical which will react to give the covalent C-C bond with the substrate is thought to occur through a concerted process which consists of an electron transfer step involving the carbon support, and the subsequent release of nitrogen (N_2)[40,44,46-48].

A peculiarity of diazonium chemistry is to lead to the change in hybridization of the reacted carbon atoms from sp^2 to sp^3, thus to the introduction of defects in the aromatic structure of carbon materials[29,44,49].

It has been studied that the reaction occurs preferentially at the edges or at defect sites on the basal plane of carbon materials, which are more prone to react and can easily accommodate strain[26,33,40]. However, it has been observed that with prolonged reaction time, the grafting of phenyl moieties proceeds throughout the substrate surface leading to a coverage extent similar to the one of a theoretical monolayer, as demonstrated on HOPG[33,38,50].

The method is highly versatile: several carbon substrates, from graphite[51] to graphene oxide and carbon nanotubes (CNTs)[45,52,53], as well as metal surfaces[54,55] can be modified with this procedure. Moreover, large choice of commercially available substituted aryl amines allows for the introduction of disparate functionalities as carboxylic acid (-COOH), sulfonic acid (-SO_3H), halogens (particularly Br and Cl), alkyl chains (-R), and nitro-group (-NO_2)[35,37].

Those functionalities can undergo further chemical derivatization when used as grafting sites to which covalently bind functional molecules, for example *via* formation of amide or ester bonds[33]. Likewise, aryl diazonium compounds can be used as coupling agents for anchoring inorganic nanoparticles and thus fabricate carbon-inorganic composites[27,45,51].

3.1.2. Carbon-inorganic nanoparticles composites for application as hybrid supercapacitor electrodes

The demand for high power density energy storage devices rapidly increased in the last decade due to the fast-growing market of portable electronic devices and hybrid vehicles, and to the need of finding alternative energy sources to fossil fuels[56]. A wide branch of research is focused on supercapacitors because they exhibit higher power density and longer cycle life than batteries, thus representing a promising alternative device[57,58]. There exist two kinds of supercapacitors which differ for the way charge is stored: electrical double layer capacitors (EDLCs) and pseudocapacitors. The former store charge by electrostatic interactions at the electrode surface in contact with the electrolyte, while the latter store charge through reversible redox (Faradaic) processes[56,59]. EDLCs are usually carbon-based materials and are featured by high power densities[60-62]. Transition metal oxides present pseudocapacitive behaviour but have the drawback of suffering high fade of capacitance when operated at high charge/discharge rates and this limits their power densities[63-65]. That limit is usually overcome by depositing metal oxide nanoparticles on carbon substrates and creating a so-called "hybrid" supercapacitor, which brings both EDLC and pseudocapacitive performances of the component materials[66,67]. In view of its high electrical conductivity, carbon substrates promote charge transport processes for the anchored metal oxide nanoparticles; interest is focused on nanosized metal oxides because Faradaic reactions present reduced diffusion resistance than in bulk materials[14,68,69]. Iron oxide,

especially magnetite (Fe_3O_4), is a promising pseudocapacitive material because of its low cost, ease of preparation, minimum environmental impact and because of its high theoretical capacitance[69-71].

In-situ synthesis of iron oxide nanoparticles, either by co-precipitation method or by sol-gel approaches, is the most employed strategy to fabricate carbon-iron oxide composite materials to be further on investigated as hybrid supercapacitor electrodes[14,72]. Synthesis of inorganic nanoparticles in presence of the desired carbon substrate (*in-situ*) offers indeed several advantages: (i) carbon-substrates are referred to as 2D supports for the nucleation, growth and stabilization of the synthesized inorganic (e.g. metal oxide) nanoparticles, (ii) oxygen-containing functionalities at carbon-materials surface are believed to act as nucleation sites for the desired metal oxide nanoparticles, (iii) graphene-based supports behave as a conductive platform to improve charge transport of metal oxide, and (iv) the as-synthesized particles are thought to limit the re-stacking of graphene layers[64,65,73].

However, *in-situ* approaches might suffer of the drawback of inducing undesired chemical or structural modifications in the carbon substrate. Undesired structural modifications of the support might be avoided using *ex-situ* approaches, which often consist in simply mixing the carbon material and pre-synthesized metal oxide nanoparticles[13,65].

In general, it might be said that some challenges need to be overcome in order to improve the synthesis and properties of carbon-metal oxide composites. Particularly, understanding the surface chemistry and way of interact of the components would help controlling over the interface between the two phases, thus achieving more defined structures. Modifying the chemical composition of carbon substrates might help improving interactions between the composite phases. Particularly, introduction of selected chemical functionalities could help defining the desired structure for the final composite, accomplishing better fabrication reproducibility, and widen the range of applications.

Finally, a better understanding of the interactions between the phases and control over the chemical and structural properties of the composite should favour elucidation on the structure-properties relationships, which is a fundamental task for any application [65,66,69,74].

The aim of the present work is to fabricate a graphene oxide-iron oxide composite material *via* an *ex-situ* approach. Particularly, the main interest is focused on the investigation about the non-covalent interactions between the component phases and to study whether it is possible to tune structural and morphological properties of the final material by selectively altering the surface chemical composition of the carbonaceous support.

When adsorbing particles through non-covalent interactions (van der Waals, hydrogen bonding, electrostatic interactions and π-π stacking), surface functionalities of the support likely determine the efficacy of the deposition process by influencing the interfacial interactions between the component phases. In particular, distribution of functional groups at the surface of the carbonaceous layers is believed to play a role in defining the morphological features of the final composite.

The choice of performing the decoration of the substrate with iron oxide nanoparticles *via* an *ex-situ* approach is dictated by the necessity of not altering the substrate structural and chemical properties. Only in this way it will be possible to assess whether the distribution of the nanoparticles is driven by the establishment of specific interactions with selected and rationally designed functionalities.

Graphene oxide represents a good candidate to be used as carbon support because it is characterized by oxygen-containing functionalities which might act as potential sites for the adsorption of iron oxide nanoparticles. However, the random distribution and composition of those oxygen moieties and the scarcity of functional groups affine to iron oxide make of graphene oxide a valid platform for establishing unspecific interactions with oxide nanoparticles. For those reasons it will be used as basic comparison material.

The effects of surface functionalities on the loading and distribution of iron oxide nanoparticles will be investigated by introducing selected moieties at graphene oxide surface.

In view of the well-known affinity between carboxyl moieties and iron oxide[75,76], it is believed that a carbon support rich in surface carboxyl moieties would promote the loading of iron oxide nanoparticles at a higher extent and eventually with a better distribution throughout the whole carbon sheets than what expected on conventional graphene oxide.

For this reason, 4-carboxyphenyl groups will be covalently grafted *via* diazonium chemistry at graphene oxide surface.

Finally, due to the potential applicability of these materials as hybrid supercapacitors, structure-properties relationship will be investigated by analysing their electrochemical performances.

Indeed, it is of great interest to verify whether the rational tuning of the material structure by solely modulating the interactions between the component phases might influence the electrochemical properties at the same time.

In details, the work will be structured in three main steps. In the first step, synthesis of graphene oxide and its chemical modification will be performed and the related materials will be characterized in terms of chemical and structural properties. Decoration of the as-obtained carbonaceous supports with pre-synthesized iron oxide nanoparticles and chemical-structural characterization will be the core objective of the second step of this project. Electrochemical properties will be further investigated in the third step.

3.2. Experimental section

3.2.1. Materials

Iron(III) acetylacetonate ($Fe(acac)_3$, anhydrous 99% - STREM) and benzyl alcohol (puriss. 99% - Sigma-Aldrich) were stored in a glovebox and used as received.

Sodium nitrate ($NaNO_3$, 98%), potassium permanganate ($KMnO_4$, 98%), sodium nitrite ($NaNO_2$, 98%), undecanoic acid (98%), 4-aminobenzoic acid (99%), tetraethylammonium tetrafluoroborate ($N(Et)_4BF_4$, 99%), and N,N'-dimethylformamide (DMF, 99%) were purchased from ABCR. Sulfuric acid (H_2SO_4, 95-

97%) and hydrochloric acid (HCl, 37-38%) were purchased from J.T.Baker. Hydrogen peroxide (H_2O_2, 30%) was obtained from VWR-Prolabo. Graphite (powder, <20μm), sodium sulphate (Na_2SO_4, ≥99%), polytetrafluoroethylene (PTFE - aqueous suspension, 60% wt.), and acetonitrile (ACN, ≥99.5%) were purchased from Aldrich. All the materials were used as received.
Carbon black (Vulcan VXC72R) was purchased from Cabot and stored at 65°C in an oven prior to use.
All the used solvents were of the highest grade and used as received.

3.2.2. Methods

3.2.2.1. Preparation of graphene oxide

Graphene oxide was prepared following a slightly modified Hummers method[77]. Briefly, 2 g (0.167 mol) of graphite were weighed in a flask, which was then placed in an ice bath, followed by the addition of 1 g (0.012 mol) of $NaNO_3$. 50 mL of H_2SO_4 were added slowly under magnetic stirring in order to keep the temperature of the mixture below 5°C. Subsequently, 7.3 g (0.046 mol) of $KMnO_4$ were added very slowly under magnetic stirring in order for the temperature not to rise above 20°C. The as-obtained suspension was subsequently transferred to a 35°C water bath and allowed to react under magnetic stirring for 2 hours. Further on, the reaction flask was removed from the water bath and the reaction quenched by carefully adding 90 mL of deionized water under vigorous stirring; the temperature of the reaction mixture was kept below 98°C during this step. Finally, under vigorous stirring, 62 mL of an aqueous H_2O_2 dilution (H_2O_2: deionized H_2O 1:6 v:v) were added causing the colour of the suspension turning from brown to green-yellow and light brown again. The as-obtained warm suspension was filtered on paper filters and the solid was washed three times with 150 mL of aqueous HCl (3 wt. %). The solid was then dried overnight at 50°C in a vacuum oven. The reaction yielded 3.3 g of graphene oxide (**GO**).

3.2.2.2. Chemical modification of graphene oxide via *grafting of 4-carboxyphenyl groups*

Chemical modification of graphene oxide was performed following the method reported by Martin et al.[45,51], modified to a small extent.
In a typical reaction, 200 mg of graphene oxide (16.6 mmol) were dispersed in 100 mL of aqueous HCl (0.5 M) using an ultrasonic bath. To that dispersion, 2.27 g (16.6 mmol) of 4-aminobenzoic acid were added, followed by 3.44 g (49.8 mmol) of $NaNO_2$. The reaction was allowed to proceed under magnetic stirring at room temperature overnight. The as-modified graphene oxide was then separated from the reaction medium through filtration under reduced pressure on a Nylon membrane (Millipore, 0.2 μm as pore size), and thoroughly washed with ultrapure water. Subsequently, the Nylon membrane was exchanged by a polytetrafluoroethylene (PTFE) membrane (Sartorius, 0.2 μm as pore size) and the solid was further on washed through filtration under reduced pressure using DMF, methanol and acetone in sequence. The as-

purified functionalized graphene oxide was then dried at 50°C in a vacuum oven overnight. The reaction brought to 175 mg of 4-carboxyphenyl-modified graphene oxide (***f*-GO**).

3.2.2.3. Synthesis of magnetite nanoparticles and their functionalization with undecanoic acid

Magnetite (Fe_3O_4) nanoparticles were synthesized through the "benzyl alcohol route", according to the literature[78]. The procedure was carried out in a glovebox (H_2O< 0.1 ppm and O_2< 0.1ppm). In a typical reaction, 1 g (2.83 mmol) of $Fe(acac)_3$ was dissolved in 20 mL of benzyl alcohol in a 45 mL-inner volume Teflon cup which was then slid inside a stainless steel autoclave. After being carefully sealed, the autoclave was taken outside of the glovebox and heated in an oven at 175°C for 48 hours. The dark brown precipitate was collected by centrifugation and carefully washed twice with absolute ethanol and once with dichloromethane. The as-purified precipitate was then redispersed in 20 mL of hexane by means of an ultrasonic bath. 240 mg (1.29 mmol) of undecanoic acid were added to the hexane dispersion which was then sonicated for 10 minutes at room temperature. Uncoated nanoparticles and large aggregates were separated through a last step of centrifugation from which the supernatant containing undecanoic acid coated-magnetite nanoparticles (indicated with the general nomenclature **Fe_xO_y-UA**) was saved and the precipitate discarded.

3.2.2.4. Deposition of Fe_xO_y-UA nanoparticles on GO and f-GO

The deposition of Fe_xO_y-UA nanoparticles on carbonaceous supports was performed *via* a "phase transfer" approach. In a round-bottom flask equipped with a magnetic stirrer, 100 mg of the investigated carbon-material (either GO or *f*-GO) were dispersed through sonication in 20 mL of the proper solvent, being ultrapure water for GO and DMF in the case of *f*-GO. Further on, 5 mL of Fe_xO_y-UA hexane dispersion were carefully added to the carbon-material suspension in order for the two phases not to mix. The underlying carbon-material dispersion was moderately stirred in order to continuously exchange the GO-based support at the interface between the two phases.
The GO-based materials were recovered through centrifugation and washed with hexane, their proper dispersion solvent (ultrapure water or DMF) and absolute ethanol, in sequence. They were dried in a vacuum oven at 50°C, overnight.

3.2.3. Characterizations techniques

3.2.3.1. Chemical and structural properties

X-ray powder diffraction (XRD) technique was used in order to study the crystallinity and the structural properties of the materials.

XRD patterns were measured using a Seifert XRD 3003TT diffractometer (Cu Kα radiation at 40 kV and 40 mA). The diffractograms were measured in the 2θ range from 5.00° to 80.00° with a scanning step of 0.2°.

Fourier transform infrared (FTIR) spectroscopy analysis was performed in order to elucidate the chemical composition of the investigated materials and to study the interactions existing between the composite material components.

FTIR analysis was performed on a Thermo Scientific Nicolet iS5 spectrometer. Spectra were acquired in transmission mode (using the KBr pellets method) in the wavenumber range from 4000 to 400 cm^{-1}. All the spectra were acquired using a 4 cm^{-1} resolution and collecting 128 scans.

Baseline correction was applied to all the measured spectra.

Thermogravimetric analysis (TGA) was performed in order to evaluate the thermal stability of the carbon supports and determine the iron oxide loading in the composite materials. It was carried out on a NETZSCH (STA 409PC) TG analyser. GO and *f*-GO materials were analyzed under nitrogen at a heating rate of 5°C/min and in the temperature range between room temperature and 600°C. GO-Fe_xO_y, *f*-GO-Fe_xO_y and Fe_xO_y-UA were investigated in air using a heating rate of 5°C/min in the temperature range between room temperature and 850°C.

Transmission electron microscopy (TEM) analysis was carried out in order to investigate the morphology of the composite materials. TEM analysis was carried out on a Philips CM200 (LaB_6) microscope operating at an acceleration voltage of 200 kV.

Samples were prepared by depositing few drops of ethanol suspension of each sample on a 300 mesh carbon film-coated copper grids. The solvent was allowed to evaporate prior to the analysis.

Carbon, hydrogen, nitrogen and sulphur elemental analysis (CHN-S) was performed in order to determine the principal elements constituting the carbonaceous supports and to determine their relative ratio. CHN-S analysis was performed on a EURO EA elemental analyzer with standard combustion conditions and handling the samples in air.

X-ray photoelectron spectroscopy (XPS) allowed investigating the chemical and bonding configuration of the synthesized materials, to elucidate about the surface chemical composition of carbonaceous materials and the interfacial interactions between the carbon substrate and iron oxide nanoparticles. X-ray photoelectron spectra were acquired on a K-Alpha system from Thermo Scientific equipped with a monochromatic Al Kα source (1486.6 eV) and operating in constant analyser energy mode with a pass energy of 200 and 50 eV for survey and high resolution spectra, respectively. A spot size of about 400 μm in diameter was adopted. Surface charging effects were avoided using an electron flood gun. The binding energy shifts were calibrated keeping the C 1*s* position fixed and Gauss-Lorentzian shaped bands were used to reproduce the spectra profiles. The relative elemental concentrations were estimated from the areas under the C 1*s*, O 1*s*, and Fe 2*p* photoelectron peaks weighed by the relative sensitivity factors supplied by the ThermoAvantage analysis software.

Micro-Raman spectroscopy (MRS) was performed to investigate about the occurrence of chemical modification and the occurrence and strength of interfacial interactions between the carbonaceous support

and adsorbed iron oxide nanoparticles. Raman scattering was measured at room temperature with a Jobin Yvon spectrometer using a 100X objective; excitation energy was 2.33 eV, unless differently specified. Spectra were collected from several random positions on each specimen on account of the possible structural non-homogeneity of the samples. Measurements were performed using a low laser power in order to prevent laser-induced damage or heating. Spectra were analysed using a commercially available spectroscopic analysis software package. A Lorentzian line and a Breit-Wigner-Fano (BWF) line, superimposed to a constant background, were used to reproduce the spectral profile in the region of the C-sp^2 vibration modes; a least square best fit chose the wavenumber position, width and intensity of the bands.

3.2.3.2. Electrochemical properties

1) Preparation of the electrodes for electrochemical characterization

Electrodes were prepared as follow. The electrode paste was produced by mixing the investigated material with carbon black and polytetrafluoroethylene (PTFE - aqueous suspension, 60 wt. %) in ethanol in the weight ratio 75:15:10, respectively. Carbon black acts as conducting agent while PTFE as binder to provide a good mechanical integrity to the electrode. The mixture was heated at 50°C under stirring to evaporate the solvent and obtain a homogeneous paste which was then manually rolled into a 100 μm-thick film. Upon drying the film at 70°C, a disc-shape of 6 mm diameter was cut-out from it and pressed (9 tons, applied pressure) within a 1 cm-width stainless steel grid which acts as the current collector.

2) Electrochemical characterization

Electrochemical properties were investigated using a three-electrodes-cell configuration and a platinum wire as counter electrode. Ag/AgCl was used as reference electrode in aqueous electrolyte, while $Ag/AgNO_3$ TBAP (0.1 M in acetonitrile) was used as reference electrode in organic electrolyte. The measurements were performed both in 1M Na_2SO_4 aqueous solution and 1M $N(Et)_4BF_4$ in acetonitrile solution as electrolytes. All the electrochemical measurements were acquired on a Bio-Logic VMP3 potentiostat/galvanostat. Cyclic voltammograms were recorded in a potential window ranging from -0.8/+0.7 V (vs. reference electrode) for all of the GO-based materials and within the -0.8/+0.2 V (vs. reference electrode) for Fe_xO_y-UA. Cyclic voltammetry was measured at different scan rates of 5, 10, 20, 50, and 100 mV/s. Galvanostatic measurements were performed over 1500 cycles in the same potential windows of cyclic voltammetry measurement, by applying to each sample the maximum current density experimentally determined from the correlated voltammogram acquired at a scan rate of 20 mV/s.

Electrochemical impedance spectroscopy (EIS) measurements were carried out in the frequency range between 1 MHz to 10 mHz at open circuit potential with an AC perturbation of 5 mV.

3.3. Results and discussion

3.3.1. Synthesis of graphene oxide and its chemical modification

Graphene oxide (GO) was produced following a classic Hummers method[77], modified to a small extent. The oxidation of graphite to graphene oxide with this method was introduced by Hummers and Offeman in 1958. It represents a quite safe method when compared to even earlier developed procedures[79,80] and at the same time it is reasonably faster than other strategies which were further on elaborated[81], still providing an effective oxidation result.

Typical Hummers method uses a combination of sodium nitrate ($NaNO_3$), sulphuric acid (H_2SO_4) and potassium permanganate ($KMnO_4$). Although $NaNO_3$ could act as oxidizing agent and $KMnO_4$ is commonly used in organic chemistry as a quite powerful oxidant, some studies suggested that the real oxidizing agent is dimanganese heptoxide (Mn_2O_7), which is formed by the reaction between H_2SO_4 and $KMnO_4$ (equation 3.1)[1,12].

$$KMnO_4 + 3\ H_2SO_4 \rightarrow K^+ + MnO_3^+ + H_3O^+ + 3\ HSO_4^-$$
$$MnO_3^+ + MnO_4^- \rightarrow Mn_2O_7 \qquad \text{eq. 3.1}$$

The addition of an aqueous hydrogen peroxide (H_2O_2) solution allows reducing the residual $KMnO_4$ and the side-product manganese dioxide (MnO_2) to the soluble manganese sulphate ($MnSO_4$), which can subsequently be removed by filtration[77]. Usually the reaction produces a dark-brown solid product (GO) in a quantitative yield.

The as-synthesized GO presents a variable composition of oxygen functionalities, being in prevalence hydroxyl groups, epoxides and carboxylic acid moieties. As previously anticipated, the presence of carboxyl groups at the surface of GO sheets is expected to promote the adsorption of metal oxide particles. However, carboxylic acid functionalities in GO are usually present in lower amount than the other oxygen-containing groups and are situated preferentially at the edges of the layers[82]. For this reason, additional carboxyl groups are introduced by grafting 4-carboxyphenyl functionalities on pre-synthesized GO through the diazonium chemistry.

Introduction of 4-carboxyphenyl groups was achieved *via* a spontaneous grafting approach and the *in-situ* generation of the desired diazonium compound.

A schematic representation of the grafting process and of the chemical structures expected for the investigated materials is depicted in figure 3.2.

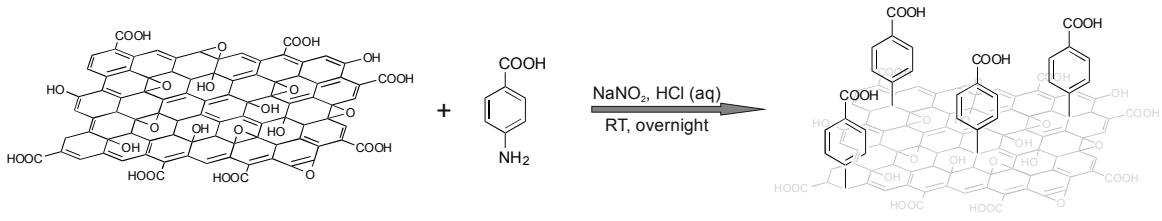

Figure 3.2: Representation of the chemical modification reaction carried out in acidic aqueous medium using 4-aminobenzoic acid as diazonium compound precursor and $NaNO_2$ as diazotization agent. Graphene oxide (GO) and the corresponding 4-carboxyphenyl-modified GO (*f*-GO) are depicted through models of their expected chemical structures.

In a typical process, the investigated carbon-material was dispersed in acidic aqueous medium together with the precursor of the diazonium compound, namely 4-aminobenzoic acid. The latest addition of the diazotization agent, sodium nitrite ($NaNO_2$), led to the conversion of the amino group to the corresponding diazonium cation. The further reduction of the aryl diazonium cation to the corresponding more reactive 4-carboxyphenyl radical, and the consequent release of nitrogen, is believed to occur by means of a concerted electron transfer process involving the carbon support[46-48]. The grafting of the phenyl radical on the carbon support through formation of a covalent carbon-carbon bond occurs in sequence, being the reaction almost instantaneous[35,36,44].

For sake of simplicity, the chemically modified GO will be indicated as *f*-GO from here on.

3.3.1.1. Structural and chemical characterization

X-ray powder diffraction (XRD) analysis was performed on the materials in order to acquire information on their structural properties (figure 3.3).

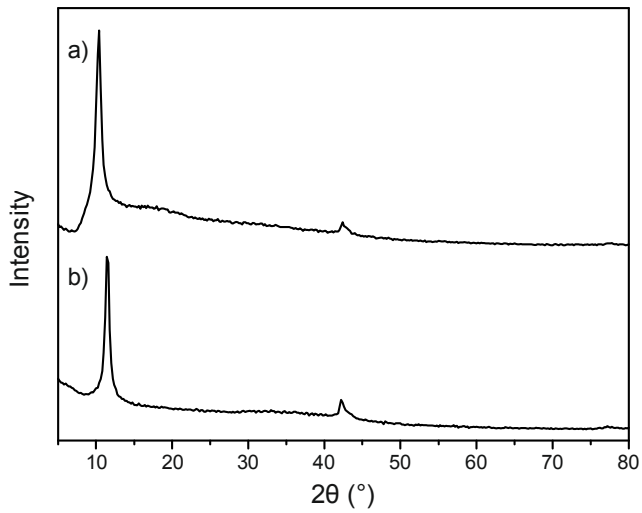

Figure 3.3: X-ray diffractograms of GO (a) and *f*-GO (b).

Diffractograms of GO (figure 3.3a) shows the characteristic (001) reflection of oxidized graphene centred at 10.6°; the typical (002) graphite reflection at 26.4° (JCPDS card 04-014-0362) is not noticeable[83]. This change is significant of an expansion of the distance between the GO sheets with respect to graphite. It is generally accepted that GO layers are more spaced than graphite because of the newly-formed oxygen-containing groups and adsorbed water molecules at their surface[83,84].

Diazonium chemistry is expected to favour an enhancement of the GO interlayer distance since, theoretically, grafting can occur at both faces of GO layers[26,29].

However, no remarkable shift in GO reflection position was observed for *f*-GO (11.2°; figure 3.3b). This suggests that 4-carboxyphenyl groups might have been grafted preferentially at the surface of the outermost layers composing GO flakes.

Further characterization by CHN-elemental analysis showed an increase in carbon content for *f*-GO, as expected from the grafting of 4-carboxyphenyl groups (table 3.1).

Table 3.1: Elemental composition expressed as carbon (C), hydrogen (H), nitrogen (N), and sulphur (S) content (weight percentages; wt. %) for the synthesized carbonaceous materials.

Material	C (wt. %)	H (wt. %)	N (wt. %)	S (wt. %)
GO	43.3	2.55	0	3.82
f-GO	51.9	2.50	0.569	0.534

The increase in nitrogen content might be ascribed to the formation of azo-bonds (C–N=N–C) originating from characteristic side reactions of the diazonium chemistry processes[43,85].

Figure 3.4 shows the thermal analysis curves of GO and *f*-GO measured under nitrogen at a heating ramp of 5°C/min.

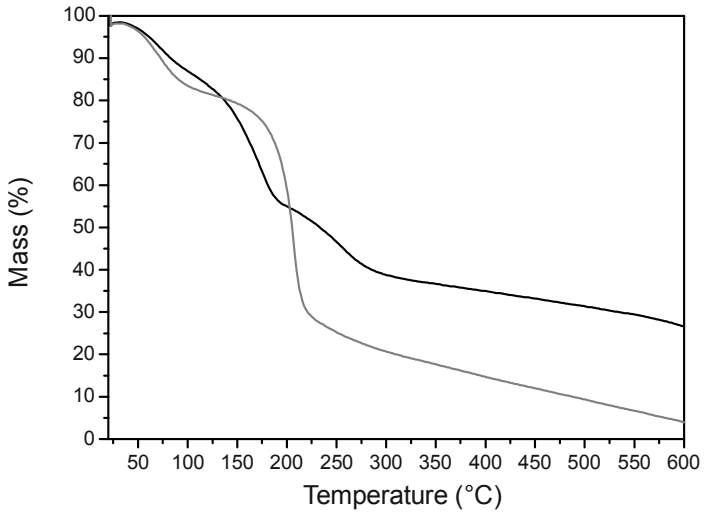

Figure 3.4: TGA curves of GO (black line) and *f*-GO (grey line) treated under nitrogen at a heating rate of 5°C/min.

Thermal analysis revealed remarkable differences in the thermal stability of the carbonaceous supports. The starting GO presented a significant mass loss throughout the temperature range from room temperature up to 285°C, within which three consecutive steps were noticed. The first minor loss at temperature up to 100°C is

likely due to the evaporation of adsorbed water[10]. The other two major losses might be ascribed to the decomposition of oxygen containing groups to CO and CO_2[10], likely owing to different chemical functionalities.

Differently, *f*-GO showed two well-defined mass losses. The minor one occurred at temperature below 100°C; hence it is similarly assigned to the removal of adsorbed water. The major mass loss was observed between 130 and 250°C. The steep profile of the curve in this region is likely due to the predominant decomposition of a specific chemical species that is presumably present only at limited amount in GO. This suggests that the chemical composition of *f*-GO differs from the one of GO; therefore, it lets infer that chemical modification successfully occurred. The larger mass loss observed for *f*-GO is in accordance to the higher content of thermally labile organic functionalities expected for this material, in view of the chemical modification procedure.

The chemical nature of the surface functional groups of the materials was studied by Fourier transform infrared (FTIR) spectroscopy, as depicted in figure 3.5.

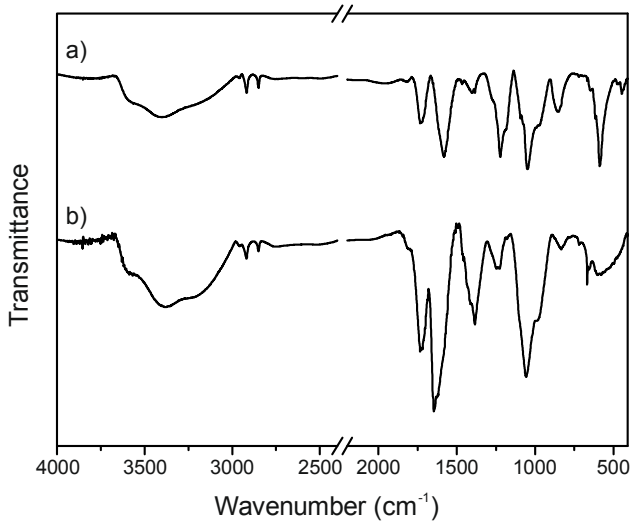

Figure 3.5: FTIR spectra of GO (a) and *f*-GO (b). For sake of clarity, spectra are represented stacked by an offset value and the signal due to atmospheric CO_2 was omitted by introducing a break in the 2400-2200 cm^{-1} spectral region.

The occurrence of chemical modification was reflected in some differences between the GO and *f*-GO FTIR spectra. It must be taken into account that the interpretation of infrared spectra of oxidized carbon materials is usually not as straightforward as it might be for simple aromatic compounds. It is of general acceptance that the most prominent oxygen-containing functionalities generated during oxidation of graphite are hydroxyls, epoxy and carboxyl moieties, as proposed by the Lerf-Klinowski model[1,82]. However, the presence of keto-groups as quinones can not be excluded[86]. The infrared absorptions of those groups generally fall in close spectral regions (between 1800 and 900 cm^{-1}) and they often overlap. This, in addition to the random distribution and chemical composition, renders an accurate assignation of the observed peaks quite challenging.

In general, the broad peaks in GO and *f*-GO spectra at 3400 cm^{-1} is due to stretching vibrations of surface hydroxyl O-H bonds and adsorbed water. The weak peaks at 2919 and 2850 cm^{-1} are due to the C-H stretching modes of aliphatic domains that are usually present in oxidized graphene[87]. The band at about 1730 cm^{-1} is common to both the materials and didn't change remarkably during the chemical modification step; it is generally ascribed to the stretching of carbonyl moieties of carboxyl groups and possibly ketones[88]. The band at 1585 cm^{-1} for GO spectrum (figure 3.5a) arises from the aromatic skeletal (C=C) stretching modes[86] and is generally regarded as characteristic for oxidized carbon materials; its shape remarkably changed upon GO chemical modification. The peak maximum indeed shifted at higher wavenumbers (1643 cm^{-1}) and the contribution at 1585 cm^{-1} appears only as a shoulder in the *f*-GO spectrum (figure 3.5b). This change is regarded as indicative of the occurrence of chemical modification for few reasons. Contribution from the 1585 cm^{-1} band only as a shoulder suggests that a significant modification of the aromatic skeleton of GO occurred upon chemical modification. As previously reported, this reaction is believed to induce a change in hybridization of the reacted C atoms from sp^2 to sp^3. As a consequence, a rearrangement of the surrounding aromatic structure will likely take place[89,90] and might be reflected in an alteration of the FTIR spectral profile. Particularly, the maximum at 1643 cm^{-1} might be ascribed to the carbonyl (C=O) stretching of 4-carboxyphenyl functionalities. The lower wavenumber with respect to the one observed for pure 4-aminobenzoic acid (1667 cm^{-1}) and the reported theoretical[91] value for carboxylic C=O groups might be caused by a complex surrounding chemical environment. It should be taken into account that phenyl radicals generated from diazonium compounds can react with aromatic species previously grafted on the carbon support thus leading to phenyl oligomers and a rather complex chemical environment[29,42,53]. The possibility of the presence of carboxylate groups whose asymmetric (COO^-) stretching might cause the 1643 cm^{-1} band can not be ruled out. Nevertheless, the acidic conditions in which the grafting reaction is performed let regard this hypothesis as less probable.

Other spectral changes occurred in the 1500-1370 cm^{-1} region: GO 1385 cm^{-1} band became sharper and several other contributions appeared as shoulders in *f*-GO spectrum. Additional hydroxyl functionalities from 4-carboxylphenyl groups are supposed to cause the sharpening of GO 1385 cm^{-1} band, typically ascribed to O-H bending modes[88]. Yet, introduction of non-conjugated phenyl moieties and structural changes might be responsible of the other minor spectral changes. A broadening of the epoxy (C-O-C stretching) band at 1222 cm^{-1} [92] in the *f*-GO spectrum could reflect a modification of the chemical environment of epoxy groups upon GO chemical modification. Lastly, the band generally ascribed to C-O stretching modes in carboxyl functionalities[93] broadened and shifted at higher wavenumber (1052 cm^{-1} in GO and 1062 cm^{-1} in *f*-GO) upon chemical modification.

Further investigation by Raman spectroscopy revealed that both the materials are characterized by the Raman fingerprint of the graphitic crystalline arrangement (G-band) and the "disorder" band (D-band). In general, the G-band (at 1582 cm^{-1} in graphite) arises from the E_{2g} symmetry in-plane optical mode associated to the stretching of all pairs of sp^2 hybridized carbon atoms[94,95]. The D-band (at 1346 cm^{-1} for 2.33 eV excitation energy) is related to the in-plane A_{1g} symmetry breathing-mode of the C hexagonal ring. Forbidden

in graphite, it becomes Raman-active when disorder is present in the carbon aromatic structure[94,95]. Then, it progressively broadens and intensifies (relative to the G-band) with increasing deviation from perfect hexagonally-organized planar carbon lattice, for instance, with decreasing in-plane correlation length. Hence, the D/G intensity ratio (I_D/I_G) is commonly used to monitor the average size of sp^2 domains[96]. At fixed laser energy, both the D- and G-bands may shift downward or upward due to the presence of tensile or compressive stress acting on the carbon network and/or occurrence of charge transfer from or to the π-states[95,97]. In graphene oxide, the presence of oxygen-containing functionalities breaks the conjugated structure of the sp^2 bonding networks and localizes π-electrons, reducing size of the in-plane sp^2 domains and introducing a sp^3 bonding fraction component[98]. As a result, the Raman bands broaden and shift upward with respect to graphite.

Raman spectra of GO and *f*-GO are showed in figure 3.6.

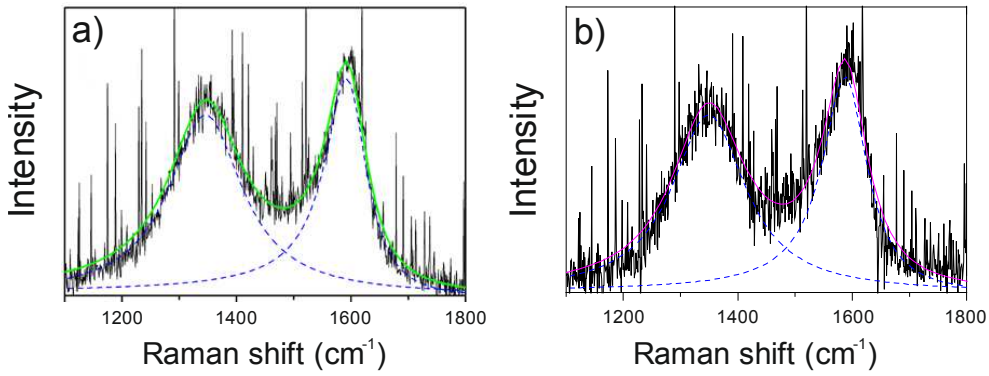

Figure 3.6: Region of the C-sp^2 vibration modes in the Raman spectra of GO (a) and *f*-GO (b).

In *f*-GO both the D- and G-bands shifted towards higher wavenumbers with respect to GO (table 3.2). The up-shift might be regarded as an effect of the electron transfer from the π states of the C network to the 4-carboxyphenyl functionalities introduced through the chemical modification process[95,97]. The lower value of I_D/I_G in *f*-GO with respect to GO indicates that the density of non-sp^2 lattice defects (most likely sp^3), which, as known, does not contribute to the D-band intensity[94], increased at expenses of that of the sp^2-type ones.

D- and G- bands wavenumber positions and widths are resumed in table 3.2, together with the I_D/I_G ratio.

Table 3.2: D- and G-bands features obtained by spectra fitting. ω_D and ω_G indicate the wavenumber positions while γ_D and γ_G represent the widths of the D- and G- bands, respectively; I_D/I_G indicates the D/G intensity ratio, calculated as amplitude ratio.

Material	ω_D (cm^{-1})	γ_D (cm^{-1})	ω_G (cm^{-1})	γ_G (cm^{-1})	I_D/I_G
GO	1346.0±0.6	156.2±1.8	1585.9±0.6	87.4±0.7	0.83±0.02
f-GO	1349.0±0.9	155.6±2.4	1587.5±1.0	94.9±1.4	0.79±0.02

GO and *f*-GO were characterized also by X-ray photoelectron spectroscopy (XPS). The survey spectra of both the materials (figure 3.7a, b) show the C 1*s* and O 1*s* peaks, which are the predominant species. Additionally, the spectrum of *f*-GO reveals the presence of nitrogen-containing species, as indicated by the weak N 1*s* peak. No presence of nitrogen was detected in GO. Deconvolution of the high resolution N 1*s* core level spectrum for *f*-GO revealed two contributions at 399.6 and 401.3 eV (figure 3.7c).

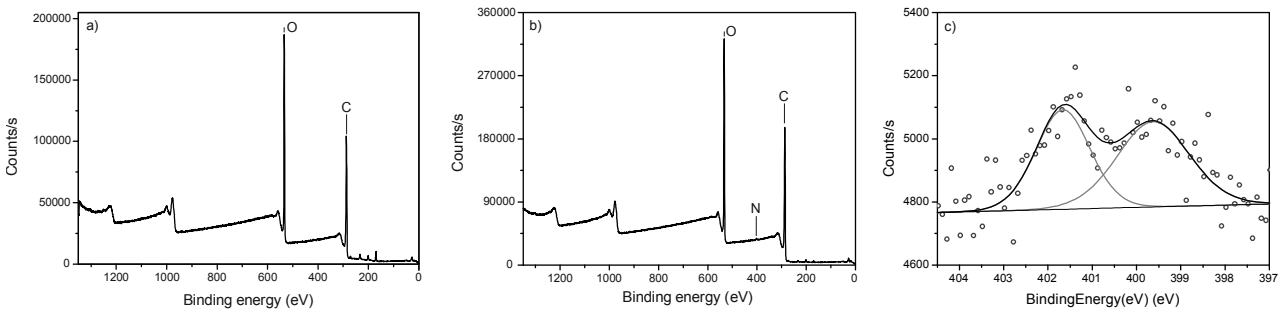

Figure 3.7: Survey X-ray photoelectron spectra of GO (a) and *f*-GO (b). High resolution spectrum of the N 1*s* core level in *f*-GO (c).

The contribution at 399.6 eV can be associated to azo-bonds, of the general formula (C–N=N–C). Formation of azo-bonds usually takes place when diazonium compounds are grafted in ortho-position with respect to a phenolic group, and it is commonly observed for oxidized carbonaceous supports treated with this kind of chemistry[43,85]. Therefore, detection of a contribution ascribable to azo-linkages in the N 1*s* core level spectra of treated materials is generally regarded as indicative of the occurrence of the target chemical modification. In these terms, it should be highlighted that azo-bonds may form additionally to the formation of the covalent C–C bonds[43]. The signal at 401.3 eV might be associated to the sum of single-oxidized nitrogen groups (NO) deriving from the grafting procedure, and a shakeup peak correlated to the conjugated system of azo-bonds. However, compositional analysis performed from the *f*-GO survey X-ray photoelectron spectrum pointed out that the nitrogen-containing species are present only as traces (0.46 at. %) with respect to the predominant carbon (68.59 at. %) and oxygen (29.99 at. %). High resolution O 1*s* and C 1*s* core level spectra allowed gaining more insight on the occurrence of the desired chemical modification. Analysis of the C 1*s* spectra of the carbon supports shows two main contributions at 284.5 eV, which is attributed to C-C/C=C bonds, and 286.6 eV, ascribable to C-O bonds. Further minor contributions at 288.2 and 289.0 eV are associated to C=O and COOH species, respectively (figure 3.8a, b). Upon chemical modification, no remarkable changes are observed in the spectrum of *f*-GO, whose signature is in agreement with the one of GO. Nevertheless, the *f*-GO O 1*s* spectrum shows an increment of the aromatic C-O bond fraction, with respect to pristine GO. Such result can be associated to the novel introduced carboxyl groups (figure 3.8c, d) and therefore it further supports the occurrence of the desired functionalization[99-102].

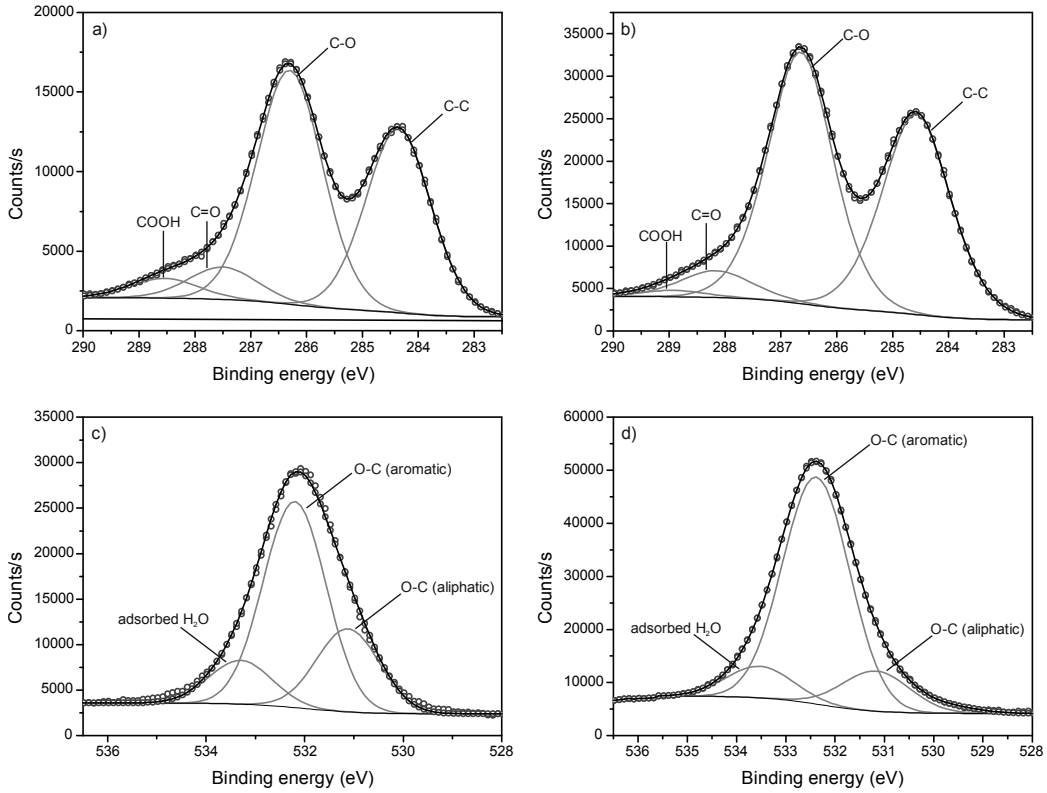

Figure 3.8: High resolution X-ray photoelectron spectra of C 1*s* core level of GO (a) and *f*-GO (b). High resolution X-ray photoelectron spectra of O 1*s* core level of GO (c) and *f*-GO (d).

3.3.2. Decoration of carbon substrates with iron oxide nanoparticles

Iron oxide nanoparticles, particularly magnetite (Fe_3O_4), used for the decoration of GO-based supports were synthesized in an earlier step through the typical "benzyl alcohol route"[78]. Upon synthesis, nanoparticles were usually kept in suspension in the more suitable solvent in order to limit their aggregation. However, preliminary experiments performed using as-synthesized iron oxide particles revealed that only large agglomerates of particles were deposited at carbon surface. In order to prevent particles from aggregation and favour a homogeneous distribution of oxide nanoparticles on the carbon layers, iron oxide nanoparticles underwent a post-synthesis functionalization step using undecanoic acid as stabilizing agent. The surface alkyl-chains layer of the as-functionalized nanoparticles (Fe_xO_y-UA from here on) permitted to produce a stable dispersion in apolar solvents (particularly hexane). Additionally, a good dispersion of graphene oxide is necessary to favour a homogeneous distribution of oxide nanoparticles all over the carbon layers and not only on the few accessible surfaces of stacks of several sheets.

It must be pointed out that the involved materials show good dispersibility in different media. While Fe_xO_y-UA are dispersible in apolar solvents, GO-based materials show good dispersibility in polar media as water or N,N'-dimethylformamide (DMF).

Based on those considerations, decoration of GO and *f*-GO sheets with iron oxide nanoparticles was performed through a so-called "phase transfer" approach. The "phase transfer" approach allowed, at the same time, to achieve good dispersibility of both the carbon materials and the iron oxide nanoparticles in the

corresponding most suitable media, and their interaction at the interface between the two immiscible phases (figure 3.9a). Moreover, applying a mild stirring to the underlying phase (polar medium) enabled a continuous exchange of carbon material at the interface thus favouring the distribution of oxide particles throughout the carbon sheets. The expected structures for the resulting composite materials are depicted in figure 3.9.

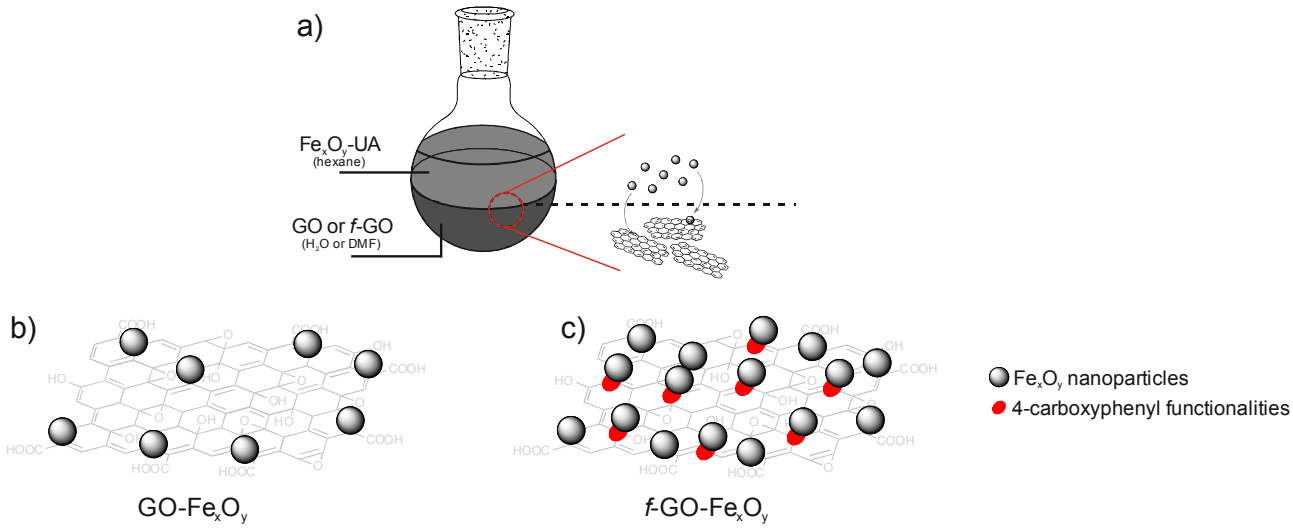

Figure 3.9: (a) Illustration of the "phase transfer" approach: the lower phase consists of the dispersion of either GO or *f*-GO, while the upper phase is the hexane dispersion of Fe_xO_y-UA nanoparticles. On the right side, schematic representation of the "phase transfer" process through which nanoparticles are believed to adsorb on the carbon material and thus transfer in the lower phase. For sake of clarity, the nanoparticles surface undecanoic acid layer is omitted. (b, c) Representation of the expected distribution of adsorbed Fe_xO_y nanoparticles on GO and *f*-GO, respectively. Fe_xO_y nanoparticles are represented by grey circles while the red dots indicate the sites at which 4-carboxyphenyl functionalities are grafted.

In association with the deposition and interaction of iron oxide nanoparticles on the carbonaceous materials, surface undecanoic acid molecules are believed to be partially replaced by functional groups present on GO and *f*-GO substrates.

3.3.2.1. Deposition of iron oxide nanoparticles on GO

XRD analysis of GO-iron oxide composite led to the unexpected shift of the typical GO reflection towards higher angles (11.6°) than pristine GO (10.6°), as shown in figure 3.10. Indeed, deposition of nanoparticles on the surface of graphene sheets is generally believed to hinder their re-stacking thus keeping the sheets more separated[73]. Nevertheless, the observed shift is significant of a reduction of the interlayer spacing of GO in the composite. It might be inferred that an eventual low surface coverage by iron oxide nanoparticles and/or a inhomogeneous distribution on the carbon support (thus leading to the presence of large uncovered GO areas) could lead to a certain re-stacking during the centrifugation step performed when purifying the final material (see experimental section) and upon drying the product.

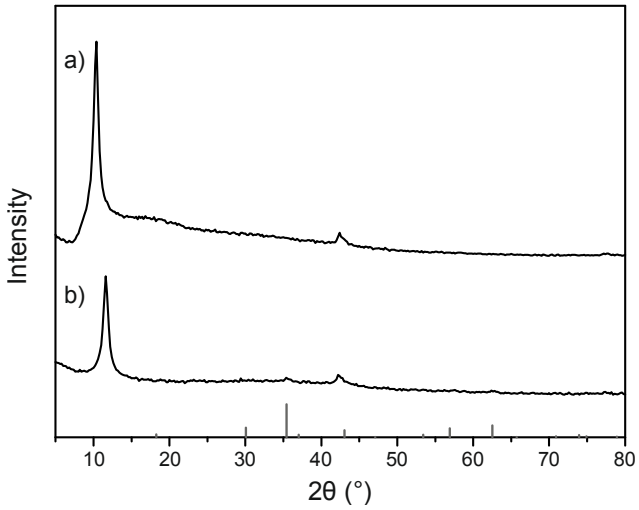

Figure 3.10: X-ray diffractograms of GO (a) and the corresponding GO-iron oxide composite (b). The grey columns at the bottom indicate the XRD pattern for magnetite (Fe_3O_4).

The presence of iron oxide is only suggested by very low intense reflections at 35.4° and 62.6° in the GO-iron oxide composite diffractogram (figure 3.10b). They might correspond either to magnetite (Fe_3O_4) or maghemite (γ-Fe_2O_3) due to the very similar X-ray diffraction patterns of the two oxides. Since it is not possible to doubtlessly assign the crystallographic phase, nanoparticles will be referred to as iron oxide (Fe_xO_y) from here on. Furthermore, being the reflections not well defined and so low in intensity, it could be claimed that a rather low amount of oxide particles was loaded onto GO sheets. Thermogravimetric (TG) analysis (figure 3.11) of GO-Fe_xO_y revealed indeed that the amount of adsorbed iron oxide accounts only for a 1.3 wt. %.

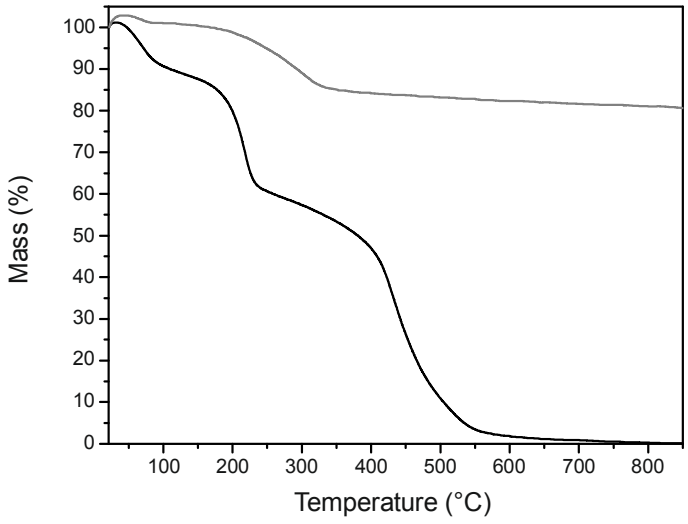

Figure 3.11: TGA curves of GO-Fe_xO_y (black line) and the deposited Fe_xO_y-UA nanoparticles (grey line) treated in air at a heating rate of 5°C/min.

The thermal analysis of the composite material showed a minor mass loss at temperature below 100°C due to the removal of adsorbed water. The mass loss observed between 100 and 275°C is likely due to decomposition of oxygen-containing functionalities in part typical of the carbon support and in part likely

ascribable to residual organic ligand (undecanoic acid) adsorbed at iron oxide nanoparticles surface. This hypothesis is in accordance with the mass loss observed for undecanoic acid-coated iron oxide nanoparticles in the same temperature range (grey line). A third mass loss observed between 275 and 575°C might be assigned to the decomposition of the carbon skeleton of the composite material[16].

The presence of iron oxide nanoparticles was further on confirmed by transmission electron microscopy (TEM) analysis, which was performed in order to investigate the morphology of the composite material (figure 3.12). Electron diffraction patterns measured from a selected area (figure 3.12c) might be attributed to magnetite phase; however, presence of maghemite phase can not be excluded.

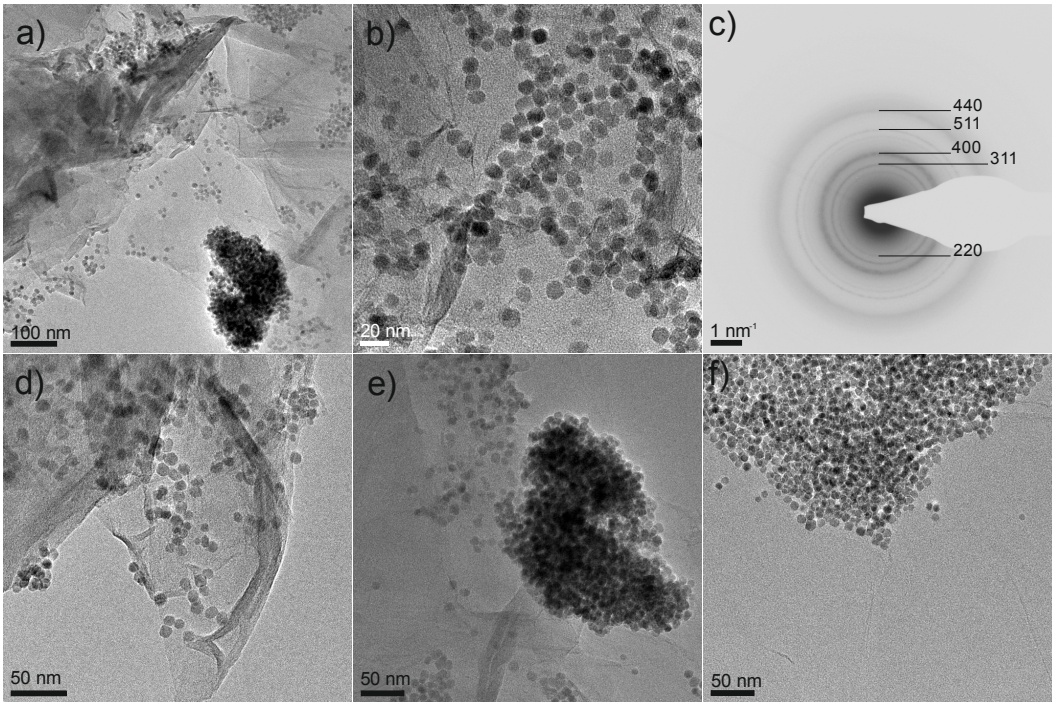

Figure 3.12: TEM images of the GO-Fe_xO_y composite showing the overview (a) and details (b, d, e, f) of iron oxide particles distribution over the carbon substrate. Electron diffraction patterns (c) of the selected area showed in (f).

Iron oxide particles size determined by TEM analysis is comprised between 7 and 9 nm, and it is in accordance with the size distribution determined for undecanoic acid-coated nanoparticles (Cf. chapter 2).

TEM images of GO-Fe_xO_y composite show that oxide particles were preferentially distributed at the edges and on wrinkles of GO sheets and randomly adsorbed on the basal plane in agglomerate islands.

Although Fe_xO_y nanoparticles distributed at the periphery of the carbon sheets looked well dispersed and almost not aggregated, they grouped into agglomerates when adsorbed onto the basal plane. This difference might be correlated to diverse typologies of interactions between the two materials, noted that the chemical composition of GO is likely not homogeneous throughout the sheets. Moreover, TEM images revealed that large areas of GO were left uncoated upon decoration with oxide nanoparticles, supporting the evidence of the very low amount of deposited particles brought by TGA analysis.

Absence of isolated nanoparticles not loaded on carbon sheets suggests the capability of the "phase transfer" approach to upload from the hexane phase only those iron oxide particles which can selectively interact with the carbon support.

The kind of interactions between GO and Fe_xO_y nanoparticles were first investigated by FTIR spectroscopy (figure 3.13).

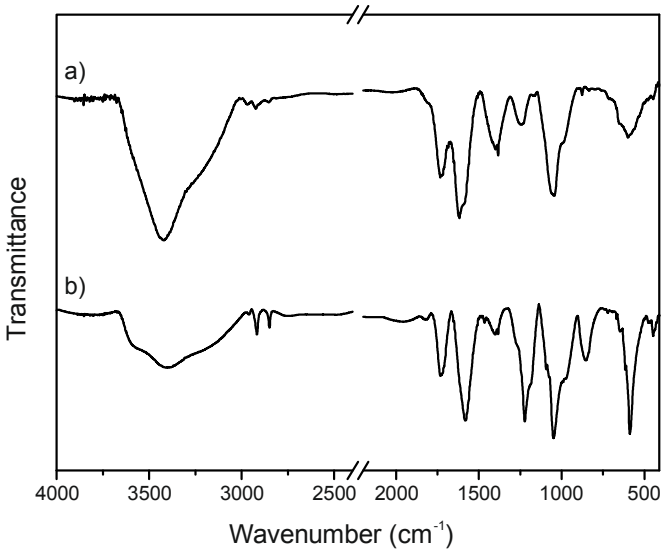

Figure 3.13: FTIR spectra of GO-Fe_xO_y (a) and GO (b). For sake of clarity, spectra are represented stacked by an offset value and the signal due to atmospheric CO_2 was omitted by introducing a break in the 2400-2200 cm^{-1} spectral region.

FTIR spectrum of GO-Fe_xO_y composite (figure 3.13a) showed two main significant differences with respect to the one of individual GO. The band at 1585 cm^{-1} associated to the skeletal C=C vibration typical of oxidized carbon materials remarkably changed: the peak maximum shifted to 1620 cm^{-1} in GO-Fe_xO_y and the contribution from the original 1585 cm^{-1} band appeared only as a weak shoulder. This variation might originate as the consequence of the interaction between oxide particles and GO aromatic skeleton which likely produced the observed random distribution into agglomerate islands. Nanoparticles indeed expose surface alkyl chains (undecanoic acid) that might contribute, through hydrophobic interactions, to the adsorption on the basal plane. Nevertheless, no evidence of the presence of the organic ligand could be proven by infrared analysis.

The most appreciable change, however, occurred in the 1500-1000 cm^{-1} region. Particularly, the band at 1222 cm^{-1} attributed to epoxy C-O-C stretching mode decreased in intensity and shifted to 1246 cm^{-1}. That change might be correlated to either direct interactions of nanoparticles with epoxy groups or, indirectly, with a modification of the surrounding chemical environment induced by the adsorption of the nanoparticles. The other representative GO band at 1052 cm^{-1} and ascribed to C-O stretching of carboxyl functionalities broadened and shifted at about 1062 cm^{-1}. Those results suggest that nanoparticles adsorbed on GO through diverse interactions. In accordance with particles distribution observed from TEM images, nanoparticles might preferentially interact with carboxyl and hydroxyl groups situated at the periphery of the carbon sheets[8,103]. Interactions with epoxy and hydroxyl groups situated on the basal plane (Lerf-Klinowski model)

are feasible and might be partially responsible of adsorption of nanoparticles on the GO basal plane. On the other hand, eventual hydrophobic interactions with the aromatic skeletal through residual surface alkyl chains of undecanoic acid can not be excluded. The evident lack of predominant interactions with specific functionalities, together with the usually weak interactions between iron oxide and hydroxyl, epoxy and aromatic moieties, might be regarded as the reason of the ineffective stabilization of the oxide particles and their consequent agglomeration on the GO basal plane.

No significant change in position, width and intensity of the Raman D- and G-bands is observed upon decoration of GO sheets with iron oxide nanoparticles, as shown in figure 3.14.

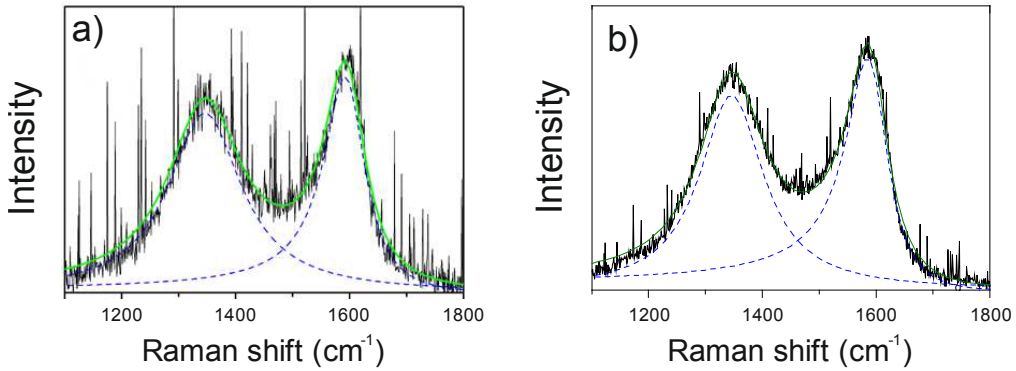

Figure 3.14: Region of the C-sp^2 vibration modes in the Raman spectra of GO (a) and GO-Fe_xO_y (b).

These results suggest that the interfacial interactions between the carbonaceous support and the adsorbed iron oxide nanoparticles have a non-covalent character. Indeed, remarkable G-band shift is reported for GO-iron oxide nanohybrids for which specific interactions and charge transfer processes are observed[97].

XPS analysis revealed that the amount of iron oxide loaded onto GO sheets is very low and the iron concentration accounts for 0.36 at. % (corresponding to the 2.05 wt. %, assuming magnetite as the principal iron oxide form), thus confirming the TGA results for the same material.

Iron atomic fraction was determined from the compositional analysis carried out on the survey spectrum of GO-Fe_xO_y; however, no high-resolution spectrum is available for this element. Presence of iron oxide nanoparticles in the nanocomposite is highlighted by the contribution at 530.0 eV in the high resolution O 1*s* core level XPS spectrum of GO-Fe_xO_y (figure 3.15d), which is assigned to the O-Fe bond.

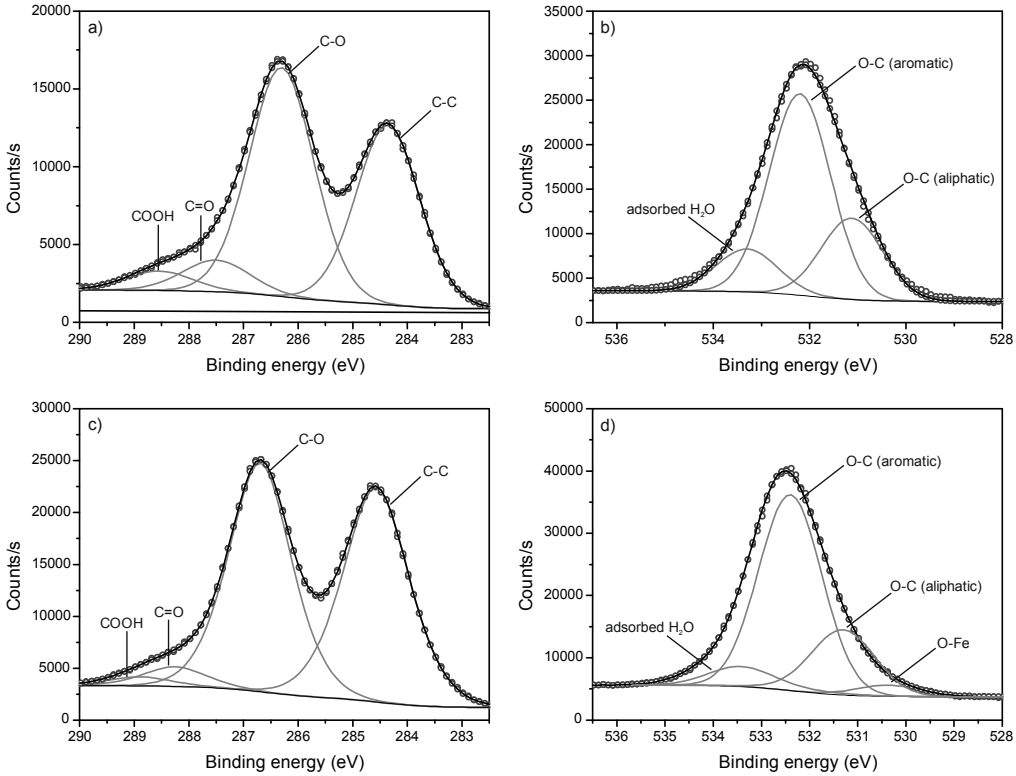

Figure 3.15: High resolution X-ray photoelectron spectra of C 1*s* core level in GO (a) and GO-Fe_xO_y (c). High resolution X-ray photoelectron spectra of O 1*s* core level in GO (b) and GO-Fe_xO_y (d).

Analysis of the C 1s and O 1*s* core level spectra of GO-Fe_xO_y, and their comparison with those of the starting carbon material brought additional information to support the aforementioned hypothesis. In particular, deconvolution of the high resolution O 1*s* core level spectra (figure 3.15b, d) shows that the ratio between the aromatic-to-aliphatic C-O binding fractions of GO did not change upon synthesis of the nanocomposites. Despite the restrained loading of Fe_xO_y nanoparticles, it is inferred that simultaneous and non-specific interaction of the nanoparticles with diverse oxygenated functionalities is consistent with such observation. Similar information is provided by the high resolution C 1*s* core level XPS spectra (figure 3.15a, c). Upon synthesis of the nanocomposite, a collective decrement of the contributions due to oxygen-containing functionalities with respect to the one due to the carbon skeleton supports the hypothesis of the adsorption of the nanoparticles mainly through aspecific interactions with such functional groups. Nevertheless, direct interaction with the carbon skeleton can not be ruled out.

3.3.2.2 Deposition of iron oxide nanoparticles on f-GO

Decoration of chemically modified GO (*f*-GO) with iron oxide nanoparticles was performed following the same "phase transfer" approach used for the production of GO-iron oxide composite.

As observed by X-ray diffractograms (figure 3.16), *f*-GO reflection in the composite material was shifted to 9.7°, while it fell at 11.2° in individual *f*-GO. Such shift towards lower angles is significant of an expansion

of the interlayer distance of *f*-GO, and it is likely correlated to iron oxide nanoparticles acting as spacers when uniformly adsorbed on the *f*-GO sheets.

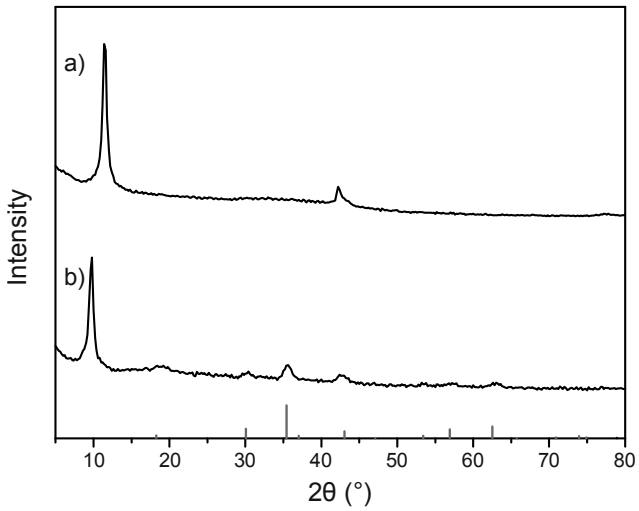

Figure 3.16: X-ray diffractograms of *f*-GO (a) and the corresponding *f*-GO-iron oxide composite (b). The grey columns at the bottom indicate the XRD pattern for magnetite (Fe_3O_4).

The peaks at 18.3°, 30.4°, 35.5°, and 63.4° are consistent with the presence of iron oxide either in the magnetite or maghemite phases (JCPDS files: 01-071-4918 and 00-039-1346 respectively). However, their low intensity let infer that the oxide loading might be low also for this composite.

From thermogravimetric analysis, the iron oxide loading was determined to be about 10.2 wt. %, which is noticeably higher than what determined from the corresponding GO-composite (figure 3.17).

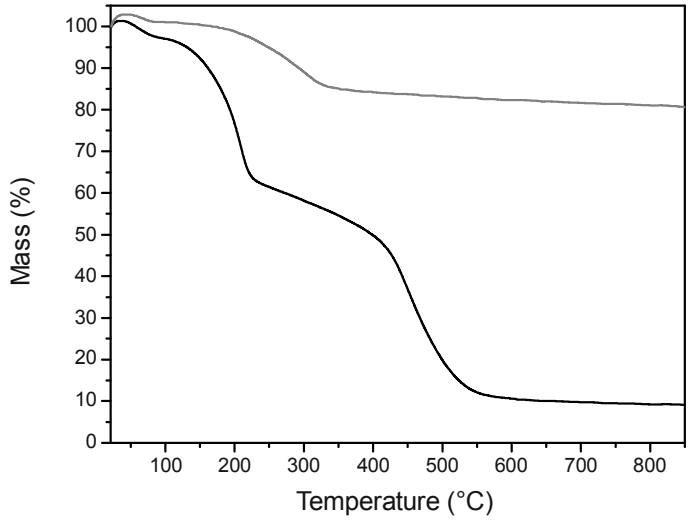

Figure 3.17: TGA curves of *f*-GO-Fe_xO_y (black line) and the deposited Fe_xO_y-UA nanoparticles (grey line) treated in air at a heating rate of 5°C/min.

Figure 3.17 shows that *f*-GO-iron oxide composite (*f*-GO-Fe_xO_y) resemble the thermal behaviour of GO-Fe_xO_y. Indeed it presents three main mass losses: one below 100°C, one between 100 and 275°C and the last one in the temperature range between 275°C and 575°C. Therefore, the same discussion brought about for GO-Fe_xO_y composite likely describes the thermal behaviour of *f*-GO-based composite. However, *f*-GO-Fe_xO_y

presents a more restrained mass loss in the range between 100 and 275°C, suggesting that likely a lower amount of organic ligand remained adsorbed at the surface of the particles deposited at *f*-GO surface.

Similarly to what observed for GO-Fe_xO_y materials, Fe_xO_y particles size determined by TEM images (figure 3.18) ranges between 7 and 9 nm, well in accordance with the particles size distribution typically obtained for undecanoic acid-coated iron oxide nanoparticles (Cf. chapter 2).

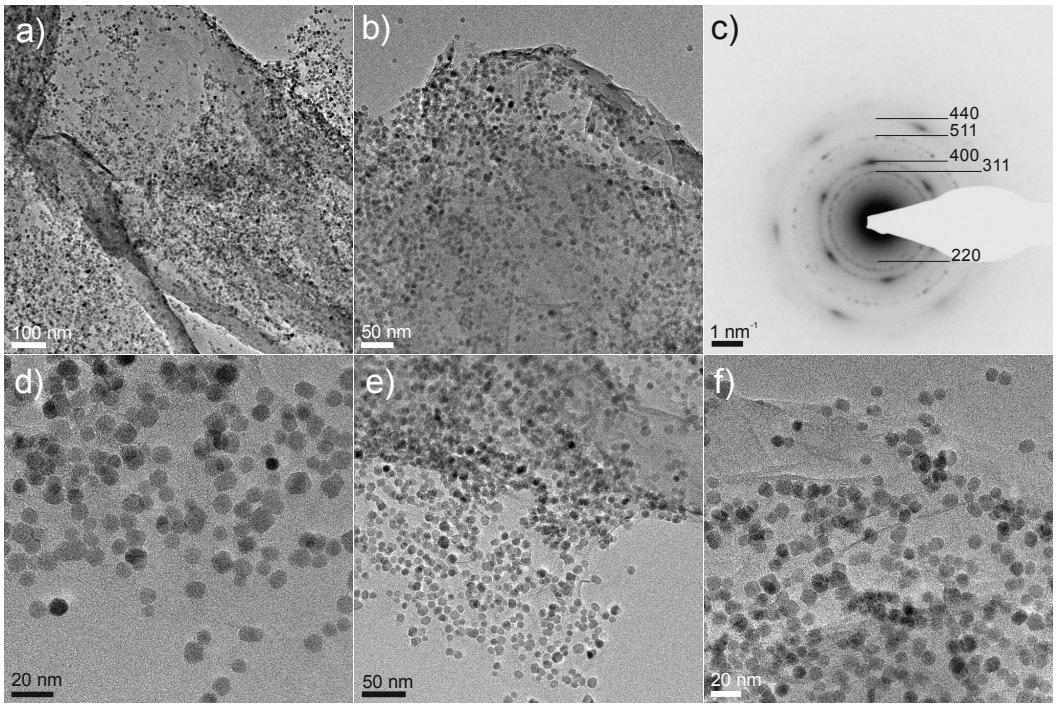

Figure 3.18: TEM images of the *f*-GO-iron oxide composite showing overviews (a, b) and details (d, e, f) of iron oxide particles distribution over the carbon substrate. Electron diffraction patterns (c) of the area showed in (a).

Electron diffraction patterns (figure 3.18c) from a large area of the sample are in accordance with the magnetite phase. TEM images reveal that iron oxide nanoparticles are distributed at the edges of the *f*-GO sheets but most remarkably, they are adsorbed quite uniformly all over the surface of the carbon support and aggregates are not observed. Also in this case, isolated particles not deposited at the carbon surface were not noticed confirming the specificity of the "phase transfer" procedure.

Moreover, TEM images support what observed from TGA measurements: although the presence of uncoated areas on *f*-GO sheets let infer that a limited amount of particles was adsorbed on the carbon substrate, the oxide loading on *f*-GO appears higher than on GO.

These findings suggest that different interactions likely drove the deposition of iron oxide particles on GO and *f*-GO sheets.

The observed morphology might be in part explained on the basis of the FTIR measurements. *f*-GO-Fe_xO_y composite FTIR spectrum showed remarkable variations in two diverse spectral regions when compared to the individual *f*-GO (figure 3.19).

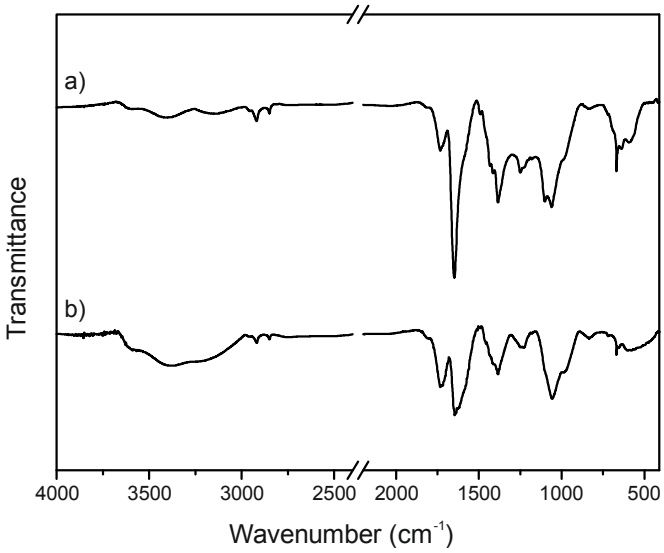

Figure 3.19: FTIR spectra of *f*-GO-Fe_xO_y (a) and *f*-GO (b). For sake of clarity, spectra are represented stacked by an offset value and the signal due to atmospheric CO_2 was omitted by introducing a break in the 2400-2200 cm^{-1} spectral region.

The most considerable difference occurred in the region comprised within 1700 and 1500 cm^{-1}. The band centred at 1643 cm^{-1} of individual *f*-GO became sharper and shifted to 1647 cm^{-1} in *f*-GO-Fe_xO_y (figure 3.19a). As previously reported in the discussion of *f*-GO infrared spectrum, this band might be ascribed to the C=O stretching of carboxyl moieties presumably deriving from the grafted 4-carboxyphenyl functionalities. Despite the peak position didn't change significantly, the striking different shape of this band suggests that those groups are likely involved in interacting with iron oxide nanoparticles. On the other hand, due to the complexity of the system, is rather difficult to deduce the feature interaction between carboxyl groups and Fe_xO_y nanoparticles.

Additional changes occurred in the 1500-1000 cm^{-1} region where the absorption profile visibly changed although noteworthy shifts in the band positions were not observed. This might be correlated to the concomitant participation of all of the functional groups responsible for those bands in the interaction with nanoparticles. Among the others, the bands related to the hydroxyl deformation modes (1385 cm^{-1}) and to the carboxyl C-O stretching vibration (1062 cm^{-1}) suffered the more noticeable changes. Although adsorption *via* simple hydroxyl groups such as phenols can not be ruled out, these results let infer that nanoparticles interact preferentially with carboxyl functionalities. The latter might be identified in major part in 4-carboxyphenyl groups. Moreover, those groups are expected to be homogeneously grafted throughout the surface of *f*-GO layers, likely favouring in this way the uniform distribution of iron oxide particles all over the *f*-GO sheets observed from TEM images. The absence of agglomerate islands let suggest that nanoparticles interacted mainly through specific and not too weak interactions (e.g. with carboxyl groups rather than epoxy functionalities) that would represent stable anchoring sites hence limiting aggregation of the same particles.

Presence of residual undecanoic acid molecules can not be confirmed by FTIR spectroscopy.

Similarly to what observed for GO-iron oxide, positions and relative intensity of the D- and G-bands remained substantially unchanged for *f*-GO-Fe_xO_y. However, in this case, both D- and G-bands narrowed. This is indicative of a reduction of the spreads in the values of bonding angles and lengths (figure 3.20).

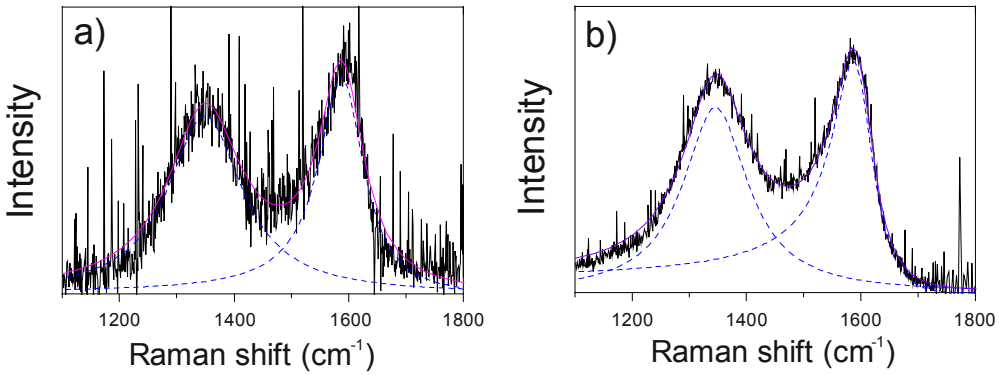

Figure 3.20: Region of the C-sp^2 vibration modes in the Raman spectra of *f*-GO (a) and *f*-GO-Fe_xO_y (b).

XPS analysis revealed that, although iron oxide loading is quite low, being the determined iron concentration equal to 2.25 at. %, this value is remarkably higher than the oxide loading on GO (0.36 at. %). Evidence of the higher iron oxide content is brought by the intensity of the contribution at 530.0 eV ascribed to O-Fe bonds in the O 1*s* core level XPS spectra of the nanocomposite (figure 3.21e), which is significantly higher than in GO-Fe_xO_y. Assuming, for sake of simplicity, that magnetite is the principal form of iron oxide, the iron atomic fractions estimated by XPS analysis correspond to oxide contents of 12 wt. % and 2 wt. % for *f*-GO-Fe_xO_y and GO-Fe_xO_y, respectively. These findings confirm the iron oxide contents estimated by thermogravimetric analyses.

This result suggests that likely more specific and eventually stronger interactions between iron oxide nanoparticles and *f*-GO are responsible of the higher oxide nanoparticle loading in *f*-GO-Fe_xO_y.

High resolution X-ray photoelectron spectra profiles of C 1*s* and O 1*s* core levels are reported in figure 3.21.

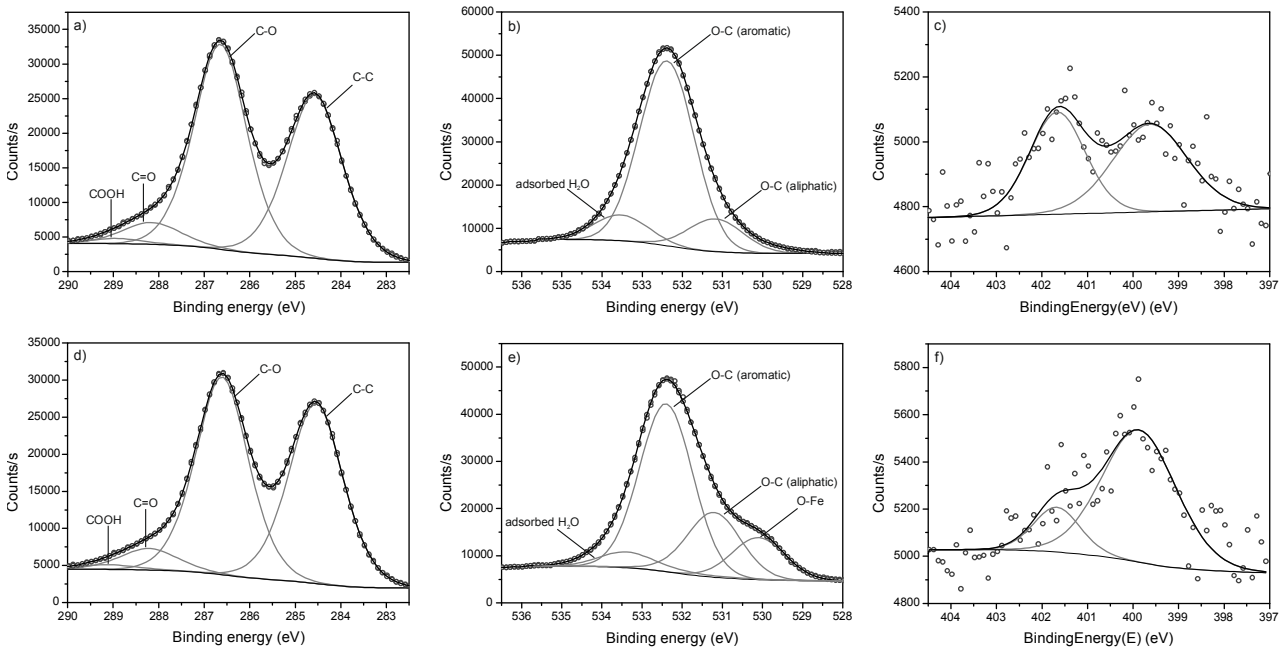

Figure 3.21: High resolution X-ray photoelectron spectra of C 1*s* core level in *f*-GO (a) and *f*-GO-Fe_xO_y (d). High resolution X-ray photoelectron spectra of O 1*s* core level in *f*-GO (b) and *f*-GO-Fe_xO_y (e). High resolution X-ray photoelectron spectra of N 1s core level in *f*-GO (c) and *f*-GO-Fe_xO_y (f).

Although no remarkable changes are observed in the C 1*s* core level spectrum of *f*-GO-Fe_xO_y with respect to *f*-GO, the O 1*s* spectrum gives more information. The comparison between the O 1*s* core level spectrum of *f*-GO-Fe_xO_y with the corresponding starting carbon material reveals that the ratio between the aromatic-to-aliphatic C-O binding fractions of *f*-GO remarkably decreased upon deposition of the Fe_xO_y nanoparticles (figure 3.21b, e). Such result might be associated to a preferential interaction of the nanoparticles with aromatic oxygen-containing groups, which in turn can be partially ascribed to the novel introduced 4-carboxyphenyl moieties.

The N 1*s* spectrum still present the peak at 399.6 eV associated to azo-bonds, which increased in intensity at expenses of the peak at 401.3 eV (figure 3.21f). The latter decreased, supporting the hypothesis that it mainly derived from physisorbed NO species introduced with the functionalization procedure.

Finally, the X-ray photoelectron spectrum of Fe 2*p* core level in *f*-GO-Fe_xO_y is reported in figure 3.22.

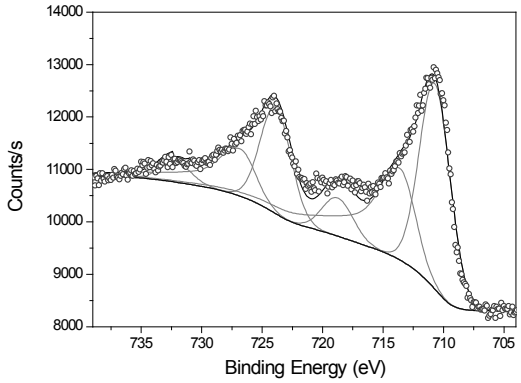

Figure 3.22: High resolution X-ray photoelectron spectrum of Fe 2*p* core level in *f*-GO-Fe_xO_y.

The most intense contributions in the high resolution Fe 2*p* X-ray photoelectron spectrum of sample *f*-GO-Fe_xO_y are ascribed to the Fe $2p_{3/2}$ and Fe $2p_{1/2}$ spin-orbit components. Their binding energies (710.7 and 724.2 eV, respectively) are typical of the Fe_3O_4 phase[104,105]. However, the presence of the satellite peak centred approximately at 719 eV, which is the most significant difference between maghemite (γ-Fe_2O_3) and Fe_3O_4[106], suggests the coexistence of both magnetite and maghemite phases.

3.3.3. Electrochemical properties investigation

Electrochemical properties of all the materials were investigated in both aqueous sodium sulphate (Na_2SO_4) (1 M) and acetonitrile (ACN)-based tetraethylammonium tetrafluoroborate ($N(Et)_4BF_4$) (1 M) electrolytes, using a three-electrodes cell configuration. The choice of performing the study in both aqueous and organic electrolytes was driven by the possibility to distinguish between the electrical double layer capacitive (EDLC) and the pseudocapacitive contributes of the components of composite materials[69,107].

Electrochemical performance of all the GO-based samples was studied by cyclic voltammetry in the -0.8/+0.7 V (vs. reference electrode) potential window. The same analysis for individual undecanoic acid-coated iron oxide (Fe_xO_y-UA) nanoparticles was carried out in a narrower potential window (-0.8/+0.2 V vs. reference electrode). In fact, preliminary tests revealed that iron oxide is not active at potentials higher than +0.2 V. Cyclic voltammetry was run at different scan rates, particularly 5, 10, 20, 50, and 100 mV/s. The cyclic voltammograms of all the materials as a function of the scan rate, measured in aqueous electrolyte, are reported in figure 3.23.

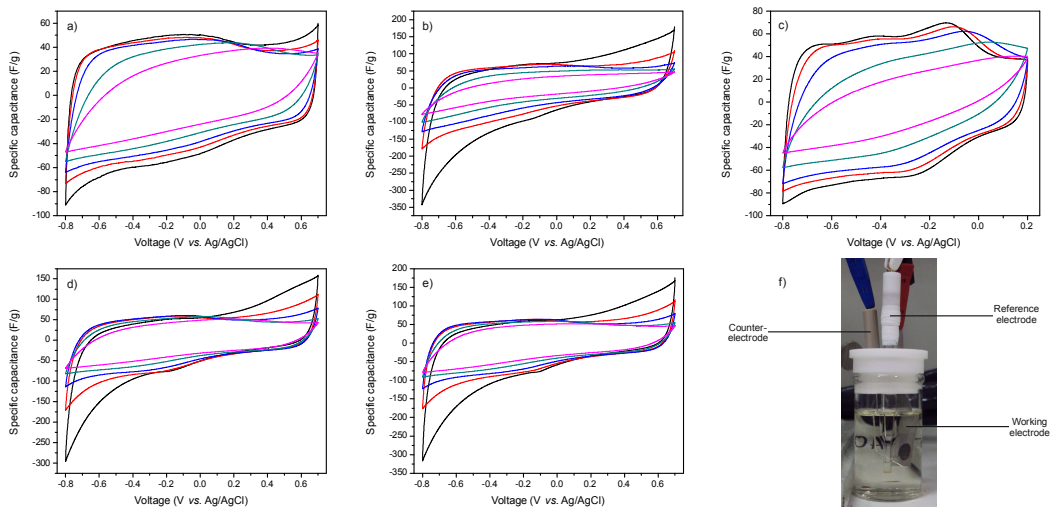

Figure 3.23: Cyclic voltammograms measured in aqueous electrolyte at several scan rates for GO (a), GO-Fe_xO_y (b), Fe_xO_y-UA (c), *f*-GO (d), and *f*-GO-Fe_xO_y (e). For all the material the voltammograms measured at the following scan rates are reported: 5 mV/s (black like), 10 mV/s (red line), 20 mV/s (blue line), 50 mV/s (green line), and 100 mV/s (purple line). Digital image of the three-electrodes cell used for the measurements (f).

As showed by cyclic voltammetry, GO presented a nearly rectangular curve at low scan rates (5-10 mV/s; figure 3.23a). On the contrary, *f*-GO curves deviated from the ideal rectangular shape expected for a perfect

EDLC-material likely because of occurrence of water decomposition at the lowest and highest voltages. Both the composites showed the same behaviour of *f*-GO. However, the rectangular shape was "restored" for all of them at medium scan rates (20 mV/s). Interestingly, both GO and *f*-GO presented two Faradaic contributions which might be due to the participation of oxygen functionalities in reversible charge transfer processes (figure 3.23a,d). It has been reported in literature that in oxidized carbon materials the transition from quinone to hydroquinone groups might take place[60,74]. On the other hand it could be hypothesized a charge transfer reaction involving also carboxyl functionalities in the case of *f*-GO. However, since Faradaic contributions appeared as waves and no significant difference in their position (voltage) was noticed between the materials, it is not possible to distinguish whether different functionalities contributed to the observed Faradaic waves from cyclic voltammetry analysis.

The shape of the Fe_xO_y-UA voltammograms differed from GO-based materials curves. Particularly, it exhibits a well defined pair of peaks at -0.13/-0.3 V (vs. Ag/AgCl) presumably due to redox reactions involving the surface Fe(II)/Fe(III) species[108,109] (figure 3.23c). Those Faradaic contributions represent the pseudocapacitive nature of Fe_xO_y. It has been reported in the literature that the pseudocapacitive behaviour of magnetite (Fe_3O_4), depends on the used electrolyte since electrolyte ions adsorbed on the oxide at the electrode surface may be actively involved in those redox processes[71,109]. Thus, participation of the electrolyte ions in the observed Faradaic peaks can not be ruled out.

Faradaic waves were observed in both of the composites. However, assignment of their position is not that simple (figure 3.23b, e) because of their broad profile. Although it might be a straightforward conclusion that both oxygen functionalities from the carbon material and the iron oxide particles contributed to the observed Faradaic waves, it is difficult to infer whether one of the materials contributed more than the other. As a general observation, the Faradic peaks observed for all the materials disappear when increasing the scan rate at values higher than 20 mV/s. On the one hand this could be due, especially for iron oxide nanoparticles, to a limitation induced by the kinetics of the involved processes[69]. On the other hand, those charge transfer processes might have turn irreversible[60,64,107].

Furthermore, when increasing charge/discharge rate, the voltammograms became narrower and partially lost their nearly rectangular shape. High scan rate might indeed hinder the charge storage at the electrode/electrolyte interface.

A better representation of the oxide contribution to the composite materials is depicted in figure 3.24.

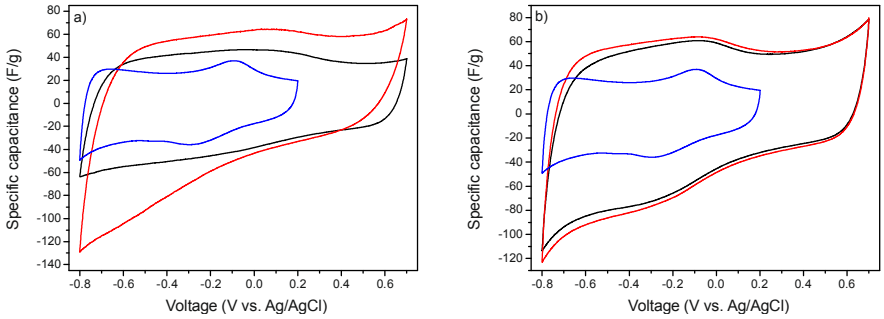

Figure 3.24: Cyclic voltammograms in aqueous electrolyte acquired at the scan rate of 20 mV/s of GO (black line), GO-Fe_xO_y (red line) and Fe_xO_y-UA (blue line; panel a); corresponding cycling voltammograms of *f*-GO (black line), *f*-GO-Fe_xO_y (red-line), and Fe_xO_y-UA (blue line; panel b).

Plotting the 20 mV/s curves for the composites and the corresponding component materials revealed that in case of *f*-GO-Fe_xO_y (figure 3.24b, red line) the capacitance increased mostly in the negative potential window, while it increased throughout the whole potential window in the case of GO-Fe_xO_y (figure 3.24a, red line). The increment observed for *f*-GO-Fe_xO_y is consistent with the presence of Fe_xO_y since it occurred in the potential range (-0.8/+0.2 V vs. Ag/AgCl) where the oxide is active. The capacitance in the other part of the potential window is equal to the one of raw *f*-GO. Observations regarding GO-Fe_xO_y are still consistent with the contribution of Fe_xO_y in the more negative potential range. The increment observed at potential more positive than +0.2 V might be ascribed to a synergistic effect between the carbon material and Fe_xO_y particles, which looked more pronounced than *f*-GO-Fe_xO_y. Presumably, the nature of the interactions between carbon material and iron oxide nanoparticles determined the observed results.

Figure 3.25 describes the variations of relative capacitances as a function of the scan rates. Relative capacitances, for a particular material, were obtained by dividing each of the values of specific capacitance by the one determined at the scan rate of 5 mV/s.

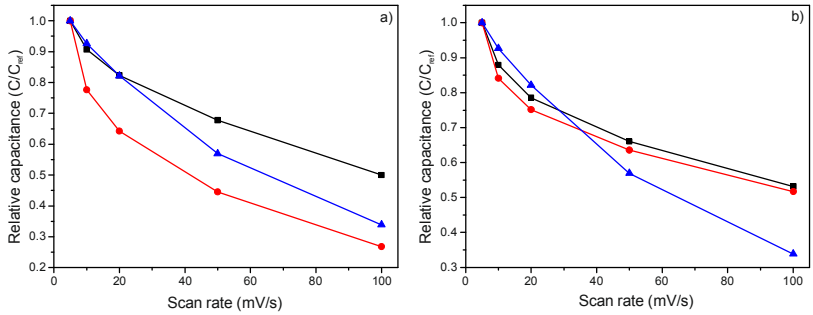

Figure 3.25: Relative capacitances reported as a function of the scan rate for GO (black squares), GO-Fe_xO_y (red dots), and Fe_xO_y-UA (blue triangles; panel a); relative capacitances for *f*-GO (black squares), *f*-GO-Fe_xO_y (red dots), and Fe_xO_y-UA (blue triangles; panel b).

In particular, specific capacitances of all the investigated materials were calculated by integrating over the cyclic voltammetry curves corresponding to the fifth charge/discharge cycle reported in figure 3.23. The as-obtained values were then divided by a factor of "2" due to the fact that the investigated material in the used three-electrodes cell configuration represented only the negative electrode of a complete supercapacitor.

Raw GO and *f*-GO presented the same trend: relative capacitance drop off at similar extent while increasing the scan rate, but *f*-GO always presented higher specific capacitance than GO. At 20 mV/s, the specific capacitance for GO is 55.2 F/g while is 73.5 F/g for *f*-GO.

Such results could be interpreted in terms of chemical composition: in general, it is well accepted that oxidized carbon materials do not have remarkable electrochemical properties when compared to the corresponding non-oxidized materials. Indeed, the introduction of oxygen-containing groups would lead to a partial disruption of the sp^2-carbon network and correlated delocalized π-electrons, that consequently hinder the efficient charge transfer in the carbon network[4,110]. Chemical modification of GO is believed to bring new defects in the material, by causing the change of hybridization from sp^2 to sp^3 of some carbon atoms. On the other hand, assuming that at the working conditions the carboxyl functionalities are partially dissociated into the corresponding carboxylate form, the adsorption of positive ions from the electrolyte would be favoured during the charging step. This would positively influence the EDLC character of the materials and amend to the formation of additional "defect" sites (sp^3-C). Partial dissociation is likely to take place if we assume that the dissociation constant for 4-carboxyphenyl groups doesn't differ significantly from the one of benzoic acid (logarithmic constant, pK_a= 4.2) and knowing that the electrolyte solution presents neutral pH[111].

The positive contribution of Fe_xO_y to the electrochemical behaviour of the composite described in the previous page is reflected in the calculated total capacitance. In particular, it reached 75.6 F/g for GO-Fe_xO_y and 79.7 F/g for *f*-GO-Fe_xO_y. Consistent with what observed in figure 3.24, the major increment was observed for GO-Fe_xO_y. Unlike GO-Fe_xO_y, where nanoparticles are believed to be in direct contact with the carbon support, in *f*-GO-based composite Fe_xO_y nanoparticles are thought to interact preferentially with carboxyl groups of 4-carboxyphenyl functionalities. The latter might be regarded as bridges that hinder a direct contact of the nanoparticles with the underlying support. Moreover, as-adsorbed nanoparticles would occlude some of the carboxylate moieties which could otherwise contribute to the EDLC character of the material by adsorbing electrolyte cations. Those reasons might explain the larger contribution brought by iron oxide in GO-composite rather than in *f*-GO-composite.

The difference between the materials is better noticeable when comparing the trend in specific capacitance as a function of all the investigated scan rates. Although at mid-low scan rates (up to 20 mV/s) GO-Fe_xO_y and *f*-GO-Fe_xO_y presented comparable properties, when further increasing the charge/discharge rate specific capacitance of GO-Fe_xO_y (31.5 F/g at 100 mV/s) drop off much remarkably than *f*-GO-Fe_xO_y (54.8 F/g at 100 mV/s). This observation might be mainly related to the interactions existing between the two component phases in the composites. In fact, the capacitance decrement of Fe_xO_y nanoparticles which is likely related to the kinetics of its Faradaic processes was not as pronounced as to explain the significant drop occurred in the case of GO-Fe_xO_y. Indeed, whether the capacitive drop of both the composites would have been determined mainly by the electrochemical properties of Fe_xO_y, one would expect similar decrease extent and trend for both GO-Fe_xO_y and *f*-GO-Fe_xO_y.

On these considerations, it might be inferred that a loss of the composite structure in GO-Fe_xO_y through desorption of oxide nanoparticles took place faster than *f*-GO-Fe_xO_y, likely due to the prevalence of weaker interactions between the iron oxide particles and carbon support.

Galvanostatic measurements were carried out in order to evaluate the cycling performance of the materials over 1500 cycles. They were performed in the same potential window of cyclic voltammetry, and applying to each sample the maximum current density experimentally determined from the correlated voltammogram acquired at a scan rate of 20 mV/s.

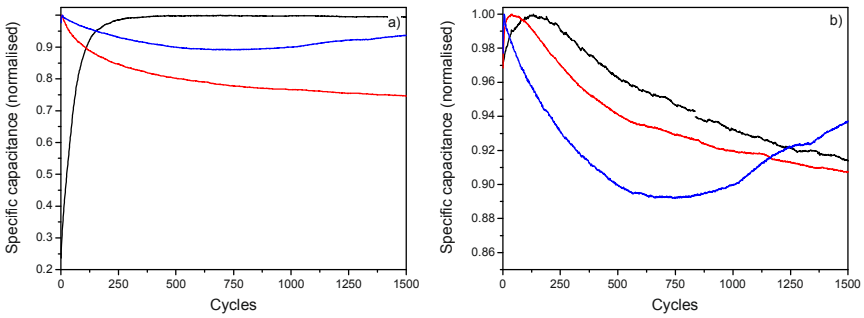

Figure 3.26: Cycling behaviour of GO (black line), GO-Fe_xO_y (red line), and Fe_xO_y-UA (blue line; panel a). Cycling behaviour of *f*-GO (black line), *f*-GO-Fe_xO_y (red-line), and Fe_xO_y-UA (blue line; panel b). For sake of simplicity, only charge curves are showed.

Figure 3.26 illustrates the cycling performances of all the investigated materials. Individual carbon-materials showed an activation step within the first 200 cycles in which an increment of capacitance is noticed. This could be due to the need for the electrolyte to permeate the electrode material. Nevertheless, unlike GO, *f*-GO underwent a 10% capacitance loss during the whole measurement cycles; GO performance was stable instead. Interestingly, Fe_xO_y nanoparticles showed that after a first decrease, their capacitance increased during the measuring time.

The behaviour of the composite materials is in line with what observed previously by cyclic voltammetry: both suffered capacitive loss, but GO-Fe_xO_y at a higher extent than *f*-GO-Fe_xO_y. These results likely support the hypothesis put forward for explaining cyclic voltammogram results, that is the nature of the carbon support-iron oxide nanoparticles interactions likely determine the overall electrochemical behaviour.

The influence of the structural properties of the materials on the charge transfer reaction kinetics and ion diffusion process was evaluated by electrochemical impedance spectroscopy (EIS) over a frequency range from 1 MHz to 10 mHz. The results are depicted in Nyquist plots in which the imaginary part (Z″) of the complex impedance is represented as function of the real part (Z′) (figure 3.27).

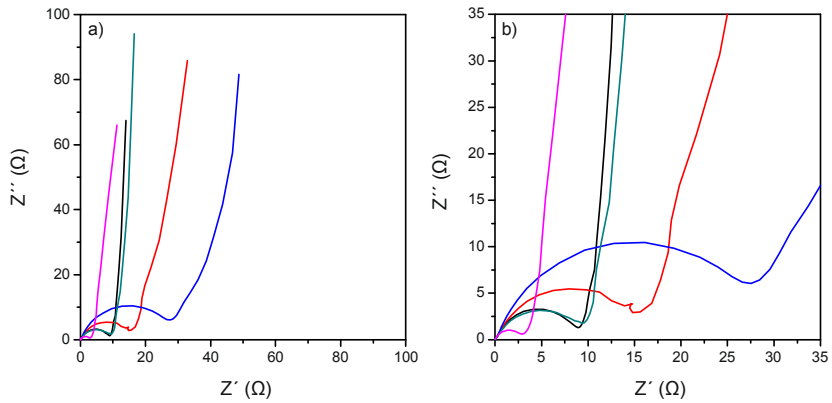

Figure 3.27: (a) Electrochemical impedance spectroscopy of GO (black line), *f*-GO (red line), GO-Fe_xO_y (blue line), *f*-GO-Fe_xO_y (green line), and Fe_xO_y-UA (purple line), measured in aqueous electrolyte. The graph (b) shows a detail of low-to-mid frequency region for all the collected EIS curves. All the reported curves were normalized by subtracting the value of the resistance of the electrolyte (R_s) in order for the curves to intercept the *x*-axis at the origin. The resistance of the electrolyte solution (R_s) is the value of Z′ at which, usually, the curves intercept the *x*-axis and it is similar for all of the samples.

All the materials present incomplete semicircles of different widths in the mid-high frequency region: they represent the charge transfer resistance (R_{ct})[64]. GO showed a lower R_{ct} with respect to *f*-GO likely because of the excess of carboxyl groups present on the latter that might give rise to additional charge transfer reactions compared to GO, as it was also supposed from cyclic voltammetry results. The addition of iron oxide nanoparticles theoretically introduces new charge transfer processes which should lead to a general increase of R_{ct}. The observed trend is partially different from what expected, being the R_{ct} value of Fe_xO_y-UA < GO < *f*-GO-Fe_xO_y < *f*-GO < GO-Fe_xO_y. Undecanoic acid-coated iron oxide nanoparticles were expected to present the largest value, since they should mainly display pseudocapacitive behaviour. It might be suggested that such a low value for R_{ct} could be due to the fact that the surface organic capping ligand prevented nanoparticles from aggregation. This is likely reflected in a higher surface area and, as a consequence, in a reduced R_{ct} value.

Among the carbon materials, GO had the lowest R_{ct} value, as expected due to its EDLC nature[69]. The intermediate position occupied by *f*-GO between the two composites might be explained in terms of a balance between species participating to charge transfer processes. Assuming that the carboxyl groups in *f*-GO participated to charge transfer reactions, part of it would be "inactivated" by the adsorption of Fe_xO_y nanoparticles which, on the other hand, are quite uniformly distributed throughout the carbon sheets. This determines a high surface area which in turns is reflected in a minor R_{ct} due to the high number of active sites available. The sum of the two effects might determine the observed trend. On the contrary, R_{ct} of GO-Fe_xO_y is mostly determined by Fe_xO_y particles which are, unlike in *f*-GO-Fe_xO_y, adsorbed in agglomerate islands. This fact would lead to a lower surface area available for redox reactions hence to a higher resistance.

The line in the low frequency range represents the ion diffusion process or Warburg impedance (W_s). In general the more vertical is this part of the curve, which corresponds to lower W_s values, the easier is the access of the electrolyte ions at the electrode surface[64]. GO is expected to have a largely accessible surface and therefore an almost vertical line; this is confirmed by practical results. The Warburg impedance of the

other GO-based materials follows the same trend observed for R_{ct}: *f*-GO-Fe_xO_y < *f*-GO < GO-Fe_xO_y. As a general consideration, Fe_xO_y nanoparticles should render GO surface less accessible to the electrolyte ions. This is confirmed by GO-Fe_xO_y having the highest W_s value. The lowest W_s value observed for *f*-GO-Fe_xO_y might be related to the higher interlayer distance characterizing *f*-GO-Fe_xO_y when compared to *f*-GO, and thus its higher accessibility. In the case of GO-Fe_xO_y, deposition of Fe_xO_y nanoparticles was followed by a decrease of the GO interlayer spacing.

As already anticipated, in order to distinguish between the EDLC and pseudocapacitive contributions, the measurements were carried out also in organic electrolyte. Cyclic voltammetry and galvanostatic measurement were performed in the same conditions used for the study in aqueous electrolyte.

Cyclic voltammograms of all the materials are depicted in figure 3.28.

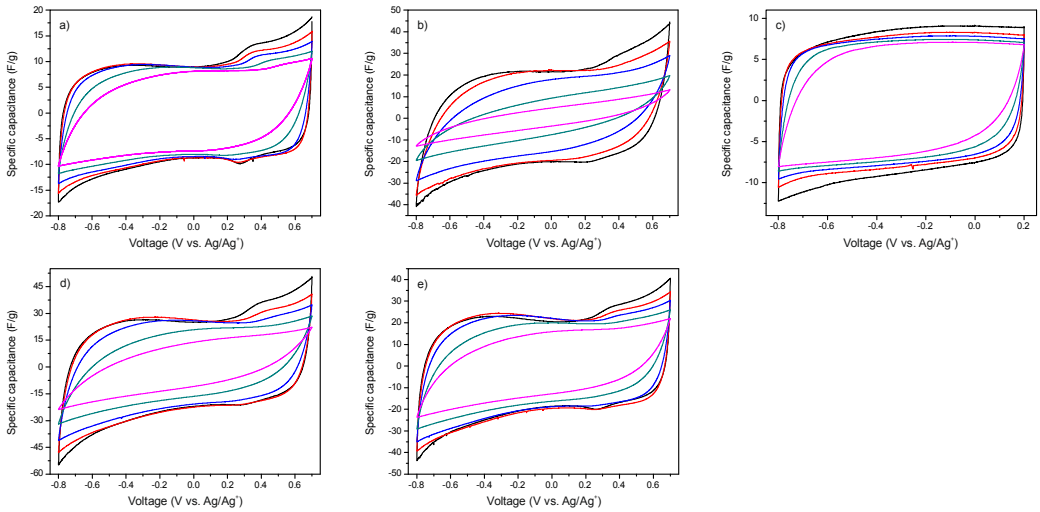

Figure 3.28: Cyclic voltammograms measured in organic electrolyte at several scan rates for GO (a), GO-Fe_xO_y (b), Fe_xO_y-UA (c), *f*-GO (d), and *f*-GO-Fe_xO_y (e). For all the material the voltammograms measured at the following scan rates are reported: 5 mV/s (black like), 10 mV/s (red line), 20 mV/s (blue line), 50 mV/s (green line), and 100 mV/s (purple line).

It is interesting to observe that GO and *f*-GO presented Faradaic peaks at different potentials with respect to the waves appearing in aqueous electrolyte, being them at more positive potentials in ACN-based electrolyte. It might be inferred that either the same active species may undergo different reactions depending on the electrolyte, or functionalities responsible for Faradaic processes in aqueous electrolyte vary from the ones which are active in ACN-based electrolyte. As a general observation, regardless the employed electrolyte, the active species are likely the same in GO and *f*-GO thus suggesting that they might preferentially be functional groups originated during the graphite oxidation process.

Composites cyclic voltammograms showed other noteworthy characteristics: while Faradaic peaks were almost not observed for GO-Fe_xO_y even at low scan rates, they were still present in *f*-GO-Fe_xO_y. This consideration is believed to support the hypothesis that Fe_xO_y particles adsorbed on the carbonaceous substrates through interactions with different functional groups. In particular, there are no appreciable Faradaic peaks in GO-Fe_xO_y suggesting that oxygen-containing functionalities were not available anymore for participating to the same redox processes observed for GO. This might be plausible in case those

functionalities were directly interacting with the adsorbed particles. On the other hand, the sill noticeable Faradaic peaks in the *f*-GO-based composite, suggests that iron oxide nanoparticles were adsorbed by interacting with different functionalities, likely with 4-carboxyphenyl groups. In that way, oxygen-containing functionalities common to both GO and *f*-GO would be still available for redox reactions, hence be responsible of the observed Faradaic peaks.

As observed in figure 3.28, voltammograms of all the GO-based materials still presented a rectangular-like shape, which is typical for EDLC materials. Fe_xO_y-UA electrode displayed a rectangular shape too, highlighting that also Fe_xO_y performance was partially derived from a double layer capacitive behaviour. However, it is interesting to notice that none Faradaic peak is observed for raw Fe_xO_y, as expected.

As a general consideration, *f*-GO curves are larger than GO, and for both materials voltammograms tend to loose the rectangular shape when increasing the scan rate. Particularly, this is more significant for *f*-GO than GO. The values of specific capacitance for the materials were lower than in aqueous electrolyte, being 13.3 F/g for GO and 31.5 F/g for *f*-GO at 20 mV/s.

On the contrary of what observed in aqueous electrolyte, it is not possible to interpret the voltammograms for GO and *f*-GO and their corresponding composites in terms of contribution brought by Fe_xO_y particles. Indeed, it is noticed that Fe_xO_y nanoparticles did not introduce significant improvements to the composite materials properties. They actually led to a little worsening of the composites properties with respect to the individual components. This is likely because in organic electrolytes, a material as Fe_xO_y (that shows mainly pseudocapacitive behaviour) almost acts as a dead weight since Faradaic reactions are hindered, thus retarding electrolyte ions to reach the real electrode active material.

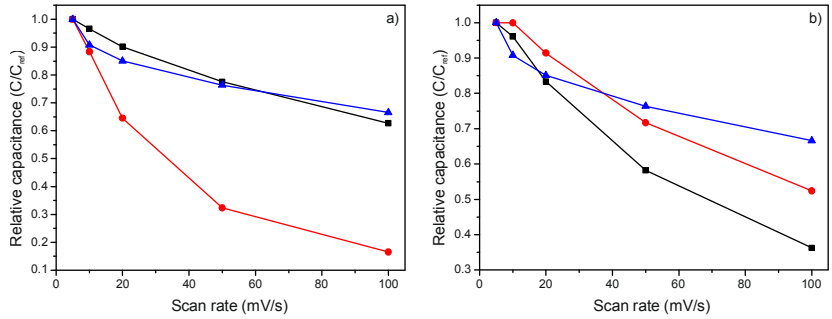

Figure 3.29: Relative capacitances reported as a function of the scan rate for GO (black squares) and GO-Fe_xO_y (red dots), and Fe_xO_y-UA (blue triangles; panel a). Relative capacitances for *f*-GO (black squares), *f*-GO-Fe_xO_y (red dots), and Fe_xO_y-UA (blue triangles; panel b).

The drop in capacitance (figure 3.29) was much more pronounced for *f*-GO and *f*-GO-Fe_xO_y composites than for GO-materials, likely because of a higher tendency of *f*-GO support to suffer degradation in the investigated conditions.

This is confirmed by galvanostatic measurements, where cycling behaviour (figure 3.30) showed a larger capacitive drop for *f*-GO (45%) than GO (10%) over the entire cycling time.

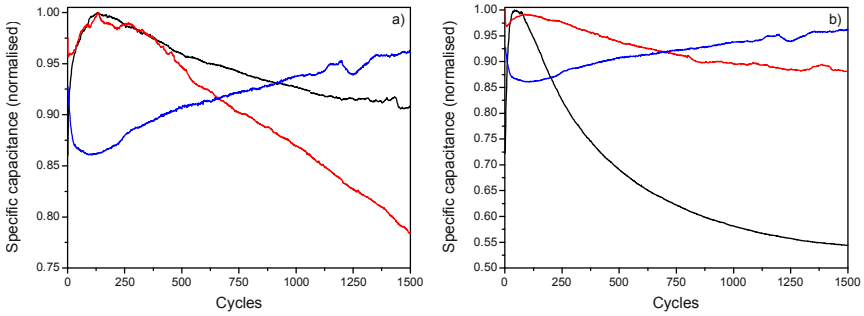

Figure 3.30: Cycling behaviour of GO (black line), GO-Fe_xO_y (red line), and Fe_xO_y-UA (blue line; panel a). Cycling behaviour of *f*-GO (black line), *f*-GO-Fe_xO_y (red-line), and Fe_xO_y-UA (blue line; panel b). For sake of simplicity, only charge curves are showed.

However, as observed from figure 3.29 and 3.30, *f*-GO-Fe_xO_y presented better properties than its correlated individual carbon substrate and than its analogue composite. It might be suggested that, in view of the higher oxide loading and more uniform distribution throughout the carbon sheets, Fe_xO_y nanoparticles could protect the underlying carbon support from fast degradation more efficiently in *f*-GO composite than in GO-composite.

Nevertheless, measurements in organic electrolyte are regarded as not particularly representative for understanding whether the observed behaviour is driven by different interactions between component materials in the composites. For this reason, EIS analysis in organic electrolyte was not performed.

3.4. Conclusions

The aim of this work was to fabricate graphene oxide-iron oxide composites through an *ex-situ* approach based on non-covalent interactions between the component phases. Indeed, the main objective of the project was to investigate whether understanding the relationship between chemical composition of the carbon support and the way of interact with the oxide nanoparticles would have helped to achieve materials presenting more defined structures. On this basis, chemical modification of graphene oxide was performed by grafting 4-carboxyphenyl functionalities through diazonium chemistry. The generally accepted affinity of carboxyl groups for iron oxide would drive, through preferential interactions, a more defined adsorption and distribution of oxide nanoparticles over the carbon substrate. On the other hand, the random distribution of oxygen-containing groups on graphene oxide, all of them showing low affinity for iron oxide, made of this substrate the ideal platform for distinguishing on the interfacial interactions between the two phases. Chemical and structural characterization by FTIR suggested that specific interactions with carboxyl groups introduced via chemical modification prevailed over unspecific interactions with other oxygen-containing groups that are common to both the carbon substrates. The prevalence of specific interfacial interactions between *f*-GO and iron oxide nanoparticles was reflected in a more homogeneous distribution throughout the carbon sheets and to a higher iron oxide loading than on pristine GO. Investigation about electrochemical performances of the materials showed that in both of the cases iron oxide nanoparticles contributed leading to an enhancement of specific capacitance with respect to the corresponding bare carbon substrate. A direct

interaction between the carbon substrate and the oxide phase in GO-composite is believed to be the reason of a more significant capacitance increase than *f*-GO-based composite. In the latter, the grafted 4-carboxyphenyl functionalities which are supposed to preferentially interact with oxide particles are thought to act as bridging groups between the particles and the underlying substrate. This might limit a direct interaction between the phases and thus be responsible of the observed restrained capacitance increase. However, capacitance drop as a function of the working scan rate, and cycling behaviour, supported the hypothesis that iron oxide nanoparticles interact through stronger and more specific interactions with *f*-GO than GO.

Therefore, it was showed that by rationally designing the chemical composition of the carbonaceous support it is possible to improve the fabrication of carbon-metal oxide composite exhibiting a more defined structure and enhanced electrochemical properties. The latter indeed, were shown to be dependent on the interfacial interaction between the component phases thus on the composite structure.

Optimization of the chemical modification procedure in order to extend grafting coverage, introduce even more suitable functionalities and reduce re-staking of graphene sheets is believed to lead to the improvement of those composite properties which are dependent on the interfacial interactions between the components phases. In that way, it might be possible to tailor the properties of the materials depending on the desired final applications.

3.5. Bibliography

(1) Dreyer, D. R.; Park, S.; Bielawski, C. W.; Ruoff, R. S.: The chemistry of graphene oxide. *Chemical Society Reviews* **2010**, *39*, 228-240.

(2) Loh, K. P.; Bao, Q.; Ang, P. K.; Yang, J.: The chemistry of graphene. *Journal of Materials Chemistry* **2010**, *20*, 2277-2289.

(3) Zhu, Y.; Murali, S.; Cai, W.; Li, X.; Suk, J. W.; Potts, J. R.; Ruoff, R. S.: Graphene and Graphene Oxide: Synthesis, Properties, and Applications. *Advanced Materials* **2010**, *22*, 3906-3924.

(4) Chen, D.; Feng, H.; Li, J.: Graphene Oxide: Preparation, Functionalization, and Electrochemical Applications. *Chemical Reviews* **2012**, *112*, 6027-6053.

(5) Compton, O. C.; Nguyen, S. T.: Graphene Oxide, Highly Reduced Graphene Oxide, and Graphene: Versatile Building Blocks for Carbon-Based Materials. *Small* **2010**, *6*, 711-723.

(6) Edwards, R. S.; Coleman, K. S.: Graphene synthesis: relationship to applications. *Nanoscale* **2013**, *5*, 38-51.

(7) Wassei, J. K.; Kaner, R. B.: Oh, the Places You'll Go with Graphene. *Accounts of Chemical Research* **2013**, *46*, 2244-2253.

(8) Gao, W.; Alemany, L. B.; Ci, L.; Ajayan, P. M.: New insights into the structure and reduction of graphite oxide. *Nature Chemistry* **2009**, *1*, 403-408.

(9) Park, S.; An, J.; Potts, J. R.; Velamakanni, A.; Murali, S.; Ruoff, R. S.: Hydrazine-reduction of graphite- and graphene oxide. *Carbon* **2011**, *49*, 3019-3023.

(10) Stankovich, S.; Dikin, D. A.; Piner, R. D.; Kohlhaas, K. A.; Kleinhammes, A.; Jia, Y.; Wu, Y.; Nguyen, S. T.; Ruoff, R. S.: Synthesis of graphene-based nanosheets via chemical reduction of exfoliated graphite oxide. *Carbon* **2007**, *45*, 1558-1565.

(11) Dimiev, A.; Kosynkin, D. V.; Alemany, L. B.; Chaguine, P.; Tour, J. M.: Pristine Graphite Oxide. *Journal of the American Chemical Society* **2012**, *134*, 2815-2822.

(12) Dimiev, A. M.; Tour, J. M.: Mechanism of Graphene Oxide Formation. *ACS Nano* **2014**, *8*, 3060-3068.

(13) Bai, S.; Shen, X.: Graphene-inorganic nanocomposites. *RSC Advances* **2012**, *2*, 64-98.

(14) Huang, X.; Qi, X.; Boey, F.; Zhang, H.: Graphene-based composites. *Chemical Society Reviews* **2012**, *41*, 666-686.

(15) Stankovich, S.; Dikin, D. A.; Dommett, G. H. B.; Kohlhaas, K. M.; Zimney, E. J.; Stach, E. A.; Piner, R. D.; Nguyen, S. T.; Ruoff, R. S.: Graphene-based composite materials. *Nature* **2006**, *442*, 282-286.

(16) Zhang, Y.; Zhu, Y.; Lin, G.; Ruoff, R. S.; Hu, N.; Schaefer, D. W.; Mark, J. E.: What factors control the mechanical properties of poly (dimethylsiloxane) reinforced with nanosheets of 3-aminopropyltriethoxysilane modified graphene oxide? *Polymer* **2013**, *54*, 3605-3611.

(17) Georgakilas, V.; Otyepka, M.; Bourlinos, A. B.; Chandra, V.; Kim, N.; Kemp, K. C.; Hobza, P.; Zboril, R.; Kim, K. S.: Functionalization of Graphene: Covalent and Non-Covalent Approaches, Derivatives and Applications. *Chemical Reviews* **2012**, *112*, 6156-6214.

(18) Liu, Z.; Robinson, J. T.; Sun, X.; Dai, H.: PEGylated Nanographene Oxide for Delivery of Water-Insoluble Cancer Drugs. *Journal of the American Chemical Society* **2008**, *130*, 10876-10877.

(19) Niyogi, S.; Bekyarova, E.; Itkis, M. E.; McWilliams, J. L.; Hamon, M. A.; Haddon, R. C.: Solution Properties of Graphite and Graphene. *Journal of the American Chemical Society* **2006**, *128*, 7720-7721.

(20) Veca, L. M.; Lu, F.; Meziani, M. J.; Cao, L.; Zhang, P.; Qi, G.; Qu, L.; Shrestha, M.; Sun, Y.-P.: Polymer functionalization and solubilization of carbon nanosheets. *Chemical Communications* **2009**, 2565-2567.

(21) Zhang, X.; Huang, Y.; Wang, Y.; Ma, Y.; Liu, Z.; Chen, Y.: Synthesis and characterization of a graphene–C60 hybrid material. *Carbon* **2009**, *47*, 334-337.

(22) Park, S.; Dikin, D. A.; Nguyen, S. T.; Ruoff, R. S.: Graphene Oxide Sheets Chemically Cross-Linked by Polyallylamine. *The Journal of Physical Chemistry C* **2009**, *113*, 15801-15804.

(23) Yang, H.; Li, F.; Shan, C.; Han, D.; Zhang, Q.; Niu, L.; Ivaska, A.: Covalent functionalization of chemically converted graphene sheets via silane and its reinforcement. *Journal of Materials Chemistry* **2009**, *19*, 4632-4638.

(24) Yang, H.; Shan, C.; Li, F.; Han, D.; Zhang, Q.; Niu, L.: Covalent functionalization of polydisperse chemically-converted graphene sheets with amine-terminated ionic liquid. *Chemical Communications* **2009**, 3880-3882.

(25) Sarkar, S.; Bekyarova, E.; Haddon, R. C.: Chemistry at the Dirac Point: Diels–Alder Reactivity of Graphene. *Accounts of Chemical Research* **2012**, *45*, 673-682.

(26) Quintana, M.; Vazquez, E.; Prato, M.: Organic Functionalization of Graphene in Dispersions. *Accounts of Chemical Research* **2012**, *46*, 138-148.

(27) Ensafi, A. A.; Jafari-Asl, M.; Rezaei, B.: A new strategy for the synthesis of 3-D Pt nanoparticles on reduced graphene oxide through surface functionalization, Application for methanol oxidation and oxygen reduction. *Electrochimica Acta* **2014**, *130*, 397-405.

(28) Huang, P.; Jing, L.; Zhu, H.; Gao, X.: Diazonium Functionalized Graphene: Microstructure, Electric, and Magnetic Properties. *Accounts of Chemical Research* **2012**, *46*, 43-52.

(29) Koehler, F. M.; Stark, W. J.: Organic Synthesis on Graphene. *Accounts of Chemical Research* **2012**, *46*, 2297-2306.

(30) Park, J.; Yan, M.: Covalent Functionalization of Graphene with Reactive Intermediates. *Accounts of Chemical Research* **2012**, *46*, 181-189.

(31) Wei, G.; Yan, M.; Dong, R.; Wang, D.; Zhou, X.; Chen, J.; Hao, J.: Covalent Modification of Reduced Graphene Oxide by Means of Diazonium Chemistry and Use as a Drug-Delivery System. *Chemistry – A European Journal* **2012**, *18*, 14708-14716.

(32) Paulus, G. L. C.; Wang, Q. H.; Strano, M. S.: Covalent Electron Transfer Chemistry of Graphene with Diazonium Salts. *Accounts of Chemical Research* **2012**, *46*, 160-170.

(33) Delamar, M.; Hitmi, R.; Pinson, J.; Saveant, J. M.: Covalent modification of carbon surfaces by grafting of functionalized aryl radicals produced from electrochemical reduction of diazonium salts. *Journal of the American Chemical Society* **1992**, *114*, 5883-5884.

(34) Allongue, P.; Delamar, M.; Desbat, B.; Fagebaume, O.; Hitmi, R.; Pinson, J.; Savéant, J.-M.: Covalent Modification of Carbon Surfaces by Aryl Radicals Generated from the Electrochemical Reduction of Diazonium Salts. *Journal of the American Chemical Society* **1997**, *119*, 201-207.

(35) Baranton, S.; Bélanger, D.: Electrochemical Derivatization of Carbon Surface by Reduction of in Situ Generated Diazonium Cations. *The Journal of Physical Chemistry B* **2005**, *109*, 24401-24410.

(36) Baranton, S.; Bélanger, D.: In situ generation of diazonium cations in organic electrolyte for electrochemical modification of electrode surface. *Electrochimica Acta* **2008**, *53*, 6961-6967.

(37) Downard, A. J.: Electrochemically Assisted Covalent Modification of Carbon Electrodes. *Electroanalysis* **2000**, *12*, 1085-1096.

(38) Kariuki, J. K.; McDermott, M. T.: Formation of Multilayers on Glassy Carbon Electrodes via the Reduction of Diazonium Salts. *Langmuir* **2001**, *17*, 5947-5951.

(39) Belmont, J. A.: Process for preparing carbon materials with diazonium salts and resultant carbon products. Corporation, C., Ed.; Google Patents: USA, 1996.

(40) Toupin, M.; Bélanger, D.: Spontaneous Functionalization of Carbon Black by Reaction with 4-Nitrophenyldiazonium Cations. *Langmuir* **2008**, *24*, 1910-1917.

(41) Adenier, A.; Barré, N.; Cabet-Deliry, E.; Chaussé, A.; Griveau, S.; Mercier, F.; Pinson, J.; Vautrin-Ul, C.: Study of the spontaneous formation of organic layers on carbon and metal surfaces from diazonium salts. *Surface Science* **2006**, *600*, 4801-4812.

(42) Pinson, J.; Podvorica, F.: Attachment of organic layers to conductive or semiconductive surfaces by reduction of diazonium salts. *Chemical Society Reviews* **2005**, *34*, 429-439.

(43) Toupin, M.; Bélanger, D.: Thermal Stability Study of Aryl Modified Carbon Black by in Situ Generated Diazonium Salt. *The Journal of Physical Chemistry C* **2007**, *111*, 5394-5401.

(44) Barrière, F.; Downard, A.: Covalent modification of graphitic carbon substrates by non-electrochemical methods. *J Solid State Electrochem* **2008**, *12*, 1231-1244.

(45) Martin, C.; Crosnier, O.; Retoux, R.; Bélanger, D.; Schleich, D. M.; Brousse, T.: Chemical Coupling of Carbon Nanotubes and Silicon Nanoparticles for Improved Negative Electrode Performance in Lithium-Ion Batteries. *Advanced Functional Materials* **2011**, *21*, 3524-3530.

(46) Andrieux, C. P.; Pinson, J.: The Standard Redox Potential of the Phenyl Radical/Anion Couple. *Journal of the American Chemical Society* **2003**, *125*, 14801-14806.

(47) Bahr, J. L.; Yang, J.; Kosynkin, D. V.; Bronikowski, M. J.; Smalley, R. E.; Tour, J. M.: Functionalization of Carbon Nanotubes by Electrochemical Reduction of Aryl Diazonium Salts: A Bucky Paper Electrode. *Journal of the American Chemical Society* **2001**, *123*, 6536-6542.

(48) Delamar, M.; Désarmot, G.; Fagebaume, O.; Hitmi, R.; Pinsonc, J.; Savéant, J. M.: Modification of carbon fiber surfaces by electrochemical reduction of aryl diazonium salts: Application to carbon epoxy composites. *Carbon* **1997**, *35*, 801-807.

(49) Mahouche-Chergui, S.; Gam-Derouich, S.; Mangeney, C.; Chehimi, M. M.: Aryl diazonium salts: a new class of coupling agents for bonding polymers, biomacromolecules and nanoparticles to surfaces. *Chemical Society Reviews* **2011**, *40*, 4143-4166.

(50) Liu, Y.-C.; McCreery, R. L.: Reactions of Organic Monolayers on Carbon Surfaces Observed with Unenhanced Raman Spectroscopy. *Journal of the American Chemical Society* **1995**, *117*, 11254-11259.

(51) Martin, C.; Alias, M.; Christien, F.; Crosnier, O.; Bélanger, D.; Brousse, T.: Graphite-Grafted Silicon Nanocomposite as a Negative Electrode for Lithium-Ion Batteries. *Advanced Materials* **2009**, *21*, 4735-4741.

(52) Bahr, J. L.; Tour, J. M.: Highly Functionalized Carbon Nanotubes Using in Situ Generated Diazonium Compounds. *Chemistry of Materials* **2001**, *13*, 3823-3824.

(53) Salice, P.; Fabris, E.; Sartorio, C.; Fenaroli, D.; Figà, V.; Casaletto, M. P.; Cataldo, S.; Pignataro, B.; Menna, E.: An insight into the functionalisation of carbon nanotubes by diazonium chemistry: Towards a controlled decoration. *Carbon* **2014**.

(54) Laforgue, A.; Addou, T.; Bélanger, D.: Characterization of the Deposition of Organic Molecules at the Surface of Gold by the Electrochemical Reduction of Aryldiazonium Cations. *Langmuir* **2005**, *21*, 6855-6865.

(55) Liu, G.; Luais, E.; Gooding, J. J.: The Fabrication of Stable Gold Nanoparticle-Modified Interfaces for Electrochemistry. *Langmuir* **2011**, *27*, 4176-4183.

(56) Zhang, L. L.; Lei, Z.; Zhang, J.; Tian, X.; Zhao, X. S.: Supercapacitors: Electrode Materials Aspects. In *Encyclopedia of Inorganic and Bioinorganic Chemistry*; John Wiley & Sons, Ltd, 2011.

(57) Tao, X.; Du, J.; Sun, Y.; Zhou, S.; Xia, Y.; Huang, H.; Gan, Y.; Zhang, W.; Li, X.: Exploring the Energy Storage Mechanism of High Performance MnO2 Electrochemical Capacitor Electrodes: An In Situ Atomic Force Microscopy Study in Aqueous Electrolyte. *Advanced Functional Materials* **2013**, *23*, 4745-4751.

(58) Yang, P.; Ding, Y.; Lin, Z.; Chen, Z.; Li, Y.; Qiang, P.; Ebrahimi, M.; Mai, W.; Wong, C. P.; Wang, Z. L.: Low-Cost High-Performance Solid-State Asymmetric Supercapacitors Based on MnO2 Nanowires and Fe_2O_3 Nanotubes. *Nano Letters* **2014**, *14*, 731-736.

(59) Kötz, R.; Carlen, M.: Principles and applications of electrochemical capacitors. *Electrochimica Acta* **2000**, *45*, 2483-2498.

(60) Frackowiak, E.: Carbon materials for supercapacitor application. *Physical Chemistry Chemical Physics* **2007**, *9*, 1774-1785.

(61) Stoller, M. D.; Park, S.; Zhu, Y.; An, J.; Ruoff, R. S.: Graphene-Based Ultracapacitors. *Nano Letters* **2008**, *8*, 3498-3502.

(62) Wang, Y.; Shi, Z.; Huang, Y.; Ma, Y.; Wang, C.; Chen, M.; Chen, Y.: Supercapacitor Devices Based on Graphene Materials. *The Journal of Physical Chemistry C* **2009**, *113*, 13103-13107.

(63) Cottineau, T.; Toupin, M.; Delahaye, T.; Brousse, T.; Bélanger, D.: Nanostructured transition metal oxides for aqueous hybrid electrochemical supercapacitors. *Appl. Phys. A* **2006**, *82*, 599-606.

(64) Wang, G.; Zhang, L.; Zhang, J.: A review of electrode materials for electrochemical supercapacitors. *Chemical Society Reviews* **2012**, *41*, 797-828.

(65) Wu, Z.-S.; Zhou, G.; Yin, L.-C.; Ren, W.; Li, F.; Cheng, H.-M.: Graphene/metal oxide composite electrode materials for energy storage. *Nano Energy* **2012**, *1*, 107-131.

(66) Wang, Y.; Xia, Y.: Recent Progress in Supercapacitors: From Materials Design to System Construction. *Advanced Materials* **2013**, *25*, 5336-5342.

(67) Zhang, Y.; Feng, H.; Wu, X.; Wang, L.; Zhang, A.; Xia, T.; Dong, H.; Li, X.; Zhang, L.: Progress of electrochemical capacitor electrode materials: A review. *International Journal of Hydrogen Energy* **2009**, *34*, 4889-4899.

(68) Cui, S.; Mao, S.; Lu, G.; Chen, J.: Graphene Coupled with Nanocrystals: Opportunities and Challenges for Energy and Sensing Applications. *The Journal of Physical Chemistry Letters* **2013**, *4*, 2441-2454.

(69) Gao, P.-C.; Russo, P. A.; Conte, D. E.; Baek, S.; Moser, F.; Pinna, N.; Brousse, T.; Favier, F.: Morphology Effects on the Supercapacitive Electrochemical Performances of Iron Oxide/Reduced Graphene Oxide Nanocomposites. *ChemElectroChem* **2014**, 747-754.

(70) Wang, L.; Ji, H.; Wang, S.; Kong, L.; Jiang, X.; Yang, G.: Preparation of Fe_3O_4 with high specific surface area and improved capacitance as a supercapacitor. *Nanoscale* **2013**, *5*, 3793-3799.

(71) Wu, N.-L.; Wang, S.-Y.; Han, C.-Y.; Wu, D.-S.; Shiue, L.-R.: Electrochemical capacitor of magnetite in aqueous electrolytes. *Journal of Power Sources* **2003**, *113*, 173-178.

(72) Ji, Z.; Shen, X.; Zhu, G.; Zhou, H.; Yuan, A.: Reduced graphene oxide/nickel nanocomposites: facile synthesis, magnetic and catalytic properties. *Journal of Materials Chemistry* **2012**, *22*, 3471-3477.

(73) Zubir, N. A.; Yacou, C.; Motuzas, J.; Zhang, X.; Diniz da Costa, J. C.: Structural and functional investigation of graphene oxide–Fe_3O_4 nanocomposites for the heterogeneous Fenton-like reaction. *Scientific Reports* **2014**, *4*.

(74) Lai, L.; Yang, H.; Wang, L.; Teh, B. K.; Zhong, J.; Chou, H.; Chen, L.; Chen, W.; Shen, Z.; Ruoff, R. S.; Lin, J.: Preparation of Supercapacitor Electrodes through Selection of Graphene Surface Functionalities. *ACS Nano* **2012**, *6*, 5941-5951.

(75) Wu, W.; He, Q.; Jiang, C.: Magnetic Iron Oxide Nanoparticles: Synthesis and Surface Functionalization Strategies. *Nanoscale Research Letters* **2008**, *3*, 397-415.

(76) Turcheniuk, K.; Tarasevych, A. V.; Kukhar, V. P.; Boukherroub, R.; Szunerits, S.: Recent advances in surface chemistry strategies for the fabrication of functional iron oxide based magnetic nanoparticles. *Nanoscale* **2013**, *5*, 10729-10752.

(77) Hummers, W. S.; Offeman, R. E.: Preparation of Graphitic Oxide. *Journal of the American Chemical Society* **1958**, *80*, 1339-1339.

(78) Pinna, N.; Grancharov, S.; Beato, P.; Bonville, P.; Antonietti, M.; Niederberger, M.: Magnetite Nanocrystals: Nonaqueous Synthesis, Characterization, and Solubility†. *Chemistry of Materials* **2005**, *17*, 3044-3049.

(79) Brodie, B. C.: On the Atomic Weight of Graphite. *Philosophical Transactions of the Royal Society of London* **1859**, *149*, 249-259.

(80) Staudenmaier, L.: Verfahren zur Darstellung der Graphitsäure. *Berichte der deutschen chemischen Gesellschaft* **1898**, *31*, 1481-1487.

(81) Kovtyukhova, N. I.; Ollivier, P. J.; Martin, B. R.; Mallouk, T. E.; Chizhik, S. A.; Buzaneva, E. V.; Gorchinskiy, A. D.: Layer-by-Layer Assembly of Ultrathin Composite Films from Micron-Sized Graphite Oxide Sheets and Polycations. *Chemistry of Materials* **1999**, *11*, 771-778.

(82) Lerf, A.; He, H.; Forster, M.; Klinowski, J.: Structure of Graphite Oxide Revisited‖. *The Journal of Physical Chemistry B* **1998**, *102*, 4477-4482.

(83) Lian, P.; Zhu, X.; Liang, S.; Li, Z.; Yang, W.; Wang, H.: Large reversible capacity of high quality graphene sheets as an anode material for lithium-ion batteries. *Electrochimica Acta* **2010**, *55*, 3909-3914.

(84) Russo, P. A.; Donato, N.; Leonardi, S. G.; Baek, S.; Conte, D. E.; Neri, G.; Pinna, N.: Room-Temperature Hydrogen Sensing with Heteronanostructures Based on Reduced Graphene Oxide and Tin Oxide. *Angewandte Chemie International Edition* **2012**, *51*, 11053-11057.

(85) Doppelt, P.; Hallais, G.; Pinson, J.; Podvorica, F.; Verneyre, S.: Surface Modification of Conducting Substrates. Existence of Azo Bonds in the Structure of Organic Layers Obtained from Diazonium Salts. *Chemistry of Materials* **2007**, *19*, 4570-4575.

(86) Fuente, E.; Menéndez, J. A.; Díez, M. A.; Suárez, D.; Montes-Morán, M. A.: Infrared Spectroscopy of Carbon Materials: A Quantum Chemical Study of Model Compounds. *The Journal of Physical Chemistry B* **2003**, *107*, 6350-6359.

(87) Acik, M.; Lee, G.; Mattevi, C.; Pirkle, A.; Wallace, R. M.; Chhowalla, M.; Cho, K.; Chabal, Y.: The Role of Oxygen during Thermal Reduction of Graphene Oxide Studied by Infrared Absorption Spectroscopy. *The Journal of Physical Chemistry C* **2011**, *115*, 19761-19781.

(88) Mermoux, M.; Chabre, Y.; Rousseau, A.: FTIR and ^{13}C NMR study of graphite oxide. *Carbon* **1991**, *29*, 469-474.

(89) Bekyarova, E.; Sarkar, S.; Niyogi, S.; Itkis, M. E.; Haddon, R. C.: Advances in the chemical modification of epitaxial graphene. *Journal of Physics D: Applied Physics* **2012**, *45*, 154009.

(90) Sun, Z.; Pint, C. L.; Marcano, D. C.; Zhang, C.; Yao, J.; Ruan, G.; Yan, Z.; Zhu, Y.; Hauge, R. H.; Tour, J. M.: Towards hybrid superlattices in graphene. *Nature Communications* **2011**, *2*, 559.

(91) Silverstein, R. M.; Webster, F. X.: *Spectrometric identification of organic compounds*; John Wiley and Sons, Inc., 1998.

(92) Eigler, S.; Dotzer, C.; Hof, F.; Bauer, W.; Hirsch, A.: Sulfur Species in Graphene Oxide. *Chemistry – A European Journal* **2013**, *19*, 9490-9496.

(93) Hadzi, D.; Novak, A.: Infra-red spectra of graphitic oxide. *Transactions of the Faraday Society* **1955**, *51*, 1614-1620.

(94) Ferrari, A. C.; Robertson, J.: Interpretation of Raman spectra of disordered and amorphous carbon. *Physical Review B* **2000**, *61*, 14095-14107.

(95) Malard, L. M.; Pimenta, M. A.; Dresselhaus, G.; Dresselhaus, M. S.: Raman spectroscopy in graphene. *Physics Reports* **2009**, *473*, 51-87.

(96) Tuinstra, F.; Koenig, J. L.: Raman Spectrum of Graphite. *The Journal of Chemical Physics* **1970**, *53*, 1126-1130.

(97) Wang, T.; Liu, Z.; Lu, M.; Wen, B.; Ouyang, Q.; Chen, Y.; Zhu, C.; Gao, P.; Li, C.; Cao, M.; Qi, L.: Graphene–Fe_3O_4 nanohybrids: Synthesis and excellent electromagnetic absorption properties. *Journal of Applied Physics* **2013**, *113*, -.

(98) Kudin, K. N.; Ozbas, B.; Schniepp, H. C.; Prud'homme, R. K.; Aksay, I. A.; Car, R.: Raman Spectra of Graphite Oxide and Functionalized Graphene Sheets. *Nano Letters* **2007**, *8*, 36-41.

(99) Barinov, A.; Gregoratti, L.; Dudin, P.; La Rosa, S.; Kiskinova, M.: Imaging and Spectroscopy of Multiwalled Carbon Nanotubes during Oxidation: Defects and Oxygen Bonding. *Advanced Materials* **2009**, *21*, 1916-1920.

(100) Ganguly, A.; Sharma, S.; Papakonstantinou, P.; Hamilton, J.: Probing the Thermal Deoxygenation of Graphene Oxide Using High-Resolution In Situ X-ray-Based Spectroscopies. *The Journal of Physical Chemistry C* **2011**, *115*, 17009-17019.

(101) Hontoria-Lucas, C.; López-Peinado, A. J.; López-González, J. d. D.; Rojas-Cervantes, M. L.; Martín-Aranda, R. M.: Study of oxygen-containing groups in a series of graphite oxides: Physical and chemical characterization. *Carbon* **1995**, *33*, 1585-1592.

(102) Wang, Y.-Q.; Zhang, F.-Q.; Sherwood, P. M. A.: X-ray Photoelectron Spectroscopic Study of Carbon Fiber Surfaces. 23. Interfacial Interactions between Polyvinyl Alcohol and Carbon Fibers Electrochemically Oxidized in Nitric Acid Solution. *Chemistry of Materials* **1999**, *11*, 2573-2583.

(103) Cai, W.; Piner, R. D.; Stadermann, F. J.; Park, S.; Shaibat, M. A.; Ishii, Y.; Yang, D.; Velamakanni, A.; An, S. J.; Stoller, M.; An, J.; Chen, D.; Ruoff, R. S.: Synthesis and Solid-State NMR Structural Characterization of 13C-Labeled Graphite Oxide. *Science* **2008**, *321*, 1815-1817.

(104) Mulder, J.: *Handbook of X-ray photoelectron spectroscopy*; Perkin Elmer, 1982.

(105) Zhang, M.; Jia, M.; Jin, Y.: Fe_3O_4/reduced graphene oxide nanocomposite as high performance anode for lithium ion batteries. *Applied Surface Science* **2012**, *261*, 298-305.

(106) Li, X.; Si, Z.; Lei, Y.; Tang, J.; Wang, S.; Su, S.; Song, S.; Zhao, L.; Zhang, H.: Direct hydrothermal synthesis of single-crystalline triangular Fe_3O_4 nanoprisms. *CrystEngComm* **2010**, *12*, 2060-2063.

(107) Conway, B. E.; Birss, V.; Wojtowicz, J.: The role and utilization of pseudocapacitance for energy storage by supercapacitors. *Journal of Power Sources* **1997**, *66*, 1-14.

(108) Shi, W.; Zhu, J.; Sim, D. H.; Tay, Y. Y.; Lu, Z.; Zhang, X.; Sharma, Y.; Srinivasan, M.; Zhang, H.; Hng, H. H.; Yan, Q.: Achieving high specific charge capacitances in Fe_3O_4/reduced graphene oxide nanocomposites. *Journal of Materials Chemistry* **2011**, *21*, 3422-3427.

(109) Wang, S.-Y.; Ho, K.-C.; Kuo, S.-L.; Wu, N.-L.: Investigation on Capacitance Mechanisms of Fe_3O_4 Electrochemical Capacitors. *Journal of The Electrochemical Society* **2006**, *153*, A75-A80.

(110) Eigler, S.; Grimm, S.; Hof, F.; Hirsch, A.: Graphene oxide: a stable carbon framework for functionalization. *Journal of Materials Chemistry A* **2013**, *1*, 11559-11562.

(111) Saby, C.; Ortiz, B.; Champagne, G. Y.; Bélanger, D.: Electrochemical Modification of Glassy Carbon Electrode Using Aromatic Diazonium Salts. 1. Blocking Effect of 4-Nitrophenyl and 4-Carboxyphenyl Groups. *Langmuir* **1997**, *13*, 6805-6813.

Chapter 4

Surface functionalization of magnetite nanoparticles with cavitands for recoverable molecular receptors: comparison between non-covalent and covalent strategies

4.1. Introduction

Demand for highly specific and reliable sensors is increasing in several application fields, from biomedical to environment, from industry to home safety. Requirements for sensor devices lie in being active in presence of rather low concentration of the target analyte and, at the same time, being specific towards a narrow class of compounds. This means to exhibit high selectivity for the investigated analyte even when exposed to a mixture of interfering molecules[1]. Chemical sensing can be accomplished following two strategies. In the first one, namely differential sensing, the receptor or association of more receptors is able to recognize a general and wide class of compounds[2]. In the second case, the so-called specific sensing, the receptor is aimed to detect and selectively bind only a single or very few molecules owing to the same class of compounds. Thus, it would be capable of discriminating between molecules which differ only for few peculiarities (e. g. branched chains versus linear chains, presence of substituent groups on a given functionality, etc.)[2]. However, the development of a molecular sensor presenting such characteristics is not trivial. For this purpose, chemical sensors have to be designed in accordance with the target analyte structural properties. In analogy with biological receptors (e.g. enzymes), the sensor should present an arrangement of chemical functionalities able to create a binding site complementary in size and chemical structure to the molecule to recognize. A high degree of selectivity in chemical sensing requires the development of well-controlled synthetic pathways to receptor compounds in order to enable rational distribution of selected functionalities for multiple and specific non-covalent interactions with the target guest. Examples of specific chemical sensors are crown ethers and cavitands.

Cavitands are synthetic organic molecules having rigid cavities of molecular dimension and used as molecular receptors[3]. In particular, a bridged resorcin[4]arene scaffold constitutes the cavity[4]. Appropriate design of cavitands, in terms of size, shape and functionalities on the cavity, determines the selectivity of the molecular recognition process. In addition, if properly designed, it may promote the discrimination between molecules owing to the same class of compounds. In particular, functionalities situated at the upper rim as bridging groups of the phenolic hydroxyls of the resorcin[4]arene scaffold play a fundamental role[5].

Phosphonate cavitands, which possess from one to four phosphoryl (P=O) bridging groups at the wider cavity rim, show outstanding recognition properties for molecules capable of interactions through hydrogen bonding[1,6]. For instance, they were demonstrated to be able to complex linear and branched short chain alcohols[7]. It was observed that the orientation of the P=O bond determines the efficiency of the recognition process. Indeed, only when it is directed inward the cavity, molecular recognition was observed. The higher the number of P=O bonds, the higher the H-bonding possibilities and the more stabilized will be the host-guest complex. In general, additional CH–π and dipole-dipole interactions contribute to the host-guest complex formation and stability[1,6]. On these bases, tetraphosphonate cavitands with inward P=O bonds orientation show the best recognition properties (figure 4.1).

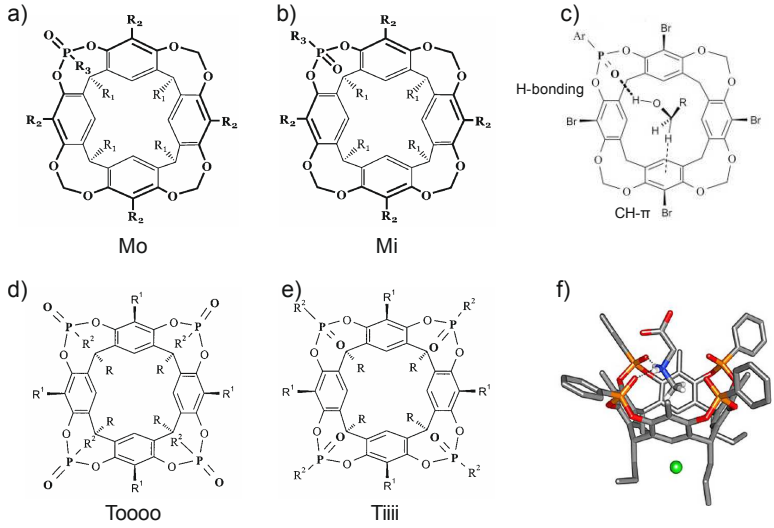

Figure 4.1: Top-view of molecular structures of monophosphonate cavitands bearing outward- (a) and inward-directed (b) phosphoryl bridging group, example of hydrogen bonding and CH-π interaction of an alcohol molecule complexed in the cavity of a monophosphonate cavitand (c)[6]. Top-view of molecular structures of tetraphosphonate cavitands bearing outward- (d) and inward-directed (e) phosphoryl bridging groups, example of hydrogen bonding and CH_3-π interaction of a sarcosine molecule complexed in the cavity of a tetraphosphonate cavitand (f)[1].

In particular, tetraphosphonate cavitands present outstanding recognition selectivity for N-methyl ammonium ions. The origin of such properties derives from the multiple interaction modes that can be established with this particular compounds: (i) $N^+\cdots O{=}P$ cation-dipole interactions, (ii) two hydrogen bonds between the two nitrogen protons and two of the oxygen of O=P groups, (iii) CH_3–π interaction between the N^+–CH_3 group and the π scaffold of the cavity[1,8].

This peculiar property of tetraphosphonate cavitands renders them promising candidates for the detection of diverse biologically active compounds, which often bear N-methylated residues. As an example, sarcosine is referred as a biomarker of the prostate cancer since it was proposed that its presence in human urine is likely correlated to such a disease[9]. Ability of tetraphosphonate cavitands in recognizing sarcosine both in water and biological fluids was recently studied. It was demonstrated that the appropriate cavitand was able to discriminate between sarcosine and its non-methylated

analogue glycine, in aqueous solution. Moreover, the study showed that high selectivity towards recognition of sarcosine over a wide range of potential interfering molecules successfully occurred even in urine (i. e. target working conditions)[10].

This work highlighted the challenges of employing cavitands as receptors for biomarkers or, more general, in biological applications. For such applications, cavitands are needed to be dispersed in aqueous environment. However, most of the suitable tetraphosphonate cavitands are usually insoluble in water[10]. To address the latter problem, cavitands might be grafted onto a solid support. In fact, silicon substrates were successfully used and recognition was proven to occur in solution as well as at the solid-liquid and solid-gas interfaces[11,12].

Magnetic nanoparticles, such as iron oxide nanoparticles, represent a valid alternative to silicon substrates due to their ease of synthesis and surface functionalization, and to their magnetic properties. In particular, when the size is equal or smaller than 20 nm in diameter, iron oxide nanoparticles exhibit superparamagnetic behaviour at room temperature. In this size domain, each nanoparticle is regarded as a single magnetic domain, and it exhibits a fast response to an external magnetic field and negligible remnant magnetization[13-15]. These properties are particularly appealing for biomedical applications, such as magnetic separation of proteins, magnetic resonance imaging (MRI) contrast agents, and targetable drug delivery devices[16,17].

An important requirement for receptors to be employed for the detection of drugs or the screening of cancer biomarkers is to operate directly in the investigated biological environment, limiting sample manipulations in order to minimize the possibility to alter sample composition[10]. For this purpose, the cavitand-magnetic nanoparticle system would represent a valid solution. Due to their magnetic properties, particles can be easily separated from the surrounding medium applying an external magnetic field. This will allow collecting the target analyte/guest species adsorbed on nanoparticles upon formation of the complex with surface cavitand molecules. The reversibility of the cavitand-guest complex enables the facile displacement of the targeted guest and its consequent quantification[18-20].

The several methods developed for functionalization of magnetic nanoparticles, in particular iron oxide nanoparticles, demonstrated that multifunctional particles can be easily synthesized by choosing the proper capping agents[21]. This would make possible the creation of an iron oxide nanoparticles-based system which is, at the same time, dispersible in water and capable of molecular recognition due to the presence of the cavitand at its surface.

Polymers like polyethylene glycol (PEG) or organo alkoxysilanes coupling agents are widely used to provide water dispersibility[22], desired property for application in biological fluids. Furthermore, organo alkoxysilanes coupling agents represent an ideal system: due to the availability of organo-alkoxysilanes bearing diverse functionalities, they can simultaneously provide water solubility (*via* polar functionalities or hydrophilic short-chain polymers) and anchoring sites for covalent grafting of cavitand molecules[23-25].

Finally, the ideal chemical sensor device should present receptor molecules (cavitands) firmly grafted on the solid substrate in order to minimize the risk of leaching of the receptor active component.

The aim of the work described in this chapter is to illustrate the functionalization approaches that can be adopted for the fabrication of a recoverable molecular receptor suitable for the recognition and quantification of biomarkers or drugs metabolites in biological fluids. In particular, the chapter will focus on the description of the functionalization of preformed magnetite nanoparticles with cavitand molecules through two approaches, namely non-covalent and covalent. The investigated cavitand molecules present a carboxyl functional group at the cavity lower rim. Therefore, the non-covalent approach will be based on the coordination affinity of carboxylate species with surface iron atoms of magnetite nanoparticles. On the other hand, the covalent approach will be based on the use of organo alkoxysilanes as coupling agents, which will allow cavitand conjugation through formation of an amide bond. The functionalization strategies will be performed for anchoring two cavitand molecules. The first molecule is a tetraphosphonate cavitand and it represents the target species, because it is active in the selective recognition and binding of N-methyl ammonium moieties. The second cavitand molecule lacks of phosphoryl bridging groups at the cavity upper rim, therefore it is unable of selectively bind N-methyl ammonium species. For this reason, it will be used as reference compound in further tests of molecular recognition.
Advantages and drawbacks of the adopted strategies will be illustrated in terms of the desired applications as supramolecular sensors.
Preliminary molecular recognition tests based on an optical "dye-displacement" method will be described. The tests were firstly performed on covalently-functionalized magnetite nanoparticles because they are regarded as the most promising system.
The work described in this chapter arises from an ongoing collaboration with the group of Professor Enrico Dalcanale (University of Parma - Italy), who kindly provided the cavitand molecules and performed the preliminary molecular recognition tests.

4.2. Experimental section

4.2.1. Materials

Iron(III) acetylacetonate ($Fe(acac)_3$, anhydrous 99% - STREM) and benzyl alcohol (puriss. 99% Sigma-Aldrich) were stored in a glovebox and used as received.
Cavitand molecules were synthesized by the group of Prof. E. Dalcanale (University of Parma - Italy) following a procedure similar to the one described in the literature[18].
Acetic acid (≥99.7%), N,N'-dicyclohexylcarbodiimide (DCC, 99%), and 4-(dimethylamino)pyridine (DMAP, 99%) were purchased from Aldrich and used as received.

(3-Aminopropyl)trimethoxysilane (APTMS, 96%) and 2-[methoxy(polyethylenoxy)propyl] trimethoxysilane (PEOS, 90%, 6-9 PE units) were purchased from ABCR; they were store in a glovebox and used as received.
Dichloromethane (DCM) was dried over activated aluminium oxide (neutral, Brockmann I) and stored on molecular sieves (4Å).
All the used solvents were of the highest grade and used as received.

4.2.2. Methods

4.2.2.1. Synthesis of magnetite nanoparticles

Magnetite (**Fe_3O_4**) nanoparticles were synthesized following the traditional "benzyl alcohol route", as previously reported[26].
Briefly, the preparation of the reaction mixture was carried out in a glovebox (H_2O< 0.1 ppm, and O_2< 0.1 ppm). In a typical synthesis, 1.0 g (2.83 mmol) of iron(III) acetylacetonate was placed in a 45-mL inner volume Teflon cup and solubilised in 20 mL of benzyl alcohol. The Teflon cup was then slid into a steel autoclave which was carefully sealed and taken out from the glovebox. The reaction was performed in an oven heated at 175°C for 48 hours. The resulting nanoparticles were collected by centrifugation and washed twice with absolute ethanol and once with DCM. Finally, nanoparticles were redispersed either in 20 mL of ultrapure water or in 20 mL of DCM and used for further functionalization procedures.

4.2.2.2. Non-covalent functionalization of magnetite nanoparticles with cavitands

1) *Functionalization with the reference cavitand (**Mod**):*
A DCM solution of the reference cavitand (Mod) (2.6 mg/mL; 3.3 mM) was prepared and 7 mL of it were added dropwise to 3 mL of a DCM dispersion of Fe_3O_4 nanoparticles (10 mg/mL). The obtained suspension was sonicated at room temperature during 20 minutes for five times, being each sonication step spaced out by 1 hour rest. Nanoparticles were recovered via magnetic sedimentation and washed with DCM; finally the precipitate was dispersed in 10 mL of DCM (**Fe_3O_4-Mod**).

2) *Functionalization with the target cavitand (**Tiiii**):*
A solution of the target cavitand (Tiiii) (4.1 mg/mL; 3.3 mM) in tetrahydrofuran (THF) was prepared and 7 mL of it were added dropwise to 3mL of a DCM dispersion of Fe_3O_4 nanoparticles (10 mg/mL). The obtained suspension was sonicated at room temperature during 20 minutes for five times, being each sonication step spaced out by 1 hour rest. Nanoparticles were recovered via magnetic

sedimentation and washed with DCM; finally the precipitate was dispersed in 10 mL of THF (**Fe_3O_4-Tiiii**).

4.2.2.3. Covalent functionalization of magnetite nanoparticles with cavitands

1) Preparation of 3-aminopropyl/PEG-silane-derivatized magnetite nanoparticles

In a 10 mL microwave vial, 1.5 mL of an aqueous Fe_3O_4 nanoparticles (10 mg/mL) dispersion were placed, followed by the sequential addition of 1.8 mL of ultrapure water, 533 μL (1.25 mmol) of PEOS, 175 μL of APTMS (1 mmol) and 1 mL of an aqueous acetic acid solution (7 mM). The vial was rapidly sealed with a proper cap and the reaction was carried out at 75°C for 25 minutes in a laboratory microwave reactor (Anton Paar). The as-obtained solid was collected via magnetic sedimentation and thoroughly washed once with ultrapure water and twice with absolute ethanol. The precipitate was finally dispersed in 2 mL of dry DCM and stored under Ar atmosphere until the following step of functionalization (**Fe_3O_4-NH_2/PEG**).

2) Grafting of cavitands on Fe_3O_4-NH_2/PEG nanoparticles

In a three necks-round-bottom flask equipped with a rubber septum and a magnetic stirrer, 0.04 mmol of the proper cavitand (31.5 mg of Mod and 49 mg of Tiiii, respectively) were dissolved in 3 mL of dry DCM under Ar-flow and magnetic stirring; the solution was then cooled down to 0°C. Consecutively, 8.3 mg (0.04 mmol) of DCC were added very slowly followed by 2.5 mg (0.02 mmol) of DMAP. Finally, 2 mL of Fe_3O_4-NH_2/PEG nanoparticles dispersion were added dropwise through the rubber septum. The reaction was performed under inert atmosphere at room temperature for 6 days.

The solid was collected via magnetic sedimentation and thoroughly washed twice with DCM and once with absolute ethanol, and finally dispersed in 3 mL of ultrapure water. The obtained materials will be indicated as **Fe_3O_4-NH_2/PEG-Mod** and **Fe_3O_4-NH_2/PEG-Tiiii** from here on.

4.2.2.4. Molecular recognition tests on covalently-functionalized nanoparticles through the optical "dye-displacement" method

Prior to perform the molecular recognition tests, the nanoparticles were separated from the solvent by magnetic sedimentation and redispersed in 3 mL of chloroform.

A $1 \cdot 10^{-7}$ M solution of fluorescent pyridinium guest (**1**) in chloroform was prepared and a starting point spectrum was recorded. Subsequently, the solution was titrated adding increasing amount of the chloroform dispersion of Fe_3O_4-NH_2/PEG-Tiiii (nanoparticles estimated concentration= 1 mg/mL; added aliquots varied between 10 μL and 200 μL). After each addition, the solution was vigorously stirred and left to stabilize for one minute in order to achieve the complexation equilibrium.

Subsequently, a fluorescence spectrum was recorded (λ_{exc} = 350 nm). The aliquots were added until no more changes in the spectra were observed. This required the addition of 730 μL of Fe_3O_4-NH_2/PEG-Tiiii.

100 μL of ultrapure water were added to the obtained mixture in order to determine if the biphasic system can interfere with the fluorescence signal.

The biphasic solution was then titrated adding increasing amount of a water solution of ephedrine hydrochloride (**Eph**; $2.0 \cdot 10^{-3}$ M; added aliquots varied between 5 μL and 200 μL). After each addition the solution was vigorously stirred and left to stabilize for 3-5 minutes in order to achieve the complexation equilibrium. Subsequently, a fluorescence spectrum of the organic phase was recorded (λ_{exc} = 350 nm). The aliquots were added until no more changes in the spectra were observed. This required the addition of 860 μL of Eph.

The aforementioned procedure was repeated using magnetite nanoparticles functionalized with the reference cavitand (Fe_3O_4-NH_2/PEG-Mod). This experiment required the addition of 260 μL of a Fe_3O_4-NH_2/PEG-Mod chloroform dispersion (nanoparticles estimated concentration = 1mg/mL) for the first step (chloroform one-phase titration), and 920 μL of Eph for the second (biphasic) titration.

4.2.3. Characterization techniques

Fourier transform infrared (FTIR) spectroscopy analysis was performed in order to investigate the presence of an organic layer at the nanoparticles surface; for a complete comparison bare nanoparticles and pure ligands were also analyzed.

FTIR analysis of the covalently functionalized magnetite nanoparticles was performed on a Bruker Vertex70 and Thermo Scientific Nicolet iS5 spectrometers. Spectra were acquired both in ATR (attenuated total reflectance) and transmission mode (using the KBr pellets method) in the wavenumber range from 4000 to 400 cm^{-1}. All the spectra were acquired using a 4 cm^{-1} resolution and collecting 128 scans. Characterization of non-covalently functionalized magnetite nanoparticles was performed in transmission mode (using the KBr pellet method) on a Bruker Tensor 27 equipment in the wavenumber range from 4000 to 600 cm^{-1} (4 cm^{-1} resolution and 128 scans).

Baseline correction was applied to all the reported spectra.

Thermogravimetric analysis (TGA) was performed on the non-covalently functionalized nanoparticles in order to determine the amount of cavitand molecules adsorbed at particles surface.

Measurements were carried out in air using a heating rate of 20°C/min and in the temperature range between 30 and 900°C.

X-ray photoelectron spectroscopy (XPS) analysis was carried out on covalently functionalized nanoparticle in order to prove the presence of cavitand molecules at particles surface and to quantify the amount of grafted molecules. The analysis was performed only on Fe_3O_4-NH_2/PEG-Tiiii nanoparticles.

Measurements were carried out using a K-Alpha system of Vacuum Science, equipped with a monochromatic Mg-K_α source (1253.6 eV) and a hemispherical electron energy analyzer (PSP Vacuum Technology), and operating at pass energy of 50 eV for both survey and high resolution spectra.

Transmission electron microscopy (TEM) analysis was carried out in order to investigate the morphology and size distribution of magnetite nanoparticles at different stages of the covalent functionalization procedure. TEM analysis was carried out on a Philips CM200 (LaB_6) microscope operating at an acceleration voltage of 200 kV.

Samples were prepared by depositing few drops of aqueous dispersion of each sample on a 300 mesh carbon film-coated copper grids. The solvent was allowed to evaporate prior to the analysis.

Fluorescence spectroscopy analysis was used in order to evaluate the complexation efficiency of the functionalized nanoparticles with a fluorescent guest molecule. Analysis was performed on a Perkin Elmer Luminescence Spectrometer LS 55, operating at the excitation wavelength of 350 nm.

4.3. Results and discussion

Functionalization of magnetite nanoparticles with cavitand molecules was performed following two approaches, namely a non-covalent and a covalent procedure. The chosen cavitand molecules present one carboxyl group at the lower rim of the resorcina[4]arene-based cavity, which is expected to directly interact with nanoparticles likely through a carboxylate-surface iron atoms coordination. Such interaction is used in the non-covalent functionalization approach.

On the other hand, the carboxyl group is susceptible of reaction with amino functionalities leading to the formation of covalent amide bonds. Conjugation of the cavitand molecules through formation of amide bonds on amino-functionalized nanoparticles constitutes the basic concept of the covalent functionalization strategy.

Functionalization with two cavitand molecules will be investigated: one is a tetraphosphonate cavitand, which represents the target species for further molecular sensing applications. The four phosphoryl (P=O) bridging moieties at the upper rim are oriented inward ($_i$) the cavity ensuring the optimal conformation for highly selective recognition and high binding stability of N-methyl ammonium ions. On the contrary, the other molecule differs for the lack of phosphonate groups; therefore it doesn't exhibit selective molecular recognition properties towards the same species. It usually represents the reference compound for control experiments in host-guest chemistry studies. Molecular structures for the investigated cavitands are reported in figure 4.2.

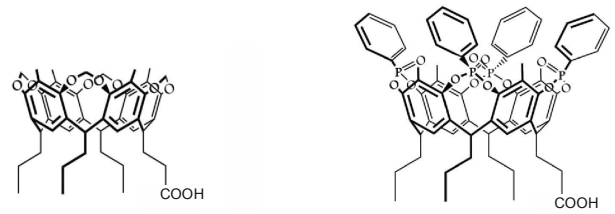

***Mod**-cavitand* ***Tiiii**-cavitand*

Figure 4.2: Molecular structures for reference "Mod" cavitand (left) and tetraphosphonate "Tiiii" cavitand (right).

For sake of simplicity, the reference and tetraphosphonate cavitands will be referred to as, respectively, "Mod" and "Tiiii" from here on.

4.3.1. Non-covalent approach

The non-covalent functionalization procedure consisted in a simple post-synthesis modification strategy. A dispersion of preformed nanoparticles was added dropwise to a cavitand solution; the obtained mixture was then sonicated in order to favour adsorption of the cavitand and concurrently limit particles aggregation.

Upon coating procedure, nanoparticles surface chemical composition was investigated by Fourier transform infrared (FTIR) spectroscopy. Figure 4.3 shows the FTIR spectrum of Fe_3O_4-Mod nanoparticles; for sake of comparison, pristine magnetite particles and pure model cavitand spectra are also shown.

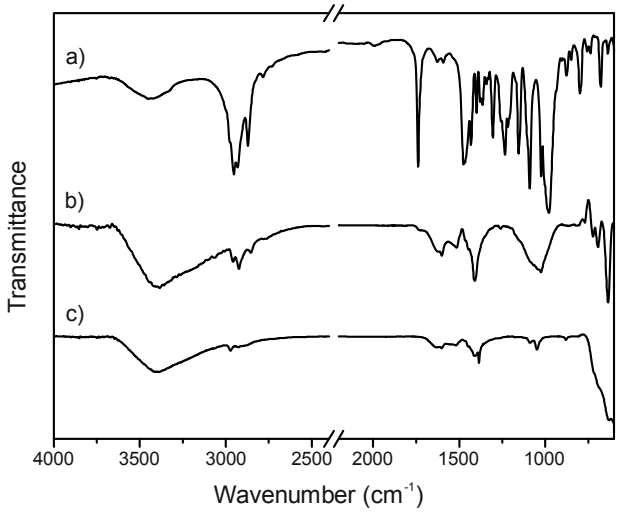

Figure 4.3: FTIR spectra of pure reference (Mod) cavitand (a), Fe_3O_4-Mod nanoparticles (b), and pristine Fe_3O_4 nanoparticles (c). For sake of clarity, spectra are represented stacked by an offset value and the signal due to atmospheric CO_2 was omitted by introducing a break in the 2400-2200 cm^{-1} spectral region.

Pristine Fe_3O_4 nanoparticles (figure 4.3c) spectrum presents a broad band centred at 3400 cm^{-1} associated to the stretching of O-H bonds of surface hydroxyl groups and adsorbed water. Few low-

intensity absorptions at 2920 and 2856 cm^{-1}, ascribed to aliphatic C-H bond stretching vibrations and at 1634 and 1420 cm^{-1}, characteristic of oxygen-containing functional groups, might originate from side-products formed during the nanoparticles synthesis. However, in view of the low intensity, it may be suggested that such organic species are present in low amount.

Fe_3O_4-Mod nanoparticles (figure 4.3b) show intense peaks at 2956, 2923, and 2853 cm^{-1}, which are assigned to the aliphatic C-H stretching vibrations of methyl groups and C-H asymmetric and symmetric stretching mode of methylene moieties, respectively. The position of these peaks is comparable to the stretching modes of propyl chains found at the lower rim of the molecular cavity of Mod. Therefore, they are indicative of the presence of the cavitand at particles surface. Further information supporting adsorption of Mod molecules is provided by the band at 1595 cm^{-1}, which might be assigned to the aromatic skeletal (C=C/C-C) stretching vibrations of the phenyl rings constituting the cavity. The absence of the 1733 cm^{-1} C=O stretching mode of carboxyl groups in pure Mod-molecules and the appearance of a peak at 1513 cm^{-1} in the spectrum of functionalized nanoparticles suggest that the cavitand likely adsorbed on particles surface through the carboxyl functionalities in the carboxylate form. In particular, the 1513 cm^{-1} peak might be assigned to the carboxylate asymmetric stretching mode. However, the correlated symmetric stretching band can not be undoubtedly identified because it overlaps the aromatic skeletal stretching modes in the region around 1400 cm^{-1}. For these reason, it is not possible to unequivocally determine the Fe-carboxylate coordination mode.

As expected, Fe_3O_4-Tiiii nanoparticles (figure 4.4b) show several similarities with the analogous Fe_3O_4-Mod nanoparticles. The cavitand molecules indeed differ only for the bridging groups at the wider cavity rim.

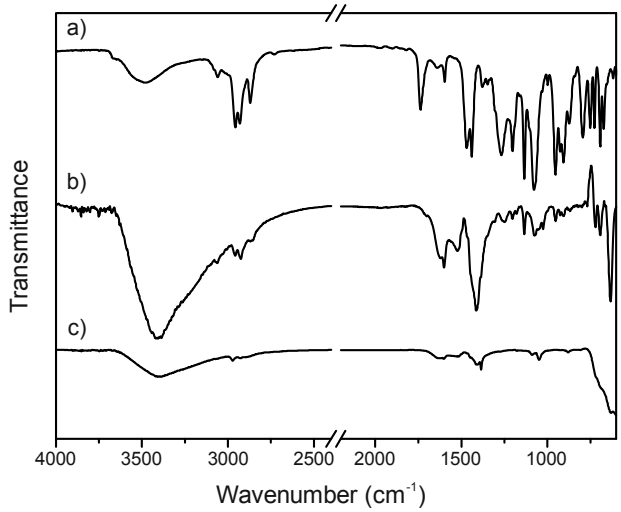

Figure 4.4: FTIR spectra of pure target (Tiiii) cavitand (a), Fe_3O_4-Tiiii nanoparticles (b), and pristine Fe_3O_4 nanoparticles (c). For sake of clarity, spectra are represented stacked by an offset value and the signal due to atmospheric CO_2 was omitted by introducing a break in the 2400-2200 cm^{-1} spectral region.

Sharp peaks at 2957, 2924, and 2854 cm^{-1}, are assigned to the aliphatic C-H stretching vibrations assigned to methyl and methylene groups of the alkyl chains featuring the Tiiii-cavity lower rim. The

band centred at 1596 cm^{-1} is ascribed to aromatic skeletal (C=C/C-C) stretching modes of the resorcin[4]arenes-based cavity. Similarly to Fe_3O_4-Mod, these peaks are regarded as representative of the adsorption of Tiiii-molecules at particles surface.

Furthermore, the absence of the 1737 cm^{-1} band ascribed to carboxyl C=O stretching modes of pure Tiiii and the appearance of a band at 1522 cm^{-1} suggest that Tiiii-cavitand adsorbed at particles surface through the carboxyl functionality, likely in a iron-carboxylate coordination. Also in this case, the carboxylate-iron coordination mode (monodentate or bidentate) can not be unequivocally assigned because of the partial overlap with the aromatic skeletal vibration modes in the 1400 cm^{-1} region. Characteristic P-O and P=O vibration modes fall in the 1300-1000 cm^{-1} spectral region. As observed, the absorption profile in this region changed upon functionalization procedure. In view of the cavitand steric hindrance, the observed changes might arise from interactions between neighbouring cavitand molecules at particles surface. The possibility that the observed spectral changes could derive from a direct interaction of the phosphoryl oxygen atoms with nanoparticles surface can be considered as unlikely. In fact, the phenyl substituents on the P centre and the consequent steric hindrance of phosphoryl groups could prevent the direct interaction with iron oxide nanoparticles. This observation is important for the following employment of Fe_3O_4-Tiiii nanoparticles as molecular sensors. Indeed, the specific recognition of target functionalities (N-methyl ammonium groups) is accomplished by the P=O bridging groups at the cavity upper rim (figure 4.5).

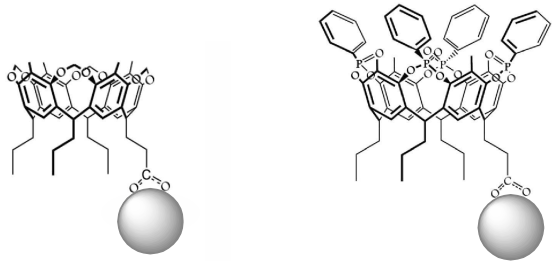

Figure 4.5: Schematic representation of the suggested adsorption of Mod (left) and Tiiii (right) on iron oxide nanoparticles (grey sphere) surface; the upper rim of the cavity is exposed in the surrounding medium.

Coating extent for each material was determined by thermogravimetric analysis (TGA) that revealed a total 4.3 % of mass loss associated to the oxidative decomposition of the adsorbed cavitand for Fe_3O_4-Mod nanoparticles (figure 4.6a). This value corresponds to 117 molecules of model cavitand per magnetite nanoparticle, equal to the 42% of the theoretical value for a cavitand monolayer. The theoretical value for a cavitand monolayer was calculated for particles of 11 nm in diameter and assuming the target molecule to adsorb "orthogonal" to the particles surface, with a foot-area of 1.4 nm^2 [27].

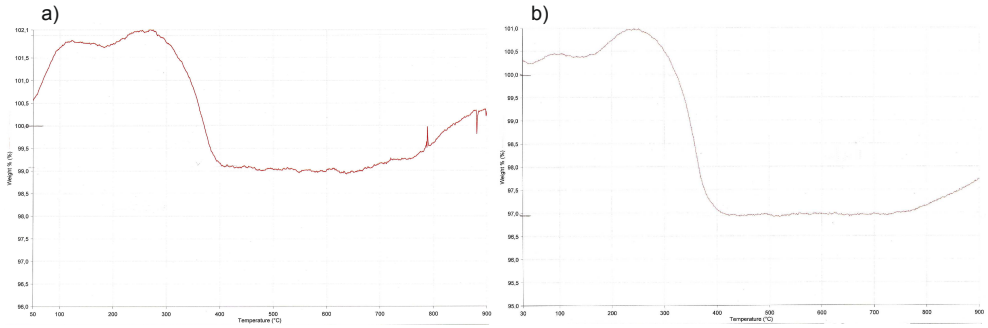

Figure 4.6: TGA curves of Fe_3O_4-Mod (a) and Fe_3O_4-Tiiii (b) treated in air at the heating rate of 20°C/min.

TGA of Fe_3O_4-Tiiii nanoparticles (figure 4.6b) revealed a 6.3 % of mass loss, corresponding to 107 molecules per nanoparticles and equal to the 39% of the theoretical coating extent. A slightly lower coverage extent in the case of Fe_3O_4-Tiiii nanoparticles is likely due to the higher steric hindrance associated to the functionalities at the cavity upper rim.

The described results demonstrated that post-synthesis non-covalent functionalization approach was successful in introducing complex molecules characterized by a large steric hindrance at nanoparticles surface. The molecules interacted through their carboxyl groups situated at the lower rim, thus exposing the cavity upper rim on particles surface. This is a fundamental requisite for further performing molecular recognition.

Regardless the adsorbed cavitand, as-functionalized particles showed good dispersibility in chloroform and tetrahydrofuran. In view of the hydrophobic character of the cavitand molecules, nanoparticles could not be redispersed in aqueous media.

4.3.2. Covalent approach

Although the described non-covalent functionalization approach represents a very simple and rapid strategy, it suffers some drawbacks. Desorption of the surface organic layer might occur in real working conditions. It should be taken into consideration that the purpose of the functionalization described in this chapter is to fabricate nanoparticles suitable as recoverable and recyclable molecular sensors. This implies the formation of a host-guest complex between the surface cavitand layer and the target guest molecules present in the working medium. The magnetic properties of iron oxide nanoparticles will allow collecting the magnetic system and consequently the guest molecules forming the complex at the surface. At the same time, reversibility of the host-guest complex will be exploited for the displacement and quantification of the guest molecules. However, desorption of the surface cavitand concurrently to the host-guest complex dissociation might occur. This issue could be addressed by covalently grafting the cavitand molecules at nanoparticles surface. The carboxyl functionality at the lower rim of the cavitands is particularly susceptible of nucleophilic attack from

amino groups, leading to stable amide linkages. Amino groups can be easily introduced at particles surface through silanization reaction using (3-aminopropyl)trimethoxy silane as coupling agent.

Another drawback is represented by the hydrophobic nature of the investigated cavitand molecules. However, application of the magnetic supramolecular sensor in biological fluids (e. g. urine) requires a hydrophilic system in order to ensure good dispersibility in the working medium, thus higher recognition efficiency. Colloidal stability in aqueous media could be obtained via a mixed coating layer at the particles surface. In other terms, simultaneous adsorption of cavitand and a second molecule that could expose a hydrophilic functionality in the surrounding medium should enable a better colloidal stability to the nanoparticles without affecting the molecular recognition properties of the cavitand. While mixed surface coating can be regarded as poorly controllable adopting non-covalent approaches, covalent strategies may be regarded as likely more reliable. Grafting of mixed organosilane layers was already described in the literature and it represents a valid approach to provide aqueous dispersibility[24,28]. Organosilane precursors bearing a short polyethylene glycol (PEG) chain are often used for this purpose[29]. A covalent mixed functionalization might allow the control over surface chemical composition in terms of amino-to-PEG ratio, and consequently on the cavitand conjugation extent.

Organo alkoxysilanes bearing amino groups and short PEG chains ((3-aminopropyl)trimethoxy silane (APTMS) and 2-[methoxy(polyethylenoxy)propyl]trimethoxysilane (PEOS), respectively) were simultaneously added to an aqueous dispersion of iron oxide nanoparticles in the PEOS-to-APTMS molar ratio of 1.25:1. On the bases of previous experiments, a small excess of PEOS on APTMS was chosen in order to confer water dispersibility. The condensation reaction of the organosilane precursors on particles surface hydroxyl groups was performed in a laboratory microwave[30,31].

In a second step, conjugation of the desired cavitand molecule was performed by carbodiimide-based chemistry, which is a strategy widely reported in the literature for conjugating biomolecules on solid substrates, such as iron oxide nanoparticles and quantum dots.

The reaction involves a first step of activation of the cavitand carboxyl moieties using N,N'-dicyclohexylcarbodiimide (DCC). The resulting highly reactive intermediate (*O*-acylisourea) easily undergoes nucleophilic attack from the nanoparticles surface amino groups. The reaction leads to the formation of a stable amide bond between the cavitand carboxyl moieties and the particles surface amino groups (figure 4.7).

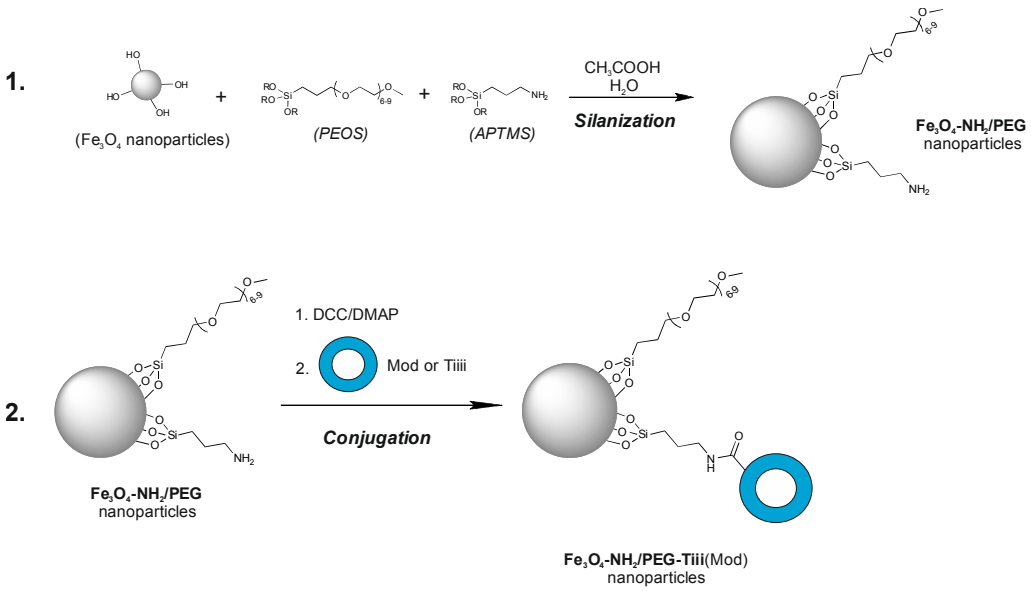

Figure 4.7: Schematic representation of the covalent functionalization strategy and the expected nanoparticles surface chemical structure.

Qualitative investigation about the surface chemical composition of functionalized nanoparticles was performed by FTIR spectroscopy.

FTIR spectrum of pristine magnetite nanoparticles (figure 4.8 b) presents only few absorption peaks. The band peaking at 586 and 632 cm^{-1} is assigned to the Fe-O stretching vibration modes of nanosized iron oxide particles, while the broad band centred at about 3400 cm^{-1} is ascribed to O-H stretching modes of particles surface hydroxyl groups and adsorbed water.

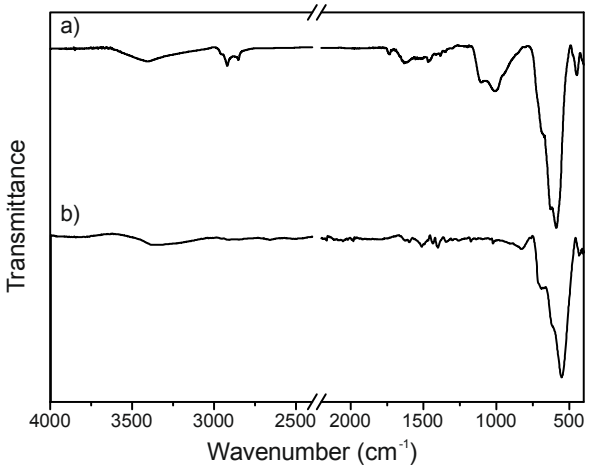

Figure 4.8: FTIR spectra of Fe_3O_4-NH_2/PEG nanoparticles (a) and pristine Fe_3O_4 nanoparticles (b). For sake of clarity, spectra are represented stacked by an offset value and the signal due to atmospheric CO_2 was omitted by introducing a break in the 2400-2200 cm^{-1} spectral region.

Upon silanization reaction, the spectral region comprised between 1700 and 800 cm^{-1} remarkably changed (figure 4.8a). The broad band centred at 1010 cm^{-1} is generally regarded as representative of grafted organosilane layers and it originates from the Si-O-Si bonds stretching modes[32].

The broadness of the band is likely due to the overlapping of multiple vibration modes, particularly of silanol groups (Si-OH) stretching modes (940 cm^{-1})[32]. The contribution that emerged at 1095 cm^{-1} might be ascribed to the overlap of C-N stretching mode in γ-aminopropyl chains and C-O-C stretching vibrations of PEG chains. Similarly, the broad band comprised between 1550 and 1200 cm^{-1} originated from the overlap of several vibration modes ascribable to γ-aminopropyl and PEG chains, such as aliphatic C-H bending and C-O-C asymmetric stretching modes[23]. A rather broad contribution at 1630 cm^{-1} could be ascribed to bending vibrations of primary amino groups. Finally, C-H stretching modes of methylene functionalities at 2903 (asymmetric) and 2861 (symmetric) cm^{-1} provide further evidence of the surface organosilane layer. The shift toward shorter wavenumbers with respect to theoretical position expected for methylene groups[33] might originate from the overlap of -CH_2- vibration modes within the PEG chains.

Upon conjugation reaction of Mod molecules some changes in the 1650-1400 cm^{-1} spectral region are observed (figure 4.9b).

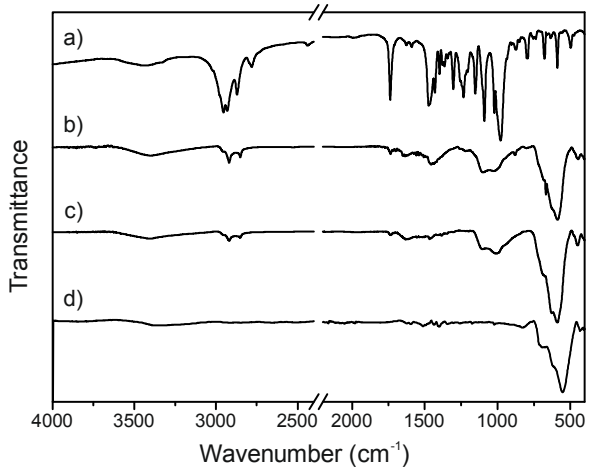

Figure 4.9: FTIR spectra of pure Mod cavitand (a), Fe_3O_4-NH_2/PEG-Mod nanoparticles (b), Fe_3O_4-NH_2/PEG nanoparticles (c), and pristine Fe_3O_4 nanoparticles (d). For sake of clarity, spectra are represented stacked by an offset value and the signal due to atmospheric CO_2 was omitted by introducing a break in the 2400-2200 cm^{-1} spectral region.

In particular, the broad contributions at 1630 and 1465 cm^{-1} shifted towards 1645 and 1450 cm^{-1}, respectively. Those changes might be associated to the introduction of cavitand molecules at particles surface. The broad band centred at 1645 cm^{-1} might arise from the formation of an amide bond between particles surface amino groups and the reference (Mod) cavitand molecules. Particularly, it could be ascribed to the C=O stretching mode of the amide linkage. The shift of the other contribution to 1450 cm^{-1} could originate from the aromatic C=C/C-C stretching vibrations of the resorcin[4]arene scaffold. Moreover, conjugation of cavitand molecules will likely occur with an increase of steric hindrance in the surface organic layer. This might induce a rearrangement of the PEG and γ-aminopropyl chains and a consequent change of the spectra profile. Further indication of the occurrence of cavitand conjugation is brought by the peak emerging at 880 cm^{-1}, which can be assigned to the out-of-plane bending of aromatic C-H bonds. Finally, sharpening of the band at 2920

and 2850 cm^{-1} could be ascribed to the additional C-H stretching vibrations of methylene groups of the propyl chains and methylene bridging groups of Mod-cavitand.

Conjugation of the tetraphosphonate cavitand on Fe_3O_4-NH_2/PEG nanoparticles partially caused similar spectral changes, although they look less pronounced than in the previous system (figure 4.10b).

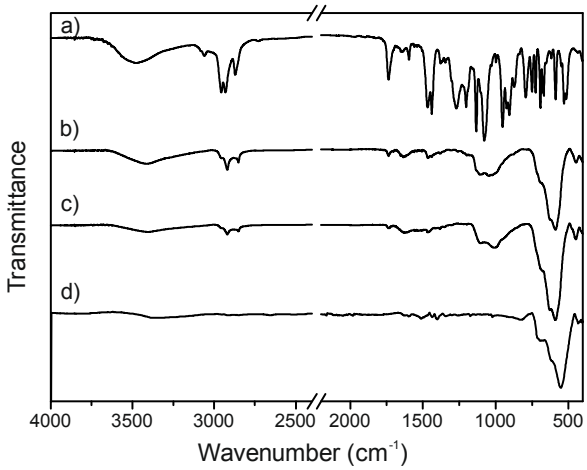

Figure 4.10: FTIR spectra of pure Tiiii cavitand (a), Fe_3O_4-NH_2/PEG-Tiiii nanoparticles (b), Fe_3O_4-NH_2/PEG nanoparticles (c), and pristine Fe_3O_4 nanoparticles (d). For sake of clarity, spectra are represented stacked by an offset value and the signal due to atmospheric CO_2 was omitted by introducing a break in the 2400-2200 cm^{-1} spectral region.

Sharpening of the 2920 and 2850 cm^{-1} band due to methylene C-H stretching vibrations could be ascribed to the contribution of propyl chains and methylene bridging groups of Tiiii. Further hint on conjugation occurrence is brought by the change in shape of the contribution at 1465 cm^{-1}. The band becomes slightly more defined and this could be ascribed to the overlap of the aromatic skeletal C=C/C-C stretching vibrations from the resorcin[4]arene scaffold and the phenyl substituents on the phosphoryl moieties. Moreover, broadening of the typical band of grafted organosilanes could arise from the overlap with phosphonate vibration modes.

In both of the cases, spectral changes are indicative of the presence of cavitand species at nanoparticles surface. However, the less pronounced absorption bands could infer that a rather restrained number of cavitand molecules was grafted. In order to support infrared studies, deeper investigation by X-ray photoelectron spectroscopy (XPS) was performed. Particularly, XPS was carried out on the most relevant system, namely Fe_3O_4-NH_2/PEG-Tiiii nanoparticles.

The measurement of XPS survey spectrum of the system allowed identifying the nanoparticles surface chemical composition. The analysis revealed that iron, carbon and oxygen are the most prominent elements. Presence of silicon, nitrogen and phosphorus was also detected, and it is representative of the mixed organosilanes layer and of the tetraphosphonate cavitand, respectively. The C 1*s*, O 1*s*, Fe 2*p*, and P 2*p* core level spectra are represented in figure 4.11.

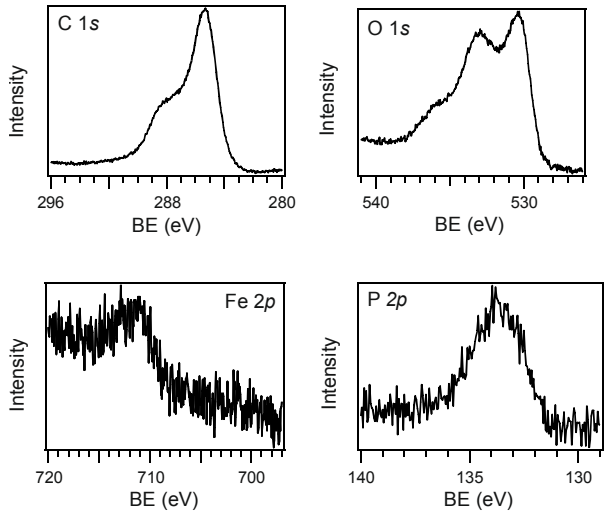

Figure 4.11: High resolution photoelectron spectra of C 1*s*, O 1*s*, Fe 2*p*, and P 2*p* core levels of Fe_3O_4-NH_2/PEG-Tiiii nanoparticles.

The analysis of the C 1*s* core level spectrum revealed that the band is formed by two main contributions, at 285 and 287 eV, respectively. The more prominent contribution at 285 eV can be assigned to aliphatic carbon atoms, while aromatic and oxygen-bonded carbon atoms can be associated to the second and less intense contribution (287 eV). The O 1*s* core level spectrum presents several contributions. The more prominent signal is located at 531 eV and it is possibly originated from the overlap of few contributions. In fact, both amide C=O bonds and Si-O bonds in organosilanes give rise to signals at 531 eV[34,35]. Particularly, both signals are consistent with the expected chemical functionalization at nanoparticles surface, thus supporting the formation of an organosilane layer and the conjugation of Tiiii through an amide bond. Oxygen bound to iron in magnetite nanoparticles is expected to give a signal at 530 eV[34], but it can not be unambiguously assigned because of the overlap with the aforementioned contributions. The further contributions at 533 and 536 eV are likely associated to the oxygen atoms of the PEG chains and cavitand molecules[36]. In particular, oxygen in single C-O bonds (e.g. ethers) is regarded as mainly responsible of the 533 eV component, which is therefore associated to PEG chains[34].

Diagnostic of the presence of Tiiii-cavitand is the P 2*p* band at 134 eV, which is assigned to the phosphoryl bridges of the target cavitand Tiiii[36]. This analysis, demonstrated the effectiveness of the coupling reaction at introducing the target cavitand at particles surface.

However, XPS quantitative compositional analysis revealed that only a very low amount of Tiiii cavitand was grafted at particles surface (table 4.1).

Table 4.1: XPS compositional analysis; results are expressed as atomic percentage.

C (at. %)	O (at. %)	Fe (at. %)	P (at. %)	N (at. %)
71.5	24.5	1.9	1.3	0.8

As previously mentioned, the complex nanoparticles surface chemical composition and the steric hindrance associated to both cavitand molecules and grafted organosilane layer are regarded as the

main reason of the rather low amount of grafted Tiiii. Additionally, the amount of amino groups at particles surface and the mechanism of the coupling reaction significantly affect the number of cavitands grafted at particles surface. Although it was not possible to quantitatively assess the amount of surface amino groups, in the best scenario one should assume to have a PEG-to-NH_2 surface groups molar ratio of 1.25:1 (PEOS and APTMS were used in a 1.25:1 molar ratio). Therefore, only the 44% of the nanoparticles surface groups could participate in the conjugation reaction. Moreover, carbodiimide-based coupling processes usually suffer side-reactions such as coupling of two carboxyl groups to form the corresponding anhydride or formation of N-acylurea from rearrangement of the *O*-acylisourea active intermediate. Therefore, reaction yields might be restrained, especially for systems as complex as nanoparticles. Indeed, similar chemistry-based approaches usually report about the coupling of 10-20 molecules per nanoparticles[37].

Transmission electron microscopy (TEM) analysis was performed at each step of the functionalization process (figure 4.12).

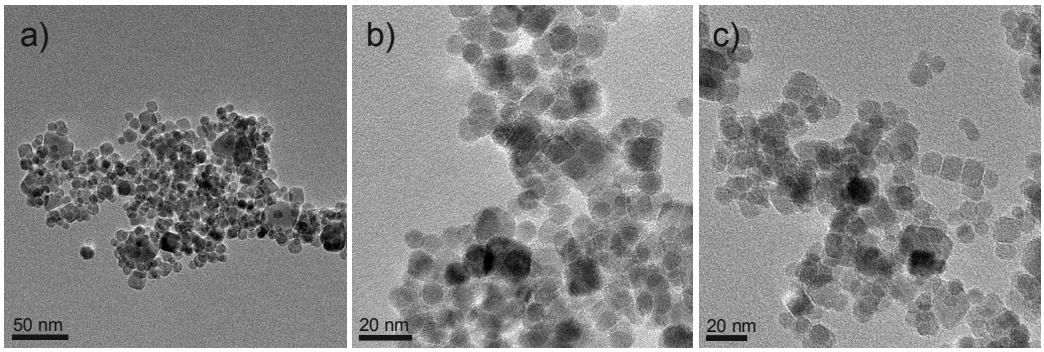

Figure 4.12: TEM images of pristine Fe_3O_4 (a), Fe_3O_4-NH_2/PEG (b) and Fe_3O_4-NH_2/PEG-Tiiii (c) nanoparticles. All the TEM images refer to nanoparticles aqueous dispersions.

TEM analysis showed that the functionalization process, particularly the microwave-assisted silanization procedure (Cf. experimental section), did not lead to any remarkable alteration of particles morphology. No significant change in size distribution (nanoparticles diameter varying from 8 and 15 nm; average size of 11 nm) was observed throughout the entire functionalization procedure. Moreover, TEM images revealed that particles tend to partially agglomerate, suggesting that the coating procedure is not highly efficient in stabilizing nanoparticles in the aqueous medium.

As previously mentioned, aqueous dispersibility of the functionalized nanoparticles is required for biological applications. Mixed organosilane-functionalized nanoparticles (Fe_3O_4-NH_2/PEG) presented only partial stability in aqueous medium (pH 6). Assuming that the dissociation constant of nanoparticles surface amino groups does not differ significantly from the one of propylamine (pKa of the conjugated acid equal to 10.9), it is expected for nanoparticles to bear positively charged surface groups at the dispersion conditions (pH 6), that should promote stability through electrostatic repulsion. However, it should be taken into account that the stability of a dispersion of nanoparticles presenting a heterogeneous organic shell likely arises from a combination of electrostatic repulsion and steric effects. Moreover, the balance between those effects is regulated by the overall

nanoparticles surface chemical composition. Therefore, possible reasons of the partial stability can be found in: (i) a rather short PEG chain length (6-9 monomeric units); (ii) mixed surface chemical composition responsible to provide insufficient either steric or electrostatic stabilization, (iii) likely not entirely coated particles surface. Determination of the nanoparticles surface charge could be carried out by Z-potential measurements; nevertheless, due the partial aqueous stability, the samples are not suitable for such analysis.

Furthermore, conjugation of cavitand species, both for Mod and Tiiii, induced a significant decrease of the stability in aqueous medium compared to the organosilane-functionalized nanoparticles. While organosilane-functionalized nanoparticles partially sediment within few days, cavitand-functionalized nanoparticles deposit at the bottom within few hours.

Therefore, it could be inferred that the PEG chains anchored at particles surface are not sufficient to contrast the hydrophobicity introduced with the grafted cavitand. However, further increase of the theoretical PEOS-to-APTMS molar ratio could only lead to even more hindered conjugation reaction and a more restrained cavitand grafting extent.

4.3.3. Molecular recognition

The activity of the cavitand-functionalized nanoparticles in molecular recognition was tested through an optical method. The tests were carried out on covalently-functionalized magnetite nanoparticles because they are regarded as the most suitable system for the target application. Recognition efficiency of tetraphosphonate cavitands is often investigated by the fluorescence "dye-displacement" test[10,18,19]. The method consists in a first step of complexation of the target cavitand molecule with a fluorescent compound. Largely employed is the guest **1** illustrated in figure 4.13, which bears an N-methylpyridinium unit connected with a pyrene moiety through diester tether. In view of the outstanding recognition properties of tetraphosphonate cavitands for N-methyl residues, the guest is expected to interact with the cavitand molecular cavity. The pyrene moiety connected to the N-methylpyridinium residue represents the fluorescent unit. Such molecule was chosen because of the high emission efficiency of the pyrene moiety, and in particular because of the possibility to give rise to an electron transfer process with the pyridinium moiety. It was demonstrated that the electron-transfer process between the two residues is responsible for partial fluorescence quenching in the isolated compound. Nevertheless, inclusion of the pyridinium moiety in the cavity causes a decrease of the efficiency of the electron-transfer process and a consequent increase of the pyrene fluorescence (figure 4.13i). It was studied that interaction of electron-poor pyridinium group with the electron-rich cavity renders the electron transfer process more energy demanding and thus less prone to occur[18,19]. The consequent increase in pyrene fluorescence intensity is remarkable, being usually reported as a six-fold increase, thus easily detected even in very low guest concentrations[18]. The second step of the fluorescence-based investigation consists in displacing the fluorescent guest from the molecular cavity

by adding a competitive guest to the pre-complexed nanoparticles. For this reason the method is usually referred to as "dye-displacement". The replacement of the fluorescent guest by a non-fluorescent molecule causes the restoration of the electron-transfer process; consequently, a remarkable decrease of the fluorescence intensity is expected (figure 4.13ii). In view of the interest of creating a chemical sensor for detecting and quantifying biomarkers and illicit drugs in biological fluids, ephedrine (particularly ephedrine hydrochloride) was chosen as competitor guest. Ephedrine is often illegally assumed as stimulant by athletes and it is used as a precursor for illicit methamphetamine drugs[38].

In view of the lack of affinity of the reference cavitand with N-methyl ammonium residues, complexation neither of the fluorescent guest nor of ephedrine molecule is expected to occur; consequently no variation in fluorescence intensity should be observed.

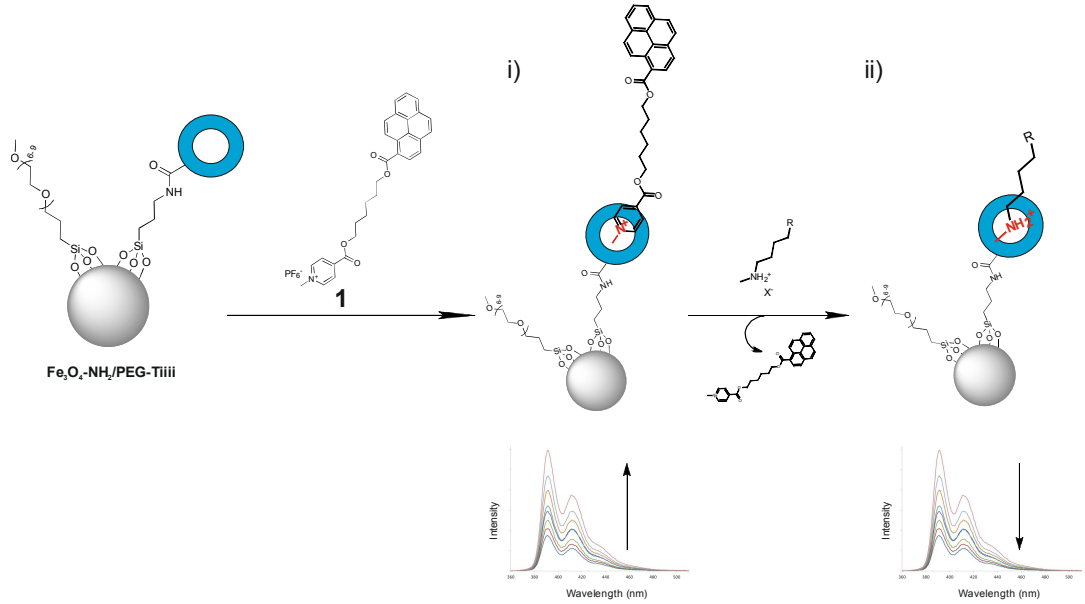

Figure 4.13: Schematic representation of the recognition-displacement mechanism at the base of the analytical test. The first step of the test consists in the complexation of nanoparticles with the fluorescent guest **1**; increase of the fluorescence intensity is expected (i). In the following step (ii) addition of a competitive guest is expected to displace **1** from the nanoparticles-**1** complex and a decrease of the fluorescence intensity is expected.

Experimentally, the "dye-displacement" method was carried out as follow: a solution of fluorescent pyridinium guest was titrated with an increasing amount of a chloroform dispersion of Fe_3O_4-NH_2/PEG-cavitand; fluorescence variations were monitored at every addition step and titration was stopped only when no further changes in fluorescence intensity were observed. Constant fluorescence intensity is indicative of the complete complexation between the cavitand and the guest **1** species.

The experimental observation provided results in contradiction to what expected. For the system Fe_3O_4-NH_2/PEG-Tiiii a complete quenching of the fluorescence was observed, while increase, or possibly no variation, was expected (figure 4.14).

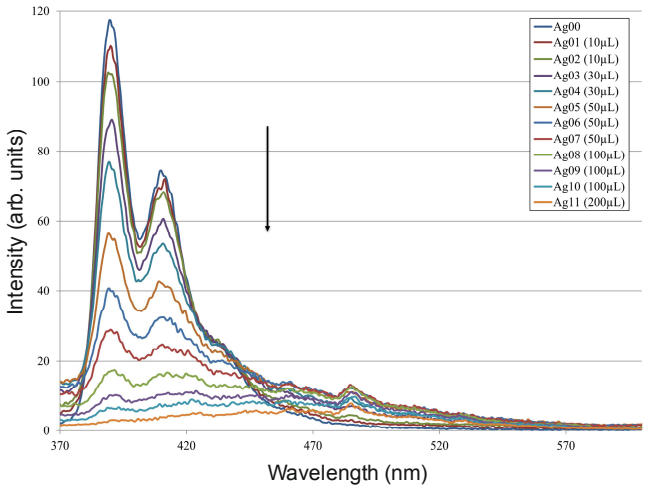

Figure 4.14: Fluorescence spectra (λ_{exc} = 350 nm) of a chloroform solution of guest **1** (blue line, "Ag00") and upon addition of an increasing amount of the Fe_3O_4-NH_2/PEG-Tiiii nanoparticles.

Although the results of the pre-complexation step did not meet expectations, the second step of the recognition test was performed. An aqueous ephedrine hydrochloride solution was gradually added to the chloroform mixture in order to promote guest displacement. In these terms, ephedrine (2 mM in the aqueous solution) was added in a large excess with respect to guest **1** (0.1 µM, in the organic phase). Addition of ephedrine causes the formation of a biphasic system: the fluorescent guest is insoluble in water, thus it is expected for the displaced molecules of **1** to remain in the organic phase. For this reason, fluorescence of the organic phase is monitored.

A gradual phase-transfer of nanoparticles was observed during the addition of ephedrine solution. The transfer of particles in aqueous medium was accompanied by a gradual restoration of the fluorescence of the organic phase. The observed trend for fluorescence intensity variations measured during the "dye-displacement" test is depicted in figure 4.15.

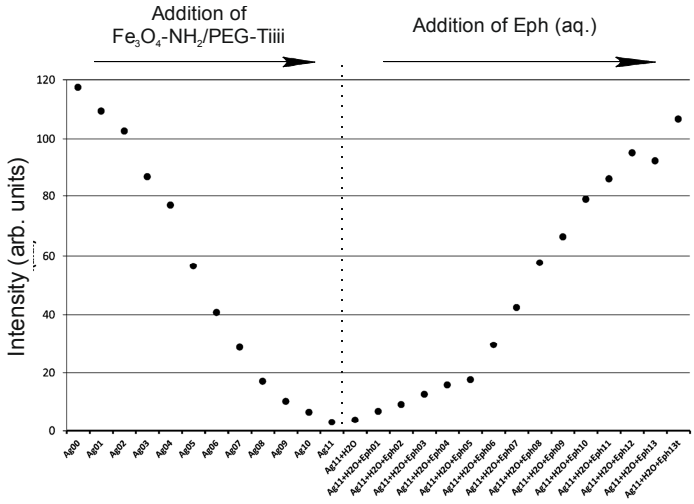

Figure 4.15: Fluorescence intensity (λ_{exc} = 350 nm; λ_{em} = 390 nm) of a chloroform solution of **1** ($1.2 \cdot 10^{-6}$ M) upon a subsequent addition of Fe_3O_4-NH_2/PEG-Tiiii nanoparticles ("Ag00-Ag11"), water ("Ag11+H_2O") and an increasing amount of aqueous solution of Eph ($2.0 \cdot 10^{-3}$ M; "Ag11+H_2O+Eph01-Ag11+H_2O+Eph13").

These results suggest that the decrement observed for the fluorescence intensity during the titration of **1** with the nanoparticles might be due to the interference of nanoparticles. Indeed, investigation of the optical properties of uncoated magnetite nanoparticles (figure 4.16) reveals not negligible scattering effect, which likely causes the observed fluorescence decrease.

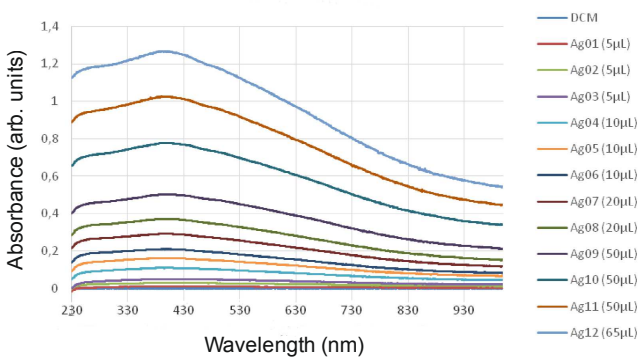

Figure 4.16: UV-Visible spectra of uncoated magnetite nanoparticles DCM dispersion measured at increasing Fe_3O_4 concentration.

Diverse factors may be responsible of the observed phase-transfer of nanoparticles when adding ephedrine. Surface PEG chains confer partial water dispersibility to the investigated nanoparticles, which consequently might be transferred to the aqueous phase with progressive addition of ephedrine aqueous solution. Moreover, ephedrine hydrochloride is expected to interact with the cavitand *via* inclusion of the N-methyl-ammonium residue in the Tiiii cavity, by replacing guest **1**. The resulting complex might exhibit partial water dispersibility, hence contributing to promote the observed phase-transfer phenomenon.

As a control experiment, titration was repeated using the Fe_3O_4-NH_2/PEG-Mod nanoparticles. The results followed the same trend observed for the nanoparticles functionalized with the target cavitand Tiiii: fluorescence was progressively quenched when adding the nanoparticles. Furthermore, nanoparticles phase-transfer was observed also in this case. Similarly to the system described above, restoration of the initial fluorescence of the organic phase was observed upon complete transfer of nanoparticles in the aqueous phase (figure 4.17).

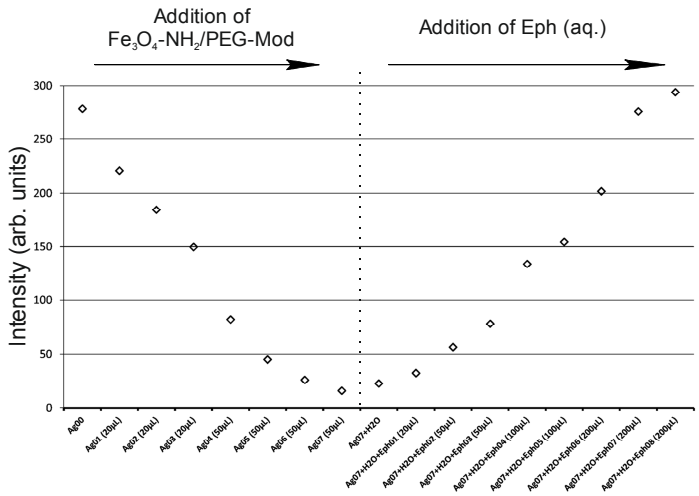

Figure 4.17: Fluorescence intensity (λ_{exc} = 350 nm; λ_{em} = 390 nm) of a chloroform solution of **1** ($1.2 \cdot 10^{-6}$ M) upon a subsequent addition of Fe_3O_4-NH_2/PEG-Mod nanoparticles ("Ag00-Ag07"), water ("Ag07+H_2O") and an increasing amount of aqueous solution of Eph ($2.0 \cdot 10^{-3}$ M; "Ag07+H_2O+Eph01-Ag07+H_2O+Eph08").

Similarly to what suggested for the Fe_3O_4-NH_2/PEG-Tiiii system, fluorescence quenching is likely due to absorption of iron oxide nanoparticles in the investigated spectral region. Despite the presence of surface PEG chains might promote the observed nanoparticles phase-transfer, other mechanisms could be hypothesized to explain this phenomenon. Direct interaction of ephedrine species on nanoparticles surface should be taken into consideration. Hydrogen bonding with surface PEG and free amino groups or direct ephedrine-iron oxide interactions could have taken place.

Although these results did not rule out the activity of Fe_3O_4-NH_2/PEG-Tiiii nanoparticles as molecular sensors, they showed that the largely employed fluorescence "dye-displacement" test was not suitable for studying the properties of this system. It is suggested that direct complexation of the as-functionalized nanoparticles with the target guest should be carried out. Magnetic separation could be exploited for removing the complexed target guest species from their original environment. Subsequent dissociation of the reversible host-guest complex by using competitive guest compounds (e.g. simple salts like NaCl or K_2CO_3) will allow the isolation of the interested species for further characterization. Moreover, the potential recyclability of the system might allow the repetition of the complexation procedure several times in order to completely remove the target guest from its original environment. This should enable quantification of the isolated species. Finally, identification and quantification of the isolated guest could be performed by standard analytical methods, such as chromatography (e.g. HPLC).

4.4. Conclusions

The work described in this chapter showed two approaches for post-synthesis functionalization of iron oxide nanoparticles. It was demonstrated that both non-covalent and covalent approaches were successful in introducing at particles surface the desired functional molecules, namely cavitands. The

aim of the functionalization is to create a system which could act as recoverable and recyclable molecular receptor for detecting and quantifying drugs or biomarkers in biological fluids.

Both the functionalization strategies exploited terminal carboxyl groups at the lower rim of the molecular cavities to introduce the cavitands at particles surface.

Iron-carboxylate coordination enabled adsorption of cavitands at nanoparticles surface through non-covalent procedure, as demonstrated by FTIR spectroscopy. Amide bonds were likely formed during the covalent functionalization strategy, which consisted in conjugation of the target molecules on previously amino-functionalized iron oxide nanoparticles.

The chapter described both advantages and disadvantages of the two approaches. Non-covalent functionalization is a rather simple and rapid approach. It was demonstrated that although the target molecules presented a large steric hindrance that could limit the coating extent, this simple strategy allowed coating the surface for less than half of a theoretical monolayer. Moreover, FTIR spectroscopy suggested that the molecules adsorbed only through the carboxyl groups, exposing to the surrounding media the upper rim of the cavity. This last observation was fundamental for the final application of the system. Nevertheless, due to the hydrophobicity of the cavitand molecules, the as-functionalized nanoparticles are not dispersible in aqueous media, as it is instead required for the target application. Moreover, the coating layer is regarded as labile and might not address the requirement of recyclability for the final system.

On the other hand, covalent strategy consisted of a multi-steps procedure, thus more complex and time-consuming than the non-covalent approach. However, upon a first silanization step through which a mixed amino/PEG organosilane layer was grafted at iron oxide surface, partial aqueous dispersibility was achieved. Cavitands conjugation was carried out in a second step exploiting surface amino groups. The complexity of the nanoparticles surface chemical composition affected the conjugation extent and only a restrained number of cavitand molecules were bound.

Further investigation should be carried out in order to optimize the nanoparticles surface composition for improving water-dispersibility and enhancing the conjugation extent.

Although the preliminary tests of molecular recognition could not confirm the efficiency of the covalently-functionalized nanoparticles, the activity of Fe_3O_4-NH_2/PEG-Tiiii nanoparticles in selectively bind target analytes can not be ruled out. Studies are now focused in developing a more suitable analytical test for investigating the molecular recognition efficiency.

4.5. Bibliography

(1) Pinalli, R.; Dalcanale, E.: Supramolecular Sensing with Phosphonate Cavitands. *Accounts of Chemical Research* **2012**, *46*, 399-411.

(2) Lavigne, J. J.; Anslyn, E. V.: Sensing A Paradigm Shift in the Field of Molecular Recognition: From Selective to Differential Receptors. *Angewandte Chemie International Edition* **2001**, *40*, 3118-3130.

(3) Cram, D. J.: Cavitands: Organic Hosts with Enforced Cavities. *Science* **1983**, *219*, 1177-1183.

(4) Moran, J. R.; Karbach, S.; Cram, D. J.: Cavitands: synthetic molecular vessels. *Journal of the American Chemical Society* **1982**, *104*, 5826-5828.

(5) Suman, M.; Freddi, M.; Massera, C.; Ugozzoli, F.; Dalcanale, E.: Rational Design of Cavitand Receptors for Mass Sensors. *Journal of the American Chemical Society* **2003**, *125*, 12068-12069.

(6) Pinalli, R.; Suman, M.; Dalcanale, E.: Cavitands at Work: From Molecular Recognition to Supramolecular Sensors. *European Journal of Organic Chemistry* **2004**, *2004*, 451-462.

(7) Pinalli, R.; Nachtigall, F. F.; Ugozzoli, F.; Dalcanale, E.: Supramolecular Sensors for the Detection of Alcohols. *Angewandte Chemie International Edition* **1999**, *38*, 2377-2380.

(8) Kalenius, E.; Neitola, R.; Suman, M.; Dalcanale, E.; Vainiotalo, P.: Hydrogen Bonding in Phosphonate Cavitands: Investigation of Host–Guest Complexes with Ammonium Salts. *Journal of the American Society for Mass Spectrometry* **2010**, *21*, 440-450.

(9) Sreekumar, A.; Poisson, L. M.; Rajendiran, T. M.; Khan, A. P.; Cao, Q.; Yu, J.; Laxman, B.; Mehra, R.; Lonigro, R. J.; Li, Y.; Nyati, M. K.; Ahsan, A.; Kalyana-Sundaram, S.; Han, B.; Cao, X.; Byun, J.; Omenn, G. S.; Ghosh, D.; Pennathur, S.; Alexander, D. C.; Berger, A.; Shuster, J. R.; Wei, J. T.; Varambally, S.; Beecher, C.; Chinnaiyan, A. M.: Metabolomic profiles delineate potential role for sarcosine in prostate cancer progression. *Nature* **2009**, *457*, 910-914.

(10) Biavardi, E.; Tudisco, C.; Maffei, F.; Motta, A.; Massera, C.; Condorelli, G. G.; Dalcanale, E.: Exclusive recognition of sarcosine in water and urine by a cavitand-functionalized silicon surface. *Proceedings of the National Academy of Sciences* **2012**, *109*, 2263-2268.

(11) Biavardi, E.; Favazza, M.; Motta, A.; Fragalà, I. L.; Massera, C.; Prodi, L.; Montalti, M.; Melegari, M.; Condorelli, G. G.; Dalcanale, E.: Molecular Recognition on a Cavitand-Functionalized Silicon Surface. *Journal of the American Chemical Society* **2009**, *131*, 7447-7455.

(12) Tudisco, C.; Betti, P.; Motta, A.; Pinalli, R.; Bombaci, L.; Dalcanale, E.; Condorelli, G. G.: Cavitand-Functionalized Porous Silicon as an Active Surface for Organophosphorus Vapor Detection. *Langmuir* **2011**, *28*, 1782-1789.

(13) Frey, N. A.; Peng, S.; Cheng, K.; Sun, S.: Magnetic nanoparticles: synthesis, functionalization, and applications in bioimaging and magnetic energy storage. *Chemical Society Reviews* **2009**, *38*, 2532-2542.

(14) Lu, A.-H.; Salabas, E. L.; Schueth, F.: Magnetic nanoparticles: Synthesis, protection, functionalization, and application. *Angewandte Chemie-International Edition* **2007**, *46*, 1222-1244.

(15) Miles, W. C.; Goff, J. D.; Huffstetler, P. P.; Reinholz, C. M.; Pothayee, N.; Caba, B. L.; Boyd, J. S.; Davis, R. M.; Riffle, J. S.: Synthesis and Colloidal Properties of Polyether−Magnetite Complexes in Water and Phosphate-Buffered Saline. *Langmuir* **2008**, *25*, 803-813.

(16) Laurent, S.; Forge, D.; Port, M.; Roch, A.; Robic, C.; Elst, L. V.; Muller, R. N.: Magnetic iron oxide nanoparticles: Synthesis, stabilization, vectorization, physicochemical characterizations, and biological applications. *Chemical Reviews* **2008**, *108*, 2064-2110.

(17) Wu, W.; He, Q.; Jiang, C.: Magnetic Iron Oxide Nanoparticles: Synthesis and Surface Functionalization Strategies. *Nanoscale Research Letters* **2008**, *3*, 397-415.

(18) Biavardi, E.; Battistini, G.; Montalti, M.; Yebeutchou, R. M.; Prodi, L.; Dalcanale, E.: Fully reversible guest exchange in tetraphosphonate cavitand complexes probed by fluorescence spectroscopy. *Chemical Communications* **2008**, 1638-1640.

(19) Dionisio, M.; Maffei, F.; Rampazzo, E.; Prodi, L.; Pucci, A.; Ruggeri, G.; Dalcanale, E.: Guest-controlled aggregation of cavitand gold nanoparticles and N-methyl pyridinium-terminated PEG. *Chemical Communications* **2011**, *47*, 6596-6598.

(20) Dionisio, M.; Schnorr, J. M.; Michaelis, V. K.; Griffin, R. G.; Swager, T. M.; Dalcanale, E.: Cavitand-Functionalized SWCNTs for N-Methylammonium Detection. *Journal of the American Chemical Society* **2012**, *134*, 6540-6543.

(21) Turcheniuk, K.; Tarasevych, A. V.; Kukhar, V. P.; Boukherroub, R.; Szunerits, S.: Recent advances in surface chemistry strategies for the fabrication of functional iron oxide based magnetic nanoparticles. *Nanoscale* **2013**, *5*, 10729-10752.

(22) Amstad, E.; Gillich, T.; Bilecka, I.; Textor, M.; Reimhult, E.: Ultrastable Iron Oxide Nanoparticle Colloidal Suspensions Using Dispersants with Catechol-Derived Anchor Groups. *Nano Letters* **2009**, *9*, 4042-4048.

(23) De Palma, R.; Peeters, S.; Van Bael, M. J.; Van den Rul, H.; Bonroy, K.; Laureyn, W.; Mullens, J.; Borghs, G.; Maes, G.: Silane Ligand Exchange to Make Hydrophobic Superparamagnetic Nanoparticles Water-Dispersible. *Chemistry of Materials* **2007**, *19*, 1821-1831.

(24) Feng, B.; Hong, R. Y.; Wang, L. S.; Guo, L.; Li, H. Z.; Ding, J.; Zheng, Y.; Wei, D. G.: Synthesis of Fe_3O_4/APTES/PEG diacid functionalized magnetic nanoparticles for MR imaging. *Colloids and Surfaces A: Physicochemical and Engineering Aspects* **2008**, *328*, 52-59.

(25) Frickel, N.; Messing, R.; Gelbrich, T.; Schmidt, A. M.: Functional Silanes as Surface Modifying Primers for the Preparation of Highly Stable and Well-Defined Magnetic Polymer Hybrids. *Langmuir* **2009**, *26*, 2839-2846.

(26) Pinna, N.; Grancharov, S.; Beato, P.; Bonville, P.; Antonietti, M.; Niederberger, M.: Magnetite nanocrystals: Nonaqueous synthesis, characterization, and solubility. *Chemistry of Materials* **2005**, *17*, 3044-3049.

(27) Condorelli, G. G.; Motta, A.; Favazza, M.; Fragalà, I. L.; Busi, M.; Menozzi, E.; Dalcanale, E.; Cristofolini, L.: Grafting Cavitands on the Si(100) Surface. *Langmuir* **2006**, *22*, 11126-11133.

(28) Yoon, T.-J.; Yu, K. N.; Kim, E.; Kim, J. S.; Kim, B. G.; Yun, S.-H.; Sohn, B.-H.; Cho, M.-H.; Lee, J.-K.; Park, S. B.: Specific Targeting, Cell Sorting, and Bioimaging with Smart Magnetic Silica Core–Shell Nanomaterials. *Small* **2006**, *2*, 209-215.

(29) Butterworth, M. D.; Illum, L.; Davis, S. S.: Preparation of ultrafine silica- and PEG-coated magnetite particles. *Colloids and Surfaces A: Physicochemical and Engineering Aspects* **2001**, *179*, 93-102.

(30) Park, J. C.; Gilbert, D. A.; Liu, K.; Louie, A. Y.: Microwave enhanced silica encapsulation of magnetic nanoparticles. *Journal of Materials Chemistry* **2012**, *22*, 8449-8454.

(31) Stutz, C.; Bilecka, I.; Thunemann, A. F.; Niederberger, M.; Borner, H. G.: Superparamagnetic core-shell nanoparticles as solid supports for peptide synthesis. *Chemical Communications* **2012**, *48*, 7176-7178.

(32) Smith, A. L.: Infrared spectra-structure correlations for organosilicon compounds. *Spectrochimica Acta* **1960**, *16*, 87-105.

(33) Silverstein, R. M.; Webster, F. X.: *Spectrometric identification of organic compounds*; John Wiley and Sons, Inc., 1998.

(34) NIST X-ray Photoelectron Spectroscopy Database, NIST Standard Reference Database 20, Version 4.1 (Web Version), http://srdata.nist.gov/xps/.

(35) Rouxhet, P. G.; Genet, M. J.: XPS analysis of bio-organic systems. *Surface and Interface Analysis* **2011**, *43*, 1453-1470.

(36) Tudisco, C.; Bertani, F.; Cambria, M. T.; Sinatra, F.; Fantechi, E.; Innocenti, C.; Sangregorio, C.; Dalcanale, E.; Condorelli, G. G.: Functionalization of PEGylated Fe_3O_4 magnetic nanoparticles with tetraphosphonate cavitand for biomedical application. *Nanoscale* **2013**, *5*, 11438-11446.

(37) Benyettou, F.; Guenin, E.; Lalatonne, Y.; Motte, L.: Microwave assisted nanoparticle surface functionalization. *Nanotechnology* **2011**, *22*, 055102.

(38) World Anti-Doping Agency (WADA) - Prohibited list 2014 (www.wada-ama.org/Documents/World_Anti-Doping_Program/WADP-Prohibited-list/2014/WADA-prohibited-list-2014-EN.pdf).

Chapter 5

Chiral-functionalization of magnetite nanoparticles for the enantioselective recognition and resolution of an inherently chiral biphosphonate cavitand racemate

5.1. Introduction

Cavitands are defined as synthetic organic compounds featured by a rigid cavity of molecular dimensions[1]. Cavitands are well known molecular receptors whose recognition properties derive from the possibility of establish hydrogen bonding, CH–π and dipole-dipole interactions with the proper guest molecule[2]. Among them, phosphonate cavitands, thus bearing at least one phosphoryl bridging group at the upper rim of the cavity, demonstrate outstanding recognition properties towards amino functionalities. Particularly, phosphonate cavitands show high recognition and binding selectivity for N-methyl ammonium groups due to the additional $N^{+}\cdots O{=}P$ cation-dipole and CH_3–π interactions between the N^{+}–CH_3 and the aromatic scaffold of the cavity, with respect to simple amino groups[3]. Such a specific recognition for N-methyl ammonium groups is of potential exploitation for the detection of a broad range of biological compounds, like drugs, biomarkers and neurotransmitters, which often bear such functionality[3-5].

It is of general knowledge that compounds of biological importance often carry stereocentres, which render their recognition by proper biological receptors extremely specific. Due to the interest of mimicking biological functions in living systems for understanding complex biological pathways, and due to the need of distinguishing enantiomers in several fields of chemical applications, one of the requirement for synthetic molecular receptors (like cavitand) is the ability to exert enantioselective recognition[6,7].

For this purpose, several chiral supramolecular receptors have been synthesized in the last decades[8]. For most of the investigated compounds, chirality was achieved by grafting functional groups bearing stereocentres at the upper rim of the cavity. Many examples reported about coupling Salen bridges, leading to the so-called Salen-cavitands[6,9], or enantiopure amino acids, which contribute to the class of deep-chiral cavitands (figure 5.1)[10,11].

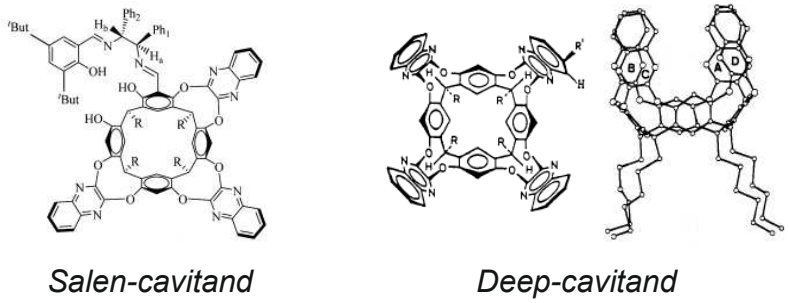

Figure 5.1: Schematic representation of chiral Salen-cavitand (left)[9] and deep-cavitand (right)[12].

Although the synthesis approach for their production is slightly more complicate, inherent chiral cavitands were also described[12].

The term inherent chirality with reference to supramolecular receptors was introduced for the first time by Böhmer et al., who stated that chirality doesn't derive from the presence of a stereocentre, but from the absence of a symmetry plane, an inversion centre or an alternating axis in the whole molecule[13].

Inherently chiral cavitands are synthesized by introducing different bridging groups at the upper rim of the cavity. Desimmetrization of the molecule can be achieved by inserting either three or four different bridging groups, thus obtaining compounds of AABC or ABCD type, respectively[8]. Compounds bearing three identical bridging units, namely the AAAB type, are an additional typology of inherent chiral cavitands; in this case desimmetrization is brought about by the fourth and different bridging moiety. However, studies revealed that they show lower efficiency as enantioselective receptors than the AABC or ABCD typologies, thus they are usually not employed[14]. Examples of the possible typologies of chiral cavitands are reported in figure 5.2.

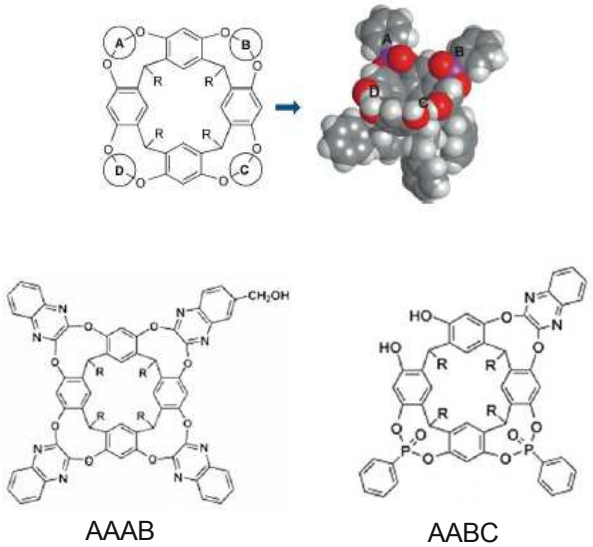

Figure 5.2: Schematic illustration of the concept of inherent chirality (top) and of the possible typologies of inherently chiral cavitands, namely AAAB (bottom left) and AABC (bottom right)[14].

In view of their peculiar selectivity in recognizing ammonium and N-methyl ammonium groups, phosphonate cavitands are regarded as promising candidates for the fabrication of inherent chiral compounds. Several works reported the synthesis of inherently chiral phosphonate cavitands and

demonstrated their capability in enantioselective recognition. Chiral phosphonate cavitands were largely investigated by the groups of Dutasta and Naubron. They reported the efficient enantioselective recognition of AABC-type cavitands towards adrenaline, nicotine and ephedrine. These compounds bear N-methyl ammonium functionalities and are known to be of biological importance because of their participation in transfer processes in the neuronal system[7,14].

Sfrazzetto et al. synthesized Salen-based cavitands bearing two distinct elements of chirality, namely a chiral Salen bridge and the inherent chirality of the host cavity. They investigated about the efficiency of those molecules in discriminating among α-amino acid ammonium salts and demonstrated that, depending on the working conditions, the two chiral elements of the cavitand molecule were able to recognize opposite enantiomers of the same amino acid pair. In particular, when the cavitand interacted via its Salen bridge with a uranyl cation, chiral recognition was driven only by the inherently chiral cavity and a trend in the host-guest configurations was observed[9].

Studies are usually carried out by incubating the cavitand racemate with the pure enantiomer of the investigated guest molecule in order to promote the formation of the host-guest complex. Chiral discrimination ability is then investigated by ^{1}H NMR spectroscopy (or for other representative nuclei, such as ^{13}C or ^{31}P). In fact, the interaction of an enantiopure compound with the enantiomers composing a racemic mixture leads to the generation of diastereomers which are distinguishable through this technique[6,10]. In this way it is possible to assess whether chiral discrimination occurred, and to define the enantioselectivity of the process determining the association constant for both the formed complexes. This is possible only upon assignment of the configuration of the as-formed diastereomers. For this purpose, the absolute configuration of the participating molecules has to be determined. Moreover, complexes between the pure enantiomers of both guest and host are commonly analysed separately as reference compounds. Nevertheless, while enantiopure guest molecules such as amino acids are commercially available, resolution of racemic mixture of the desired synthetic cavitands might be difficult[7,9]. Synthesis of chiral cavitands is indeed expensive and time-consuming and it involves complicate purification steps, chiral resolution being likely the more difficult one. In most of the cases, chiral resolution is achieved through semi-preparative high-performance liquid chromatography (HPLC). However, this technique allows separating only restrained amounts of product and requires the use of chiral stationary phases which are often expensive[8]. This is one of the reasons that causes the use of chiral cavitands to be limited, in most of the cases, to theoretical studies[15].

Therefore, development of alternative purification methods to enable a facile and rapid cavitand chiral resolution, possibly at larger extent, is intriguing.

The aim of the work described in this chapter is the fabrication of a recoverable and recyclable system for the heterogeneous resolution of an inherently chiral cavitand racemate.

As previously anticipated, several works described the outstanding properties of inherently chiral cavitands in discriminating between the enantiomers of biologically active molecules, such as amino acids. These findings suggest that the peculiar enantioselectivity of phosphonate cavitands for biological compounds, especially bearing N-methyl ammonium ions, might be exploited for more practical goals other than application in biology, sensing or pharmaceutical fields.

By employing commercially available enantiopure N-methylated amino acid molecules, it would be possible to create devices for a rapid and facile chiral resolution of synthetic cavitand racemates.

Whereas the amino acid is covalently grafted on a solid support, a heterogeneous recognition could be performed. Particularly, the cavitand enantiomer which preferentially interacts with the supported amino acid will be easily removed from the medium containing its stereoisomer counterpart by simply collecting the solid support. Several materials might be employed as solid supports for accomplishing this goal, like silica or synthetic resins. The widespread functionalization strategies developed for conjugating biological compounds at iron oxide nanoparticles suggest that the latter might represent a valid alternative solid support[16,17]. Moreover, iron oxide nanoparticles present remarkable magnetic properties. When their size is equal or smaller than 20 nm they show superparamagnetic behaviour, presenting fast response to an external magnetic field and negligible remnant magnetization[18-20]. Therefore, the application of an external magnetic field would enable the ease and rapid separation of the device and correlated adsorbed molecules from the surrounding environment. Furthermore, recyclability will be achieved due to the reversible nature of the host-guest cavitand-amino acid complex[21,22]. Indeed, the use of competitive guest molecules (often simple salts like NaCl or K_2CO_3) might lead to the dissociation of such kind of complexes and the replacement of the amino acid molecule by the compound showing more affinity for the host molecule, with the consequent liberation of the cavitand.

For these purposes, magnetite nanoparticles will be covalently functionalized by grafting at their surface enantiopure amino acid molecules. Organosilanes coupling agents will be used to opportunely functionalize nanoparticles surface and to introduce anchoring sites for the conjugation of the guest molecules, namely N-methyl-L-alanine. The enantiopure surface amino acid molecules will be exploited in a further step to bind a chiral phosphonate cavitand. In particular, a cavitand racemate will be used in order to investigate the ability of the as-functionalized nanoparticles to selectively recognize and complex to only one of the two cavitand enantiomers. Chromatographic analysis (HPLC) performed on a chiral stationary phase will be employed to prove the enantioselectivity of the molecular recognition process, thus the resolution efficiency of the system.

The present work was performed in collaboration with the group of Professor Enrico Dalcanale (University of Parma - Italy), who synthesized the chiral cavitand and carried out the enantioselective recognition tests.

5.2. Experimental section

5.2.1. Materials

Iron(III) acetylacetonate ($Fe(acac)_3$, anhydrous 99% - STREM) and benzyl alcohol (puriss. 99% - Sigma-Aldrich) were stored in a glovebox and used as received.
Acetic acid (≥99.7%), N,N'-dicyclohexylcarbodiimide (DCC, 99%), 4-(dimethylamino)pyridine (DMAP, 99%), Fmoc-N-methyl-L-alanine (97%), and piperidine (reagent plus) were purchased from Aldrich and used as received.
(3-Aminopropyl)trimethoxysilane (APTMS, 96%) was purchased from ABCR; it was stored in a glovebox and used as received.
Dichloromethane (DCM) and N,N'-dimethylformamide (DMF) were dried over activated aluminium oxide (neutral, Brockmann I) and stored on molecular sieves (4Å).
All the used solvents were of the highest grade and used as received.
Inherently chiral cavitand molecules were synthesized by the group of Prof. E. Dalcanale (University of Parma - Italy). A description of the molecular structure is reported in the following paragraphs (synthesis procedure not published yet).

5.2.2. Methods

5.2.2.1. Synthesis of magnetite nanoparticles

Magnetite (**Fe_3O_4**) nanoparticles were synthesized following the traditional "benzyl alcohol route", as previously reported[23].
Briefly, the preparation of the reaction mixture was carried out in a glovebox (H_2O< 0.1 ppm, and O_2< 0.1 ppm). In a typical synthesis, 1.0 g (2.83 mmol) of iron(III) acetylacetonate was placed in a 45-mL inner volume Teflon cup and solubilised in 20 mL of benzyl alcohol. The Teflon cup was then slid into a steel autoclave which was carefully sealed and taken out from the glovebox. The reaction was performed in an oven heated at 175°C for 48 hours. The resulting nanoparticles were collected by centrifugation and washed twice with absolute ethanol and once with DCM. Finally, nanoparticles were redispersed in 20 mL of ultrapure water and used for further functionalization procedures.

5.2.2.2. Covalent functionalization of magnetite nanoparticles with N-methyl-L-alanine

1) Preparation of 3-aminopropylsilane-derivatized magnetite nanoparticles
The reaction was carried out in a round-bottom flask, equipped with a magnetic stirrer. To 4.5 mL of an aqueous Fe_3O_4 nanoparticles dispersion (6 mg/mL), 7.1 mL of ultrapure water, 7 mL of methanol,

1.4 mL (8 mmol) of APTMS and 80 μL of an aqueous acetic acid solution (0.35 M) were added in sequence. The reaction was performed at room temperature for 24 hours.
The as-obtained solid was collected via magnetic sedimentation and consecutively washed once with ultrapure water and twice with absolute ethanol. The precipitate was finally redispersed in 3 mL of dry DMF and stored under Ar atmosphere until the following functionalization step (**Fe_3O_4-NH_2**).

2) Coupling of Fe_3O_4-NH_2 nanoparticles with Fmoc-N-methyl-L-alanine
In a three-necks round-bottom flask equipped with a rubber septum, 73 mg (0.224 mmol) of Fmoc-N-methyl-L-alanine were dissolved in 10 mL of dry DCM under Ar-flow and magnetic stirring; the solution was then cooled down to 0°C. Consecutively, 47 mg (0.227 mmol) of DCC were slowly added, followed by 11 mg (0.09 mmol) of DMAP. Finally, 3 mL of the Fe_3O_4-NH_2 dispersion were added dropwise through the rubber septum. The reaction was performed under inert atmosphere at room temperature for 72 hours.
The solid was collected *via* magnetic sedimentation and washed twice with diethyl ether and once with DMF. The as-obtained Fmoc-N-methyl-L-alanine-functionalized Fe_3O_4 nanoparticles (**Fe_3O_4-MeAla-Fmoc**) were redispersed in 10 mL of dry DMF and stored under Ar atmosphere until the following step.

3) Cleavage of the Fmoc- group
Cleavage of the Fmoc- group was performed by adding a DMF solution of piperidine (2 % , 50 μL) to the DMF Fe_3O_4-MeAla-Fmoc nanoparticles dispersion under Ar flow. The reaction was carried out at room temperature overnight. The solid (**Fe_3O_4-MeAla**) was recovered *via* magnetic separation and washed twice with DMF and once with diethyl ether, and finally redispersed in 3 mL of absolute ethanol.

5.2.2.3. Enantioselective recognition test

In order to perform the enantioselective recognition test, Fe_3O_4-MeAla nanoparticles were collected through magnetic separation and redispersed in 3 mL of DCM. 0.9 mg (0.9 μmol) of the investigated chiral cavitand ((AB)2POii1PSiMe) racemate were added to the nanoparticles dispersion and the resulting mixture was mechanically stirred for 24 hours. Subsequently, nanoparticles were collected through magnetic sedimentation and the supernatant was saved (**S1**). The collected nanoparticles were added to a solution containing 3 mL of DCM, 10 μL of brine and 10 μL of ethanol. This mixture was mechanically stirred for 24 hours in order to dissociate the cavitand-amino acid complex. The nanoparticles were collected through magnetic sedimentation and the supernatant was saved (**S2**).

5.2.3. Characterization techniques

Fourier transform infrared (FTIR) spectroscopy analysis was performed in order to investigate nanoparticles surface chemical composition; for a complete comparison bare nanoparticles and pure ligand were also analyzed.

FTIR analysis of the covalently functionalized magnetite nanoparticles was performed on a Thermo Scientific Nicolet iS5 spectrometer. Spectra were acquired in transmission mode (using the KBr pellets method) in the wavenumber range from 4000 to 400 cm^{-1}. All the spectra were acquired using a 4 cm^{-1} resolution and collecting 128 scans.

Baseline correction was applied to all the reported spectra.

Transmission electron microscopy (TEM) analysis was carried out in order to investigate the morphology and size distribution of magnetite nanoparticles at different stages of the functionalization procedure. TEM analysis was carried out on a Philips CM200 (LaB_6) microscope operating at an acceleration voltage of 200 kV. Samples were prepared by depositing few drops of ethanol dispersion of each sample on a 300 mesh carbon film-coated copper grid. Solvent was allowed to evaporate prior to the analysis.

Chiral high-performance liquid chromatography (chiral HPLC) was used in order to evaluate the enantioselectivity of the molecular recognition process. It was performed on an analytical Chiralpack IC column (4.6 x 250 mm) using an acetonitrile/water (80/20 v/v) mixture as eluent.

5.3. Results and discussion

Functionalization of nanoparticles was performed following an approach similar to that described in chapter 4. The chosen amino acid molecules were conjugated through formation of a covalent amide bond at the surface of amino-functionalized nanoparticles. The choice of performing a covalent functionalization was principally dictated by the requirement for the organic surface layer to be stable under the working conditions. The aim of this project is the fabrication of a recoverable and recyclable system for enenatioselective separation of a cavitand racemate. Recyclability of the device is based on the reversible nature of the cavitand-amino acid host-guest complex[21,22]. This implies that the selectively complexed cavitand molecules will be recovered and isolated through dissociation of the formed complex, which is carried out by exploiting competitive guest species. To avoid their concurrent desorption during the dissociation step, amino acid molecules should be firmly grafted at particles surface, thus ensuring the recyclability of the device.

Amino-functionalized magnetite nanoparticles were fabricated by grafting organosilane precursors in a first post-synthesis functionalization step. Particularly, (3-aminopropyl)trimethoxysilane (APTMS) was chosen. Enantiopure N-methyl-L-alanine was conjugated in a second step, using the carbodiimide-based chemistry. It has to be taken into account, that in order to avoid amino acid

intermolecular conjugation, the corresponding Fmoc-amino acid was used (Fmoc-N-methyl-L-alanine). Protection of amino groups is commonly carried out by conjugation of tert-butoxycarbonyl (Boc) or 9-fluorenylmethoxycarbonyl (Fmoc) groups at the desired nitrogen atom, leading to formation of a carbamate group. Removal of the protecting group is then performed through a mild "hydrolysis" reaction. While the Boc group is usually removed in acidic conditions (commonly hydrochloric acid or trifluoroacetic acid), cleavage of the Fmoc protective group occurs in basic conditions, generally using an organic base such as piperidine.

In view of the possibility for iron oxide nanoparticles to undergo etching in acidic conditions, the Fmoc-protected amino acid was chosen. The entire functionalization procedure is illustrated in figure 5.3.

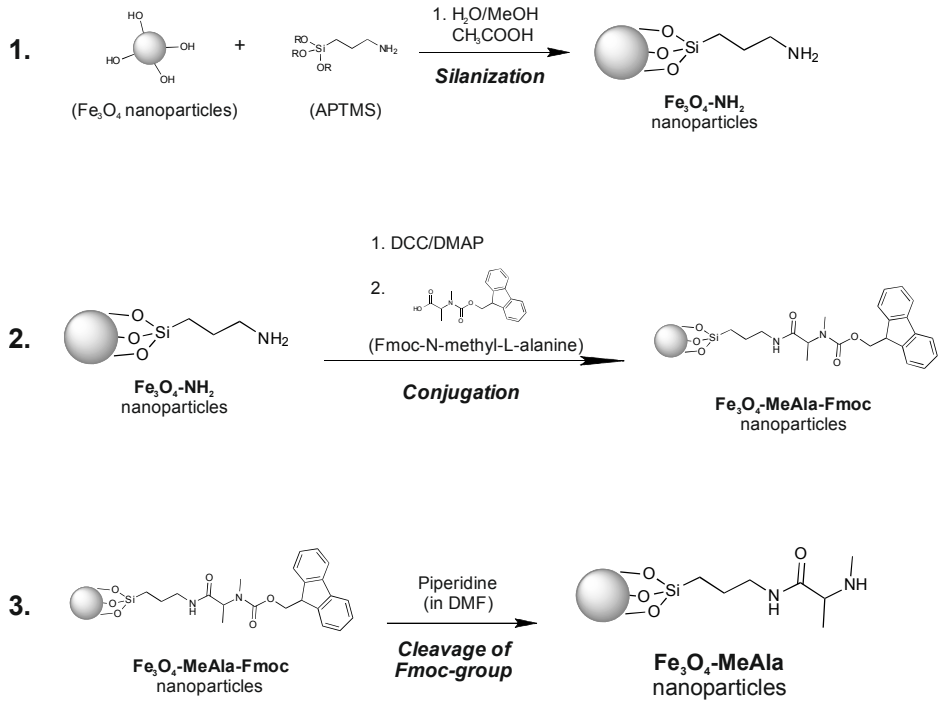

Figure 5.3: Schematic representation of the functionalization procedure.

Finally, the choice of using N-methyl-L-alanine was dictated by few reasons: (i) in view of the high selectivity and binding affinity of phosphonate cavitands for N-methyl ammonium ions[3,24], the N-methyl-amino acid is expected to provide the highest selectivity and complex stability; (ii) enantiopure amino acid molecules are commercially available, also in the N-methylated form, thus avoiding additional synthesis steps for the fabrication of the desired guest; finally (iii) alanine is the simplest chiral amino acid.

This chapter will describe preliminary results, thus only a qualitative particles surface investigation and a chromatographic study on the efficiency in chiral separation will be described. More detailed characterizations are still ongoing in our laboratories.

5.3.1. Investigation of the nanoparticles surface chemical composition

Qualitative investigation of the nanoparticles surface chemical composition was performed by FTIR spectroscopy, upon silanization step and on the final material.

Since silanization reaction takes place at nanoparticles surface hydroxyl groups[25], it is important that magnetite nanoparticles exhibit a mostly bare surface (negligible presence of other adsorbed species).The spectrum of pristine magnetite nanoparticles (figure 5.4d) presents only few absorption peaks. The broad band centred at about 3400 cm^{-1} is typical of O-H stretching modes of adsorbed water and particles surface hydroxyl groups, while the band peaking at 590 and 631 cm^{-1} is assigned to the Fe-O stretching vibration modes of nanosized magnetite particles. Although traces of adsorbed organic species can not be undoubtedly ruled out, the infrared analysis suggests that mostly hydroxyl groups are exposed at particles surface. Therefore, particles exhibit a surface chemical composition favourable to the silanization reaction.

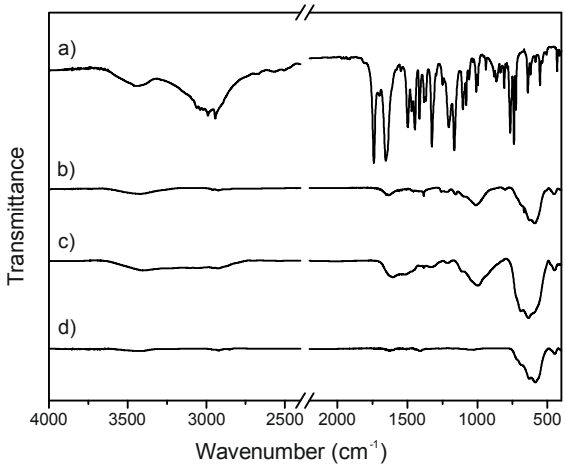

Figure 5.4: FTIR spectra of Fmoc-N-methyl-L-alanine (a), N-methyl-L-alanine-functionalized nanoparticles (b), amino-functionalized nanoparticles (c), and pristine magnetite nanoparticles (d). For sake of clarity, spectra are represented stacked by an offset value and the signal due to atmospheric CO_2 was omitted by introducing a break in the 2400-2200 cm^{-1} spectral region.

The infrared spectrum of the material resulting from grafting organosilane species is depicted in figure 5.4c. The broad band centred at 1015 cm^{-1} is typical of grafted organosilane layers[26] and it is constituted of few contributions. The main absorption at 1015 cm^{-1} and the weak contribution at 1040 cm^{-1}, are generally ascribed to Si-O-Si stretching modes, while silanol Si-OH stretching vibrations are referred as responsible for the contribution at 940 cm^{-1} [27]. Confirmation of the successful grafting of the organosilane precursors arises from the 1214 cm^{-1} peak, which is generally ascribed to Si-CH_2 stretching modes in propyl residues at the silicon atom[27]. Presence of propyl chains is further supported by the characteristic C-H bond stretching vibration modes of methylene groups at 2926 (asymmetric) and 2855 (symmetric) cm^{-1}. The weak absorption at 2960 cm^{-1} is likely related to methyl functionalities deriving from an incomplete hydrolysis of methoxy groups (Si-OCH_3) of APTMS. Finally, the contribution at 1100 cm^{-1}, overlapping with the grafted organosilane band, could be

ascribed to C-N bonds stretching vibrations. Further spectral features supporting the presence of the desired surface amino groups are provided by the absorptions at 1600 and 1520 cm^{-1}, which might be regarded as deriving from the asymmetric and symmetric bending modes of protonated primary amino ($-NH_3^+$) groups[28].

Upon conjugation reaction, few spectral changes were observed, indicating the successful grafting of amino acid molecules (figure 5.4b). Particularly, the bands associated to the bending vibrations of surface protonated primary amino groups remarkably decreased in intensity and a new band centred at 1640 cm^{-1} emerged. This band is referred to as amide bonds formed between the amino acid carboxyl groups and surface amino functionalities. Particularly it derives from the overlapping of C=O stretching vibration and N-H bending mode of the amide moiety. Further spectral features supporting the occurrence of the conjugation step arise from the 1270-1150 cm^{-1} spectral region. Particularly, the peak at 1260 cm^{-1} is indicative of the amide group and usually ascribed to the interaction between the N-H bending mode and C-N stretching mode of the amide bond. The sharp peak at 1380 cm^{-1} is assigned to the symmetrical bending vibration of methyl groups, introduced by the amino acid. Moreover, it could be inferred that the conjugation reaction did not affect the characteristic absorption of the grafted organosilane layer, which band does not show remarkable changes.

The absence of any absorptions ascribable to the Fmoc group, such as aromatic C-C and C-H stretching modes, suggests that cleavage of the Fmoc group successfully occurred, thus indicating the presence of N-methylated amino groups available for further host-guest recognition.

Transmission electron microscopy (TEM) analysis was performed at each step of the functionalization process (figure 5.5).

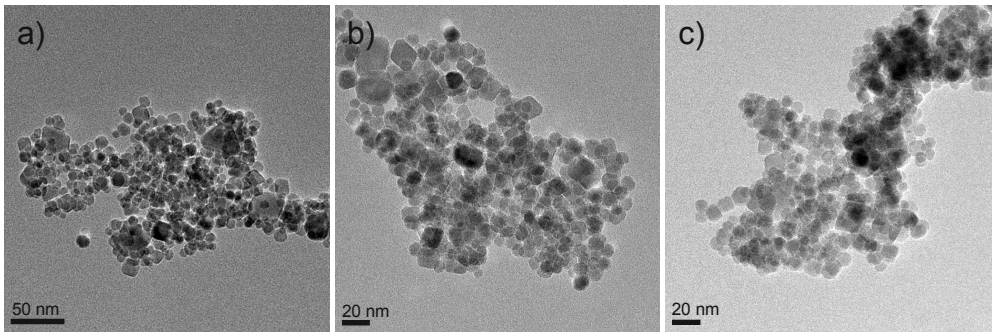

Figure 5.5: TEM images of pristine magnetite nanoparticles (a), amino-functionalized nanoparticles (b) and N-methyl-L-alanine-functionalized nanoparticles (c).

As observed from TEM images, nanoparticles morphology and size distribution (nanoparticles diameter varying from 8 to 15 nm; average size of 11 nm) did not significantly change upon each step of the functionalization procedure. Furthermore, TEM images show that nanoparticles tent to agglomerate, suggesting that the organic functionalization is not completely efficient in stabilizing nanoparticles. The observed partial agglomeration might be due to a likely not-continuous organic coating on nanoparticles surface and/or to a poorly suitable dispersing medium.

5.3.2. Enantioselective recognition

Enantioselective recognition tests were performed using a racemic mixture of the biphosphonate cavitand of general formula (AB)2POii1PSiMe[(i)] (figure 5.6); the general name 2POii will be used from here on.

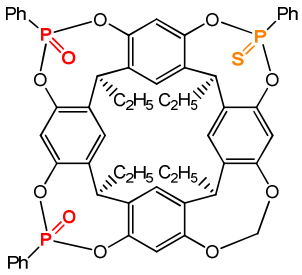

Figure 5.6: Molecular structure of the (AB)2POii1PSiMe cavitand.

The cavitand molecule exhibits two phosphoryl, one thiophosphoryl and one methylene bridging groups at the cavity upper rim. The presence of three different bridging groups imparts inherent chirality at the cavitand molecule, which structure is referred to as the AABC typology.

The enantioselective recognition test consisted of two steps: in a first step, amino acid-functionalized nanoparticles were incubated with a racemic mixture of the 2POii cavitand. Upon separation of nanoparticles through magnetic sedimentation, the supernatant (**S1**) was saved for further characterization. The as-separated nanoparticles were further on treated with a base, which acts as a competitor guest for the cavitand. In this way, dissociation of the Fe_3O_4-MeAla-2POii complex is achieved. The cavitand solution (**S2**) is recovered by separating nanoparticles through magnetic sedimentation (figure 5.7).

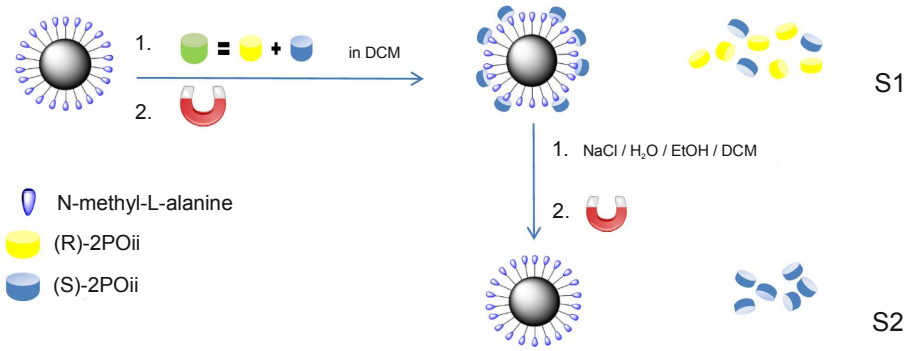

Figure 5.7: Schematic representation of the enantioselective recognition test.

The efficiency of the enantioselective recognition was investigated by analytical high-performance liquid chromatography (HPLC) on a chiral stationary phase.

[(i)] The synthesis procedure for the used molecule is not published yet.

Preliminary chromatographic enantioseparation of the 2POii cavitand racemate (rac-2POii) was performed in order to determine the elution time of the two enantiomers. Results showed that the (S)-enantiomer exhibits the shorter elution time (23 minutes; figure 5.8a). Chiral-HPLC analysis results of the **S1** and **S2** supernatants are reported in figure 5.8.

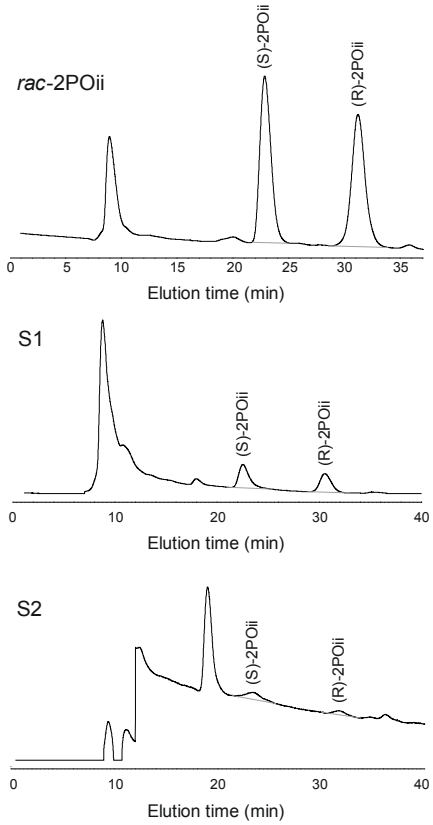

Figure 5.8: Chromatograms for the chiral resolution of 2POii racemate (top), of the fraction **S1** (centre) and **S2** (bottom).

The chromatogram of the **S1** fraction recovered upon incubation of nanoparticles with 2POii racemate shows the presence of both the cavitand enantiomers in similar percentage (table 5.1). This fraction is expected to contain the not-complexed cavitand molecules. However, it has to be taken into account that the enantioselective recognition test was performed using an excess of cavitand on the estimated concentration of amino acid species grafted at particles surface. On the contrary, analysis of the **S2** fraction should provide the most representative results. **S2** fraction derives from the guest-displacement procedure carried out on the iron oxide nanoparticles, therefore it is expected to contain only those cavitand molecules that effectively interacted with surface amino acid species. On this basis, whether enantioselective recognition successfully occurred, an excess of the preferentially bounded 2POii enantiomer is expected. Analysis of the chromatogram of the **S2** fraction revealed that complexation occurred preferentially with the (S)-enantiomer, as demonstrated by peak area integration (table 5.1).

Table 5.1: quantitative analysis performed through peak area integration for the investigated racemate, **S1** and **S2** fractions.

Analyzed fraction	(S)-enantiomer (area %)	(R)-enantiomer (area %)
rac-**2POii**	50.6	49.4
S1-fraction	54.0	46.0
S2-fraction	70.3	29.7

The two diastereomeric complexes formed in a 2.3:1 ratio, in favour of the (S)-2POii enantiomer.
This finding suggests that enantioselective recognition was successfully achieved at nanoparticles surface. Presence of a residual amount of (R)-2POii in the **S2** fraction reveals that the enantioselectivity is not complete. This can be explained in terms of the chemical structure of the molecular cavity of 2POii. In view of the large binding affinity for N-methyl ammonium moieties, the two phosphoryl bridging groups are potentially able to recognize both of the enantiomers of N-methyl-L-alanine. It is then suggested that the inherent chirality of the cavity will determine the stability of the formed complexes. A predominance of the (S)-2POii-L-amino acid lets infer that this complex is more stabilized, and thus more prone to form, than the corresponding (R)-2POii-L-amino acid complex.
The latter is presumably formed at minor extent because of the lower stability of the complex, likely originating from a more disordered allocation of the amino acid molecules in the cavity of the R-cavitand enantiomer. A better resolution would be accomplished by more finely designing the chemical structure of the cavitand. In analogy with enzyme active sites, the introduction of bridging functional groups that can selectively interact with specific residues on the guest molecule should lead to a better stability of the related host-guest complex, and thus to its preferential formation. In this contest, orientation of such bridging groups at the cavity upper rim is a fundamental issue to be taken into account.
Moreover, the efficiency of the chiral resolution could be enhanced by recycling the amino acid-functionalized nanoparticles and repeating the enantioselective separation on the fraction that contains only a minority amount of one of the enantiomers.

5.4. Conclusions

The work described in this chapter illustrated the functionalization approach to fabricate chiral iron oxide nanoparticles. Enantiopure N-methyl-L-alanine was covalently grafted on iron oxide nanoparticles surface using APTMS as coupling agent. The covalent character of the functionalization was a fundamental requirement for the target application of the fabricated system. Such functionalization was designed with the purpose of fabricating a recoverable device for a rapid and facile chiral resolution of cavitand racemates. Inherently chiral phosphonate cavitands were demonstrated to exhibit outstanding enantioselective recognition properties, discriminating among enantiomers of a given chiral guest. The reversibility of the formed complex implies that, upon

dissociation of the latter, the selectively bound cavitand species will be recovered and isolated. Consequently, the amino acid-functionalized magnetic nanoparticles might be reutilized in further chiral separations. The covalent character of the organic functionalization will likely ensure the recyclability of the magnetic device. Chromatographic enantioseparation performed by analytical chiral HPLC revealed that enantioselective recognition was successfully achieved at nanoparticles surface. Particularly, it was observed that the formation of the (S)-cavitand-L-amino acid host-guest complex is preferentially formed over the (R)-cavitand-L-amino acid host-guest complex.

Therefore, it was demonstrated that by functionalizing iron oxide nanoparticles with an enantiopure N-methyl-amino acid it is possible to fabricate a recoverable device for a fast and facile chiral resolution of cavitand racemates.

More detailed investigation is still ongoing in our laboratories to fully characterize and optimize the surface chemical properties of the chiral-functionalized nanoparticles in order to favour a more efficient chiral resolution.

5.5. Bibliography

(1) Cram, D. J.: Cavitands: Organic Hosts with Enforced Cavities. *Science* **1983**, *219*, 1177-1183.

(2) Pinalli, R.; Suman, M.; Dalcanale, E.: Cavitands at Work: From Molecular Recognition to Supramolecular Sensors. *European Journal of Organic Chemistry* **2004**, *2004*, 451-462.

(3) Pinalli, R.; Dalcanale, E.: Supramolecular Sensing with Phosphonate Cavitands. *Accounts of Chemical Research* **2012**, *46*, 399-411.

(4) Biavardi, E.; Tudisco, C.; Maffei, F.; Motta, A.; Massera, C.; Condorelli, G. G.; Dalcanale, E.: Exclusive recognition of sarcosine in water and urine by a cavitand-functionalized silicon surface. *Proceedings of the National Academy of Sciences* **2012**, *109*, 2263-2268.

(5) Pinalli, R.; Barboza, T.; Bianchi, F.; Massera, C.; Ugozzoli, F.; Dalcanale, E.: Detection of amphetamine precursors with quinoxaline-bridged cavitands. *Supramolecular Chemistry* **2013**, *25*, 682-687.

(6) Amato, M. E.; Ballistreri, F. P.; D'Agata, S.; Pappalardo, A.; Tomaselli, G. A.; Toscano, R. M.; Sfrazzetto, G. T.: Enantioselective Molecular Recognition of Chiral Organic Ammonium Ions and Amino Acids Using Cavitand–Salen-Based Receptors. *European Journal of Organic Chemistry* **2011**, *2011*, 5674-5680.

(7) Vachon, J.; Harthong, S.; Dubessy, B.; Dutasta, J.-P.; Vanthuyne, N.; Roussel, C.; Naubron, J.-V.: The absolute configuration of an inherently chiral phosphonatocavitand and its use toward the enantioselective recognition of l-adrenaline. *Tetrahedron: Asymmetry* **2010**, *21*, 1534-1541.

(8) Brotin, T.; Guy, L.; Martinez, A.; Dutasta, J.-P.: Enantiopure Supramolecular Cages: Synthesis and Chiral Recognition Properties. In *Differentiation of Enantiomers II*; Schurig, V., Ed.; Springer International Publishing, 2013; Vol. 341; pp 177-230.

(9) Pappalardo, A.; Amato, M. E.; Ballistreri, F. P.; Tomaselli, G. A.; Toscano, R. M.; Trusso Sfrazzetto, G.: Pair of Diastereomeric Uranyl Salen Cavitands Displaying Opposite Enantiodiscrimination of α-Amino Acid Ammonium Salts. *The Journal of Organic Chemistry* **2012**, *77*, 7684-7687.

(10) Li, N.; Yang, F.; Stock, H. A.; Dearden, D. V.; Lamb, J. D.; Harrison, R. G.: Resorcinarene-based cavitands with chiral amino acid substituents for chiral amine recognition. *Organic & Biomolecular Chemistry* **2012**, *10*, 7392-7401.

(11) Mann, E.; Rebek Jr, J.: Deepened chiral cavitands. *Tetrahedron* **2008**, *64*, 8484-8487.

(12) Soncini, P.; Bonsignore, S.; Dalcanale, E.; Ugozzoli, F.: Cavitands as versatile molecular receptors. *The Journal of Organic Chemistry* **1992**, *57*, 4608-4612.

(13) Vysotsky, M.; Schmidt, C.; Böhmer, V.: Chirality in calixarenes and calixarene assemblies In *Advances in supramolecular chemistry*; G., G., Ed., 2000; Vol. 7.

(14) Vachon, J.; Harthong, S.; Jeanneau, E.; Aronica, C.; Vanthuyne, N.; Roussel, C.; Dutasta, J.-P.: Inherently chiral phosphonatocavitands as artificial chemo- and enantio-selective receptors of natural ammoniums. *Organic & Biomolecular Chemistry* **2011**, *9*, 5086-5091.

(15) Szumna, A.: Inherently chiral concave molecules-from synthesis to applications. *Chemical Society Reviews* **2010**, *39*, 4274-4285.

(16) Laurent, S.; Forge, D.; Port, M.; Roch, A.; Robic, C.; Vander Elst, L.; Muller, R. N.: Magnetic Iron Oxide Nanoparticles: Synthesis, Stabilization, Vectorization, Physicochemical Characterizations, and Biological Applications. *Chemical Reviews* **2008**, *108*, 2064-2110.

(17) Turcheniuk, K.; Tarasevych, A. V.; Kukhar, V. P.; Boukherroub, R.; Szunerits, S.: Recent advances in surface chemistry strategies for the fabrication of functional iron oxide based magnetic nanoparticles. *Nanoscale* **2013**, *5*, 10729-10752.

(18) Frey, N. A.; Peng, S.; Cheng, K.; Sun, S.: Magnetic nanoparticles: synthesis, functionalization, and applications in bioimaging and magnetic energy storage. *Chemical Society Reviews* **2009**, *38*, 2532-2542.

(19) Lu, A.-H.; Salabas, E. L.; Schüth, F.: Magnetic Nanoparticles: Synthesis, Protection, Functionalization, and Application. *Angewandte Chemie International Edition* **2007**, *46*, 1222-1244.

(20) Miles, W. C.; Goff, J. D.; Huffstetler, P. P.; Reinholz, C. M.; Pothayee, N.; Caba, B. L.; Boyd, J. S.; Davis, R. M.; Riffle, J. S.: Synthesis and Colloidal Properties of Polyether−Magnetite Complexes in Water and Phosphate-Buffered Saline. *Langmuir* **2008**, *25*, 803-813.

(21) Biavardi, E.; Battistini, G.; Montalti, M.; Yebeutchou, R. M.; Prodi, L.; Dalcanale, E.: Fully reversible guest exchange in tetraphosphonate cavitand complexes probed by fluorescence spectroscopy. *Chemical Communications* **2008**, 1638-1640.

(22) Dionisio, M.; Maffei, F.; Rampazzo, E.; Prodi, L.; Pucci, A.; Ruggeri, G.; Dalcanale, E.: Guest-controlled aggregation of cavitand gold nanoparticles and N-methyl pyridinium-terminated PEG. *Chemical Communications* **2011**, *47*, 6596-6598.

(23) Pinna, N.; Grancharov, S.; Beato, P.; Bonville, P.; Antonietti, M.; Niederberger, M.: Magnetite nanocrystals: Nonaqueous synthesis, characterization, and solubility. *Chemistry of Materials* **2005**, *17*, 3044-3049.

(24) Yebeutchou, R. M.; Dalcanale, E.: Highly Selective Monomethylation of Primary Amines Through Host−Guest Product Sequestration. *Journal of the American Chemical Society* **2009**, *131*, 2452-2453.

(25) Posthumus, W.; Magusin, P.; Brokken-Zijp, J. C. M.; Tinnemans, A. H. A.; van der Linde, R.: Surface modification of oxidic nanoparticles using 3-methacryloxypropyltrimethoxysilane. *Journal of Colloid and Interface Science* **2004**, *269*, 109-116.

(26) Du, H.; Hamilton, P. D.; Reilly, M. A.; d'Avignon, A.; Biswas, P.; Ravi, N.: A facile synthesis of highly water-soluble, core–shell organo-silica nanoparticles with controllable size via sol–gel process. *Journal of Colloid and Interface Science* **2009**, *340*, 202-208.

(27) Smith, A. L.: Infrared spectra-structure correlations for organosilicon compounds. *Spectrochimica Acta* **1960**, *16*, 87-105.

(28) Aissaoui, N.; Bergaoui, L.; Landoulsi, J.; Lambert, J.-F.; Boujday, S.: Silane Layers on Silicon Surfaces: Mechanism of Interaction, Stability, and Influence on Protein Adsorption. *Langmuir* **2011**, *28*, 656-665.

Chapter 6

Gold-iron oxide hetero-nanostructures by colloidal non-aqueous chemistry

6.1. Introduction

6.1.1. Metal-metal oxide hybrid nanomaterials: state of the art

The increasing demand of material featuring advanced physical and chemical properties and multifunctionalities powered efforts in nanomaterial science toward the fabrication of hybrid nanomaterials[1].

Hybrid multifunctional nanomaterials are typically composite materials consisting of several distinct phases of which each contributes a different function. The combination in a unique material of several different phases with varying properties, such as optical, magnetic, catalytic, or electronic paves the way to fabricate objects which possess novel or enhanced properties and functionalities and which are able to perform multiple tasks. The novel acquired properties and functionalities can not be identified in the individual material components and are induced by electronic, electrochemical, magnetic, mechanical, or optical interactions between them.

Several examples of hybrid nanomaterials exist such as metal-magnetic metal oxide, metal-semiconductor, magnetic metal oxide-semiconductor that can arrange into various morphologies including core-shell, peanut-like, dumbbell-like, and more complex structures[1,2].

The synthesis of hetero-functional materials through a combination of structurally or chemically different materials on a confined space of few nanometers is still very challenging[3].

It indeed requires a synthesis approach that is capable of controlling the decoration or the deposition of a material at atomic scale whilst preserving the characteristic properties of the combined interacting phase.

However, the main challenge is to avoid the isolated nucleation (homonucleation) of the diverse component phases while promoting the nucleation and growth of one material onto previously formed particles of the desired counterpart phase (heteronucleation)[1].

The most reported processes to fabricate hetero-nanostructures are multistep approaches all of them referring to the more general “seed mediated growth” method[4].

The “seed mediated growth” method consists in adding the suited precursor into a dispersion of preformed nanoparticles, which act as the nucleation seeds for the second material (figure 6.1).

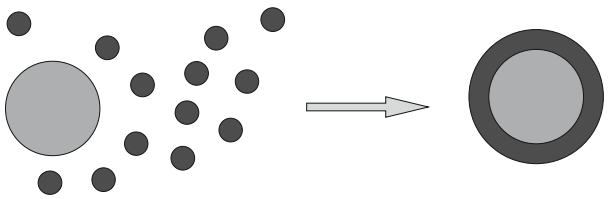

Figure 6.1: Schematic representation of the growth of a shell layer onto preformed seed through the "seed mediated growth" approach.

Control over the reaction conditions is needed in order to avoid isolated nucleation of the second material while promoting its deposition and growth preferentially on the seeds. Nevertheless, several difficulties make this process challenging, such as strain and lattice incompatibility between the two phases[3].

The preferential occurrence of heteronucleation over homonucleation is regulated by the activation energies characterizing the two phenomena. In general, wetting of the seed from the second phase will be achieved only in the condition where the activation energy of the heteronucleation process is lower than the one of the homonucleation[4].

The relationship between the free energies of substrate, interface and "coating" material (σ_s, σ_i and σ_f, respectively) sets the conditions for the heteronucleation to take place and regulates the typologies of coating, either by a continuous layer or by island[5].

In general, a continuous layer coating is achieved when the seed free energy is higher than the other terms (eq. 6.1); the opposite condition determines the growth of the coating material by islands.

$$\sigma_s > \sigma_i + \sigma_f \qquad \text{(eq. 6.1)}^{5}$$

Remarkable modifications of free energies balance and consequently of the balance between activation energies might be accomplished by introducing another element which is able to lower the surface free energy of the substrate. This role is usually taken over by a third species, which may be an organic molecule (ligand), that adsorb preferentially at the seed surface[3,5].

Condition for this purpose is for the ligands to bear at least one functional group showing affinity for the substrate material (e.g. carboxylic acid are largely employed for metal oxides). Usually, surfactants are largely present at the seeds surface for stabilizing them against aggregation. Indeed, aggregation would determine the loss of those properties peculiar of nano-sized materials and will prevent the formation of hybrid material with a defined structure[1]. However, large amounts of surfactants might represent a drawback since they could render the substrate surface inaccessible. Moreover, ligand presenting a too high binding affinity for the substrate might prevent the nucleation of the desired combined phase at the facets they adsorb on[4]. Preferential binding of some stabilizers at specific crystal facets was employed for site-preferential heterogeneous nucleation of secondary material domains leading to anisotropic hybrid materials[1,4].

It might be suggested that a surfactant dynamic adsorption/desorption mechanism could favour the growth of the secondary phase potentially over all of the crystal facets[3,6].

However, the real role of surfactants and the mechanism through which they might improve the fabrication of hybrid materials was not elucidated yet.

The broad range of material combinations and consequently the variety of experimental conditions optimized for each specific system render extremely complicate to depict a general role of surfactants. As an example, the growth of iron oxide (either maghemite or magnetite) shell onto metal and metal oxide nanoparticles through the thermal decomposition of iron pentacarbonyl ($Fe(CO)_5$) is largely investigated[7]. In this case few binary or ternary mixtures of surfactants, which are common to several procedures, are employed. While some authors suggest that desorption and eventual decomposition of the surfactants would occur at the high reaction temperature (usually above 200°C), thus excluding the possibility of a real participation in hybrid nanocrystals formation[3], other authors suggest that their interplay regulates the composite fabrication. For instance, some hypothesized that while specific ligands are needed in order to stabilize formed particles or even to promote particles formation, others have the role of modulating the accessibility of the diverse surfaces[6].

In other cases, surfactants are intentionally used to promote the assembly of composite materials. By adsorbing oppositely charged polymers at the surface of preformed particles of two or more phases, it is possible to drive their arrangement into the desired composite by electrostatic interactions[8].

As an alternative to "seed mediated growth" processes, hybrid nanocrystals can be synthesized through one-pot procedures.

A one-pot approach consists in placing all the reactants participating to the synthesis of the desired material in the same growing medium at the same time, as depicted in figure 6.2.

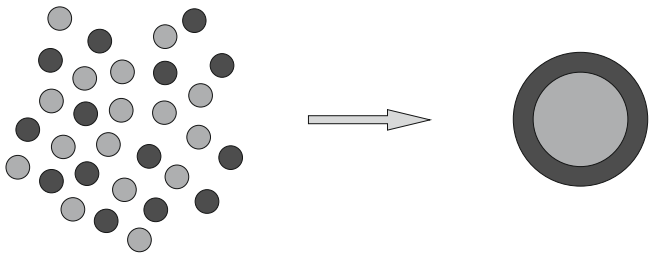

Figure 6.2: Schematic representation of a one-pot strategy for the synthesis of inorganic hetero-structured nanoparticles.

Appropriate reaction conditions have to be set in order to generate the materials in two distinct moments, but the growth of the secondary phase has to be achieved only upon its selective heterogeneous nucleation onto the surface of *in-situ* preformed particles of the counterpart material.

Although one-pot procedures benefit of several advantages when compared to multi-step strategies, such as the reduction of the number of steps (both related to the synthesis of the seed and its purification) and likely the fewer reactants involved, they are referred to be even more challenging than seeded approach[3]. In one-pot approaches indeed, the interpretation of the formation mechanism and the consequent rational manipulation of experimental conditions are complicated by the interplay of all the variables involved. For this reason, one-pot approaches are scarcely investigated.

Metal-metal oxide hetero-nanostructures are largely investigated because they can find application in a wide range of fields, from biomedicine to catalysis. Biomedical applications include imaging (magnetic resonance imaging or dual imaging) and therapeutic applications, such as hyperthermia[9].

Coupling metals with metal oxides was observed to significantly enhance the catalytic properties of the metal centre. Therefore, many researchers have focused on the synthesis of highly dispersed metal catalysts supported on metal oxides[10]. Although it is accepted that the enhancement of the catalytic properties lies in the connection between the two phases, the reasons why interactions with metal oxides could enhance the catalytic properties of metal nanoparticles are not fully elucidated yet. The hypotheses brought forward are: (i) the metal oxide support modifies the electronic structure of the metal, (ii) new reaction sites appear at the metal-metal oxide perimeter interface, and (iii) presence of a surface thin layer of the oxide of the investigated metal as the active material[11].

Pt, Pd and Ru are among the most studied metals and are often coupled with iron oxide (either Fe_2O_3 or Fe_3O_4), alumina (Al_2O_3), silica (SiO_2), and ceria (CeO_2) for applications in water gas shift reactions and oxygen reduction rections[12,13]. However, the high cost of those metals powered the effort for developing analogous catalysts based on cheaper and eventually more abundant elements, such as gold[14]. In 1989 Haruta and coworkers[15] demonstrated that gold nanoparticles acquire enhanced catalytic properties towards several reactions, when coupled to metal oxide supports. Au-Fe_2O_3 was one of the first composite materials to be studied and to show catalytic activity for carbon monoxide (CO) oxidation, which is still the most investigated model reaction[16,17]. CO oxidation is likely the simplest model reaction that allows evaluating the properties of a catalyst, since few theories were reported for the adsorption of CO and mechanism of it oxidative catalysis. Moreover, it shows practical importance due to its connection with the purification of engine exhaust gases[11].

Finally, coupling gold with a magnetic metal oxide such as iron oxide particles would provide a recoverable catalyst by magnetic separation.

Noble metal-semiconductor metal oxide structures also exhibit specific photocatalytic properties, such as in the case of gold@titania hetero-nanostructures (Au@TiO_2)[18]. They are also suitable sensor materials[19] or alternative anode materials for Li-ion batteries (e.g. gold@tin oxide, Au@SnO_2)[20,21].

6.1.2. Gold-iron oxide hetero-nanostructures: state of the art and perspective

As mentioned in the previous paragraph, gold-iron oxide composites present peculiar properties that render them suitable for numerous diverse applications, from catalysis to biomedical devices.

By simply varying the experimental approach, heterostructures showing diverse morphologies can be synthesized[2,8,22].

The creation of a core@shell structure is intriguing because it represents a way to stabilize the core particles against aggregation and sintering while preserving its chemical and physical properties[23,24].

Iron oxide-core@gold-shell particles are largely investigated as biomedical devices for medical imaging, since the magnetic core may act as contrast agent[25]. Moreover, the gold shell protects the metal oxide core from oxidation and allows the further immobilization of biomolecules through the characteristic and strong gold-sulfur interaction[26]. In this way, a multifunctional biomedical device may be obtained[9].

The opposite configuration, namely gold-core@iron oxide-shell, is less investigated partially because of the more challenging fabrication. However, the material presents potential applicability as a recoverable catalyst. One of the main drawbacks of using metal particles as catalysts lies in their ease of sintering during working conditions, and consequent loss or decrement of catalytic properties. A porous oxide shell would prevent the metal core from aggregation and, at the same time, allow the reactants to interact with the metal-catalyst interface[9].

Dumbbell-like structures are even more appealing because, while the fundamental contact between the two phases is not compromised, both the component materials expose part of their surface to the surrounding environment. The concurrent accessibility of both the phases allows for further functionalization of the metal and metal oxide surfaces, thus providing a multifunctional material[27]. For this reason, dumbbell-like structures are promising for several different fields of applications. It was demonstrated that gold-magnetite (Au-Fe_3O_4) dumbbell-like particles present catalytic activity in hydrogen peroxide reduction[28] and could be used as bifunctional biological probes[29].

The aforementioned structures are usually fabricated by "seed mediated growth" approaches. For that purpose, gold nanoparticles (*seeds*) are often synthesized through aqueous routes. The most used is the "citrate-route", developed by Turkevich in 1951[30], which provides gold particles in a narrow size distribution. Moreover, particles size can be easily controlled by acting on the reactants ratio[31]. Other largely adopted aqueous routes employ sodium borohydride or ascorbic acid as reducing agents for a faster reduction of gold(III) species, thus obtaining usually rather small particles[32].

On the contrary, non-aqueous synthetic procedures are less investigated. Among them, the phase transfer method developed by Brust and Schiffrin[33] and some polyol methods (e.g. using ethylene glycol[34]) are the more utilized. Recently few formamide methods[35,36] have emerged, but they often consist in complicated steps. However, it is believed that non-aqueous media might allow reduction of metal precursors at more moderate conditions than traditional aqueous routes and could result in higher colloid uniformity than in an aqueous systems[35].

On the contrary, several non-aqueous approaches that permit to easily synthesize various metal oxide nanoparticles were developed in the last decades[37-39]. For example, highly crystalline and homogeneous metal oxide nanocrystals are obtained through the so-called "benzyl alcohol route"[40,41]. Non-aqueous routes are often employed for the fabrication of heterostructures through the synthesis of metal oxide nanoparticles in presence of metal seeds[28]. In other cases, they provide nanoparticles that can be assembled with the preformed metal counterpart in heterostructures using appropriate organic ligands. Molecules bearing charged groups were used to assemble preformed metal and iron oxide

nanoparticles by electrostatic interactions[8,42]. Assembly was obtained also employing bifuncional molecules bearing two functionalities which show specific affinity for the component materials[43].

The main purpose of this project consists in investigating whether it is possible to extend the well-known "benzyl alcohol route" to the production of metal nanoparticles. Particularly, the present work will be focused on the development of a novel non-aqueous one-pot synthesis route for the fabrication of gold-iron oxide hetero-nanostructures.

Attention will be dedicated to the investigation of the role that several reaction parameters might have in determining the structural properties of the final materials. One of the objectives is indeed to develop a reliable synthesis strategy to gold-metal oxide composite materials presenting structural and morphological properties that depend on the experimental conditions. For this purpose, the role of surfactant will be also investigated.

In particular, in order to try to understand whether organic ligands act as intermediaries in the formation of the desired material, their use will be limited to remarkably lower amount compared to other strategies traditionally used[23]. Moreover, avoiding large excess of surfactant is believed to not remarkably affect the properties of the hybrid material, thus representing an advantage[44].

The process will be performed using a microwave-assisted technique because it should represent a more selective, faster and cleaner alternative with respect to conventional heating [45].

Microwave-assisted synthesis is a technique well known in organic chemistry that only in recent time has been applied to the fabrication of inorganic materials[46]. The main advantage of using microwave-assisted technique for the synthesis of inorganic materials relies in the possibility of remarkably reducing reaction times to hours or minutes, with respect to the more time-consuming traditional strategies. On the contrary of traditional strategies, which usually provide a slow heating of the reaction mixture and formation of temperature gradients, microwave irradiation promotes a rapid heating and more uniform bulk reaction temperatures. This is referred to as the thermal effects associated to microwave-assisted procedures[47]. In addition to thermal effects, non-thermal and specific effects are usually regarded as the distinctive characteristics of this technique. Non-thermal and specific effects are regarded as deriving from the interaction of the electromagnetic field with reactants molecules or intermediates of the reaction. Therefore, non-thermal effects are regarded as independent from the bulk reaction temperature[46]. One of these effects is represented by the selective heating of strong microwave-absorbing heterogeneous species (e.g. nanoparticles) dispersed in a medium presenting significantly lower microwave-absorbing ability. Such particular effect is believed to likely promote formation of heterodimers. Indeed, it is regarded as promoting the heterogeneous nucleation of a given phase over selectively heated nanoparticles (*hot-spots*) present in the same medium[47].

Some authors suggested the existence of specific effects in view of the different properties presented by materials synthesized through microwave-assisted procedures in, apparently, the same reaction conditions used when adopting traditional heating[48]. However, comparison between microwave-

assisted and traditionally-heated synthesis route is not that straightforward. In order to properly compare the two procedures, reactions should be performed in the same conditions (temperature, stirring, heating time, addition of reactants). Usually, microwave technique presents some technical limitations, such as impossibility of a sequential addition of reactants during the course of the reaction (as in "hot-injection") or limited control on stirring, that render unlikely to reproduce a traditional synthesis route in the microwave equipment. For this reason, the existence of specific effects is still under debate[46,48].

The "benzyl alcohol route" was already investigated by microwave-assisted processes for the synthesis of metal oxide-reduced graphene oxide composites[49-51]. In those cases it was observed that the synthesis of metal oxide in presence of the carbon support led to the preferential formation of the composite material. In fact, formation of isolated metal oxide nanoparticles was seldom observed.

On this basis, a microwave-assisted procedure was adopted in order to investigate whether it could promote a more selective synthesis and consequent formation of the desired metal-metal oxide heterostructures.

6.2. Experimental section

6.2.1. Materials

Benzyl alcohol (puriss. 99%), chlorauric acid ($HAuCl_4$, hydrate 50% gold metal basis), 11-mercaptoundecanoic acid (MUA, 95%), and 12-hydroxydodecanoic acid (HDDA, 97%), were purchased from Sigma-Aldrich.

Iron(III) acetylacetonate ($Fe(acac)_3$, anhydrous 99%) and gold(III) acetate ($Au(OAc)_3$, 99.9% gold metal basis) were purchased from STREM and Alfa Aesar, respectively.

All the products were stored in a glovebox and used as received.

6.2.2. Methods

The synthesis of Au-Fe_xO_y heterostructures was carried out by using $Fe(acac)_3$ as the metal oxide precursor and investigating the role of $HAuCl_4$ and $Au(OAc)_3$ as the metal precursors.

The experimental procedure employed for all of the investigated systems is the following: a benzyl alcohol solution of $Fe(acac)_3$, the proper metal precursor and organic ligand (when used) was prepared in a glass vial suitable for microwave instrument. The preparation of the reaction mixture was carried out in a glovebox (H_2O< 0.1 ppm, and O_2< 0.1 ppm). The reaction took place in a laboratory CEM Discover SP microwave at the reaction conditions depicted in Tables 6.1-6.2.

The resulting material was collected by centrifugation and thoroughly washed with ethanol. Upon purification, the precipitate was redispersed in 5 ml of ethanol and stored for further characterizations.

Table 6.1: Experimental conditions investigated in some selected synthesis tests of Au-Fe_xO_y heterostructures using $HAuCl_4$ as the metal precursor.

Concentration $HAuCl_4$ (mM)	Molar ratio $HAuCl_4/Fe(acac)_3$	Molar ratio HDDA/$HAuCl_4$	Molar ratio MUA/$HAuCl_4$	Molar ratio HDDA/MUA	T (ºC)	Time (min)
0.5	-	-	-	-	170	30
0.5	0.42	-	-	-	170	30
0.5	0.42	2.12	-	-	80-130-170	30-30-20
0.5	0.42	2.12	-	-	130-170	30-20
0.5	0.42	2.12	-	-	170	30
0.5	0.42	-	2.5	-	170	30
0.5	0.42	2.12	1.06	2	170	30
0.5	0.42	2.12	2.12	1	170	30

Table 6.2: Experimental conditions investigated in some selected synthesis tests of Au-Fe_xO_y heterostructures using $Au(OAc)_3$ as the metal precursor.

Concentration $Au(OAc)_3$ (mM)	Molar ratio $Au(OAc)_3/Fe(acac)_3$	Molar ratio HDDA/ $Au(OAc)_3$	T (ºC)	Time (min)
1.3	-	-	170	30
1.3	1.0	-	170	30
1.3	1.0	1.3	170	30
1.3	1.0	2	170	30
1.3	1.0	2.5	170	30
1.3	2.2	2.5	170	30
1.3	1.5	2.5	170	30
1.3	1.0	2.5	170	30
1.3	0.5	2.5	170	30

6.2.3. Characterization techniques

Ultraviolet-Visible (UV-Visible) spectroscopy was used in order to analyze the optical properties of gold particles by monitoring their characteristic surface plasmon resonance band. Spectra were acquired on a V-560 Jasco spectrophotometer at room temperature and over the wavelength range of 900-400 nm. The spectra were measured for the ethanol dispersion of the purified materials using a quartz cuvette with an optical path length of 1 cm.

Transmission electron microscopy (TEM) analysis was performed to investigate the size and shape distribution of gold nanoparticles and especially to determine the formation of the desired heterostructures. It provides complementary information to the measured optical properties. It was carried out on a H9000-NA (Hitachi) microscope operating at an acceleration voltage of 300 kV and equipped with Bruker Nano XFlash silicon drift detector. Some materials were analyzed with a Philips CM200 (LaB_6) microscope operating at an acceleration voltage of 200 kV. Electron diffraction and energy dispersive X-ray (EDX) spectroscopy analyses were performed in order to identify the crystallographic phase of the heterostructures component materials and the presence of the

corresponding characteristic elements. The samples were prepared by depositing a drop of ethanol dispersion on a 300 mesh carbon film-coated copper grids. The solvent was allowed to evaporate prior to the analysis.

6.3. Results and discussion

The possibility of extending the "benzyl alcohol route" to the synthesis of gold nanoparticles was investigated by employing two different gold precursors, particularly the traditional chlorauric acid ($HAuCl_4$) and the more rarely used gold (III) acetate ($Au(OAc)_3$). The results will be described in two separate sections, each one dedicated to one gold precursor.

6.3.1. $HAuCl_4$ as metal precursor

$HAuCl_4$ is the most used gold precursor and its reduction in the presence of appropriate reducing agent leads to gold nanoparticles with tunable properties both in aqueous (e.g. citrate route)[30] and organic media (e.g. ethylene glycol and formamide)[33-36].

The first tests were performed in absence of any organic ligands and using iron(III) acetylacetonate ($Fe(acac)_3$) as metal oxide precursor due to its well known reactivity in benzyl alcohol[52]. It is expected that benzyl alcohol would act as reducing agent for the gold precursor, due to the possibility for hydroxyl groups to undergo oxidation; therefore no further reducing species was added.

Several reaction parameters such as time and molar ratio between the reactants were investigated. The obtained material was characterized by UV-Visible spectroscopy in order to monitor the position of the gold surface plasmon resonance (SPR) band. The latter is influenced by the size, shape and surrounding environment of gold nanoparticles, hence it is diagnostic of the properties of the material[53].

Complementary information to optical properties will be provided by TEM analysis. TEM images will allow determining gold and iron oxide particles size distribution and shape. Moreover, TEM analysis will help elucidating whether observed shifts in the SPR band position arose from the formation of a gold-iron oxide heterostructure.

Due to the low amount of synthesized material it was not possible to perform XRD measurements and hence determine the crystallographic phase of the synthesized iron oxide. For this reason, the general denomination "Fe_xO_y/iron oxide" will be used from here on to refer to the oxide phase.

Figure 6.3a shows the comparison between the optical properties of gold particles synthesized both in absence and presence of the metal oxide precursor.

In detail, those samples were synthesized at 170ºC for 30' using chlorauric acid at the concentration of 0.5 mM and a molar ratio $HAuCl_4/Fe(acac)_3$ of 0.42.

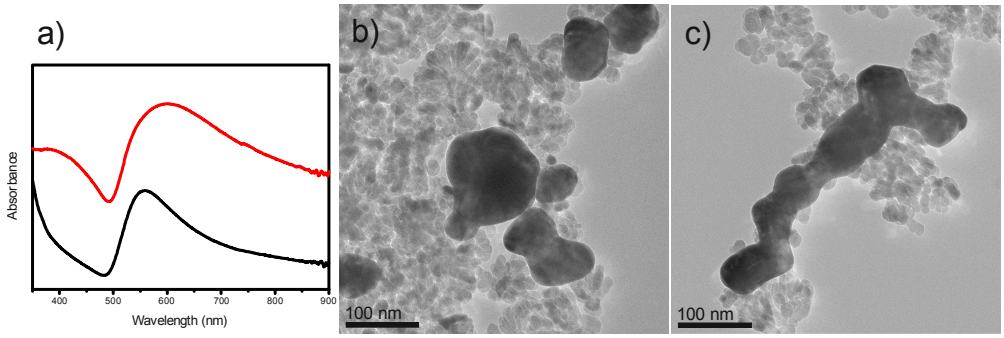

Figure 6.3: (a) UV-Visible spectra of gold nanoparticles synthesized in absence (black line) and in presence (red line) of $Fe(acac)_3$. TEM images of gold nanoparticles synthesized in presence of $Fe(acac)_3$ (b, c).

A red shift of the plasmon resonance band occurred when gold is synthesized in presence of the metal oxide precursor (red line, figure 6.3a) suggesting that either a change in the size and shape of the metal nanoparticles or a change in their surrounding environment took place. TEM images (figure 6.3b, c) show two distinct materials. The particles characterized by a darker contrast are identified as gold while the metal oxide provides a lighter contrast. As observed by TEM images, gold nanoparticles tent to melt in wire-like structures which transversal section ranges from 50 to 80 nm. Those structures are not homogeneous in shape, length and diameter and sometimes they evolved arranging in network arrays.

When the synthesis was performed using iron(III) acetylacetonate, gold particles resulted to be often surrounded by numerous iron oxide nanoparticles. However, the final material appeared simply as a mixture of the two components. Indeed, iron oxide looked randomly distributed around gold nanoparticles and no element (e.g. well-defined morphology) suggesting the formation of a hybrid material was noted.

It is suggested that the arrangement of gold into wire-like structures is likely due to concomitant effects. On the one hand, it is suggested that slow reduction of the Au(III) species by benzyl alcohol could determine a slow nucleation step and the consequent sintering of the nuclei into aggregates. Moreover, un-reacted Au(III) or Au(I) species will gradually lead to the increase of the particles size or, as hypothesized in the literature, could favour their aggregation. Some authors suggested that wire-like structures might form from the deposition of Au(I) species or gold clusters on the surface of neighbouring particles. The further reduction of Au(I) species might lead to the formation of areas of amorphous gold acting as a glue that sticks particles together in a wire-like or networked wire-like structure[54-57]. Therefore, it is expected that a faster reduction of the metal precursor should lead to a higher number of nuclei and likely to a more restrained particle size growth and aggregation. On the other hand, aggregation should be limited whether the synthesis takes place in presence of a stabilizing agent.

Based on these considerations, it was decided to introduce an organic molecule that should act as stronger reducing agent for the gold salt, as stabilizer for the metal nanoparticles, and as intermediary in the growth of the metal oxide onto the metal surface.

Two molecules were investigated both separately and together: 12-hydroxydodecanoic acid (HDDA) and 11-mercaptoundecanoic acid (MUA). The reasons of choosing those ligands are several:

- the presence of two different terminal functional groups which present different affinity toward the metal and metal oxide;
- hydroxyl and thiol moieties can interact with the metal promoting stabilization against aggregation. Moreover, hydroxyl and thiol functionalities are believed to interact at different strength with the metal phase, and this would give valuable information on the role of the ligand in the heterostructure formation;
- hydroxyl functionalities can undergo oxidation, favouring reduction of the gold salt;
- finally, the carboxylic acid might interact with the metal oxide promoting its selective heteronucleation on the gold surface.

When only HDDA was used, the formation of flower-like structures was observed. Initially, experiments varying the reaction temperature profile were performed with the aim to promote the formation of isolated gold particles prior to the metal oxide nucleation. Therefore, the reaction temperature was varied between the optimal conditions for the synthesis of the two isolated materials (80ºC and 170ºC for gold and iron oxide, respectively). Three different temperature profiles were tested. The first one consists of three consecutive steps: one at low temperature in order to favour the nucleation of gold (80°C), an intermediate step at 130°C to create a heating ramp and thus separate the formation and growth of gold particles from iron oxide nucleation, and the last step at the temperature at which usually the synthesis of Fe_3O_4 (magnetite) takes place (170°C). The second temperature profile presents only two steps, at 130°C and 170°C and the third test was performed at the constant temperature of 170°C. Gradual removal of the lower temperature steps was adopted in order to promote a faster reduction and nucleation of gold. Moreover, it should shorten the time interval separating gold particles formation and metal oxide nucleation, hence limiting aggregation of gold particles into wire-like structures.

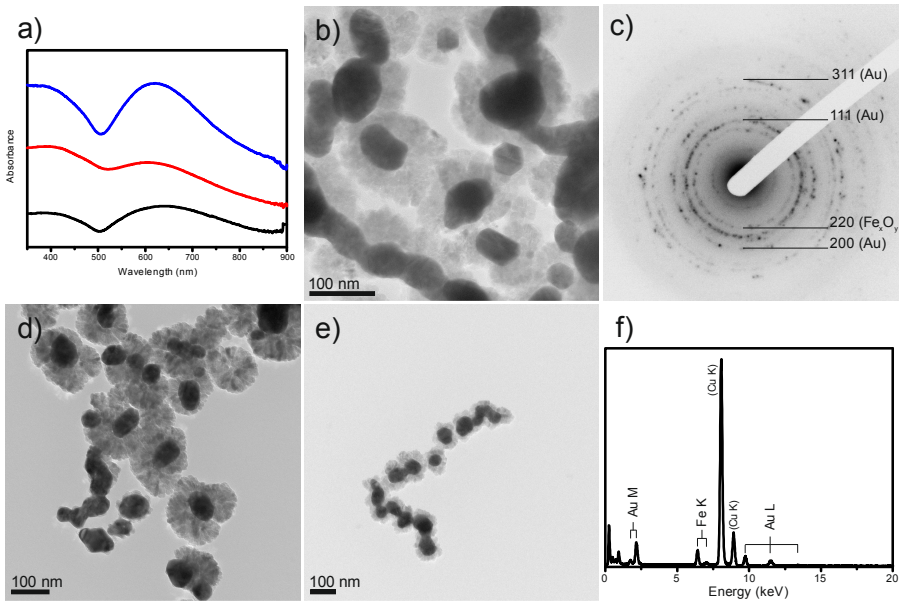

Figure 6.4: (a) UV-Visible spectra of Au-Fe_xO_y nanoparticles synthesized at a 3-steps temperature profile (80-130-170°C, black line), at a 2-steps temperature profile (130-170°C, red line) and at constant temperature (170°C, blue line). TEM images of the corresponding Au-Fe_xO_y particles synthesized at 80-130-170°C (b), at 130-170°C (d), and at 170°C (e). Electron diffraction patterns (c) measured for the material showed in (b). EDX spectrum (f) of the material showed in (e).

Figure 6.4 shows the optical properties and TEM images representative of the aforementioned samples. Electron diffraction analysis showed in figure 6.4c presents patterns partially ascribable to metallic gold. Due to the overlap of some of the characteristic patterns of both metallic gold and iron oxide (either in the magnetite or maghemite phase), a full assignment of the observed diffraction rings could not be unequivocally assessed. Nevertheless, presence of iron is confirmed by energy dispersive X-ray (EDX) spectroscopy data (figure 6.4f). It is possible to observe that in all cases, gold@iron oxide flower-like core@shell structures were obtained. Gold particles are partially organized in irregular wire-like structures, and the oxide shell always appears as discontinuous (flower-like morphology) and not homogeneous in thickness. The size range of gold core diameter or transversal section for quasi-spherical and wire-like particles respectively are reported in table 6.3, together with the iron oxide shell thickness.

Table 6.3: Experimental conditions, gold particles size and iron oxide shell thickness for the Au-Fe_xO_y materials synthesized at different temperature profiles.

Experimental conditions	Material	Au particles size (nm)	Shell thickness (nm)
Concentration $HAuCl_4$= 0.5 mM Molar ratio HDDA/$HAuCl_4$= 2.12 Molar ratio $HAuCl_4$/$Fe(acac)_3$= 0.42	Au-Fe_xO_y synthesized at 80-130-170°C	Particles diameter: 33 to 75 nm Wires transversal section: 30 to 46 nm	From 15 to 44 nm
	Au-Fe_xO_y synthesized at 130-170°C	Particles diameter and wires transversal section: 38 to 56 nm	From 12 to 48 nm
	Au-Fe_xO_y synthesized at 170°C	Particles diameter: 30 to 70 nm	From 20 to 40 nm

Table 6.3 shows that no remarkable changes were achieved in gold particles size distribution and iron oxide shell thickness when varying the temperature profile.

The gradual reduction of the temperature steps apparently led to the decrease of the number of gold particles arranged in wire-like structures, as showed by TEM images (figure 6.4b, d, e). The optical properties are in agreement with the observed changes. The surface plasmon resonance band gradually blue shifted in accordance with the reduction of the temperature steps.

It could be inferred that the higher is the number of temperature steps at which the synthesis is performed, the higher is the length of time separating the formation of the two materials. This could favour the growth and aggregation of gold nuclei into wire-like structures. When the reaction was performed at the constant temperature of 170°C mostly isolated flower-like Au-Fe_xO_y particles were obtained. This could be likely due to the shorter time length separating the formation of gold nanoparticles and the heterogeneous nucleation of iron oxide. In that case, the iron oxide shell grown at gold particles surface could act as a co-stabilizer in addition to the organic ligand, preventing metal particles from aggregation.

As a further confirmation, nanoparticles underwent magnetic separation when an external magnetic field was applied, leaving a colourless supernatant. This support the observation that gold nanoparticles are embedded in the magnetic phase, which is likely composed of Fe_3O_4 or γ-Fe_2O_3 (maghemite).

On the basis of the previous results, it was decided to perform the following tests at the constant temperature of 170ºC. Other parameters such as $Fe(acac)_3$ concentration and time of reaction were investigated and the best reaction conditions were identified. It was found that the heterostructures can be synthesized within 30 minutes and a small excess of $Fe(acac)_3$ over $HAuCl_4$ is needed.

Nevertheless, gold particles always partially arranged in wire-like structures and looked rather polydisperse in size. It is suggested that the use of organic ligands showing a higher affinity for gold particles than HDDA, such as thiols, might better stabilize the growing gold particles and prevent wire-like structures formation.

The choice of examining the effect of MUA for the synthesis of the hybrid material was strengthen by the results obtained from the investigation about the synthesis of gold nanoparticles performed during a previous work. In that case, the synthesis of gold nanoparticles in benzyl alcohol and in presence of MUA was performed through traditional heating at 130°C and using a MUA-to-$HAuCl_4$ molar ratio varying between 25 and 75. The results showed in the following page refer to the highest molar ratio (75).

Rather small particles with a size varying between 4 and 7 nm in diameter were synthesized in those experimental conditions. TEM images (figure 6.5b, c) show that particles were mostly spherical and only rather short (e.g. composed of 2 to 4 particles) wire-like structures were obtained.

Colour changes could be observed during the proceeding of the reaction, suggesting that particles size and/or morphology evolved during the synthesis.

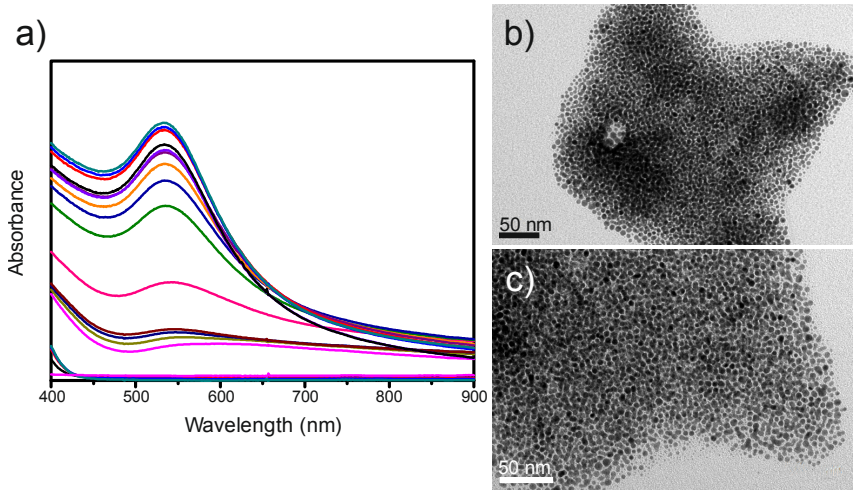

Figure 6.5: (a) UV-Visible spectra showing the shift of the surface plasmon resonance band during the synthesis of gold nanoparticles in benzyl alcohol in the presence of MUA (130ºC, 235', molar ratio $HAuCl_4$/MUA= 75). The spectra were recorded at different stages of the reaction: 0' (black line), 45', 65' (blue line), 95', 115' (pink line), 135', 165' (dark blue line), 195', 235' (cherry-like red line). TEM images of the as-synthesized particles (b, c).

The initially pale yellow reaction mixture turned gradually into colourless, grey, bluish, violet and finally ended up to a purple colour that remained unchanged during the time. Colour of gold suspensions is usually associated to particles of specific size and morphology. For instance, purple suspensions are indicative of spherical particles of about 10 nm in diameter, while blue and grey colours are representative of rod-shaped particles or wires, respectively[58].

The optical properties of the sample monitored at different stages over the entire reaction time reflect the aforementioned colour changes. When the reaction mixture appeared grey and blue flat absorption profiles were recorded (respectively, red and blue line in figure 6.5a), indicating that photons of all energies are absorbed at the same extent. Wire-like structures usually present similar optical behaviour[57]. When the mixture turned into violet, a surface plasmon band began to appear (95 minutes, green line, figure 6.5a). As the reaction proceeded, the surface plasmon band increased in intensity

until an intense peak at 550 nm, characteristic of spherical particles, was reached at the end of the reaction (235 minutes, cherry-like red line, figure 6.5a).

These considerations suggest that the synthesis likely proceeded through the initial formation of aggregated particles, such as wire-like structures, that gradually broken into individual and spherical particles. However, the latter is only a possible explanation. More information on the growth mechanism could be obtained by TEM analysis of aliquots sampled at intermediate stages of the reaction, or *in-situ* SAXS (small angle X-ray scattering) analysis.

The good stability of the final nanoparticles in solution even upon purification from the excess of ligand let infer that a thin layer of MUA was still adsorbed onto the metal nanoparticles surface limiting their aggregation.

These observations are likely driven by the high affinity showed by thiol moieties for gold and other noble metals and thus their excellent capability in stabilizing gold nanoparticles against aggregation[26].

As previously anticipated, several different hypotheses for gold wires formation were brought about in the literature, but no proposed mechanism has been accepted as general. Some studies suggest that wires formation is due to the deposition of gold nuclei or Au(I) species in the concave regions between neighbouring particles. In case of deposited Au(I) species, they might further undergo slow reduction leading, usually, to the formation of highly disordered amorphous regions composed of metallic gold. Such amorphous metallic gold regions would act as glue that sticks together gold particles into wire-like structures. The fragmentation of the wires into individual particles has not been fully elucidated yet. It has been suggested that fragmentation of wires into spherical particles could occur during the time due to interplay of Ostwald ripening and stabilization of the newly formed particles by the involved organic ligand [54-57].

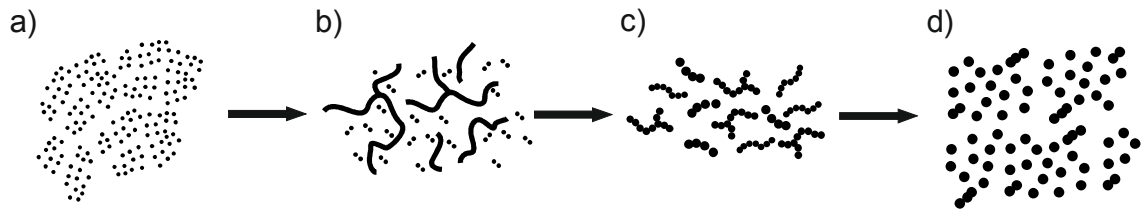

Figure 6.6: Representation of the mechanism of growth of spherical gold particles through initial wires-like structures formation. Gold nuclei grow and assemble leading to larger gold particles and wire-like structures (a, b). Subsequently wire-like structures undergo fragmentation forming shorter segments (c), which finally evolve into isolated spherical nanoparticles and few residual short wires (d).

Figure 6.6 illustrates the mechanism proposed in the literature for the formation of gold spherical particles through growth and fragmentation of wire-like structures. Gold ions are initially reduced to form gold metal nuclei, which assemble into wires and/or networked wires arrays. Subsequently, wires undergo fragmentation during the time forming short segments and finally spherical particles.

Wire-like structures observed in the described experiments might form following a similar mechanism. However, the fragmentation mechanism and the possible role that MUA might play in it have not been clearly understood yet.

When MUA was used in the fabrication of Au-Fe_xO_y material, gold nanoparticles quasi-spherical and rather polydisperse in size (from 12 to 25 nm in diameter) were formed (figure 6.7c) and appeared as embedded into an organic domain. Despite iron oxide particles were not clearly noticeable, evidence of the presence of iron was given by EDX analysis data, thus suggesting that likely rather small iron oxide particles formed. Possibly, iron oxide nanoparticles were also embedded in the observed organic domain. It must be taken into account that the purification procedure for these materials was complicated by the efficient stabilizing action of MUA on metal particles therefore it was not possible to remove all of the ligand excess, as demonstrated by TEM images.

These results significantly differ from those obtained when using only HDDA. Therefore, it is suggested that HDDA and MUA might participate in a different way to the stabilization of gold nanoparticles and heterostructures formation.

In view of the strength of the gold-sulfur interaction[26], which is almost comparable to a covalent bond, it is suggested that adsorption of MUA renders metal nanoparticles surface inaccessible to the heterogeneous growth of iron oxide.

From these considerations, a mixture of HDDA and MUA in variable ratios was investigated. Figure 6.7 illustrates a comprehensive view of the situations observed when using HDDA/MUA mixture in diverse molar ratios. Data of the particles fabricated using pure HDDA are reported for sake of comparison.

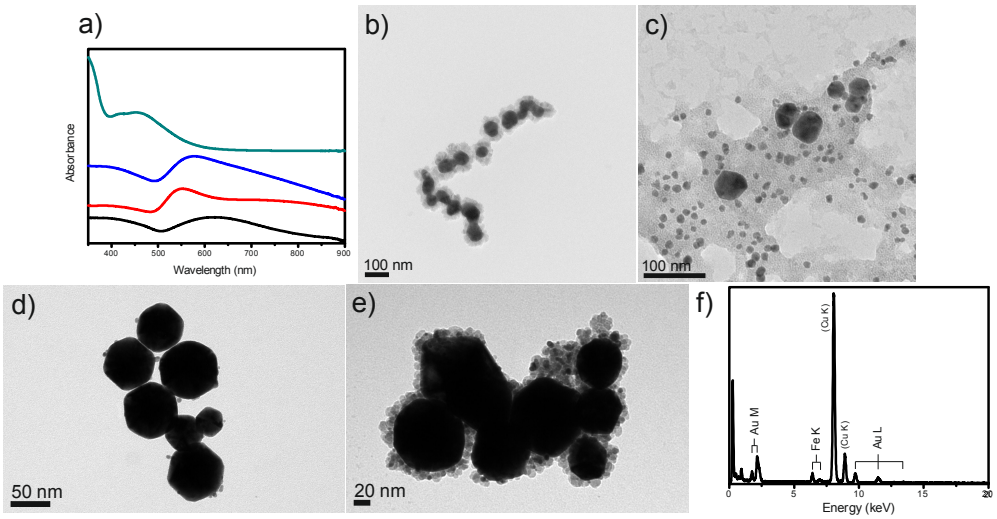

Figure 6.7: (a) UV-Visible spectra of Au-Fe_xO_y nanoparticles synthesized in presence of HDDA only (black line), using a mixture of HDDA/MUA at a molar ratio of 2 (red line) and 1 (blue line), and in the presence of pure MUA (green line). TEM images of the corresponding Au-Fe_xO_y materials synthesized using HDDA only (b), using MUA only (c), employing a HDDA/MUA molar ratio of 2 (d) and 1 (e). EDX spectrum (f) of the material showed in (c).

The introduction of MUA is reflected in the optical properties (figure 6.7a) of the as-fabricated particles. Particularly, the gold SPR band blue shifted with respect to the particles synthesized in presence of only HDDA. A blue shift is generally indicative of a reduction of particle size or of a change in the chemical environment surrounding the metal centres[53].

TEM analysis revealed that, regardless the HDDA/MUA molar ratio, no wire-like structure was obtained. However, gold particles looked rather polidisperse in size (50 to 110 nm) and shape. Interestingly, when using an excess of HDDA on MUA (HDDA/MUA of 2, figure 6.7d), almost no growth of iron oxide at gold particles surface was noticed. However, performing the reaction at a HDDA/MUA molar ratio equal to 1 led to the growth of an iron oxide shell at gold particles surface. The oxide shell looked discontinuous and not homogeneous in thickness (from 8 to 20 nm). No remarkable change in gold particle size was noticed.

The results, compared with the observations previously reported about the synthesis of gold nanoparticles in the presence of MUA, indicate that this species could have a determinant and positive role in the formation of isolated gold particles rather then wire-like structures. On the other hand, MUA seemed to prevent the heterogeneous nucleation of iron oxide. When an organic ligand is used as a stabilizing agent during the synthesis of heterodimers, it is suggested that a surfactant dynamic adsorption/desorption mechanism could favour the growth of the secondary phase at preformed particles surface[3]. Whether the stabilizing agent interacts too strongly, the surface of the coated material will result inaccessible to the deposition of any other species. This might be a possible explanation for the not-observed gold-iron oxide heterostructure when only MUA was used. This hypothesis is supported by the evidence of the growth of oxide particles when using HDDA or a mixture of the two ligands.

Indeed, interaction of hydroxyl or carboxyl groups with noble metals is regarded as weaker than the thiol-noble metal interaction and a dynamic adsorption/desorption mechanism is more plausible, especially at the temperature (170°C) at which the reaction was performed. Assuming that the ligands adsorbed simultaneously on gold particles, the latter surface would present portion loosely stabilized on which the nucleation and growth of the metal oxide might occur.
Nevertheless, detailed surface analyses (e.g. by Fourier transform infrared spectroscopy or X-ray photoelectron spectroscopy) should be performed in order to elucidate the role of the capping agents in the formation of the observed heterostructures.

6.3.2. $Au(OAc)_3$ as metal precursor

On the contrary of chlorauric acid, gold (III) acetate ($Au(OAc)_3$) is poorly investigated and only few examples report about its use in the synthesis of gold nanoparticles[59]. It is expected that the chemical nature of the gold precursor could influence its reactivity and, in turns, it might affect the properties of the deriving gold nanoparticles. For this reason, the synthesis of gold-iron oxide heterostructures was studied using gold acetate as metal precursor.
Experiments similar to the ones described in the former paragraph were performed simply replacing $HAuCl_4$ with $Au(OAc)_3$.
In view of the properties of the previously described materials, only HDDA was employed as organic ligand and its role was investigated by varying its concentration. Additionally, the effect of the metal precursor-to-metal oxide precursor molar ratio was also investigated.

The following materials were synthesized through a microwave-assisted procedure at 170°C and using, in all the situations, a constant iron(III) acetylacetonate concentration. Only HDDA concentration was varied from 0 to 3.2 mM.
Interestingly, mostly spherical gold nanoparticles were synthesized in absence of organic ligand (figure 6.8). The nanoparticles were polydisperse in size (from 5 to 20 nm), and almost no wire-like structures were observed.

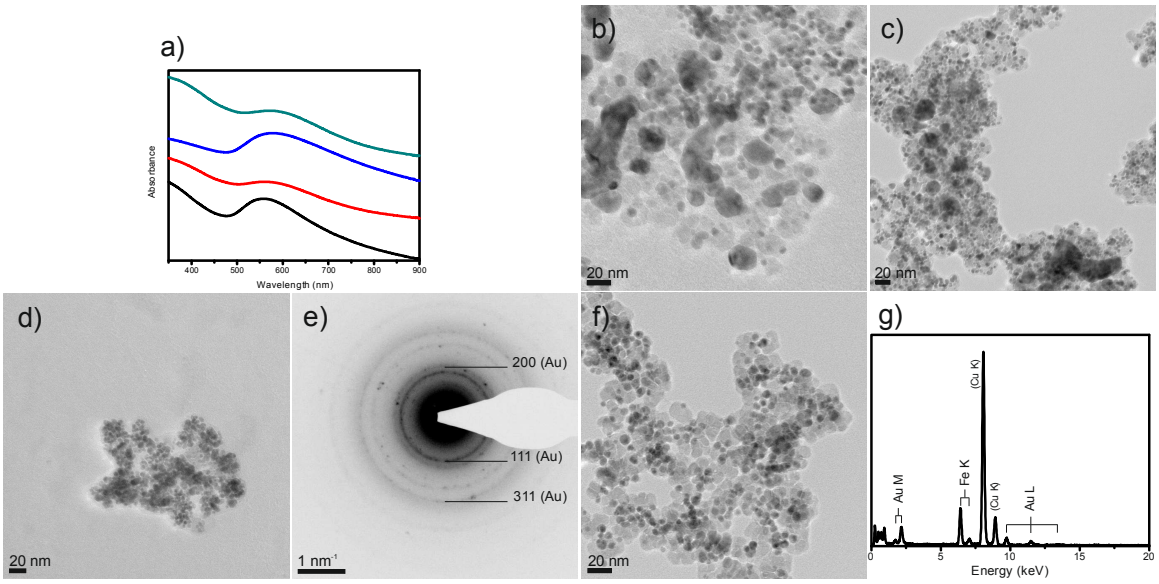

Figure 6.8: (a) UV-Visible spectra of Au-Fe_xO_y nanoparticles synthesized in absence of HDDA (black line) and at a HDDA/$Au(OAc)_3$ molar ratio of 1.3 (red line), 2 (blue line) and 2.5 (green line). TEM images of the corresponding Au-Fe_xO_y nanoparticles synthesized in absence of HDDA (b), and at a HDDA/$Au(OAc)_3$ molar ratio of 1.3 (c), 2 (d) and 2.5 (f). Electron diffraction patterns (e) of the material showed in (d). EDX spectrum (g) of the material showed in (f).

The gradual increase of HDDA led to a reduction of gold particles size and size distribution (figure 6.8b-d, f). However, the optical properties of the related materials did not reflect this trend.

On the contrary of what expected, that is a gradual blue shift and a narrowing of the plasmon resonance band, an overall red shift of about 20 nm was noticed. TEM analysis gave additional information to explain this behaviour. The TEM images (figure 6.8b-d, f) show that two different phases are present. As previously discussed, the particles presenting a darker contrast are attributable to gold while the particles with a lighter contrast are associated to iron oxide. Electron diffraction analysis showed patterns which are partially consistent with the presence of metallic gold (figure 6.8e). However, presence of iron oxide can not be unequivocally assessed due to the partial overlap of some of the characteristic patterns of the two phases. Presence of iron is confirmed by EDX analysis data (figure 6.8g).

Particularly, the relative distribution of iron oxide with respect to metal particles changed while gradually increasing HDDA concentration.

In absence of capping agent, iron oxide looked as randomly distributed around gold nanoparticles. By increasing HDDA concentration, the oxide phase looked as growing around gold particles in a defined way, suggesting the formation of a heterostructure. The most interesting example is represented by the material synthesized using the higher concentration of HDDA: in this case, iron oxide grew asymmetrically on metal particles surface, similarly to a dumbbell-like morphology (figure 6.8f).

Moreover, the amount of oxide surrounding metal nanoparticles seemed to increase when increasing HDDA. A progressively more defined distribution of iron oxide around gold nanoparticles could be the explanation for the measured optical properties of the materials. Indeed, iron oxide has a higher refracting index (n Fe_3O_4= 2.42) than ethanol (n ethanol= 1.36), that is the dispersing solvent. In

general, an increase of refractive index of the medium surrounding metal particles leads to a red shift of the SPR band position, assuming that the Au particles size is constant[60].

A closer view of the material synthesized using the higher concentration of HDDA is given in figure 6.9.

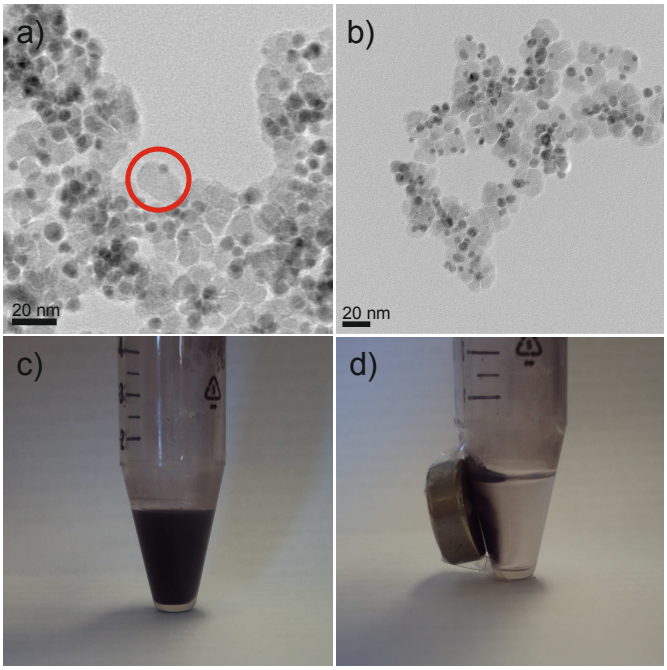

Figure 6.9: TEM images of the sample synthesized at the HDDA/$Au(OAc)_3$ molar ratio of 2.5 (a, b). Digital images of the ethanol dispersion of the same material before (c) and after (d) magnet-induced separation.

The TEM images (figure 6.9a, b) show nearly monodisperse spherical gold particles with an average diameter of 5 nm.

The as-synthesized nanoparticles underwent magnet-induced separation and the resulting supernatant was colourless, supporting the hypothesis that the two materials are interacting and no isolated gold particles are present (figure 6.9c, d).

As previously described, the oxide phase was distributed non-homogeneously all over gold particles surface, but it grew asymmetrically leading to a dumbbell-like structure, as highlighted by a red circle in figure 6.9a. The peculiarity of dumbbell-like structure is to expose the surface of both the component materials to the surrounding medium while maintaining interaction between the two components. This renders the material appealing for several applications. The rather small size of gold nanoparticles makes this material suitable for catalytic applications. Remarkable catalytic properties are indeed observed for gold nanoparticles in the 2-5 nm size range[11]. Gold-iron oxide heterostructures are regarded as promising candidates as catalysts for low temperature water gas shift reaction, important for fuel cells applications[61], and for low temperature CO oxidations[11]. Particularly, the possibility of magnetic manipulation makes the material suitable as recoverable catalyst. Finally, since the surface from both materials is exposed to the surrounding environment, additional

functionalization procedure might be carried out making the material a promising candidate as dual functional probe for diagnostic and therapeutic applications[27].

As previously suggested, iron oxide particles might play the role of co-stabilizer in addition to the organic ligand, therefore, the effect of iron(III) acetylacetonate was also investigated. In view of the properties of the material described in details above, the experiments were performed at a constant concentration of HDDA equal to 3.2 mM;. The oxide precursor concentration was varied from 0.6 to 3.1 mM.

Figure 6.10 illustrates the features of the samples synthesized at different gold-to-metal oxide precursor molar ratios.

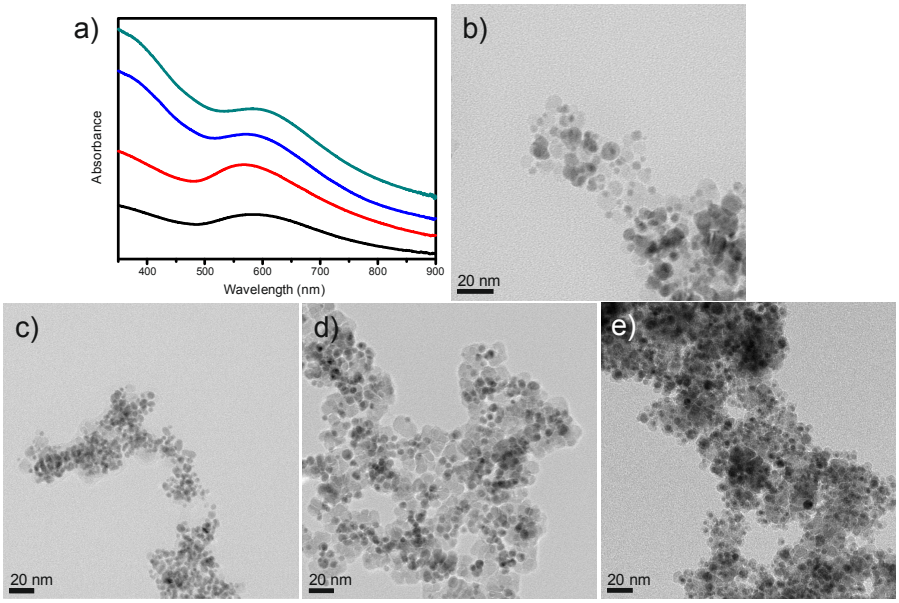

Figure 6.10: (a) UV-Visible spectra of the Au-Fe_xO_y samples synthesized at a $Au(OAc)_3/Fe(acac)_3$ molar ratio of 2.2 (black line), 1.5 (red line), 1 (blue line), and 0.5 (green line). TEM images of the Au-Fe_xO_y materials synthesized at a $Au(OAc)_3/Fe(acac)_3$ molar ratio of 2.2 (b), 1.5 (c), 1 (d), and 0.5 (e).

Similarly to what observed while increasing HDDA concentration, a gradual decrease of the $Au(OAc)_3/Fe(acac)_3$ molar ratio led to less polydisperse and smaller gold nanoparticles. Moreover, Au-Fe_xO_y hetero-nanostructures presenting a better defined morphology were synthesized. In particular, the hybrid materials mainly showed dumbbell-like morphologies (figure 6.10b-e).

This observation might support the previously mentioned hypothesis that iron oxide could play the role of co-stabilizer limiting metal nanoparticles aggregation.

Interestingly, although the majority of the synthesized particles showed dumbbell-like morphology, some gold@iron oxide core@shell structures were noticed when using the larger iron(III) acetylacetonate concentration. This observation indicates that the heterostructures morphology could be influenced varying the concentration of the iron oxide precursor. In particular, it is suggested that the change of the morphology could be influenced by the interplay between the organic intermediary and the oxide precursor. However, the mechanism is still unclear.

It is hypothesized that an excess of organic ligand over the amount of iron oxide precursor might cause the inaccessibility of some sites at gold particles surface thus hindering the nucleation and growth of the oxide phase all over the metal centres (dumbbell-like structures). On the other hand, excess of oxide precursor over the organic intermediary might create the conditions for which the entire surface of gold particles is accessible for the heteronucleation of iron oxide. It is suggested that a ligand exchange step (likely involving HDDA and acetylacetonate species) might render accessible the overall gold nanoparticles surface.

Those findings would support the hypothesis that the heterostructure formation and the obtained morphologies are regulated by the interplay of the organic ligand and metal oxide precursor.

Therefore, fundamental for the desired structure to be obtained is balancing the molar ratios and consequently the effects brought by the individual components of the reaction mixture. It could be stated that for this particular system, satisfactory experimental conditions were determined and a material presenting a structure which shows potential applicability in catalysis and biological fields was produced.

6.3.3. General discussion

The gold-iron oxide system described in this chapter is an appropriate example to demonstrate the complexity of heterodimers growth and to highlight how the properties of the final material are determined by the synergic interactions between all the reaction components.

The most significant difference between the two investigated systems is the morphology of the synthesized gold particles: wire-like structures were obtained using chlorauric acid ($HAuCl_4$), while spherical particles were synthesized using gold acetate ($Au(OAc)_3$).

Although gold arranged in wire-like structures and the corresponding iron oxide-coated heterostructures might be interesting for developing nanoscale electronics and sensor devices, the rather large size and broad size distribution of the metal phase could represent an obstacle to the real applicability of such structures[55]. Additional synthetic efforts are needed for decreasing the particles size and the size distribution.

Gold acetate appeared to be a more suitable precursor for the fabrication of gold nanoparticles in benzyl alcohol. In this case spherical and less polydisperse particles were obtained, which properties might be easily tuned by acting on the organic ligand and metal oxide precursor.

In the $Au(OAc)_3$/benzyl alcohol system, it is suggested that the interplay between metal oxide precursor and organic ligand (HDDA) influences the structural and morphological properties of the final material.

In general, either increasing ligand or metal oxide precursor concentrations, a reduction of gold particles size and size distribution is observed.

Moreover, by increasing the capping agent concentration (keeping the concentration of iron(III) acetylacetonate constant) a heterostructure presenting a defined morphology is synthesized. At particular conditions, iron oxide grows asymmetrically on gold nanoparticles surface leading to a dumbbell-like morphology. This morphology is not clearly noticeable when using lower concentrations of HDDA, where iron oxide appears as randomly distributed around gold particles. Therefore, it is suggested that the organic ligand might promote the contact between the two materials.
A similar trend is observed by increasing iron(III) acetylacetonate concentration until a critical concentration. In fact, at a given iron oxide precursor concentration a change in heterostructure morphology is observed. Iron oxide asymmetric heteronucleation occurs preferentially when the oxide precursor is quantitatively in defect with respect to the organic ligand, while gold-core@iron oxide-shell heterostructures are synthesized using a HDDA-to-$Fe(acac)_3$ molar ratio of 1.
Therefore, it might be inferred that gold-iron oxide heterostructures morphology depends on the experimental conditions. In particular, the observed structural and morphological properties are likely influenced by the interplay between the organic ligand and the metal oxide precursor.
On the contrary, no control of gold nanoparticles size and shape is observed when $HAuCl_4$ is used as the gold precursor. Moreover, flower-like morphology is always obtained when the iron oxide coating is applied.
Adapting the strength of the interaction between the organic ligand and gold particles by choosing molecules with a moderate affinity for the metal, and regulating the capping agent-to-metal precursor molar ratio likely influences the occurrence of oxide heteronucleation. Particularly, the presence of an organic ligand seems to be fundamental for the formation of the heterostructures. Indeed, regardless the chemical nature of the metal precursor, no heteronucleation is accomplished when performing the reaction in absence of any organic ligand.

As previously reported, the strategy adopted in this work is challenging because it consists in placing all the reactants in the same growing medium at the same time. Appropriate reaction conditions should be found in order to control the nucleation of the individual component materials and to favour, at the same time, the heterogeneous nucleation of one of those on the other, which was previously formed *in-situ*.
The present work showed that in the system $Au(OAc)_3$/benzyl alcohol the structural properties of the final heterostructure could be modulated acting on the molar ratio between metal and metal oxide precursors and the organic ligand.
However, some of the reported results could not be easily reproduced, confirming the complexity of heterodimers growth. Several parameters influence the properties of the final material, some of them being not predictable or controllable. It was observed that reagents and solvents purity grades can largely influence the properties of the final materials. Moreover, significant differences may be

determined by instrumental conditions proper of the microwave equipment, such as the applied power profile.

Therefore, while the role of some parameters or reaction components can be investigated, the effects brought about by other variables can not be easily predicted nor explained.

In view of the aim of this work, namely developing a simple and reliable synthesis approach to metal-metal oxide hetero-nanostructures, and of the aforementioned considerations, the project was provisionally set aside.

6.4. Conclusions

The study revealed that the benzyl alcohol route could be extended to the synthesis of metal-metal oxide hetero-nanostructures.

It was observed that the chosen metal precursor can lead to significantly different metal particles morphologies. Spherical particles were obtained using gold acetate ($Au(OAc)_3$), while wire-like structures were synthesized using chlorauric acid ($HauCl_4$). The wire-like structures could be coated by iron oxide in a flower-like morphology and are potentially applicable as nanoscale electronic and sensors devices. However, the system gold acetate/benzyl alcohol is regarded as more suitable for the fabrication of the desired heterostructures. The structural and morphological properties of the metal-metal oxide composite could be tuned by adapting organic ligand and metal oxide precursor concentrations. Particularly, the metal oxide precursor appeared as influencing the morphology of the fabricated heterostructures. In fact, both dumbbell-like and metal@metal oxide core@shell nanoparticles were synthesized. Regardless the composite morphology, rather small gold nanoparticles (about 5 nm in diameter) were obtained. On this basis, the materials are regarded as promising candidates for catalytic applications.

The presence of an organic ligand played a fundamental role in promoting the selective nucleation of the metal oxide at the metal surface. Regardless the used metal precursor, no heteronucleation is accomplished when performing the reaction in absence of any organic ligand. Particularly, heterostructures could be fabricated by controlling the organic ligand concentration and using molecules presenting a moderate affinity for the metal nanoparticles. It was demonstrated that only a restrained amount of organic ligand is needed to promote heteronucleation. This suggests that such species might work as intermediaries at the interface between the two materials, likely through a dynamic adsorption/desorption mechanism. This observation is noteworthy and in contradiction to previous studies on the use of organic species for the synthesis of hetero-nanostructures, which regarded as necessary the use of large amount of surfactants. Nevertheless, a restrained surfactant concentration is fundamental for the further applications of the material since the organic species often invalidate catalytic and electronic properties of the materials. On this perspective, the described system is simpler and cleaner.

Certainly, the results of this work showed that a full control over the formation of gold-iron oxide heterostructures is not achieved yet. Deeper investigation on the mechanism of formation of the heterostructures should provide essential information for improving the synthesis approach. However, the several parameters influencing the structural and morphological properties of the final materials and their likely synergic interaction make the full elucidation of the reaction path not trivial.

6.5. Bibliography

(1) Costi, R.; Saunders, A. E.; Banin, U.: Colloidal Hybrid Nanostructures: A New Type of Functional Materials. *Angewandte Chemie International Edition* **2010**, *49*, 4878-4897.

(2) Shi, W.; Zeng, H.; Sahoo, Y.; Ohulchanskyy, T. Y.; Ding, Y.; Wang, Z. L.; Swihart, M.; Prasad, P. N.: A General Approach to Binary and Ternary Hybrid Nanocrystals. *Nano Letters* **2006**, *6*, 875-881.

(3) Casavola, M.; Buonsanti, R.; Caputo, G.; Cozzoli, P. D.: Colloidal Strategies for Preparing Oxide-Based Hybrid Nanocrystals. *European Journal of Inorganic Chemistry* **2008**, *2008*, 837-854.

(4) Carbone, L.; Cozzoli, P. D.: Colloidal heterostructured nanocrystals: Synthesis and growth mechanisms. *Nano Today* **2010**, *5*, 449-493.

(5) Copel, M.; Reuter, M. C.; Kaxiras, E.; Tromp, R. M.: Surfactants in epitaxial growth. *Physical Review Letters* **1989**, *63*, 632-635.

(6) Buonsanti, R.; Grillo, V.; Carlino, E.; Giannini, C.; Curri, M. L.; Innocenti, C.; Sangregorio, C.; Achterhold, K.; Parak, F. G.; Agostiano, A.; Cozzoli, P. D.: Seeded Growth of Asymmetric Binary Nanocrystals Made of a Semiconductor TiO_2 Rodlike Section and a Magnetic γ-Fe_2O_3 Spherical Domain. *Journal of the American Chemical Society* **2006**, *128*, 16953-16970.

(7) Yu, H.; Chen, M.; Rice, P. M.; Wang, S. X.; White, R. L.; Sun, S.: Dumbbell-like Bifunctional Au−Fe_3O_4 Nanoparticles. *Nano Letters* **2005**, *5*, 379-382.

(8) Gole, A.; Stone, J. W.; Gemmill, W. R.; zur Loye, H.-C.; Murphy, C. J.: Iron Oxide Coated Gold Nanorods: Synthesis, Characterization, and Magnetic Manipulation. *Langmuir* **2008**, *24*, 6232-6237.

(9) Leung, K. C.-F.; Xuan, S.; Zhu, X.; Wang, D.; Chak, C.-P.; Lee, S.-F.; Ho, W. K. W.; Chung, B. C. T.: Gold and iron oxide hybrid nanocomposite materials. *Chemical Society Reviews* **2012**, *41*, 1911-1928.

(10) Glaspell, G.; Fuoco, L.; El-Shall, M. S.: Microwave Synthesis of Supported Au and Pd Nanoparticle Catalysts for CO Oxidation. *The Journal of Physical Chemistry B* **2005**, *109*, 17350-17355.

(11) Haruta, M.: Catalysis of Gold Nanoparticles Deposited on Metal Oxides. *CATTECH* **2002**, *6*, 102-115.

(12) Hong, H.; Hu, L.; Li, M.; Zheng, J.; Sun, X.; Lu, X.; Cao, X.; Lu, J.; Gu, H.: Preparation of Pt@Fe_2O_3 Nanowires and their Catalysis of Selective Oxidation of Olefins and Alcohols. *Chemistry – A European Journal* **2011**, *17*, 8726-8730.

(13) Yoon, K.; Yang, Y.; Lu, P.; Wan, D.; Peng, H.-C.; Stamm Masias, K.; Fanson, P. T.; Campbell, C. T.; Xia, Y.: A Highly Reactive and Sinter-Resistant Catalytic System Based on Platinum Nanoparticles Embedded in the Inner Surfaces of CeO_2 Hollow Fibers. *Angewandte Chemie* **2012**, *124*, 9681-9684.

(14) Cameron, D.; Holliday, R.; Thompson, D.: Gold's future role in fuel cell systems. *Journal of Power Sources* **2003**, *118*, 298-303.

(15) Haruta, M.; Yamada, N.; Kobayashi, T.; Iijima, S.: Gold catalysts prepared by coprecipitation for low-temperature oxidation of hydrogen and of carbon monoxide. *Journal of Catalysis* **1989**, *115*, 301-309.

(16) Cui, Z.-M.; Chen, Z.; Jiang, L.-Y.; Song, W.-G.; Jiang, L.: A true nanocomposite: Single crystalline Au nanoparticles on single crystalline Fe_3O_4 nanoparticles. *Materials Letters* **2011**, *65*, 82-84.

(17) Yin, H.; Ma, Z.; Chi, M.; Dai, S.: Heterostructured catalysts prepared by dispersing Au@Fe_2O_3 core–shell structures on supports and their performance in CO oxidation. *Catalysis Today* **2011**, *160*, 87-95.

(18) Wu, X.-F.; Song, H.-Y.; Yoon, J.-M.; Yu, Y.-T.; Chen, Y.-F.: Synthesis of Core−Shell Au@TiO_2 Nanoparticles with Truncated Wedge-Shaped Morphology and Their Photocatalytic Properties. *Langmuir* **2009**, *25*, 6438-6447.

(19) Yu, Y.-T.; Dutta, P.: Examination of Au/SnO_2 core-shell architecture nanoparticle for low temperature gas sensing applications. *Sensors and Actuators B: Chemical* **2011**, *157*, 444-449.

(20) Oldfield, G.; Ung, T.; Mulvaney, P.: Au@SnO_2 Core–Shell Nanocapacitors. *Advanced Materials* **2000**, *12*, 1519-1522.

(21) Chen, G.; Wang, Z.; Xia, D.: One-Pot Synthesis of Carbon Nanotube@SnO_2−Au Coaxial Nanocable for Lithium-Ion Batteries with High Rate Capability. *Chemistry of Materials* **2008**, *20*, 6951-6956.

(22) Wei, Y.; Klajn, R.; Pinchuk, A. O.; Grzybowski, B. A.: Synthesis, Shape Control, and Optical Properties of Hybrid Au/Fe_3O_4 "Nanoflowers". *Small* **2008**, *4*, 1635-1639.

(23) Shevchenko, E. V.; Bodnarchuk, M. I.; Kovalenko, M. V.; Talapin, D. V.; Smith, R. K.; Aloni, S.; Heiss, W.; Alivisatos, A. P.: Gold/Iron Oxide Core/Hollow-Shell Nanoparticles. *Advanced Materials* **2008**, *20*, 4323-4329.

(24) Zhang, Y.; Ding, H.; Liu, Y.; Pan, S.; Luo, Y.; Li, G.: Facile one-step synthesis of plasmonic/magnetic core/shell nanostructures and their multifunctionality. *Journal of Materials Chemistry* **2012**, *22*, 10779-10786.

(25) Dong, W.; Li, Y.; Niu, D.; Ma, Z.; Gu, J.; Chen, Y.; Zhao, W.; Liu, X.; Liu, C.; Shi, J.: Facile Synthesis of Monodisperse Superparamagnetic Fe_3O_4 Core@hybrid@Au Shell Nanocomposite for Bimodal Imaging and Photothermal Therapy. *Advanced Materials* **2011**, *23*, 5392-5397.

(26) Leff, D. V.; Ohara, P. C.; Heath, J. R.; Gelbart, W. M.: Thermodynamic Control of Gold Nanocrystal Size: Experiment and Theory. *The Journal of Physical Chemistry* **1995**, *99*, 7036-7041.

(27) Wang, C.; Xu, C.; Zeng, H.; Sun, S.: Recent Progress in Syntheses and Applications of Dumbbell-like Nanoparticles. *Advanced Materials* **2009**, *21*, 3045-3052.

(28) Lee, Y.; Garcia, M. A.; Frey Huls, N. A.; Sun, S.: Synthetic Tuning of the Catalytic Properties of Au-Fe_3O_4 Nanoparticles. *Angewandte Chemie* **2010**, *122*, 1293-1296.

(29) Xu, C.; Xie, J.; Ho, D.; Wang, C.; Kohler, N.; Walsh, E. G.; Morgan, J. R.; Chin, Y. E.; Sun, S.: Au–Fe_3O_4 Dumbbell Nanoparticles as Dual-Functional Probes. *Angewandte Chemie International Edition* **2008**, *47*, 173-176.

(30) Turkevich, J.; Stevenson, P. C.; Hillier, J.: A study of the nucleation and growth processes in the synthesis of colloidal gold. *Discussions of the Faraday Society* **1951**, *11*, 55-75.

(31) Frens, G.: Controlled Nucleation for the Regulation of the Particle Size in Monodisperse Gold Suspensions. *Nature Physical Science* **1973**, *241*, 20-22.

(32) Polte, J.; Ahner, T. T.; Delissen, F.; Sokolov, S.; Emmerling, F.; Thünemann, A. F.; Kraehnert, R.: Mechanism of Gold Nanoparticle Formation in the Classical Citrate Synthesis Method Derived from Coupled In Situ XANES and SAXS Evaluation. *Journal of the American Chemical Society* **2010**, *132*, 1296-1301.

(33) Brust, M.; Bethell, D.; Kiely, C. J.; Schiffrin, D. J.: Self-Assembled Gold Nanoparticle Thin Films with Nonmetallic Optical and Electronic Properties. *Langmuir* **1998**, *14*, 5425-5429.

(34) Patel, K.; Kapoor, S.; Dave, D.; Mukherjee, T.: Synthesis of Au, Au/Ag, Au/Pt and Au/Pd nanoparticles using the microwave-polyol method. *Research on Chemical Intermediates* **2006**, *32*, 103-113.

(35) Han, M. Y.; Quek, C. H.; Huang, W.; Chew, C. H.; Gan, L. M.: A Simple and Effective Chemical Route for the Preparation of Uniform Nonaqueous Gold Colloids. *Chemistry of Materials* **1999**, *11*, 1144-1147.

(36) Pastoriza-Santos, I.; Liz-Marzán, L. M.: Formation of PVP-Protected Metal Nanoparticles in DMF. *Langmuir* **2002**, *18*, 2888-2894.

(37) Jun, Y.-w.; Choi, J.-s.; Cheon, J.: Shape Control of Semiconductor and Metal Oxide Nanocrystals through Nonhydrolytic Colloidal Routes. *Angewandte Chemie International Edition* **2006**, *45*, 3414-3439.

(38) Pinna, N.; Niederberger, M.: Surfactant-Free Nonaqueous Synthesis of Metal Oxide Nanostructures. *Angewandte Chemie International Edition* **2008**, *47*, 5292-5304.

(39) Vioux, A.: Nonhydrolytic Sol−Gel Routes to Oxides. *Chemistry of Materials* **1997**, *9*, 2292-2299.

(40) Aqueous and Nonaqueous Sol-Gel Chemistry. In *Metal Oxide Nanoparticles in Organic Solvents*; Springer London, 2009; pp 7-18.

(41) Pinna, N.; Karmaoui, M.; Willinger, M.-G.: The "benzyl alcohol route": An elegant approach towards doped and multimetal oxide nanocrystals. *J Sol-Gel Sci Technol* **2011**, *57*, 323-329.

(42) Truby, R. L.; Emelianov, S. Y.; Homan, K. A.: Ligand-Mediated Self-Assembly of Hybrid Plasmonic and Superparamagnetic Nanostructures. *Langmuir* **2013**, *29*, 2465-2470.

(43) Chin, S. F.; Iyer, K. S.; Raston, C. L.: Facile and Green Approach To Fabricate Gold and Silver Coated Superparamagnetic Nanoparticles. *Crystal Growth & Design* **2009**, *9*, 2685-2689.

(44) Dong, A.; Ye, X.; Chen, J.; Kang, Y.; Gordon, T.; Kikkawa, J. M.; Murray, C. B.: A Generalized Ligand-Exchange Strategy Enabling Sequential Surface Functionalization of Colloidal Nanocrystals. *Journal of the American Chemical Society* **2010**, *133*, 998-1006.

(45) Bilecka, I.; Niederberger, M.: Microwave chemistry for inorganic nanomaterials synthesis. *Nanoscale* **2010**, *2*, 1358-1374.

(46) Kappe, C. O.: Unraveling the Mysteries of Microwave Chemistry Using Silicon Carbide Reactor Technology. *Accounts of Chemical Research* **2013**, *46*, 1579-1587.

(47) Baghbanzadeh, M.; Carbone, L.; Cozzoli, P. D.; Kappe, C. O.: Microwave-Assisted Synthesis of Colloidal Inorganic Nanocrystals. *Angewandte Chemie International Edition* **2011**, *50*, 11312-11359.

(48) Kappe, C. O.; Pieber, B.; Dallinger, D.: Microwave Effects in Organic Synthesis: Myth or Reality? *Angewandte Chemie International Edition* **2013**, *52*, 1088-1094.

(49) Baek, S.; Yu, S.-H.; Park, S.-K.; Pucci, A.; Marichy, C.; Lee, D.-C.; Sung, Y.-E.; Piao, Y.; Pinna, N.: A one-pot microwave-assisted non-aqueous sol-gel approach to metal oxide/graphene nanocomposites for Li-ion batteries. *RSC Advances* **2011**, *1*, 1687-1690.

(50) Bilecka, I.; Djerdj, I.; Niederberger, M.: One-minute synthesis of crystalline binary and ternary metal oxide nanoparticles. *Chemical Communications* **2008**, 886-888.

(51) Russo, P. A.; Ahn, M.; Sung, Y.-E.; Pinna, N.: Improved electrocatalytic stability in ethanol oxidation by microwave-assisted selective deposition of SnO_2 and Pt onto carbon. *RSC Advances* **2013**, *3*, 7001-7008.

(52) Pinna, N.; Grancharov, S.; Beato, P.; Bonville, P.; Antonietti, M.; Niederberger, M.: Magnetite Nanocrystals: Nonaqueous Synthesis, Characterization, and Solubility†. *Chemistry of Materials* **2005**, *17*, 3044-3049.

(53) Liz-Marzán, L. M.; Giersig, M.; Mulvaney, P.: Synthesis of Nanosized Gold−Silica Core−Shell Particles. *Langmuir* **1996**, *12*, 4329-4335.

(54) Fan, X.; Liu, L.; Guo, Z.; Gu, N.; Xu, L.; Zhang, Y.: Facile synthesis of networked gold nanowires based on the redox characters of aniline. *Materials Letters* **2010**, *64*, 2652-2654.

(55) Pazos-Pérez, N. s.; Baranov, D.; Irsen, S.; Hilgendorff, M.; Liz-Marzán, L. M.; Giersig, M.: Synthesis of Flexible, Ultrathin Gold Nanowires in Organic Media. *Langmuir* **2008**, *24*, 9855-9860.

(56) Pei, L.; Mori, K.; Adachi, M.: Formation Process of Two-Dimensional Networked Gold Nanowires by Citrate Reduction of $AuCl_4^-$ and the Shape Stabilization. *Langmuir* **2004**, *20*, 7837-7843.

(57) Pong, B.-K.; Elim, H. I.; Chong, J.-X.; Ji, W.; Trout, B. L.; Lee, J.-Y.: New Insights on the Nanoparticle Growth Mechanism in the Citrate Reduction of Gold(III) Salt: Formation of the Au Nanowire Intermediate and Its Nonlinear Optical Properties. *The Journal of Physical Chemistry C* **2007**, *111*, 6281-6287.

(58) Zhang, J. Z.; Noguez, C.: Plasmonic Optical Properties and Applications of Metal Nanostructures. *Plasmonics* **2008**, *3*, 127-150.

(59) Wang, L.; Park, H.-Y.; Lim, S. I. I.; Schadt, M. J.; Mott, D.; Luo, J.; Wang, X.; Zhong, C.-J.: Core@shell nanomaterials: gold-coated magnetic oxide nanoparticles. *Journal of Materials Chemistry* **2008**, *18*, 2629-2635.

(60) Chanana, M.; Liz-Marzán Luis, M.: Coating matters: the influence of coating materials on the optical properties of gold nanoparticles. In *Nanophotonics*, 2012; Vol. 1; pp 199.

(61) Andreeva, D.: Low temperature water gas shift over gold catalysts. *Gold Bull* **2002**, *35*, 82-88.

Chapter 7

Summary and conclusions

The constantly growing impact of nanotechnology in several application fields of everyday-life motivated researchers to develop novel functional materials. Because of the high surface-to-volume ratio, surface chemistry of nanoparticles significantly contributes in determining material properties. Therefore, control on surface chemical composition is regarded as a crucial issue in the fabrication of nanostructured functional materials.

This thesis described diverse approaches of chemical functionalization as a strategy to tailor the properties of a material depending on the target application; particular attention was dedicated to functionalization of iron oxide nanoparticles. Magnetite nanoparticles synthesized through the "benzyl alcohol route" present an average size of 10 nm, hence they show superparamagnetic behaviour. For this reason, they are regarded as suitable solid supports for the fabrication of recoverable systems, which is a fundamental requirement for several of the reported studies.

This thesis demonstrated, *via* the fabrication of novel hybrid materials, that the ease of functionalization of iron oxide nanoparticles renders this material a versatile platform for the development of diverse surface chemistries.

The simplicity and versatility of post-synthesis strategies was demonstrated by coating magnetite nanoparticles with undecanoic acid and citric acid, which led to stable organic and aqueous dispersions. Colloidal stability permitted to deposit isolated nanoparticles between nanometer-spaced electrodes. This allowed the investigation of the electronic properties of a single nanoparticle. The study highlighted the crucial influence that the organic coating can have on the electronic properties: while undecanoic acid behaved as an insulator and its replacement was required prior to perform the analyses, citric acid positively contributed to the charge-transfer measurements creating the necessary tunnel barrier for "on-chip" electronic tunnelling spectroscopy.

A central aspect of this thesis lies in the choice and the role of selected chemical functionalities in controlling the formation of the target material.

Designing a suitable organic shell permitted to synthesize two kinds of heterogeneous molecular receptors. In the first case, tetraphosphonate cavitands were introduced at nanoparticles surface through two approaches, namely non-covalent and covalent. Both of the strategies exploited the carboxyl moieties present at the lower rim of the molecular cavity. Coordination of carboxylate ions at surface iron atoms provided a non-covalent cavitand shell. Relatively high surface coverage was achieved, corresponding to a 40% for the theoretical monolayer. The covalent approach was a two-step strategy based on the use of organosilane as coupling agents. In the first step, amino groups and short PEG chains were grafted at particles surface. The PEG chains conferred partial aqueous

dispersibility, important property for further applications as molecular receptors for biomarkers in biological fluids. Conjugation of cavitands to the surface amino groups was successfully carried out *via* the carbodiimide chemistry. Although the covalent strategy allowed developing a multifunctional organic shell, it led to a more restrained amount of grafted cavitand molecules than non-covalent approach. The comparison between the two approaches was the central aspect of this study.

Organosilane coupling agents were used also in a second work focused on the heterogeneous resolution of a racemic mixture of a chiral cavitand. Enantiopure N-methyl-L-alanine was covalently grafted on surface amino groups for the recognition of chiral phosphonate cavitands. HPLC analysis revealed that enantioselective recognition was successfully achieved at particles surface, demonstrating the promising application as a recoverable device for a fast and facile chiral resolution of cavitand racemates.

This thesis contributed also to highlight the importance that the elucidation of the structure-properties relationships can have on the development of novel hybrid materials.

Graphene oxide-iron oxide composites were successfully fabricated through an *ex-situ* approach based on non-covalent interactions between the component phases. The effects of surface functionalities on the structural properties of the composites were studied by grafting 4-carboxyphenyl groups at graphene oxide (GO) surface through diazonium chemistry. Detailed chemical and structural characterization revealed the existence of specific interactions between functionalized graphene oxide (*f*-GO) and iron oxide nanoparticles. The prevalence of such specific interactions was reflected in a more homogeneous distribution and higher loading on *f*-GO than on pristine GO. The results were supported by the study of the electrochemical properties of the materials.

A last study revealed that the benzyl alcohol route could be extended to the one-pot synthesis of gold-iron oxide hetero-nanostructures. Particularly, $Au(OAc)_3/Fe(acac)_3$ was demonstrated to be the more suitable system for the fabrication of the desired hybrid material. Depending on the experimental conditions, dumbbell-like and gold@iron oxide core@shell nanoparticles were synthesized. The study focused on investigating the role of small organic molecules in promoting the synthesis of the heterostructures. It was shown that organic ligands were fundamental for the formation of the nanocomposite, which was found to be dependent on the ligand concentration and binding affinity to the metal phase. The restrained amount of organic molecules required to promote heteronucleation suggested that such species might work as intermediaries at the interface between the two materials.

Symbols and abbreviations

γ_D, γ_G	*Widths of D- and G- bands, respectively*
ω_D, ω_G	*Wavenumber positions of D- and G- bands, respectively*
ν_{as}	*Carboxylate asymmetric stretching mode*
ν_s	*Carboxylate symmetric stretching mode*
$\Delta\nu$	*Difference between carboxylate asymmetric and symmetric stretching modes*
σ_s, σ_i, σ_f,	*Free energies of substrate, interface and "coating" material, respectively*
ACN	*Acetonitrile*
APTMS	*(3-Aminopropyl)trimethoxysilane*
Boc	*tert-Butoxycarbonyl*
CHN-S	*Carbon, hydrogen, nitrogen and sulphur elemental analysis*
Cit	*Citric acid*
CTA^+	*Cetyltrimethylammonium cation*
CTAB	*Cetyltrimethylammonium bromide*
DCC	*N,N'-dicyclohexylcarbodiimide*
DCM	*Dichloromethane*
DLS	*Dynamic light scattering*
DLVO	*Derjaguin-Landau-Verwey-Overbeek theory*
DMAP	*4-(dimethylamino)pyridine*
DMF	*N,N'-dimethylformamide*
EDC	*1-ethyl-3-(3-dimethylaminopropyl)carbodiimide*
EDLCs	*Electrical double layer capacitors*
EDX	*Energy dispersive X-ray spectroscopy*
EIS	*Electrochemical impedance spectroscopy*
Fmoc	*9-Fluorenylmethoxycarbonyl*
FTIR	*Fourier transform infrared spectroscopy*
HDDA	*11-Hydroxydodecanoic acid*
HOPG	*Highly oriented pyrolytic graphite*
HPLC	*High-performance liquid chromatography*
MRI	*Magnetic resonance imaging*
MRS	*Micro-Raman spectroscopy*
MUA	*11-Mercaptoundecanoic acid*
NHS	*N-hydroxysuccinimide*
PEG	*Poly(ethylene glycol)*
PEOS	*2-[methoxy(polyethylenoxy)propyl] trimethoxysilane*

PTFE	*Polytetrafluoroethylene*
rac-	*Racemate*
R_{ct}	*Charge transfer resistance*
R_s	*Resistance of the bulk electrolyte*
SEM	*Scanning electron microscopy*
STM	*Scanning tunneling microscope*
T_V	*Verwey temperature*
TEM	*Transmission electron microscopy*
TGA	*Thermogravimetric analysis*
UA	*Undecanoic acid*
UV-Visible	*Ultraviolet-Visible*
W_s	*Warburg impedance*
XPS	*X-ray photoelectron spectroscopy*
XRD	*X-ray powder diffraction*
Z', Z''	*Real and imaginary parts, respectively, of the electrochemical impedance*

List of figures

Chapter 1

Chapter 2

colours indicate the three different identified regimes: polaron tunnelling (light blue area), low temperature insulating phase (yellow area), and high temperature conducting phase (green area).

Chapter 3

Chapter 4

Chapter 5

Chapter 6

wire-like structures (a, b). Subsequently wire-like structures undergo fragmentation forming shorter segments (c), which finally evolve into isolated spherical nanoparticles and few residual short wires (d).

Figure 6.7: (a) UV-Visible spectra of Au-Fe_xO_y nanoparticles synthesized in presence of HDDA only (black line), using a mixture of HDDA/MUA at a molar ratio of 2 (red line) and 1 (blue line), and in the presence of pure MUA (green line). TEM images of the corresponding Au-Fe_xO_y materials synthesized using HDDA only (b), using MUA only (c), employing a HDDA/MUA molar ratio of 2 (d) and 1 (e). EDX spectrum (f) of the material showed in (c).

Figure 6.8: (a) UV-Visible spectra of Au-Fe_xO_y nanoparticles synthesized in absence of HDDA (black line) and at a HDDA/$Au(OAc)_3$ molar ratio of 1.3 (red line), 2 (blue line) and 2.5 (green line). TEM images of the corresponding Au-Fe_xO_y nanoparticles synthesized in absence of HDDA (b), and at a HDDA/$Au(OAc)_3$ molar ratio of 1.3 (c), 2 (d) and 2.5 (f). Electron diffraction patterns (e) of the material showed in (d). EDX spectrum (g) of the material showed in (f).

Figure 6.9: TEM images of the sample synthesized at the HDDA/$Au(OAc)_3$ molar ratio of 2.5 (a, b). Digital images of the ethanol dispersion of the same material before (c) and after (d) magnet-induced separation.

Figure 6.10: (a) UV-Visible spectra of the Au-Fe_xO_y samples synthesized at a $Au(OAc)_3$/$Fe(acac)_3$ molar ratio of 2.2 (black line), 1.5 (red line), 1 (blue line), and 0.5 (green line). TEM images of the Au-Fe_xO_y materials synthesized at a $Au(OAc)_3$/$Fe(acac)_3$ molar ratio of 2.2 (b), 1.5 (c), 1 (d), and 0.5 (e).

List of tables

Chapter 3

Chapter 5

Chapter 6

Selbstständigkeitserklärung

Hiermit erkläre ich, die vorliegende Arbeit selbstständig geschrieben und erarbeitet zu haben. Alle im Text beschriebenen von anderen erarbeiteten wissenschaftlichen Inhalte und verwendeten Methoden sind als solche explizit gekennzeichnet und mit den richtigen bibliographischen Angaben im Literaturverzeichnis zitiert.

Weiterhin erkläre ich, diese Arbeit nicht an anderer Stelle eingereicht zu haben.

Declaration of independent work

Here, I declare that the present doctoral thesis was independently written and the described scientific contents were independently elaborated. All the used methods and knowledge firstly developed by others have been explicitly cited in the written text and the proper bibliographic references were reported in a dedicated section.

Furthermore, I declare that this thesis has not been submitted elsewhere before.